Modeling and Control of a Magnetically Levitated Microrobotic System

by

David Gordon Craig

A thesis
presented to the University of Waterloo
in fulfillment of the
thesis requirement for the degree of
Master of Applied Science
in
Mechanical Engineering

Waterloo, Ontario, Canada, 2006

Author's Declaration for Electronic Submission of a Thesis

I hereby declare that I am the sole author of this thesis. This is a true copy of the thesis, including any required final revisions, as accepted by my examiners.

I understand that my thesis may be made electronically available to the public.

Abstract

Magnetically levitated microrobotic systems have shown a great deal of promise for micromanipulation tasks. A new large-gap magnetic suspension system has recently been developed at the University of Waterloo in order to develop microrobotic systems for various applications. In order to achieve motion with the system, a model is needed in order to facilitate the design of various aspects of the system, such as the microrobot and the controller.

In order to derive equations of motion for the system attempts were made to characterize the force produced by the magnetic drive unit in terms of a simple analytical equation. The force produced by the magnetic drive unit was estimated with the aid of a finite element model. The derived equations were able to predict the general trend of the force curves, and with sufficient parameter tweaking the error between the force estimated by the finite element model and the force estimated by the analytical equation could be minimized.

System models describing the motion of the system in the horizontal and vertical directions are identified and compared to the actual system response. The vertical position response is identified through a least squares parameter estimate of the closed loop response combined with a partial reconstruction of the root locus diagram, with the model structure based on the known dynamics of a simplified form of magnetic levitation. This model was able to provide a reasonable prediction of the system response for a variety of PID controllers under a variety of input conditions. The horizontal models are identified using a least-squares parameter estimate of the open loop characteristics of the system. The horizontal models are able to provide a reasonable prediction of the system response under PD and PID control.

Full spatial motion of a microrobot prototype is demonstrated over a working range of 20x22x30 mm^3, with PID controller parameters and reference trajectories adjusted to minimize disturbances. The RMS error at steady state is on the order of 0.020 mm for vertical positioning and 0.008 mm for horizontal positioning. A linear quadratic regulator implemented for vertical position control was able to reduce the vertical position RMS error to 0.014 mm.

Acknowledgements

I would like to thank my supervisor, Professor Mir Behrad Khamesee, and my research colleague, Ehsan Shameli, for their support and guidance during the course of my research. The work of Jonathan Gammell must also be acknowledged, as he was heavily involved in the design and construction of our magnetic drive unit. I would also like to acknowledge the contributions of Professors Amir Khajepour and Steve Lambert towards the final product you are now reading. I would like to thank Andrew Barber and Robert Wagner for their assistance in setting up and improving our system hardware. I am also grateful for the help provided by Benjamin Zimmer in developing the data recording system for the experimental setup. I would like to thank Professor Bill Wilson for allowing me to use his system identification code during the course of my research. Finally I would like to thank my family for all of their support during my academic career.

Funding for this research was provided in part by the Natural Sciences and Engineering Research Council of Canada (NSERC).

Table of Contents

List of Figures

List of Tables

Chapter 1
Introduction

1.1 Microrobotic Propulsion Systems: An Overview

In recent years there has been a growing interest in the design and development of micro- and nano-scale robotic manipulator systems to meet growing needs in various fields. One such application of this technology is the design of micro-assembly stations for the handling of precision microparts. Such a system is described in [1], in which a series of cm^3 sized microrobots with five degrees of freedom are designed to perform operations under a light microscope or within the vacuum chamber of a scanning electron microscope. This sort of system would be very useful in the burgeoning field of nanotechnology.

Microrobotic systems also show promise in the field of inspection, particularly in-pipe inspection for cracks and other defects. A microrobot designed to travel though 10 mm diameter pipes is discussed in [2]. Another microrobot designed for travel in 1 inch pipes is described in [3].

Microrobotic systems also show a great deal of promise in biomedical fields. The micro-assembly stations described above would be suitable for the handling and manipulation of cellular or other small biological samples. Several microrobotic systems have been developed to perform endoscopic operations and investigation of the digestive tract [4] [5].

One of the more complex issues related to the design of microrobotic systems is the design of the propulsion system. As objects scale down in size, viscous forces start to become dominant, and the amount of power required to propel the system will increase [6] [7]. For example, [8] describes several microrobots that use various piezoelectric-based actuator assemblies for motion. The authors discuss how their original design required 300 volts to actuate the piezoelectric actuators, while a more recent design allowed them to reduce the required input to 60 volts. Of more recent interest is the development of ionic conducting polymer film (ICPF) actuators. Under wet conditions the ICPF actuator will deform under as little as 1.5 volts. This actuator was successfully implemented on a fish-like microrobot [9].

Depending on the size of the microrobot electromagnetic [10] [11] and pneumatic micromotors [12] may also be an option for driving wheels, tracks, or propellers.

There is also the issue of how the power is transmitted. Some of the various methods used on robotic systems include direct wiring, batteries, and solar power. The main disadvantage of direct wiring is that it limits the operating range of the microrobot, and may also hinder the motion of the microrobot [8]. There may also be issues with convenience for the end user. The endoscopic robot discussed in [4] is driven by pneumatic power. The trailing wires required to power the robot may be a source of discomfort to the patient during operation of the system. The invasiveness of the robot could be reduced significantly if an on-board power system were used to eliminate the trailing wires.

The most apparent way to overcome this issue is through the use of on board power storage, i.e. a battery. The main drawback to this technology is that the amount of power a battery can store is proportional to the volume of the battery [13]. Although batteries are able to eliminate many of the problems associated with direct wiring, the operating life of the microrobot will be significantly reduced since most batteries on the centimetre and millimetre scale cannot store the amount of energy required to operate the system actuators over an extended period of time.

Solar-powered robots have shown some promise. In [14] 90 solar cells spread out over a 2 mm^2 area are able to produce 100 μW of power, which is more than sufficient to power the simple robotic design discussed in the paper. Similarly, in [15] a solar array is used to generate a 100 volt power supply, which is theoretically capable of driving many of the propulsion systems described above but has yet to be implemented on a microrobotic system. Solar power is not without its disadvantages, one example being that it would be impossible for a robot operating in the human body to receive any sort of power from a solar array.

Further complicating matters is that the propulsion system will not be the only on-board system requiring power. There will also be actuators and communications equipment that will require a power source to operate.

One means of microrobotic propulsion that has shown a great deal of promise is the use of a magnetic propulsion system. The system consists of a magnetic drive unit which generates a magnetic field in space. A magnetic object is attached to the microrobot, and the resulting field interaction will produce a force or torque on the magnetic object that can be converted into system motion. This concept is shown schematically in Figure 1-1. The primary benefit of magnetic propulsion systems is that the magnetic field is produced external to the microrobot, and the locomotive power is transmitted "wirelessly" through the interaction between the magnetic field and magnetic object. Magnetic propulsion systems offer many benefits for micro-scale applications. Because all of the locomotive power is produced in the macro world with conventional electromagnetic and power supply technologies, it will always be possible (within reasonable limits) to produce enough force to overcome viscous and coulomb friction effects. Theoretically the microrobot would also have an infinite operating life as long as power could be provided to the drive unit. The propulsion system is completely passive, having no moving parts whatsoever. This is beneficial from a maintenance and servicing standpoint, as components with moving parts may be subject to frequent servicing (such as lubrication of joints) or the replacement of components due to failure (such as fatigue). The passive nature of the system also makes magnetic suspension suitable for use in applications where a clean operating environment is required. Systems with moving components may accumulate dust or other contaminants at joints, including but not limited to any lubricating fluids used to ensure proper functioning of the system. Magnetic suspension therefore has potential uses in industries such as semiconductor manufacturing [16] and microsurgery [17].

1.2 Propulsion via Magnetic Fields

The most common form of magnetic propulsion is magnetic levitation in air, or more generally magnetic suspension when considering motion along three axes. This form of magnetic propulsion will be discussed in more detail below. It should be noted that this is not the only possible form of magnetic propulsion. For example, [18] discusses the design of

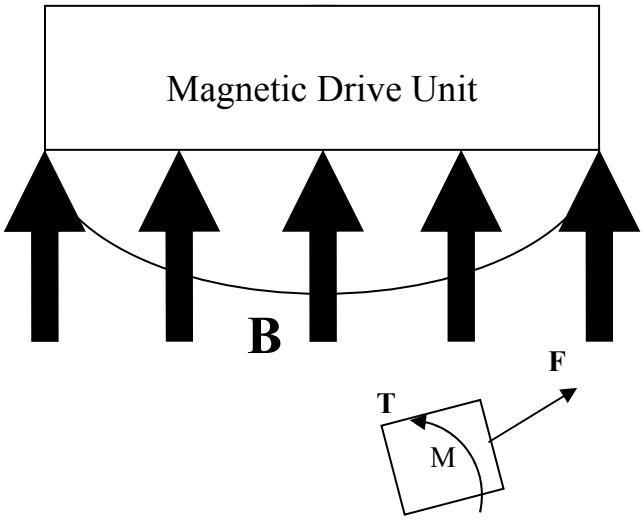

Figure 1-1: Schematic representation of a generalized magnetic propulsion system. The interaction between the flux density field *B* and the magnetic object *M* will produce forces and torques that cause motion.

a swimming microrobot that propels itself through water via the magnetic torque produced by the interactions between an external field and a permanent magnet on the microrobot's body.

Magnetic suspension involves the manipulation of the electromagnetic field of the magnetic drive unit to counteract the weight of the object being lifted, allowing it to be suspended in air. In the macro world a form of this technology is used on certain types of trains to levitate the railcars above the track. This eliminates the rail/wheel contact friction, allowing the train to travel at higher velocities. Maglev trains are capable of traveling at speeds of up to 500 km/hr, nearly twice as fast as a typical train [19]. At this rate of travel maglev trains serve as a viable mass transportation alternative to short haul airplane travel. Forward propulsion of the system is also provided by the magnetic drive unit in a manner similar to the operation of a linear motor. A scale model version of this technology is discussed in [20], while [21] discusses the modeling of the magnetic suspension of the rail car.

Magnetic suspension systems are also used to freely suspend objects in wind tunnel experiments [22]. The object being studied is floating free in the chamber and is not physically grounded at any point, allowing for a better understanding of the aerodynamic properties of the system. The position and orientation of the object can also be adjusted while the wind tunnel is in operation, minimizing downtime due to the changing of experimental parameters.

Magnetic suspension has been studied for use in applications on a smaller scale. Bridging the gap between the macro and micro world is a rail transport system used for the transport of wafers in semiconductor manufacturing [16]. While this may be useful for some applications the motion of the system is ultimately constrained by the rails. Of more general interest for microrobotic applications is the ability to generate arbitrary spatial motion of the levitated object over an arbitrary area.

General magnetic suspension has been investigated in a variety of forms. A common approach is to use a plate suspended over a series of electromagnets [23] or a linear synchronous motor [24] [25]. For example, in [23] a 173 g plate is levitated via the interaction between four electromagnets and 36 neodymium permanent magnets (each with a magnetization value of 867,000 A/m) mounted to the plate. The nominal current in each electromagnet is 0.44 A, and the minimum air gap length is 500 μm. While such systems show a large operating range in the horizontal plane, the vertical operating range is significantly less, due to the need to maintain a small air gap between the levitated object and the drive unit. The operating ranges of the levitation systems described in [23], [24], and [25] are presented in Table 1-1. These systems improve on the guided track systems as they allow for motion anywhere in the horizontal plane, but the constrained vertical travel would not be suitable for applications where the working area has multiple platforms or is otherwise irregular, such as traversing through the digestive tract of the human body.

One possible method of overcoming this problem is through the use of a two stage system. The first stage would provide “coarse” motion of the system to a desired area, while the second stage would provide finer positioning through the magnetic suspension system. Such

a system is described in [26] with the fine positioning wrist having a horizontal operating range of 4.5 mm by 4.5 mm.

In [27], the development of another magnetically levitated device that allows for a larger range of motion is presented. The preliminary design was only capable of moving 300 μm along the three primary axes [28]. The second generation prototype greatly improved on this design, allowing the microrobot to levitate up to 7 mm away from the magnetic drive unit and allow 5 mm of travel in the horizontal directions. Power consumption in each electromagnet was also reduced from 320 mW to 125 mW. The second generation levitated object weighed 267 g and was theoretically capable of lifting payloads of up to 2 kg. The magnetic drive unit consists of six electromagnets, and the microrobot is fitted with six permanent magnets. Each magnet interacts directly with one of the electromagnets to produce motion. One benefit of this configuration is that it allows for full 6 DOF motion in space, which may be useful for maneuvering around obstacles or interacting with objects that are offset at an angle from the primary axes. The primary disadvantage to such a system is that there is still relatively close contact between the levitated object and the magnetic drive unit, which would make it difficult to isolate the levitated object in a closed environment.

Reference Paper	Horizontal Range	Vertical Range
[23]	32 mm x 32 mm	1.5 mm
[24]	50 cm x 50 cm	5 mm
[25]	50 mm x 50 mm	400μm

Table 1-1: Comparison of operating ranges of various magnetic levitation devices with a small air gap.

In the systems discussed above the position of the magnetic drive unit is fixed and some other variable (normally current) is controlled to produce the magnetic field in which motion will occur. It is also possible to achieve similar results by fixing the field and varying the position of the drive unit. The system in [29] describes a 2 DOF system where the magnetic drive unit consists of permanent magnets attached to linear actuators. Motion of the actuators causes displacement of the static field produced by the permanent magnets, creating the time varying magnetic field required for stable motion. Such a system may offer an

advantage in terms of reduced input power if the linear actuators do not require as much input power as an electromagnet. The use of linear actuators to power the drive unit does create moving parts which will need maintenance and may be a source of contaminants if separation of the magnetic drive unit and levitating object cannot be achieved.

Magnetic suspension is not without its disadvantages. Limitations on input power to the magnetic drive unit for practical and safety purposes will limit the strength of the magnetic field and the amount of force the system can produce. This will limit the amount of weight that can be suspended in the field. This can be an issue with payload delivery applications, as heavy microrobots will not be able to carry as much weight as a lighter microrobot.

1.3 Large Gap Magnetic Suspension System

In a large gap magnetic suspension system, the distance between the magnetic drive unit and the suspended object is relatively large. This allows for a much larger operating range than the systems shown in Table 1-1. Another advantage of such a system is that, for sufficiently large gaps, an enclosed chamber can be built around the microrobot's workspace. This would further reduce possible environmental contamination in a clean room application as the only possible source of contaminants within the chamber is the microrobot. It would also be suitable for microsurgical applications which would require insertion and navigation of a microrobotic system inside a human body.

A large gap magnetic levitation system is discussed in [30]. A microrobot weighing 0.088 N is suspended in a flux density field produced by four electromagnets. The nominal strength of this field is approximately 0.01 T when each electromagnet is energized by 0.72 A of current. The potential vertical working envelope of this system is 30 mm, which is a considerable improvement over the vertical working ranges shown in Table 1-1. Actual motion takes place in a 29x29x26 mm^3 working envelope, with the upper edge of the envelope located 10 mm below the drive unit. This large scale motion is achieved through the design of the magnetic drive unit. The four electromagnets used to generate the magnetic field are attached to a piece of soft iron, known as a pole piece. The pole piece acts to unify and strengthen the fields produced by the individual electromagnets. The resultant field

produced underneath the pole piece will provide greater strength and better field continuity than would be possible with individual electromagnets, allowing for smooth, continuous motion in the workspace.

1.4 Applications of Large Gap Microrobotic Systems

1.4.1 Micro-Assembly and Micro-Manufacturing

The large gap magnetic suspension system is suitable for micro-assembly and micromanipulation tasks. A concept schematic is shown in Figure 1-2. The microrobot is equipped with a gripper that is designed to grasp objects within the workspace. Such grippers are typically manufactured from bimorphic materials such as shape memory alloys [30], piezoelectric materials [31], dissimilar metals [7], and ionic conducting polymer film actuators [9]. The general characteristic of these materials is that they will deform when energized by a current and return to their original shape when the current is removed. These materials provide a simple mechanical means for providing a gripping motion without the need for a complex series of mechanical components.

The workspace of the system does not necessarily have to be planar, since the microrobot is capable of motion in all three cardinal directions. The large spatial separation between the magnetic drive unit and the microrobot allows for the microrobot to operate in an enclosed space, separate from the rest of the environment. This would be useful for applications in semiconductor manufacture, such as wafer transportation or photolithography. It would also be useful in pharmaceutical or biomedical research, both to minimize environmental contaminants or to protect the operator from potentially hazardous chemicals. In all of these cases, the isolation of the magnetic drive unit from the clean room area means that it would not have to be decontaminated between work operations. Multiple robots are used so that, while one robot is being cleaned, the other robot is put into service, reducing down time. If the cost of the microrobot can be kept to a minimum it could even be disposed of after use if the cost of decontamination is prohibitively high.

1.4.2 Pipe Inspection

The microrobot could also be used for in-pipe inspection. A concept sketch is shown in Figure 1-3. In this case the microgripper would be replaced with a microcamera [4] or some other type of sensor for inspecting the structural integrity of pipes. The magnetic drive unit can be placed around the pipe diameter in order to drive the microrobot through the pipe. Such a system could consist of a coarse motion actuator to drive the magnetic drive unit over a long length of pipe. The magnetic or eddy current effects induced in metallic pipes by the magnetic drive unit could also be of use in providing the propulsive force for the microrobot. The microrobot could also navigate short sections of vertical piping.

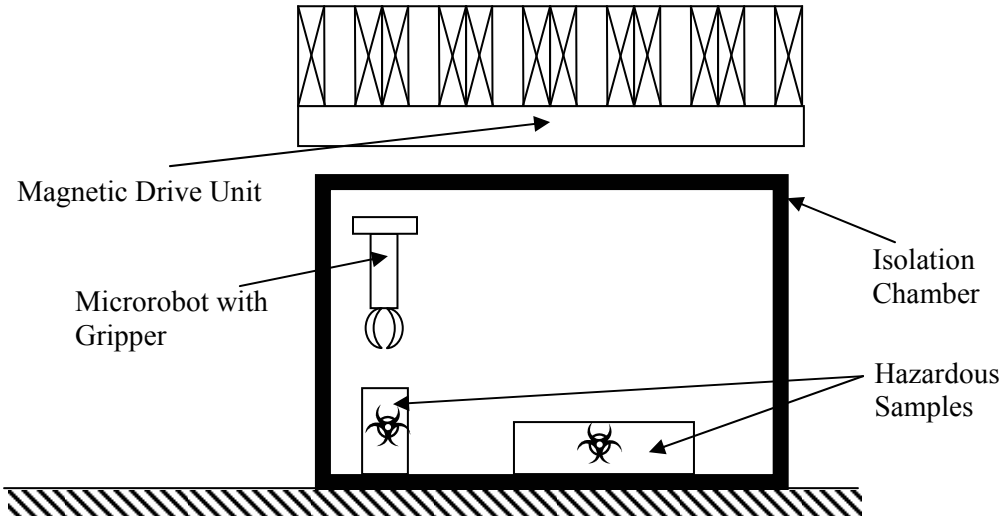

Figure 1-2: Magnetically suspended microrobot in an isolated working environment.

1.4.3 Surgical Robot

The magnetic suspension system is also suitable for medical applications, with the human body treated as the enclosed environment. A concept sketch is shown in Figure 1-4. The completely wireless microrobot could be used to perform minimally invasive endoscopic procedures, with the magnetic drive unit used to move the robot to specific areas of interest. The microrobot could be fitted with a variety of different actuators. A gripper or collector

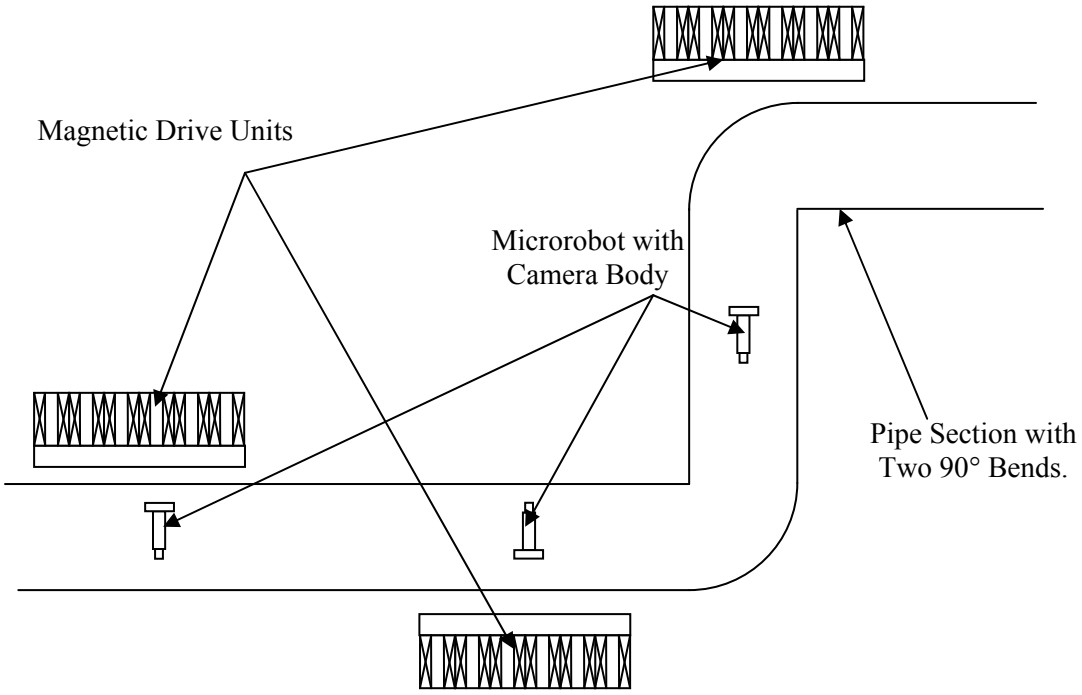

Figure 1-3: Application of a magnetically suspended robot for in-pipe inspection.

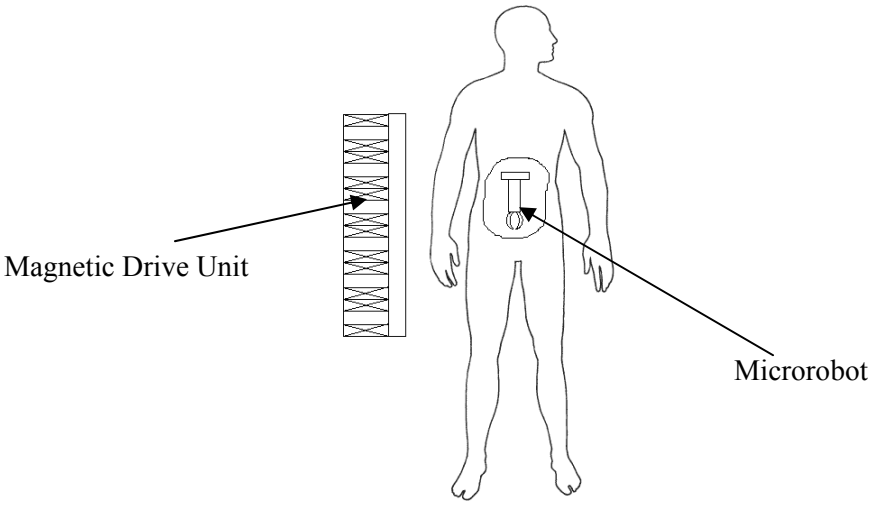

Figure 1-4: Concept image of a microrobot operating in the digestive tract.

tool could be used to collect tissue samples or manipulate foreign objects. The microrobot could also be designed to transport drugs or chemicals through the body to a specific area in order to provide targeted therapeutic care. This would be useful in the treatment of cancer, as a smaller dose of chemicals could be delivered to the target area instead of exposing the patient to a large dose affecting the entire body. Motion of the microrobot would not be confined to the digestive tract, as research has shown that microrobots could be designed for motion in the cardiovascular system [17] [32].

In all of the applications discussed herein, the microrobot could be designed to operate autonomously or it could be controlled with a teleoperation system [33].

1.5 Thesis Objectives and Scope

A new large gap magnetic suspension system based on the design in [30] has been constructed at the University of Waterloo with the purpose of improving on the designs of the microrobot and magnetic drive unit toward a practical biomedical or industrial application. This system was designed completely from scratch in order to ensure that the latest technological components were integrated into the system. Preliminary experimentation has demonstrated the capability to levitate an object weighing 0.0117 N at distances up to 100 mm away from the pole piece. The nominal current in the electromagnets at this distance is on the order of 1.5 A. In order to further develop applications for large gap microrobotics the current system must be characterized by a system model. Almost all forms of magnetic levitation are open loop unstable, and a good model is required in order to design a controller that will deliver adequate performance over the operating range of the system.

The goal of this thesis is to present several different aspects of the modeling of the new large gap magnetic system at the University of Waterloo, with the goal of demonstrating working horizontal and vertical motion of a magnetically levitated object.

Chapter 1 presents a brief overview of microrobotic systems and applications and the use of magnetic suspension as a propulsion mechanism. Large gap magnetic suspension is

presented as a viable application for several microrobotic applications. The thesis objectives and scope are also presented.

Chapter 2 presents a brief overview of the theory behind large gap magnetic suspension, starting from the derivation of the force produced by a magnetic field. The basic operating principles of the magnetic drive unit are presented to demonstrate how magnetically levitated motion is achieved, and the transfer function describing the basic operation of simple magnetic levitation is derived.

Chapter 3 presents the various components of the experimental setup and their performance characteristics. The theoretical accuracy of the system inputs and outputs are investigated in order to determine how the characteristics of the experimental setup will affect the performance of the system.

Chapter 4 discusses the attempts to derive a simplified analytical equation for the magnetic force produced by the magnetic drive unit based on the force predicted by a finite element model. The main focus of the research is on a simplified 2D model of the magnetic drive unit, with a brief discussion of the attempts to extend the modeling to a 3D model.

Chapter 5 presents the identification of the open loop model describing the vertical motion of the levitated object based on experimental measurements. The basics of closed loop system identification are discussed, as well as the system limitations that prevented them from being applied directly. The method used to derive the model is presented, and the system response is compared to the model response for various PID controllers and various types of inputs.

Chapter 6 presents the identification of the open loop horizontal model. The open loop characteristics of the system are presented, and the linearized x and y models are derived from these characteristics. The model is compared to the system under open loop, PD, and PID control in order to determine the validity of the model.

Chapter 7 discusses several aspects of the system performance. The effects of x, y, and z motion are investigated in order to determine how simple step motions along one axis impacts the motion or steady state tracking along the remaining axes. The dynamic

performance and operating range of the system under PID control is presented, with some aspects of the performance compared to the system in [30]. The performance of the microrobot is also investigated as it traces a circular trajectory in the horizontal plane. Finally, a linear quadratic regulator (LQR) for vertical position control is developed, and its performance is compared to the PID controller.

Chapter 8 presents the conclusions and recommendations of this thesis.

Chapter 2
Theoretical Modeling

2.1 Magnetic Flux Density Field Due to a Solenoid

A current in a conducting medium will produce a magnetic flux density field ***B*** in the space surrounding it. For an element *d***s** carrying current *i* the field *d**B*** at point ***P***=(x,y,z) can be found by application of the Biot-Savart law [34]:

$$d\vec{B} = \frac{\mu_0}{4\pi}\frac{id\vec{s}\times\vec{R}}{R^3} \tag{2-1}$$

Here ***R*** is the vector between element *d**s*** and the point ***P*** and μ_0 is the permeability of free space, $1.26\text{x}10^{-6}$ Wb/Am. For the magnetic suspension described in this thesis a series of electromagnets attached to a pole piece are used to produce the flux density field. These electromagnets can be modeled as solenoids consisting of numerous current carrying loops [35]. For a single current carrying loop of radius *a*, shown in Figure 2-1, the elements *d**s*** and ***R*** are defined as

$$d\vec{s} = (-a\sin\phi, a\cos\phi, 0)d\phi \tag{2-2}$$

$$\vec{R} = (x - a\cos\phi, y - a\sin\phi, (z-h)) \tag{2-3}$$

and the resulting ***B*** is computed from

$$\vec{B} = \frac{\mu_0 i}{4\pi}\int_0^{2\pi}\frac{(-a\sin\phi, a\cos\phi, 0)\times\vec{R}}{R^3}d\phi \tag{2-4}$$

Figure 2-2 extends the derivation to the case with multiple wire loops stacked on top of each other. If the solenoid has a wire turn density of *N* turns per unit length, than an element *dz* of the solenoid has *Ndz* loops. The contribution of each element to the flux density can be found by integrating over the entire length *L* of the solenoid.

$$\vec{B} = \frac{\mu_0 Ni}{4\pi}\int_{-L/2}^{L/2}\int_0^{2\pi}\frac{(-a\sin\phi, a\cos\phi, 0)\times\vec{R}}{R^3}d\phi dz \tag{2-5}$$

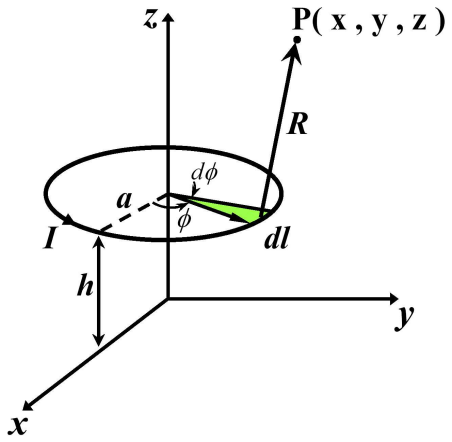

Figure 2-1: Diagram for estimating the magnetic field due to a single wire loop. [35]

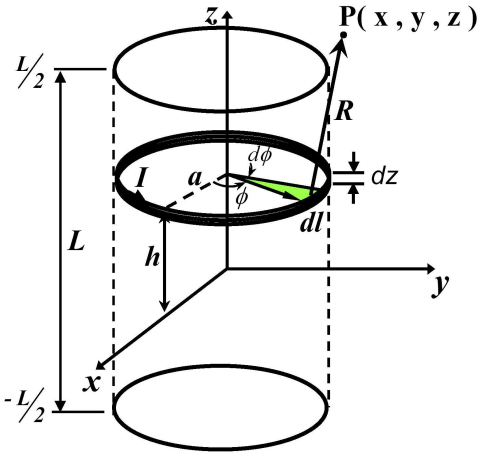

Figure 2-2: Diagram for estimating the magnetic field due to a stack of wire loops. [35]

Finally, consider the case with a multi-layered coil structure. The coil radius a is no longer a constant, instead it is an element dr that can vary from an inner loop radius of r_a to an outer loop radius of r_b. For a wire density of σ wires per unit area, there will be $\sigma dr dz$ loops. The resultant flux density at ***P*** will be

$$\vec{B} = \frac{\mu_0 i \sigma}{4\pi} \int_{r_a}^{r_b} \int_{-L/2}^{L/2} \int_0^{2\pi} \frac{r(-\sin\phi, \cos\phi, 0) \times \vec{R}}{R^3} d\phi dz dr \tag{2-6a}$$

$$\vec{R} = (x - r\cos\phi, y - r\sin\phi, (z - h)) \tag{2-6b}$$

In the case of multiple solenoids, the field at ***P*** can be found by using superposition to equate the total field at ***P*** as the sum of the individual fields produced by each electromagnet. In practice the pole piece will also contribute to the flux density field, although its' effects are difficult to quantify analytically.

2.2 Magnetic Force and Torque due to a Field

Consider a loop of wire placed in a magnetic field. This wire will have a magnetic dipole $\boldsymbol{D}=i\boldsymbol{S}\boldsymbol{n}$ where S is the cross-sectional area of the loop and ***n*** is the normal vector of the loop [30]. The torque ***T*** applied to such a wire is given by

$$\vec{T} = \vec{D} \times \vec{B} \tag{2-7}$$

When ***D*** and ***B*** are parallel vectors, there will be no torque applied to the loop. In the case where the vectors are 180° out of phase, any perturbation of the dipole will cause a torque that will turn ***D*** so that it is coincident with ***B***. The position where the vectors are aligned is considered to be a stable equilibrium point, as even under small perturbations the restoring torque will ensure that ***D*** stays aligned with ***B***. This property also ensures that when the current loop is placed in the magnetic field the coil will naturally tend to a position where ***D*** and ***B*** are aligned. This ensures that, even under small perturbations, the wire loop will remain in an equilibrium position and will not rotate.

The concept of a magnetic dipole can also be extended to a ferromagnetic object, provided said object is sufficiently small. This will allow for the assumption that the dipole of the object is uniform and can be assumed to be acting at the centre of mass. It is also possible to levitate permanent magnets in place of a ferromagnetic object. The primary advantage to using permanent magnets over ferromagnetic objects is that the dipole moment produced by the permanent magnet is greater than the dipole moment of a ferromagnetic object of comparable size. This allows heavier objects to be levitated further away from the pole piece since the resultant magnetic force will be greater. The derivations discussed herein can be applied to the case of a levitated permanent magnet with only a slight loss in precision.

The force acting on an element with a magnetic dipole can be estimated from the modified Lorentz equation [30] as

$$\vec{F} = (\vec{D} \cdot \nabla)\vec{B} \tag{2-8}$$

When the dipole $\boldsymbol{D}$=(0,0,D), the resultant force is

$$F^T = \left[D\frac{\partial B_x}{\partial z} \quad D\frac{\partial B_y}{\partial z} \quad D\frac{\partial B_z}{\partial z} \right] \tag{2-9}$$

This formula can be simplified due to the fact that this field exists in a current-free medium. This means that the curl of the field will be zero.

$$(\nabla \times \vec{B})^T = \left[\frac{\partial B_z}{\partial y} - \frac{\partial B_y}{\partial z} \quad \frac{\partial B_x}{\partial z} - \frac{\partial B_z}{\partial x} \quad \frac{\partial B_y}{\partial x} - \frac{\partial B_x}{\partial y} \right] = 0 \tag{2-10}$$

Using this property it is possible to write the force equation purely in terms of the z component of the flux density gradient.

$$F^T = \left[D\frac{\partial B_z}{\partial x} \quad D\frac{\partial B_z}{\partial y} \quad D\frac{\partial B_z}{\partial z} \right] \tag{2-11}$$

2.3 Magnetic Levitation – Principle of Operation

Magnetic levitation is achieved through the interaction between the flux density field $\boldsymbol{B}$ and the magnetic dipole moment $\boldsymbol{D}$ of the levitating object. The magnetic dipole moment is modeled as

$$D = \left(\frac{B_s}{\mu_0} \right) V \tag{2-12}$$

where B_s is the value of the flux density field at the surface of the object, μ_0 is the permeability of free space, and V is the volume of the object. In the case of a permanent magnet, it is assumed that B_s=B_r, where B_r is the remnant flux density of the magnet as provided by the manufacturer. As stated above the dipole is assumed to be uniform and that the magnetic properties are lumped at the geometric centre of the electromagnet. Figure 2-3 shows a typical magnetic levitation setup with a ferromagnetic object and an electromagnet.

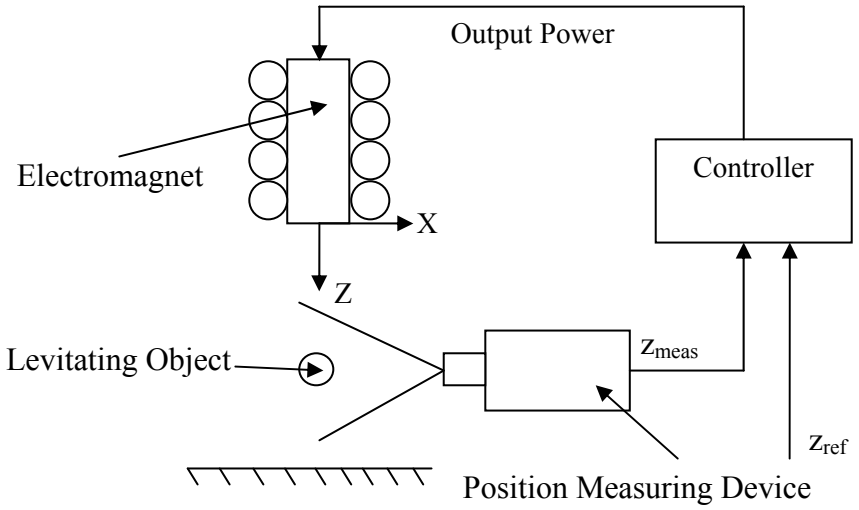

Figure 2-3: A simple one-dimensional magnetic levitation system.

From (2-11), the vertical force *F* acting on the levitated object is

$$F = \left[D \frac{\partial B_z}{\partial z} \right] \tag{2-13}$$

which acts towards the device generating the magnetic field (in this case, the electromagnet). In theory, the object would levitate in a situation where the force *F* counteracts the weight *mg* of the levitating object. In practice, a static magnetic field is incapable of producing stable levitation, as even the slightest disturbance would cause the system to go unstable. The force field produced by a magnetic field will be continuous because the magnetic field is continuous, and so the divergence of the field is always zero [34].

$$\nabla \cdot \vec{F} = 0 \tag{2-14}$$

By applying this formula to the divergence theorem, it can be seen that the net force on any surface enclosing a point will also be zero [34].

$$\int_v \nabla \cdot \vec{F} dv = \oint_s \vec{F} \cdot d\vec{s} = 0 \tag{2-15}$$

If the point of interest were a stable equilibrium point, the net force over any arbitrary surface enclosing that point would point inwards towards said point. Because the divergence of the

field is zero everywhere in the field, it is impossible to enclose any point in the field with an arbitrary surface and have the net force on that surface directed towards the point. Therefore, all points in the field are unstable. This concept is formally known as Earnshaw's Theorem [36].

In order to achieve stable magnetic levitation, a position feedback control loop is used to produce a time-varying field $\boldsymbol{B}(t)$ that will stabilize the position of the levitating object at a given reference position. For the system shown in Figure 2-3, the position of the sphere z_{meas} is measured and compared to the reference position z_{ref}, and the controller compensates for this error by adjusting the power output to the electromagnet. This will produce a change in the strength of the magnetic field (and the field gradients) produced by the electromagnet, causing the sphere to move towards the z location where the magnetic force is balanced by the weight of the sphere.

The FEMLAB finite element package is used to investigate the behavior of the system of Figure 2-3 and get a feel for what sort of field strengths are required in order to levitate objects of different masses. Details on the model can be found in Appendix A. The electromagnet model is the equivalent of an iron core solenoid with 500 turns of 15 AWG wire carrying 1 A of current. In order to minimize the computational overhead of the system these parameters were changed in order to ensure that the ampere-turns and current density remained constant in both models. This will result in a model with fewer subdomains, which means that the model can be parameterized faster and will allow for faster solution times. The exact and simplified parameters are shown in Table 2-1. The core dimensions are 40 mm by 90 mm. Figure 2-4 shows that there is negligible difference between the exact model and the simplified model in terms of the calculated flux density, meaning that the simplified model is a reasonable approximation of the real system. The levitated object is assumed to be a spherical neodymium permanent magnet. Table 2-2 shows the relevant properties of the sphere. Figure 2-5 shows the value of B_z along x=0. The gradient is calculated using a simple slope calculation.

$$\frac{\partial B_z}{\partial z} \cong \frac{\Delta B_z}{\Delta z} \tag{2-16}$$

Parameter	Exact Value	Simplified FEM Value
Current	1 A	100 A
Wire Turns	500	5
Wire Diameter	1.8 mm	18 mm

Table 2-1: Exact and simplified parameters for the FEA electromagnet simulation.

Property	Value
Diameter	1 mm
Density [37]	7400 kg/m^3
Remnant Flux Density B_r [38]	1.3 T
Volume	5.24x10^{-10} m^3
Mass	3.87x10^{-6} kg
Dipole Moment	0.000542 am^2

Table 2-2: Physical properties of levitated sphere.

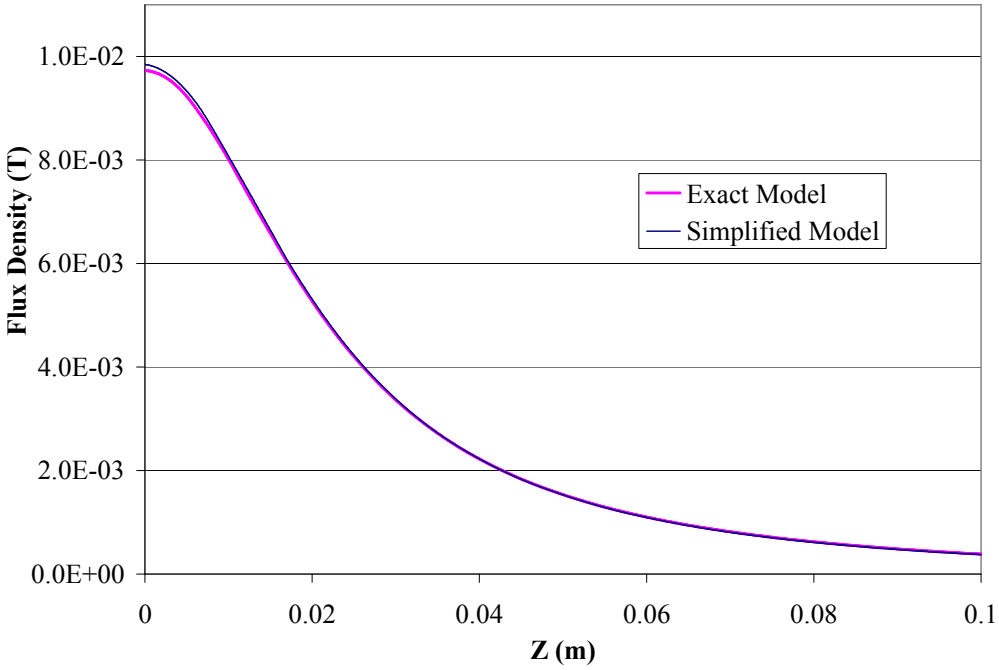

Figure 2-4: Comparison of the *z* component of the flux density along x=0 for the exact electromagnet model and the approximate electromagnet model. Coordinate system is based on Figure 2-3.

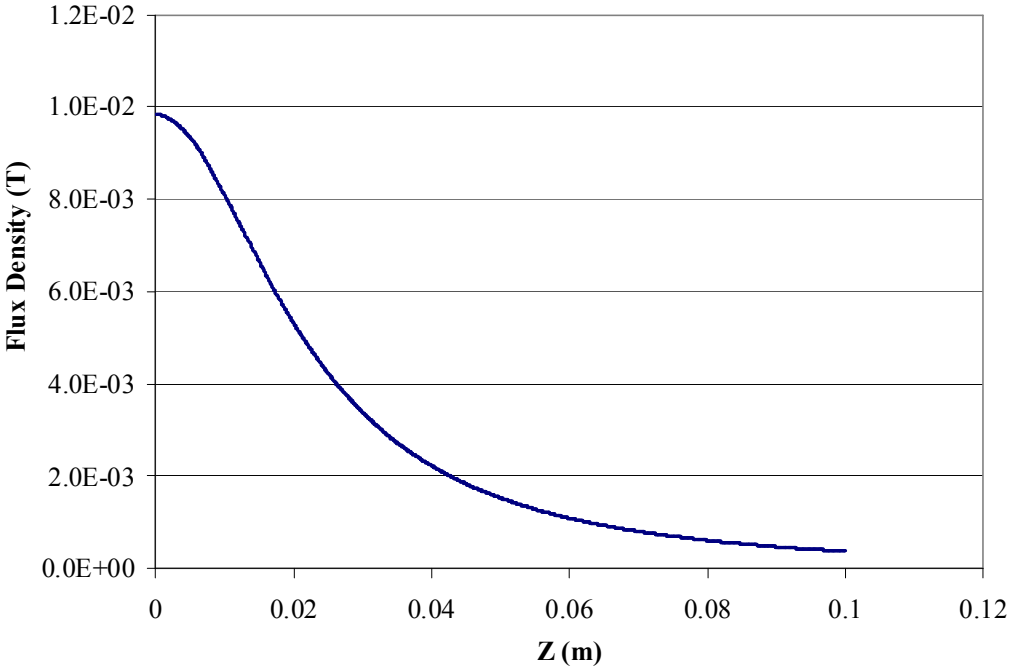

Figure 2-5: Flux density gradient for one electromagnet.

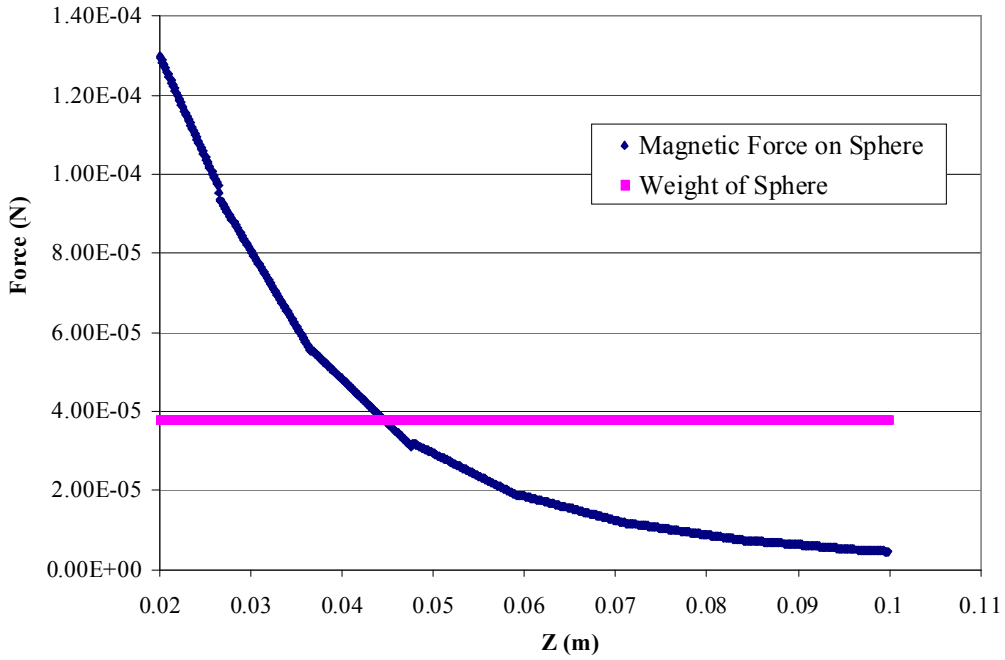

Figure 2-6: Force on a 1 mm diameter sphere. The intersection of the two plots shows the point at which the sphere will levitate.

Figure 2-6 shows the resulting force produced on the sphere. The weight of the sphere is also plotted, and the intersection of the graphs shows that the sphere will levitate approximately 44 mm below the electromagnet. It should be noted that the FEMLAB simulation is static, and does not account for the current variation required to keep the electromagnet in a stable position.

2.4 Generalized Magnetic Suspension

The setup used for magnetic suspension is shown in Figure 2-7. As before the magnetically suspended object incorporates permanent magnets that interact with the generated magnetic field to produce full spatial motion. In order to achieve full spatial motion, several electromagnets are arranged in an array configuration in order to provide the necessary workspace coverage. Attached to the electromagnets is the pole piece, which is used to unify and strengthen the individual fields produced by each electromagnet. The yoke fixture is also made of iron in order to further amplify the field strength.

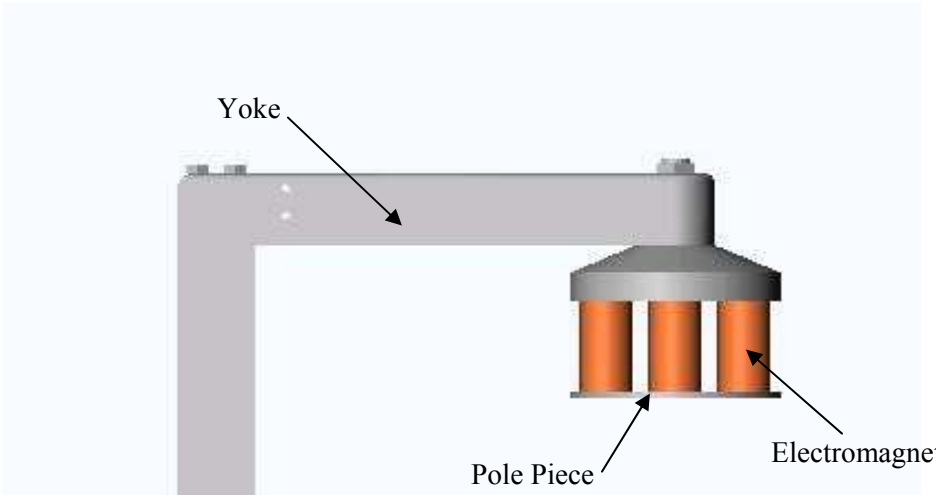

Figure 2-7: Magnetic suspension system.

In the general case, the magnetic force acting on a magnetically suspended object is given by (2-11). The magnetically suspended object is said to be at equilibrium under the following conditions:

$$\partial B_z / \partial x = 0 \qquad \partial B_z / \partial y = 0 \qquad D\,\partial B_z / \partial z = mg \tag{2-17}$$

Note that for levitation with a single electromagnet, it is only possible for such points to occur along the major axis of the electromagnet, constraining motion of the object to the vertical direction. It is generally assumed that, at the equilibrium point, the flux density field vector is aligned with the z axis, although near the extents of the pole piece air gap this may not be necessarily true. During motion between equilibrium points the curl of the field requires that the flux density vector has some horizontal component.

Vertical motion of the suspended object is achieved by applying equal power to each electromagnet in the array. The resulting effects are similar to what would be observed in the case of levitation with a single electromagnet, i.e. the resulting equilibrium point will be produced along the centreline perpendicular to the face of the pole piece.

Horizontal motion is achieved by varying the amount of power each electromagnet receives. If the total power applied to the unit is kept constant the resulting equilibrium point will be shifted in the horizontal plane but will remain unchanged in the z direction. Because of this, horizontal motion of the levitating object is considered to be open-loop stable.

Figure 2-8 shows a simplified two-dimensional version of the magnetic drive unit, with two electromagnets placed at either end of the pole piece. Out-of-plane dimensions extend to infinity. This means that the electromagnet models are not "true" electromagnets, rather it is more appropriate to consider them as long rectangular iron bars with straight current carrying wires running alongside them. The system is suitable for study using finite element methods to demonstrate the behaviour of the flux density field produced by the magnetic drive unit. Details on the model are presented in Appendix A. The electromagnet solenoid is modeled using the simplified dimensional parameters of Table 2-1, the exception being that the nominal current in each electromagnet is now 1000 A. The pole piece has a width of 340 mm and a thickness of 100 mm.

Figure 2-9 shows the horizontal flux density at z=100 mm. When the power input to both electromagnets is equal, the gradient through x=0 is observed to be zero. As the input power is shifted to the right electromagnet there is a discernable shift in the flux density field. This

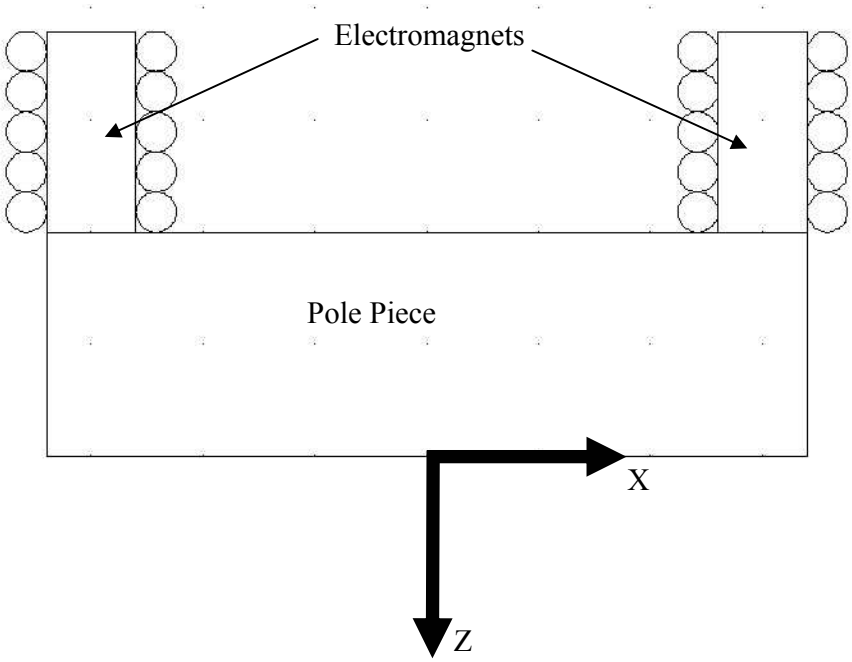

Figure 2-8: Simplified 2D magnetic drive unit.

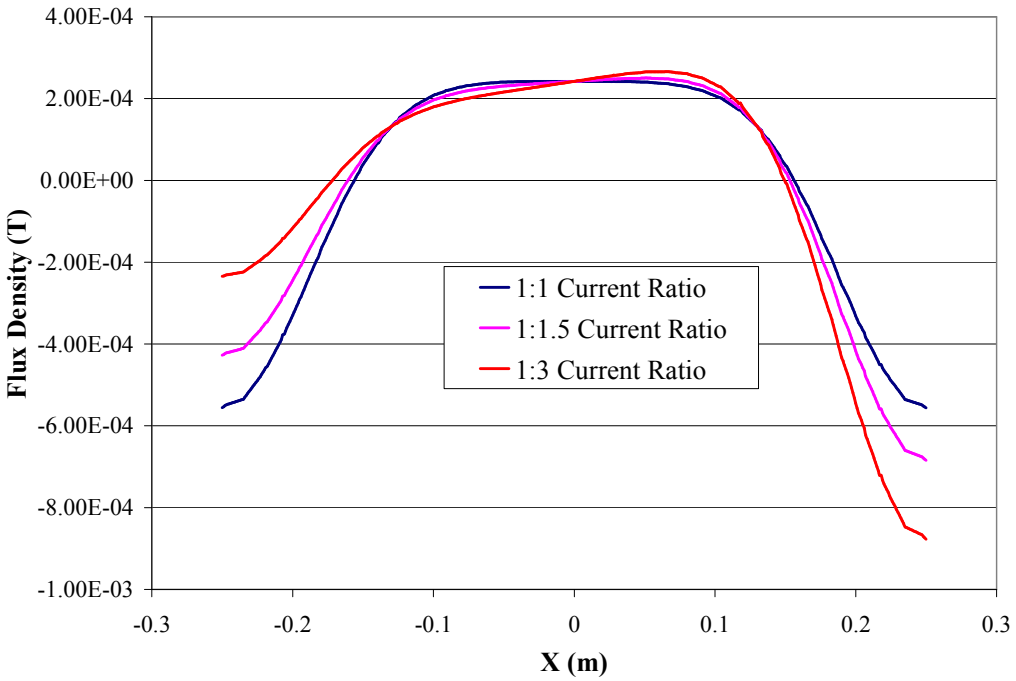

Figure 2-9: Horizontal variation in the flux density gradient at z=0.1 m.

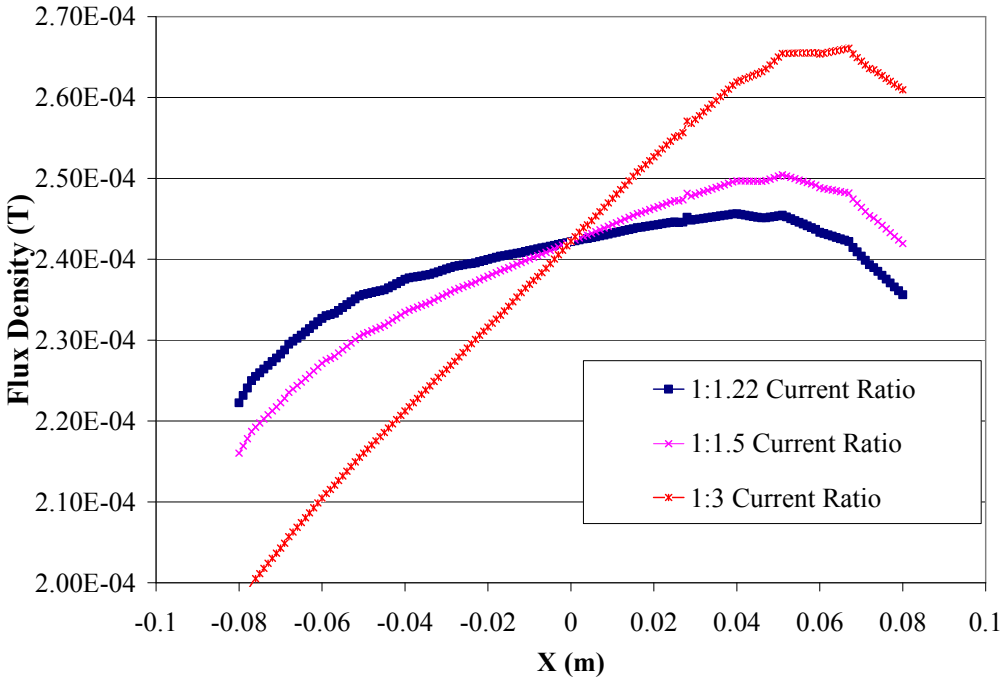

Figure 2-10: Up close inspection of the horizontal flux density gradient at z=0.1 m.

Current Ratio Between 2 Electromagnets	Location of Equilibrium Point in *x* direction
1:1	0 mm
1:1.22	39.5 mm
1:1.5	47.5 mm
1:3	61.5 mm

Table 2-3: Location of new horizontal equilibrium point as estimated from Figure 2-9 and Figure 2-10.

will produce a gradient through x=0, which will force any levitated objects at that point to move in the positive x direction towards the new equilibrium point. Figure 2-10 shows that the larger the change in input power, the greater the gradient through the origin, resulting in a greater application of force to the levitating object. The new equilibrium point will also move further away from the origin as the power in the right electromagnet is increased. The locations of the equilibrium points for different power inputs (represented as a change in the current ratio between the two electromagnets) can be estimated by determining when the slope of the curve produced by the finite element simulation is zero. These equilibrium points are shown in Table 2-3.

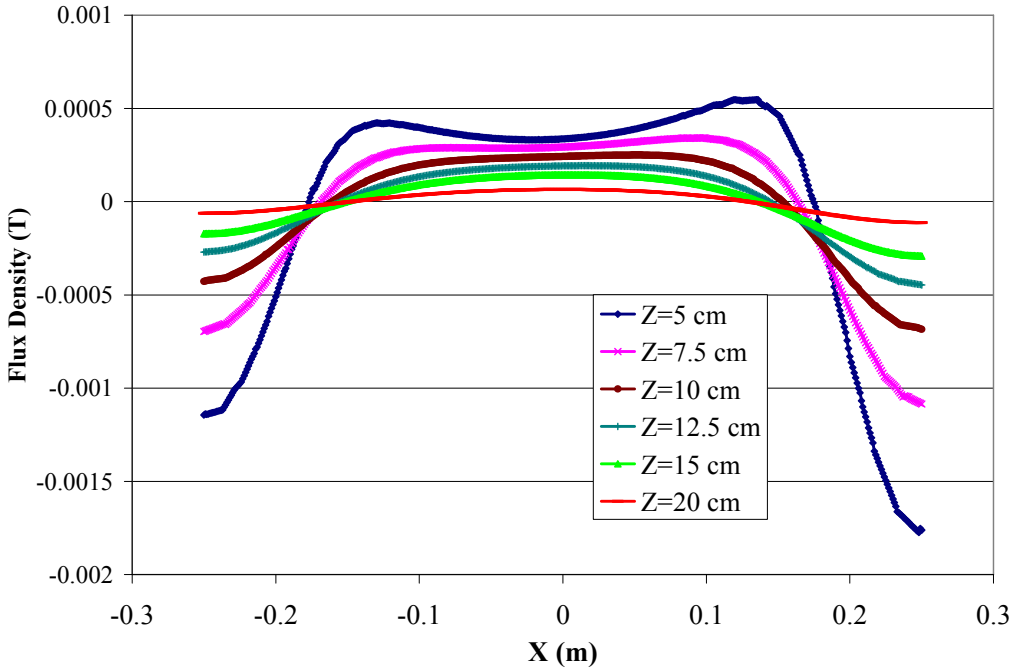

Figure 2-11: Horizontal flux density curves at different points below the pole piece.

Figure 2-11 compares the horizontal flux density at different *z* locations below the pole piece when the current ratio is 1:1.5. It is assumed that the current ratio has just been changed from 1:1 and the levitated object is starting at x=0. For positions near the pole piece (z<75 mm) there will be three points at which the horizontal gradient is equal to zero. The point near x=0 is an unstable saddle point, and it is impossible to predict to which of the stable equilibrium points the object will tend to. For points greater than z=75 mm, there is one stable equilibrium point, which the levitated object will move towards. Because the current ratios are unequal this new equilibrium point is expected to be located at some positive *x* value, but in addition to being dependent on the current ratio the position of the equilibrium point also depends on the height *z*. Table 2-4 demonstrates that, as one moves further away from the pole piece, the new equilibrium point is located closer to the origin, eventually reaching a point where no equilibrium shift is observed. This is due to the fact that the magnetic drive unit produces a flux density field over a finite range, and as one moves further away from the magnetic drive unit the magnitude of the flux density field tends to zero. This means that it will also be difficult to levitate the object at distances

sufficiently far away from the pole piece. The workspace of the microrobot is therefore restricted to z positions at which a significant flux density field exists and at which there is a single stable equilibrium point in the horizontal plane.

Distance Below Pole Piece	Location of Equilibrium Point in X Direction
z=10 cm	47.5 mm
z=12.5 cm	15 mm
z=15 cm	6 mm
z=20 cm	1 mm

Table 2-4: Location of new horizontal equilibrium point as one moves further away from the pole piece.

In general, the vertical force applied to the levitated object is greater than the horizontal force applied to the levitated object. Figure 2-12 shows the flux density field profile along x=0 for a 1:1 current ratio. At a distance of z=0.1 cm, the vertical flux density gradient is estimated as $-2.0\text{x}10^{-3}$ T/m. From Figure 2-10, the gradient through the origin when the current ratio is 1:3 is estimated as $5.6\text{x}10^{-4}$ T/m. Assuming an object is levitating at z=0.1 cm, the magnitude of the vertical force will be approximately four times greater than the horizontal force. It should be noted that, as the microrobot moves to the right, the gradient will decrease, and so the flux density gradient of $5.6\text{x}10^{-4}$ T/m represents the maximum horizontal force the microrobot will see as it moves. For current ratios less than 1:3 the flux density gradient will be even smaller, further reducing the maximum applied force. In the case where the current ratio is 1:1.22, the flux density gradient through the origin is approximately $1\text{x}10^{-4}$ T/m, which is approximately 20 times less than the vertical force. A more graphical representation of the vertical flux density gradient magnitudes is shown in Figure 2-13. It can be seen that there is a significant change in the flux density field strength as one moves closer to the pole piece, but that the field strength does not change significantly along a horizontal path until one starts to approach the extents of the pole piece. This indicates that the field gradient over the working area is greater in the vertical direction than in the horizontal direction. It is therefore expected that motion in the horizontal direction will be relatively slow. The microrobot may also have some difficulty in getting to the new equilibrium point, given that the aerodynamic drag acting on the microrobot may act to stall the motion as the propulsion force decreases.

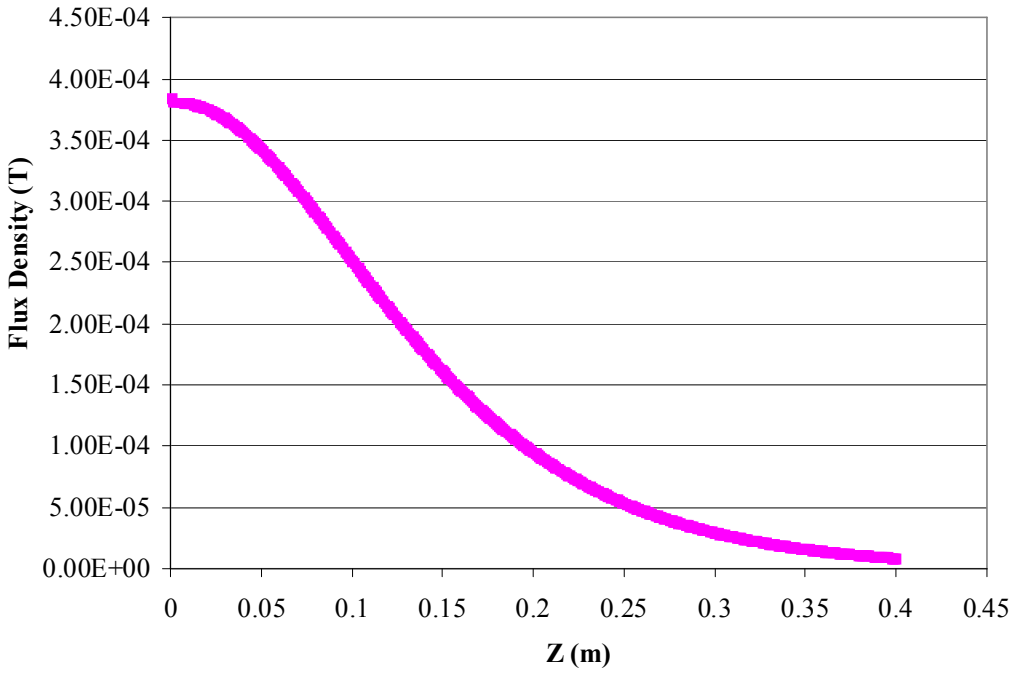

Figure 2-12: Vertical flux density gradient for the FEM model at x=0 with a current ratio of 1:1.

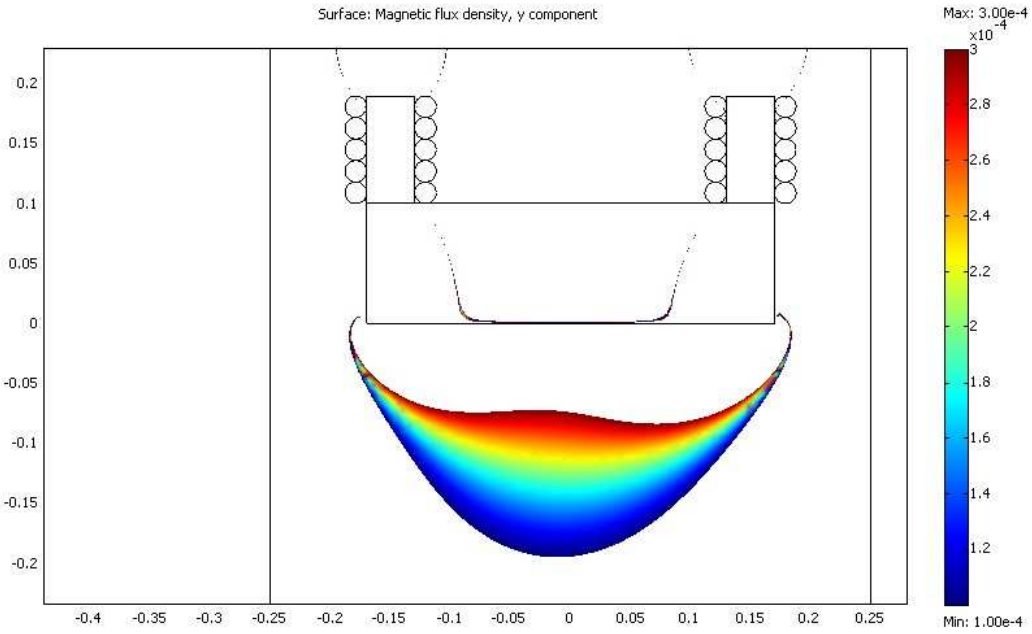

Figure 2-13: Graphical representation of the vertical component of the flux density field. The current ratio is 1:1.5 and distances are in m.

2.5 Mathematical Description of Magnetic Levitation

The following section deals with the mathematical description of magnetic levitation with a single electromagnet and a ferromagnetic object, as shown in Figure 2-3. This simplified model of the this system serves as a suitable foundation for understanding the behaviour of the complex magnetic drive unit used in the research discussed in this thesis, and serves as a basis for estimating a model structure during the system identification discussed in Chapter 5. Horizontal motion of the system is too complex to characterize within an analytical equation and is not discussed here.

It is generally difficult and time consuming to analytically compute the flux density gradient using the equations discussed in this chapter. As a result of this several simplifications are made that allow for an approximate estimation of the force. Assuming that the reluctance of the electromagnet core is negligible compared to the reluctance of the air gap between the electromagnet and levitating object, the force F produced by the electromagnet is

$$F = \frac{1}{2}\frac{dL(z)}{dz}i^2 \tag{2-18}$$

where $L(z)$ is the inductance of the coil, which is a function of the air gap length between the levitating object and the electromagnet [39]. The inductance of the electromagnet is approximated as

$$L(z) = L_1 + \frac{L_0}{1 + z/a} \tag{2-19}$$

where L_0, L_1 and a are positive constants [40]. Figure 2-14 shows a free body diagram of a magnetically levitated object.

Using Newton's second law the dynamic equation is found to be

$$M\ddot{z} = Mg + c\dot{z} - \frac{L_0 i^2}{2a\left(1 + \frac{z}{a}\right)^2} \tag{2-20}$$

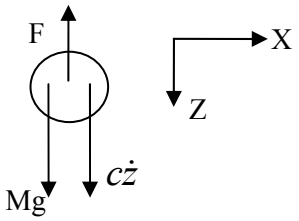

Figure 2-14: Free body diagram of a magnetically levitated object.

where M is the mass of the microrobot, z is the position of the robot and c is the drag coefficient. The resulting system model is non-linear, and so for preliminary design purposes a linearized version of the model can be used to derive a transfer function. Because of the assumption of uniform, lumped parameters, (2-20) can be used to determine the equilibrium current i_0 that will counteract the object's weight at a given position z_0. The equation can therefore be linearized around this point.

$$M\Delta\ddot{z} = c\Delta\dot{z} + \frac{L_0 {i_0}^2}{a^2\left(1+\frac{z_0}{a}\right)^3}\Delta z - \frac{L_0 i_0}{a\left(1+\frac{z_0}{a}\right)^2}\Delta i \tag{2-21}$$

The resulting linearized transfer function is

$$\frac{\Delta Z(s)}{\Delta I(s)} = \frac{-\frac{L_0 I_0}{a\left(1+\frac{z_0}{a}\right)^2}}{Ms^2 - cs - \frac{L_0 I_0^2}{a^2\left(1+\frac{z_0}{a}\right)^3}} \tag{2-22}$$

Note that the open loop system has negative gain. This is not unexpected; if the current is increased, the z position of the levitating object decreases. In general it is desirable to work with a positive gain system, since design tools such as root locus assume a positive gain. In order to achieve this, both the reference position and measured position are negated before performing the control value calculation. This effectively results in the negation of the error of the system and will turn the negative gain of the plant into an effective positive gain. The concept is shown in Figure 2-15.

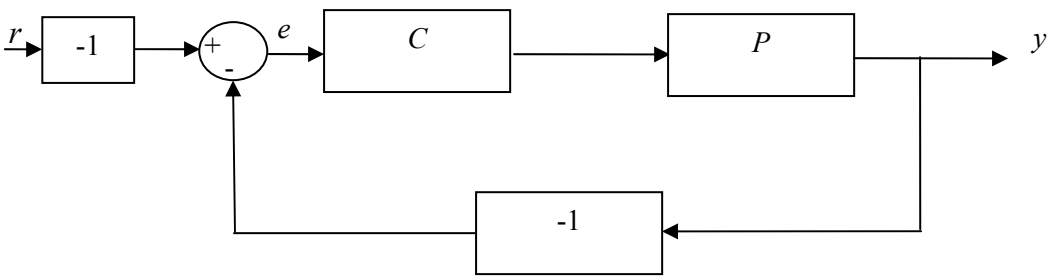

Figure 2-15: Block diagram demonstrating how the negative gain of plant *P* is eliminated in closed loop feedback control.

Chapter 3
Experimental Setup

Figure 3-1 shows a schematic of the setup of the physical system. The scanning laser micrometers report the location of the microrobot. This position is output as an analog voltage to the DAQ. The DAQ then converts the voltage measurement back into a position measurement in order to generate the control signals. The output from the controller is a voltage from the analog output cards. Based on the input voltage a specific current will be generated by the amplifier, and this current is output to the electromagnets. Up to 24 electromagnets can be connected to the amplifier. By varying the output voltage from the controller the input current to the electromagnets will be controlled, which will change the magnetic field and cause the microrobot to move.

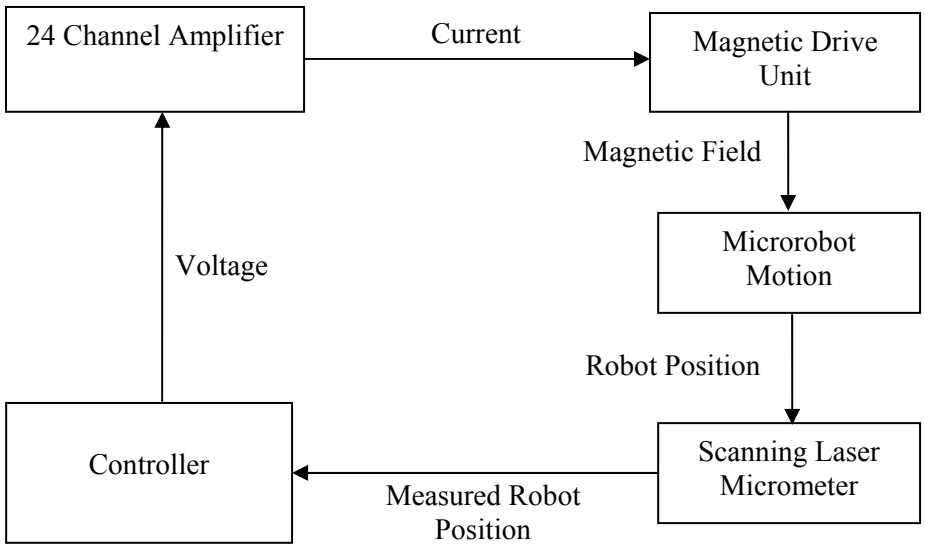

Figure 3-1: Schematic representation of the microrobot control loop.

3.1 Yoke and Pole Piece

The yoke and pole piece are shown in Figure 3-2 and Figure 3-3, respectively. The yoke and pole piece are both made from soft iron in order to improve the strength of the magnetic field produced by the magnetic drive unit. The electromagnets can be mounted to a mounting

bracket on both the upper and lower portions of the yoke. Different portions of the yoke can be reconfigured, allowing for different operating configurations. The upper portion of the yoke can be adjusted up and down relative to the lower portion of the yoke, allowing for experimentation with different air gap lengths.

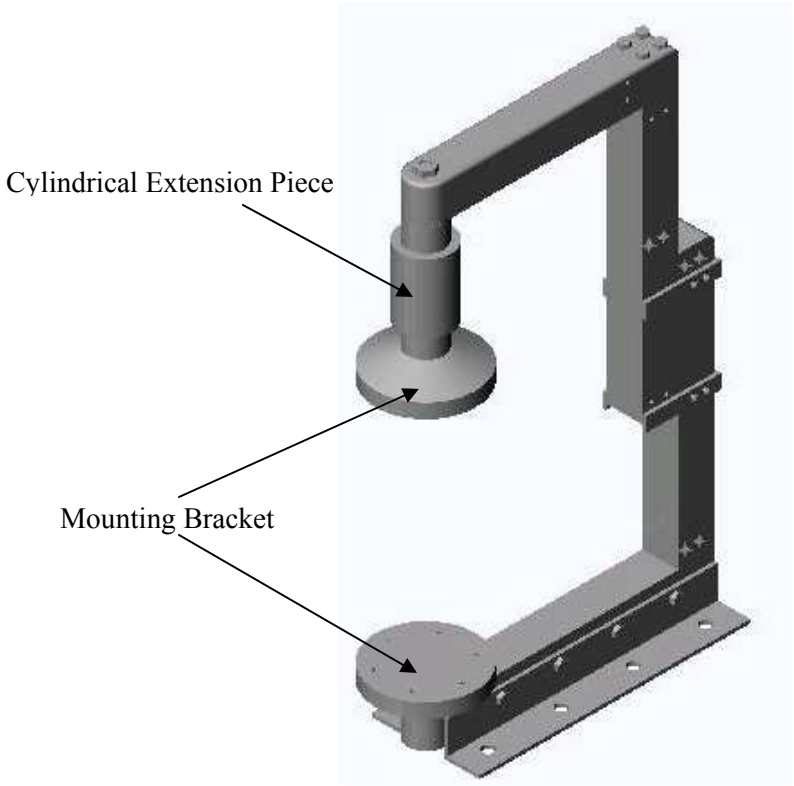

Figure 3-2: Yoke.

Permanent magnets can be inserted into the cylindrical extension piece in order to provide a constant bias field, reducing the power requirements needed for levitation. A secondary, spider-type mounting bracket for the electromagnets is also available. For the experiments in this thesis the standard cylindrical extension piece and upper mounting bracket are used. The air gap length is approximately 283 mm.

The pole piece used for experimentation in this thesis is a 132 mm x 6.35 mm cylindrical disk that attaches directly to the electromagnets. As with other yoke components, this pole piece only represents one possible configuration that could be used on the magnetic drive unit. Different pole piece configurations, from simple square plates to more complex three-

dimensional surfaces, must be evaluated by FEA software in order to examine their impact on the resultant magnetic field. The cylindrical pole piece was chosen as it was found to produce a strong magnetic field for vertical motion and a demonstrable shift in the equilibrium point during horizontal motion [41].

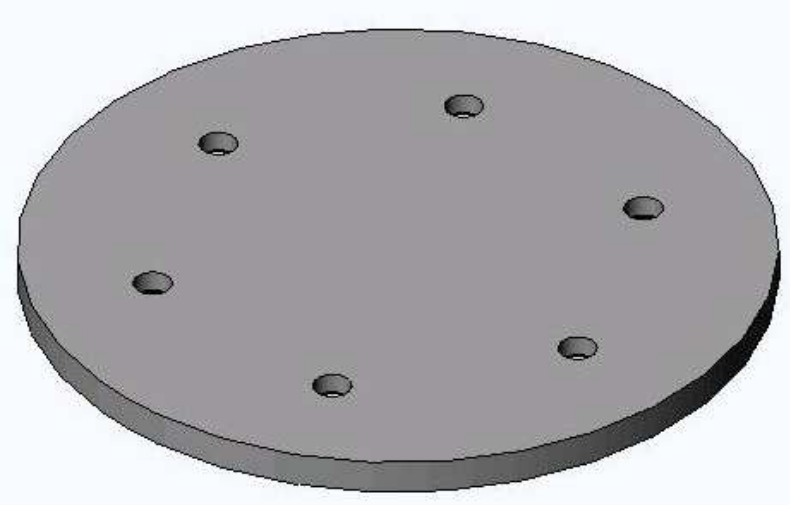

Figure 3-3: Pole piece.

3.2 Electromagnets

Up to 24 electromagnets can be installed on the magnetic drive unit. For the work discussed in this thesis six electromagnets are installed on the upper portion of the yoke. The configuration is shown in Figure 3-4. There is also an electromagnet installed in the centre position, but it is not used. The electromagnets are custom made and provided with a male thread for attachment to the mounting bracket and a female thread for attaching the pole piece to the other side of the electromagnets. Each electromagnet has approximately 840 turns of #22 AWG wire [42]. The nominal electrical parameters of each electromagnet are shown in Table 3-1.

3.3 Laser Sensor

Three Keyence LS-5000 scanning laser micrometers are used to measure the x, y, and z position of the levitating object. The sensors are mounted to a hexagonal aluminium ring that

Electromagnet	Resistance (Ω)	Inductance (mH)
1	4.27	29.68
2	4.23	28.84
3	4.25	29.08
4	4.25	28.77
5	4.29	27.65
6	4.25	29.64
7	4.31	28.83

Table 3-1: Electrical parameters of the electromagnets [43]. Note that electromagnet 7 is the centre electromagnet and is not actuated for any of the experiments discussed in this thesis. The parameters are provided for reference.

Measuring Range	0.2-40 mm
Scan Rate	1200 Hz
Analog Output Range	+/- 10 V
Analog Output Resolution	5 mV

Table 3-2: Laser micrometer characteristics [44].

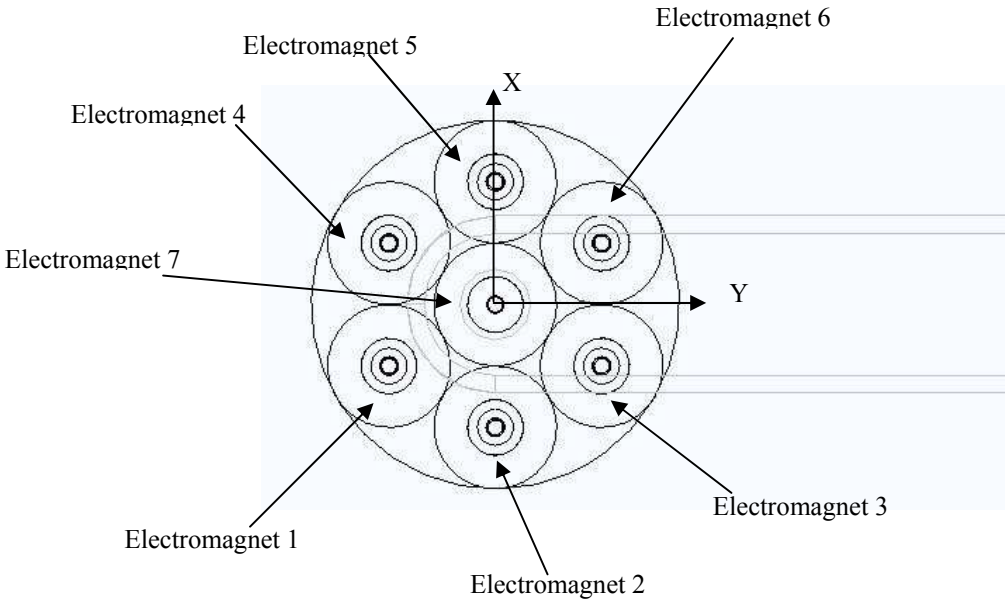

Figure 3-4: Electromagnet configuration.

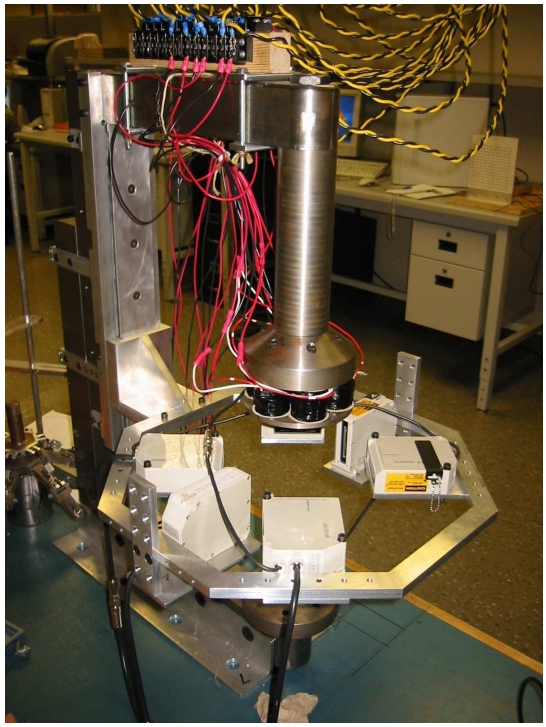

Figure 3-5: Assembled magnetic drive unit showing the layout of the laser micrometers.

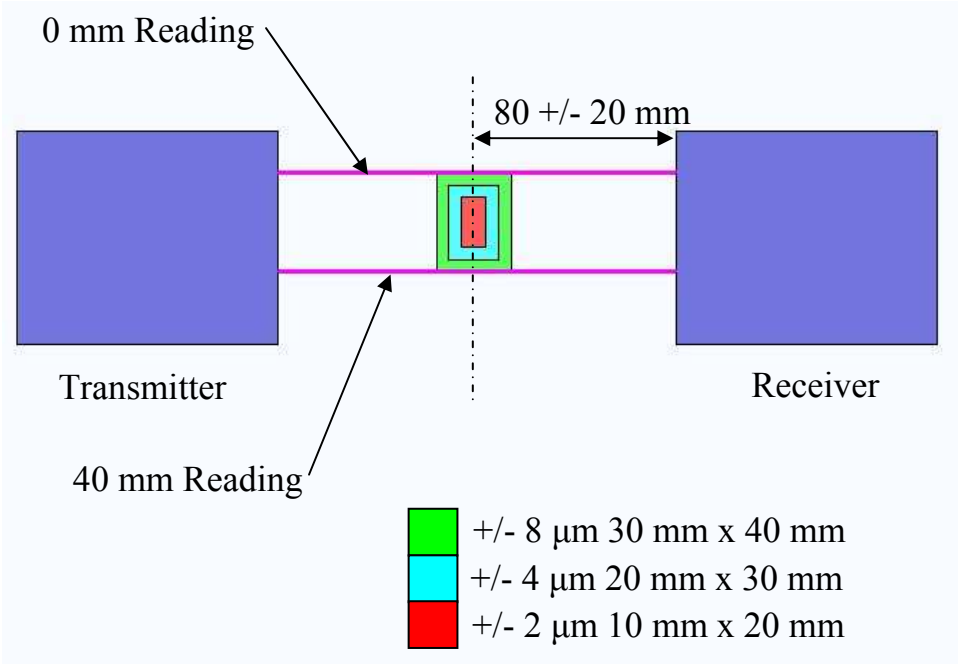

Figure 3-6: Accuracy Mapping of the Scanning Micrometer [44].

surrounds the air gap workspace of the yoke, as shown in Figure 3-5. Important characteristics of the micrometer are summarized in Table 3-2. Figure 3-6 shows how the accuracy of the laser scanner varies depending on the location of the object being measured.

Software is provided by Keyence that allows for calibration and configuration of the laser micrometers via an RS-232C serial connection through the COM1 or COM2 port on a computer. Output from the laser sensors can be obtained from this serial port or through an analog output board. For this system the analog output boards are used since they permit faster data transmission than the serial connection. The output range of the analog boards is +/- 10 volts, and the equation relating the measured position y in mm to the output voltage x is given by

$$y=2x+20 \tag{3-1}$$

The micrometers are programmed to measure the location of the microrobot that is nearest to the zero mm position. For vertical motion this means that the position of the top of the microrobot is reported by the sensor. An alternative measurement method that could be used is to measure the location of the microrobot that is closest to the 40 mm position reading, which in terms of vertical motion would mean measuring the position of the bottom of the microrobot.

3.3.1 Measurements

The local and global measurement coordinate frames are shown in Figure 3-7. All vertical position measurements are made in the local frame of the laser micrometer, and this local axis is coincident with the global axis (i.e. the zero position reading is made at the top of the laser micrometer). As with the yoke the position of the ring and the position of the sensors on the ring are adjustable to different configurations to suit the needs of the desired experimental setup The horizontal sensors are positioned so that the horizontal motion can take place at a minimum vertical position measurement of z=10 mm. For more advanced control it would be desirable to know the location of the microrobot relative to the pole piece. This can be trivially determined by measuring the distance between the base of the pole piece

and the location of the 0 mm reading on the sensor. For the existing experimental setup the zero mm reading of the vertical position sensor is located approximately 77 mm below the pole piece.

The local frame of the horizontal position sensors is not coincident with the global frame. A coordinate transform is necessary to convert these measurements from the local frame to the global frame. The mounting ring was designed so that the centreline of the outer dimensions of the sensor would pass through the global origin. The centreline of the scanning area is not coincident with the centreline of the sensor; it is offset 6 mm towards the 0 mm position. The radius *r* of the microrobot is also added to the measurement in order to control the centreline position of the microrobot, as shown in Figure 3-8. Finally, a rotational translation is required to align the local and global axes.

The transform from the global frame to the local frame is as follows:

1. Rotate 45° about the global *z* axis.
2. Translate -26+r mm in the local *x* frame and local *y* frame.

The homogeneous transformation matrix is

$$\begin{bmatrix} \frac{1}{\sqrt{2}} & -\frac{1}{\sqrt{2}} & 0 & 0 \\ \frac{1}{\sqrt{2}} & \frac{1}{\sqrt{2}} & 0 & 0 \\ 0 & 0 & 1 & 0 \\ 0 & 0 & 0 & 1 \end{bmatrix} \begin{bmatrix} 1 & 0 & 0 & -26+r \\ 0 & 1 & 0 & -26+r \\ 0 & 0 & 1 & 0 \\ 0 & 0 & 0 & 1 \end{bmatrix} = \begin{bmatrix} \frac{1}{\sqrt{2}} & -\frac{1}{\sqrt{2}} & 0 & 0 \\ \frac{1}{\sqrt{2}} & \frac{1}{\sqrt{2}} & 0 & \frac{-52+2r}{\sqrt{2}} \\ 0 & 0 & 1 & 0 \\ 0 & 0 & 0 & 1 \end{bmatrix} \tag{3-2}$$

and the resulting coordinate transform is

$$x_g = \frac{x_l - y_l}{\sqrt{2}} + B_x \tag{3-3a}$$

$$y_g = \frac{x_l + y_l - 52 + 2r}{\sqrt{2}} + B_y \tag{3-3b}$$

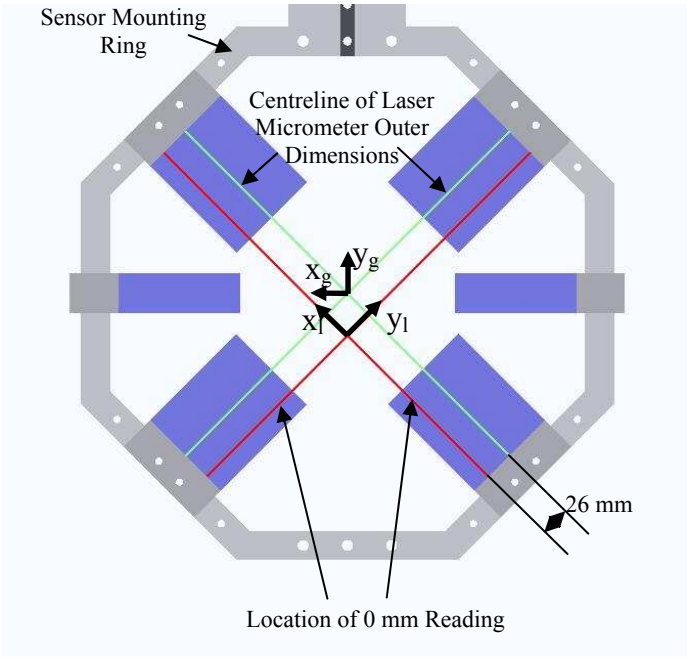

Figure 3-7: Position of the local and global frame.

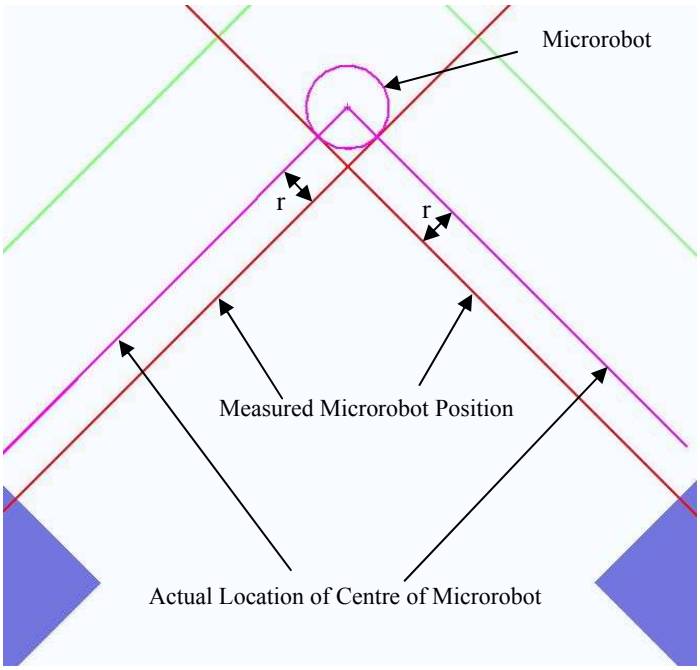

Figure 3-8: Measurement of microrobot position. When the laser sensors measure the microrobot position as (0,0), the actual centreline position is (r,r).

where the terms B_x and B_y are bias correction terms which account for the error due to variance in the radius of the microrobot and the manufacturing tolerances of the components of the sensor mounting ring. In general B_x is approximately 1 mm and B_y is 5 mm. The error in the x direction is smaller since the frame translation effects are cancelled out by the rotational translation, and the tolerance error from the bracket used to attach the mounting ring to the yoke compounds in the y direction only.

3.4 Input DAQ

The input DAQ is a National Instruments NI-PXI-6251 series DAQ card. A summary of the important characteristics are found in Table 3-3.

Input Range	+/- 10 volts
Number of Bits	16
Resolution	0.305 mV
Random Noise Variance	280 μVrms
Gain Error	83e-6 V/V
Offset Error	20e-6 V/V
Gain Temperature Sensitivity	13e-6 V/(V°C)
Offset Temperature Sensitivity	21e-6 V/(V°C)
Reference Temperature Sensitivity	1e-6 V/(V°C)
Integral Non-Linearity Error	60e-6 V/V

Table 3-3: NI-PXI-6251 Characteristics [45].

3.5 LabVIEW Controller and Software

National Instruments' LabVIEW RT software is used to develop the controller architecture and user interface. There are several benefits to using LabVIEW RT. LabVIEW provides an intuitive graphical-based method for the development of programs. There are several tools that allow for easy interface with the input and output boards. The interfacing is further simplified by the fact that the input and output boards and control processor are also manufactured by National Instruments. Many functions are also provided as standard features in the programming library, minimizing the amount of time required for writing and debugging code. Sample functions used in the course of the experiments conducted in this thesis include a PID control block and a pseudo-random binary sequence generator.

The additional benefit of LabVIEW RT is that it allows programs to be designed for and run in real time. This ensures that the program executes at a fixed time interval and that no control sampling cycles will be missed. A master-slave hardware setup is used to deploy the software. The time-critical code, written by the user, is executed on the slave under a real-time operating system, while two lower-priority programs, generated by LabVIEW, are used to pass data back and forth to the user interface via a TCP/IP connection. The slave is a NI-PXI-8186 2.2 GHz processor board running the LabVIEW RT operating system. The master is an Intel Pentium 4 2.6 GHz personal computer running the Windows XP operating system.

Data is stored in an array while the program is running, the size of which depends on the number of variables being measured, the runtime of the experiment, and the sampling frequency. The number of entries for each variable is fixed by the runtime and sampling rate at the start of the experiment, which means that data from the start of the experiment will be overwritten by the most recent data if the experiment runs longer than the specified runtime. When the experiment ends the data is written to a comma separated value (CSV) file and saved on the hard disk of the slave. The CSV files can be transferred to the master via FTP, or the slave can be booted into Windows XP mode and the files can be transferred to a disk. CSV files can be opened by Microsoft Excel for inspection and manipulation of the data.

3.6 Output Cards

The three analog output cards are National Instruments NI-PXI-6733 series cards. Important characteristics are found in Table 3-4.

Input Range	+/- 10 volts
Number of Bits	16
Resolution	0.305 mV

Table 3-4: Analog output card characteristics. [46]

3.7 Power Supplies and Amplifier

Two Sorensen DCS40-30E DC power supplies are used to provide power to the electromagnets. Each power supply is configured to provide power to up to twelve electromagnets. Only one of the power supplies is currently in use since only six

electromagnets are installed on the magnetic drive unit. The output voltage of the power supply is kept constant at 40 volts, and the maximum total output current from the power supply is 30 Amperes [47].

The amount of current drawn from the power supplies is controlled by an amplifier. The amplifier was custom built by the Faculty of Science at the University of Waterloo. The amplifier has three input connectors to connect the cables from the controller output cards and 24 output channels for the electromagnets. The amplifier is designed to output a current based on the input voltage from the controller. The approximate gain equation mapping the input voltage v to the output current i for the amplifier is

$$i = 0.355v \tag{3-4}$$

The typical input-output response is shown in Figure 3-9. Given the maximum input of 10 volts, the maximum output current on each channel is 3.55 A. The maximum potential current that can be drawn by the six electromagnets currently installed on the magnetic drive unit is approximately 20 A, which is within the output limits of the power supply.

3.8 Microrobot Prototype

The microrobot prototype is shown in Figure 3-10. This microrobot consists of one cylindrical neodymium magnet and an outer body made of plastic. The primary purpose of the prototype is to aid in investigating the performance of the magnetic drive unit and demonstrating the basic operating principles of the system. Microrobot design is in itself a fairly challenging task, and while future work will require a more advanced microrobot the test prototype was found to be suitable for initial experimentation.

The 10 mm x 10 mm neodymium magnet provides the dipole moment that interacts with the external field to produce the operating force. The plastic body is used to protect the neodymium magnet from damage due to falling out of the field or collision with the pole piece. The wider cylindrical portion at the top of the microrobot allows for a larger range of travel in the y direction, which is perpendicular to the laser beam of the z position sensor. The

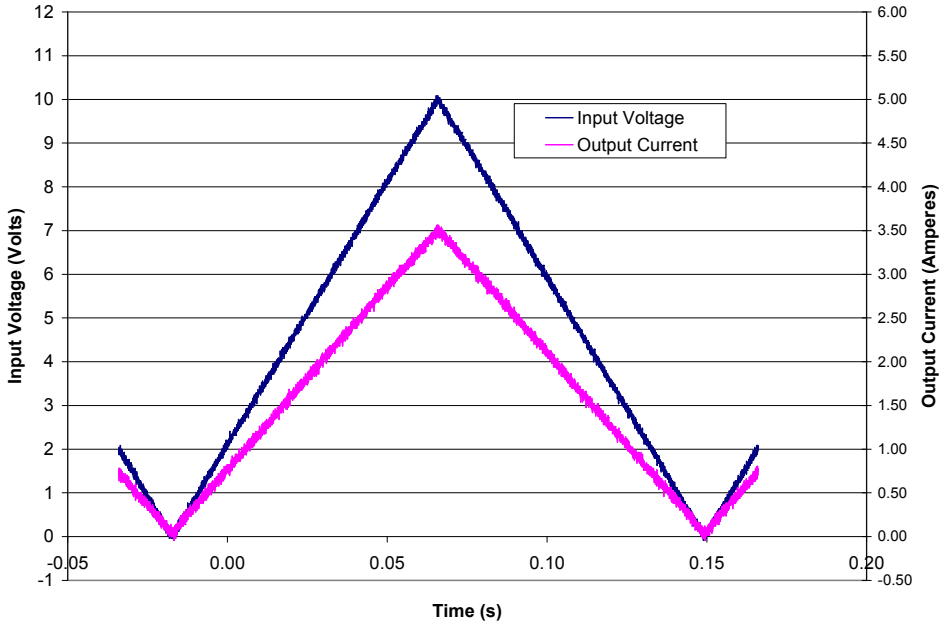

Figure 3-9: Input/output response of channel 1 of the amplifier.

remnant flux density of the magnet is 1.3 Tesla [38], giving the microrobot a dipole moment of 0.813 Am^2. The total mass of the microrobot is 11.19 grams.

3.9 Theoretical Input Accuracy

The precision of the laser scanner is affected by the number of averaging measurements used to produce an output. The scanning rate is 1200 hz, meaning one scan occurs every 0.833 ms. While more averaging measurements will produce a more precise result, the trade-off is that it will take time to perform these measurements. For example, the Keyence system is capable of performing 6144 averaging measurements. This measurement will be extremely precise (on the order of 0.01 μm), but it will take 5.118 seconds to perform a single measurement. For a magnetic levitation system it is desired to have the sampling rate be as high as possible in order to maintain stability due to the fact that the levitated object is capable of moving at relatively high velocities and accelerations. There is therefore a

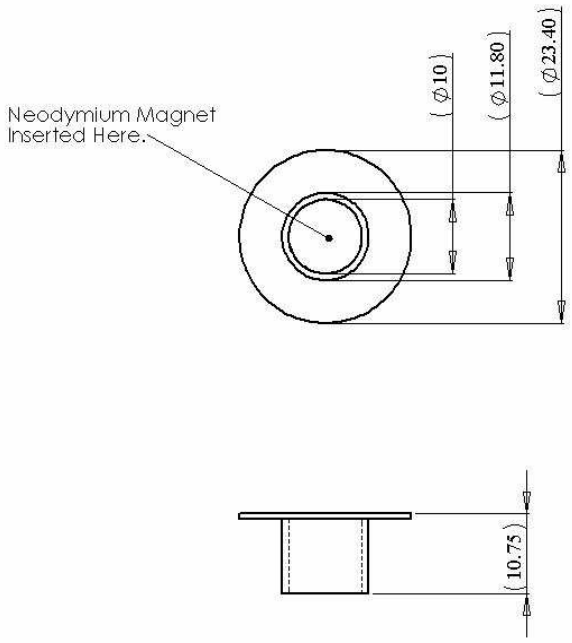

Figure 3-10: Microrobot prototype. Dimensions in mm.

tradeoff between increasing the precision of the system while at the same time decreasing the sampling rate.

It has been observed that the number of averages needed to significantly affect the precision of the vertical precision measurement adversely affects the stability of the microrobot. For the horizontal motion discussed in this thesis initial testing suggested that the use of averaging measurements could be used to improve the accuracy of the *x* and *y* measurements with minimal impact on the identified system dynamics, although this was not investigated in great detail. The system is therefore set up to obtain only one averaging measurement for each of the *x, y,* and *z* positions. The system requires a maximum of three cycles to scan and output the data, meaning that one sample is produced, at most, every 2.499 milliseconds. For the experiments discussed in this thesis the sampling rate of the controller was successfully set to run as low as 2 milliseconds.

The system accuracy and precision are also significantly affected by object position and object alignment in the field. For the measurement of a static object said object should be perfectly straight and level in the measuring field in order to obtain the best possible measurement. Angular positioning of the microrobot is also important as it may be necessary to locate the position of other points of the microrobot (such as gripper finger location) relative to the measured position, and if the robot is experiencing an angular tilt the true position of other points on the microrobot will differ from the actual position of those points. It is not possible to measure this tilt with the existing micrometers, and so an additional sensor would be needed to perform this measurement. Accuracy will also suffer if the object is located outside of the recommended measuring range as specified in Figure 3-6.

As shown in Figure 3-6, the accuracy of the micrometer varies from 2-8 μm, depending on where the object is located in the micrometers' measuring field. The resolution of the analog output board will also play a factor in determining the output of the system. Based on the data in Table 3-2, the equivalent position resolution of the analog output can be found by equating the voltage range to voltage resolution ratio (in volts) to the positional range resolution ratio (in mm). For the given system the equation is:

$$\frac{20}{0.005} = \frac{40}{x} \qquad (3\text{-}5)$$
$$x = 0.010$$

That is, the equivalent position resolution from the analog output is 0.01 mm.

3.9.1 DAQ Theoretical Accuracy

It is expected that the accuracy of the DAQ voltage will vary between 1850 μV at a zero voltage reading and 2680 μV at full scale. The basis for this calculation is discussed in [45] and is demonstrated in Appendix B. Note that there is some uncertainty as to the values that should be used to account for changes in the ambient temperature. Given that the equipment is relatively new it was believed that there should be negligible temperature effects, although this may need to be investigated further in order to see if improvements can be made to the

system. As with the laser micrometer, it is possible to obtain more accurate data by averaging the data input by the DAQ as opposed to averaging at the Keyence sensor.

3.9.2 Total Theoretical Input Accuracy

Based on the above information it is possible to get a rough idea of what the accuracy of an analog input measurement will be. For a given nominal position measurement, the laser system accuracy and analog resolution can be used to determine the range of the output voltage. This can then be converted to the actual input voltage seen by the DAQ, based on the resolution of the DAQ. At this point the DAQ errors can be factored into the voltage and the measurement can be converted back into a position measurement and compared to what the nominal voltage should be. Calculation details are discussed in Appendix C and the net result is summarized in Table 3-5. It is observed that the worst-case error is on the order of 13 micrometers, although error on the order of 5 micrometers may be more common.

Measurement (mm)	Error (mm)
30.01463	0.01363
30.00557	0.00457
29.99581	0.00519
30.00487	0.00387

Table 3-5: Sample error calculation series for a nominal measurement of 30.001 mm.

In order to test the accuracy of the vertical position sensor, a one inch gauge block was placed on a platform inside the *z* position sensors' measuring field. Measurements are then made with and without the gauge block. In each case the mean value of the measurements are found and the difference is calculated. It is expected that the net difference should be equal to 25.4 mm. The results are shown in Table 3-6. While the overall average measurement of the block height is fairly accurate, the standard deviation of the measurement indicates that there is a high degree of variation between individual measurements. This is not unexpected given the behaviour of the laser sensor.

The gauge block measurements indicated that the error should be significantly greater than what the theory indicates. A more accurate picture of the true sensor accuracy can be obtained by using the measurement hold feature on the Keyence sensor. This will eliminate

any errors due to poor measurement repeatability. The sensor will send a constant voltage to the DAQ, and the resulting variance in the measurement should be simply due to the accuracy of the DAQ. The resultant measured means and standard deviations for an arbitrary object in the measurement field are shown in Table 3-7. This standard deviation of the hold operation is more in line with what might be expected based on the theoretical error shown in Table 3-5. Based on this data it is apparent that a great deal of the measurement variance in the system is introduced directly by the laser sensor.

Calculated Average Height (mm)	Standard Deviation (mm)	Error (μm)
25.3975	0.014813	2.5
25.40501	0.018662	5
25.40577	0.017287	5.8
25.40298	0.017874	3

Table 3-6: Measurements of a one inch gauge block using the laser micrometer.

	Mean (mm)	Standard Deviation (μm)
No Hold on Output	10.2883	12.987
Hold on Output	10.27829	6.384

Table 3-7: Comparison of the mean and standard deviation produced by an object in the field. In the first case, the output from the sensor is allowed to float, while in the latter case the output voltage is held constant.

During the course of experimentation it was found that the standard deviation on the horizontal position sensors was less than that of the vertical position sensors. The comparable standard deviations on the *z* and local *x* and *y* sensors are presented in Table 3-8 for the case when the microrobot is resting on its launch platform (i.e. no control is taking place). The horizontal deviations are in line with the vertical deviation during the sample hold process. It is known that there is some sort of electric motor inside the laser sensor transmitter. The rotation of this motor may be causing small displacements of the sensor due to the fact that that its mounting bracket is cantilevered. These displacements are within the accepted alignment tolerance of the sensors, but do contribute to the increased variance of the measurement. The horizontal position sensors, by comparison, are resting on their side, which means that the rotational axis of the motor is parallel to the *z* axis. This means that there would be no induced vibrational motion in the vertical direction, and since the

horizontal mounting brackets are double bolted the horizontal torsional effects are minimal. The variance on the vertical position sensor could be improved by minimizing the vibration effects caused by the motor. One potential solution would be to increase the thickness of the mounting bracket in order to increase the moment of inertia, which would result in decreased deflections.

3.10 Output Accuracy

Unlike the input DAQ there is not as much information available regarding the accuracy of the output cards. Because they have the same range and resolution as the input cards, it is assumed that accuracy of the output voltage will be similar. That is, the output voltage will vary from 1850 μV at zero output to 2680 μV at full scale.

Table 3-9 shows the average output measured on each channel using the amplifier display and a multimeter for three different voltage inputs. It can be seen that the output on each channel is approximately the same. It is therefore expected that, if the input voltage to each channel is the same, each electromagnet will receive the same current. With the aid of data provided by the University of Waterloo Faculty of Science it is possible to derive a rough characterization of what the variance on the current will be. The output data is characterized as a saw-tooth step pattern. By collecting all of the output data points that occur at the same nominal input a rough standard deviation calculation can be performed. The standard deviations are presented in Table 3-10. The deviations for all channels lie between 0.03 and 0.04 A. In reality the current deviation is likely to be considerably less, given that the measurements in Table 3-9 are measured to a minimum precision of 0.01 A and that the measurements were not fluctuating as significantly as the rough deviation calculation would indicate. It is believed that the output from the amplifier is acceptable for maintaining a stable levitation system.

Minor fluctuations in the current and the variances in the electromagnet resistance and inductance will affect the positioning of the robot due to the resultant variations in the magnetic field. This is an issue that needs to be investigated further in order to improve the

positioning accuracy by quantifying how the minor current fluctuations and the variance in the electromagnet parameters will affect the magnetic field and field gradients.

Z Position	Local X Position	Local Y Position
0.0104 mm	0.00542 mm	0.00838 mm

Table 3-8: Standard deviations on the three measurement sensors during the measurement of the microrobot in a static position.

Channel	Amplifier Reading (A)	Multimeter Reading (A)
1	0.49	0.48
2	0.493	0.48
3	0.49	0.485
4	0.492	0.49
5	0.486	0.485
6	0.491	0.49
7	0.4895	0.49
8	0.4875	0.48
9	0.489	0.49
10	0.492	0.49
11	0.493	0.48
12	0.489	0.48
13	0.49	0.48
14	0.4875	0.48
15	0.4925	0.49
16	0.4925	0.49
17	0.489	0.49
18	0.494	0.49
19	0.485	0.48
20	0.4915	0.49
21	0.4895	0.49
22	0.4875	0.49
23	0.495	0.49
24	0.491	0.48

Table 3-9: Amplifier channel outputs due to an input of 1.4 volts.

Channel	1.4 v	2.8 v	4.2 v
1	0.033733	0.038736	0.027976
2	0.034416	0.031006	0.029823
3	0.033648	0.034495	0.032924
4	0.038142	0.035289	0.044467
5	0.030404	0.037937	0.033549
6	0.035484	0.029582	0.032961
7	0.038188	0.027289	0.028544
8	0.034203	0.032409	0.029889
9	0.038965	0.026331	0.030301
10	0.032438	0.026748	0.038088
11	0.037082	0.035852	0.030955
12	0.037751	0.033675	0.043924
13	0.03547	0.037983	0.037674
14	0.037825	0.031298	0.036648
15	0.036232	0.035336	0.027185
16	0.03472	0.036511	0.037481
17	0.032712	0.033549	0.040882
18	0.041166	0.032711	0.021112
19	0.032267	0.034249	0.030154
20	0.041018	0.024964	0.036758
21	0.031155	0.032997	0.033697
22	0.035913	0.045835	0.035032
23	0.04	0.032063	0.038867
24	0.031149	0.041179	0.034415

Table 3-10: Estimation of standard deviation of amplifier current for three input voltages.

Chapter 4
Magnetic Force Estimation – An Analytical Approach[1]

Chapter 2 discussed the basic analytical model of a magnetic suspension system. In order to make use of this model for the purposes of control design it is desired to know the equations governing the flux density field ***B*** produced by the magnetic drive unit. Although the flux density profile at any position can be found through numerical analysis of a finite element model, there are no simple analytical formulas that can be used to describe the force produced by the magnetic drive unit. The applied force will be dependant on many factors, including but not limited to the geometry of the pole piece, the physical dimensions of the components of the electromagnet, the current in the electromagnet, the number of electromagnets, and the characteristics of the levitated object.

The motivation for this portion of the research was to develop an analytical formula that could be used to approximate the flux density field produced by the magnetic drive unit. This formula would be used in the development of the system model and would allow for advanced control of the system. Possible advantages of such a formula would be improved positional accuracy and the ability to develop advanced trajectories that allow the microrobot to smoothly transition between two points.

In Chapter 2 (4-1) was developed as the levitation force produced by a single electromagnet in simple magnetic levitation. Because the magnetic drive unit behaviour is similar to simple magnetic levitation, it is possible that a more complex variation of (4-1) that accounts for full spatial motion could be used to generate an analytical model for the force produced by the magnetic drive unit.

$$F_z = \frac{-L_0 I^2}{2a\left(1 + z/a\right)^2} \tag{4-1}$$

[1] Portions of this chapter are ©2005 IEEE. Reprinted, with permission, from "Derivation of an Analytical Model for the Force Produced During the Motion of a Magnetically Suspended Object." by David G. Craig and Mir Behrad Khamesee. IEEE International Conference on Mechatronics and Automation (2005): 970-974.

4.1 Numerical Model Setup

Due to hardware limitations on the modeling computer, the initial FEA was performed on a simplified two-dimensional model of the system in FEMLAB. It was found that the behaviour of the flux density profiles produced by the numerical simulation were consistent with what would be expected from the actual three-dimensional system. This made the model suitable for preliminary analysis. Provided the preliminary analysis showed some promise, methods could be explored to extend the modeling into three dimensions.

The general setup of the numerical model is shown in Figure 4-1. Note that if another electromagnet is placed at the other end of the pole piece, this system would be capable of moving an object in the x and z directions. Analysis has shown that the flux densities produced by individual electromagnets combine by superposition to form the overall flux density profile. Provided additional electromagnets remain symmetrically spaced on the pole piece the derived analytical equation can be applied to these electromagnets through a coordinate transformation. In this model, it is assumed that any dimensions that extend out of the plane of the paper extend to infinity. The system therefore does not represent a "closed" system, but as previously stated the shapes of the flux density profiles were consistent with what would be expected from the three-dimensional system.

The relevant system parameters are presented in Table 4-1. As in Chapter 2 the electromagnet parameters are chosen to preserve the current density and ampere-turns of a more realistic electromagnet model, and the motivation for changing the parameters is to permit ease of computation. The nominal current input to the electromagnet was chosen so that the resultant force produced by two electromagnets would be capable of levitating an object with a mass of several grams. In the 3D case it is possible to incorporate more electromagnets for the force calculation since it is possible to arrange more than two electromagnets in a manner that permits the same formula to be used for each electromagnet. For example if the pole piece is a cylindrical disk, multiple electromagnets can be placed around the outer perimeter of the disk. An increased number of electromagnets will reduce the current consumption of each individual electromagnet while still allowing a sufficient amount of levitating force to be produced.

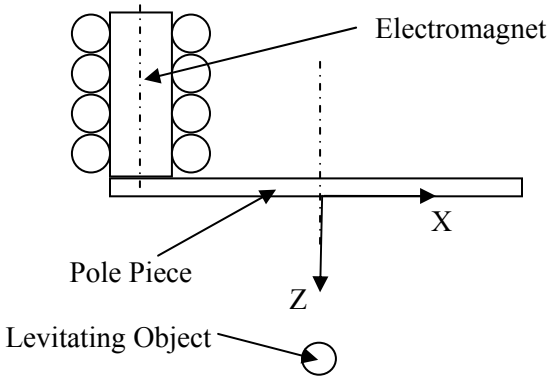

Figure 4-1: Schematic representation of the 2D model used to derive the numerical force profiles.

Parameter	Value
Nominal Current	$1x10^6$ A
Electromagnet Wire Turns	5
Electromagnet Wire Diameter	18 mm
Electromagnet Core Dimensions	40 mm x 90 mm
Pole Piece Dimensions	340 mm x 8 mm
Dipole Moment of Levitated Object	0.015625 Am^2

Table 4-1: Relevant properties of the numerical simulation.

4.2 Vertical Force Analysis

The vertical operating window of the model was estimated to be between z=10 cm and z=15 cm. Over this range the force is approximately linear. By choosing two points in this range and assuming that the line connecting them is straight, the slope and z intercept of a straight line can be determined. The resulting equation for the vertical force F_z will be of the form

$$F_z = mz + b \tag{4-2}$$

where m is the slope of the line and b is the axis intercept. Figure 4-2 shows a comparison of the numerical and analytical model. As is expected for a linear approximation the analytical model is a good fit over the range of interest.

A more appropriate equation for the vertical force is of the form

$$F = m(x)z + b(x) \tag{4-3}$$

where the slope and the intercept are now functions of the microrobot's horizontal position.

Plots of how the slope and z intercept vary with horizontal position are shown in Figure 4-3 and Figure 4-4, along with the best fit curves that estimate the slope and z intercept at any horizontal point. The slope and z intercept equations are of the form

$$y = Ae^{-b(x-x_0)} \tag{4-4}$$

where A and b are constants estimated from the generated data and x_0 is the distance to the edge of the pole piece where the electromagnet is located.

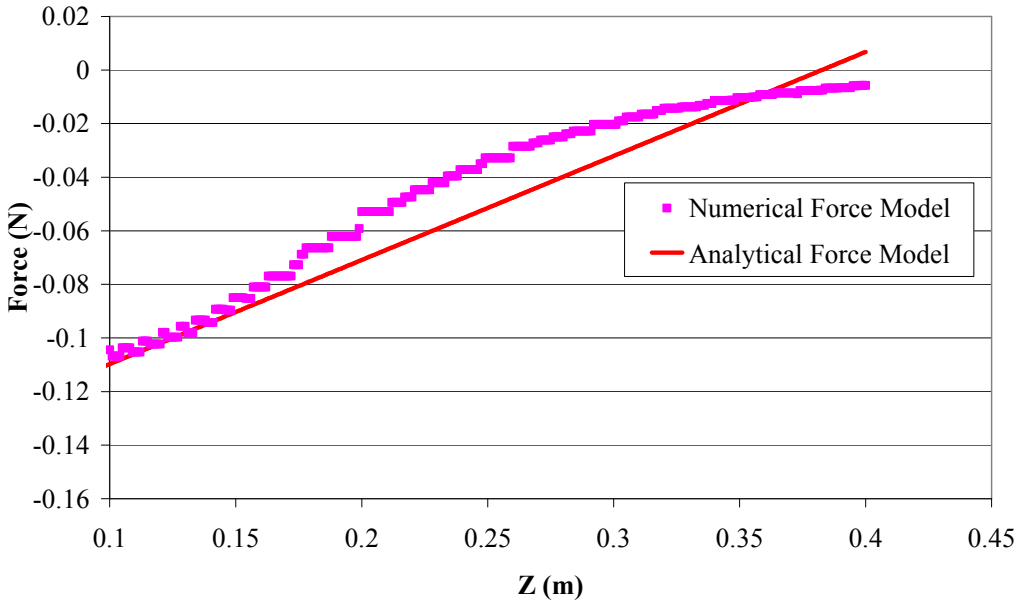

Figure 4-2: Vertical force at x=0.

4.3 Horizontal Force Analysis

Preliminary analysis indicated that a linear approximation of the horizontal force would not be suitable to cover the entire length of the pole piece. The governing equation was assumed

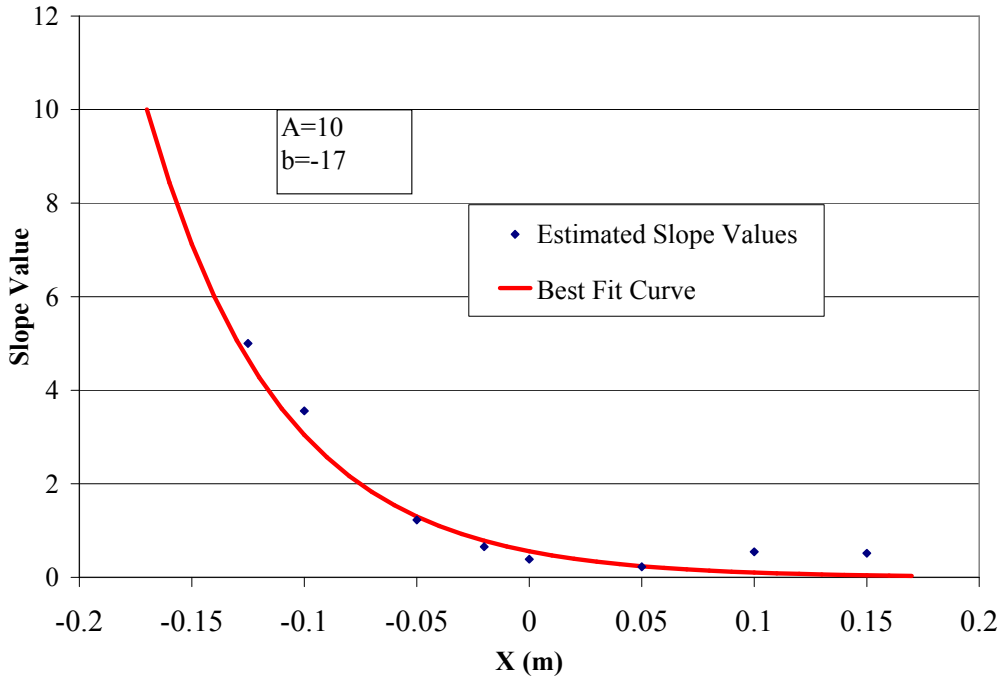

Figure 4-3: Estimate of the variation of the slope.

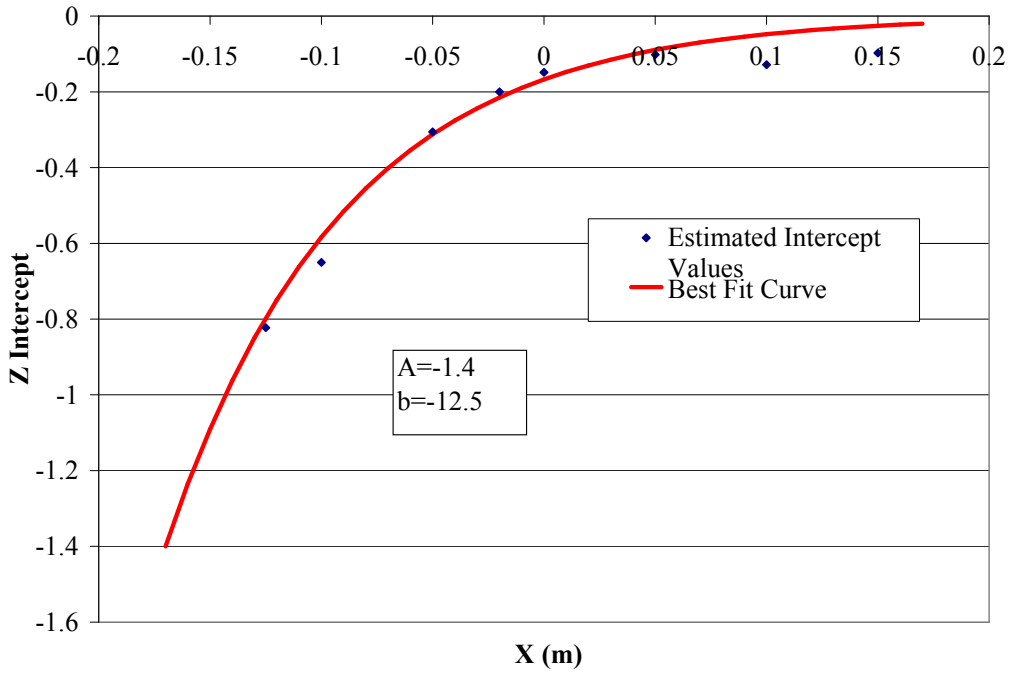

Figure 4-4: Estimate of the variation of the intercept.

to be of the form

$$F_x = \frac{-L_0 I^2}{2b\left(1+\frac{z}{a}+\frac{(x-x_0)}{b}\right)^2} + c \tag{4-5}$$

where a, b and c are constants. Note that this equation is a slightly modified form of (4-1). Preliminary estimates for L_0 and a were obtained from the preliminary work done for the vertical analysis prior to the implementation of the linear approximation. An estimate of b could then be obtained from the data and the offset c determined to provide improved model accuracy. The parameters are presented in Table 4-2.

Figure 4-5 shows one of the results of this analysis. In general, the approximation is fairly reasonable far from the electromagnet, but at distances close to the electromagnet the analytical model of the force starts to increase exponentially, while in reality the rate of force increase tends to remain linear. It is therefore reasonable to conclude that, with this model, the horizontal range of the workspace will be less than the extents defined by the edges of the pole piece.

Parameter	Value
L_0	$-2\text{x}10^{-13}$
a	0.22
b	0.05
c	-0.08

Table 4-2: Parameters used to estimate the horizontal force profile.

4.4 Effect of Current

Although the equations developed to this point have dealt with changes in the x and z coordinates, the variation of current has not yet been considered. Experimentation has shown that it is relatively simple to deal with the change in current. If the parameters are

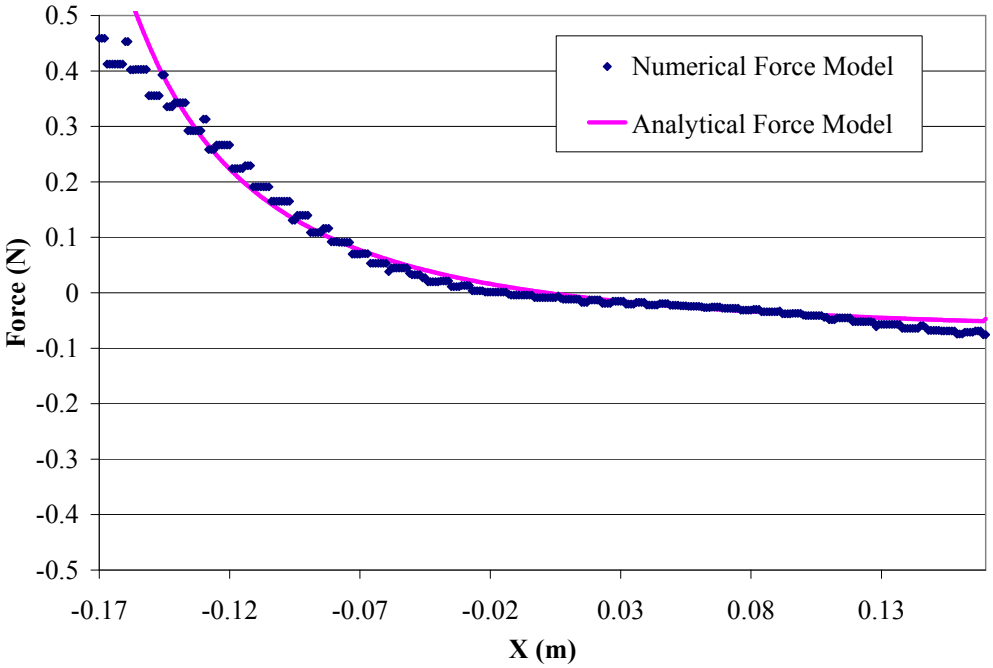

Figure 4-5: Horizontal force profiles generated at z=0.125 m.

determined at some nominal current value I_0, the force equations at the actual current I can be written as

$$F_z = (m(x)z + b(x))\frac{I}{I_0} \tag{4-6}$$

$$F_x = \frac{-II_0L_0}{2b\left(1+\frac{z}{a}+\frac{(x-x_0)}{b}\right)^2} + c\frac{I}{I_0} \tag{4-7}$$

4.5 Superposition Analysis

Now that the models have been derived, it is possible to determine the combined effects of multiple electromagnets. For this analysis, an electromagnet is placed at either end of the pole piece to produce a model symmetric about the z axis. Because the forces produced by each electromagnet combine by superposition, the analytical force produced by each electromagnet can be calculated individually and then summed together to obtain the total force. Figure 4-6 shows a test case for the vertical force. It can be seen that the numerical

and analytical models do not match each other over the expected operating window. The problem seems to be related to the estimation of the slope and z intercept. The equation that estimates the values of m and b at a given point x is an estimate, and so there will be some variation between the true value and the actual value. Individually, each error may be small. But as more and more electromagnets are added to the drive unit, these errors will compound to produce a final result that may deviate significantly from the actual value. At this point it is not clear what impact this error would have on the dynamic model of the system.

Figure 4-7 shows a test case for the horizontal force. The equation for the force produced by the right electromagnet is given by

$$F_x = \frac{II_0L_0}{2b\left(1+\frac{z}{a}+\frac{(x_0-x)}{b}\right)^2} - c\frac{I}{I_0} \tag{4-8}$$

The changes account for the fact that the flux density field produced by the right electromagnet is a mirror image of the left electromagnet, which means that the gradient will be a negative mirror image. The analytical force is a good match to the force determined by numerical calculation over most of the distance covered by the pole piece. Some further refinement of the parameters may be possible in order to improve the accuracy.

4.6 Extension of the Analysis to Three Dimensions

A 3D numerical model of the magnetic drive unit presented in Chapter 3 was developed in ANSYS by another member of the research group to investigate various magnetic field effects. The setup of this model is presented in Appendix A. ANSYS was used for the 3D simulations instead of FEMLAB as ANSYS is able to solve complex 3D finite element simulations more efficiently than FEMLAB. Attempts were made to use this numerical model to extend the 2D equations discussed above to a full 3D equation. The primary focus of the 3D analysis was on extending the horizontal force equation to the third dimension. Figure 4-8 shows the basic layout of the magnetic drive unit. Note that for the simulation z is defined as positive upwards from the base of the pole piece. In order to apply (4-7)

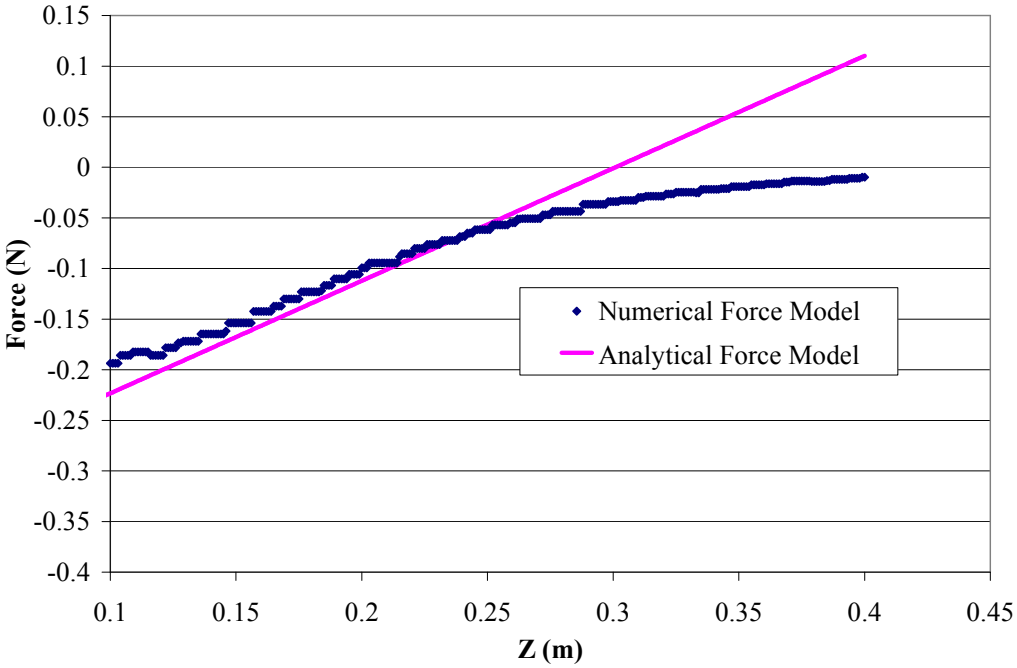

Figure 4-6: Vertical force at x=0 using (4-6).

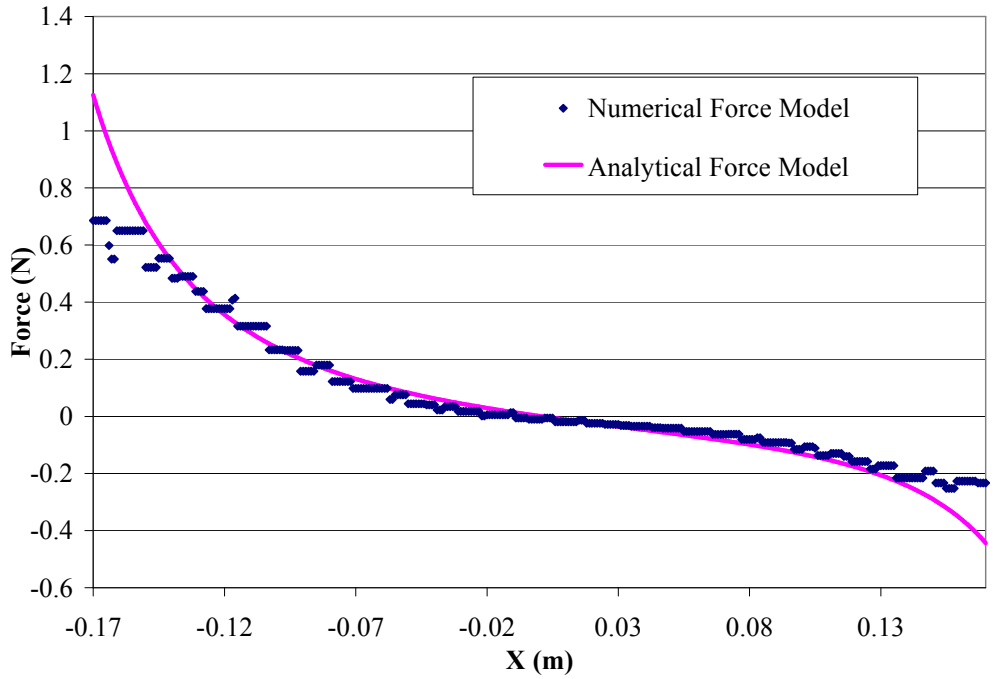

Figure 4-7: Horizontal force at z=0.125 m using (4-7) and (4-8). The current ratio is 3:1 between the left and right electromagnet.

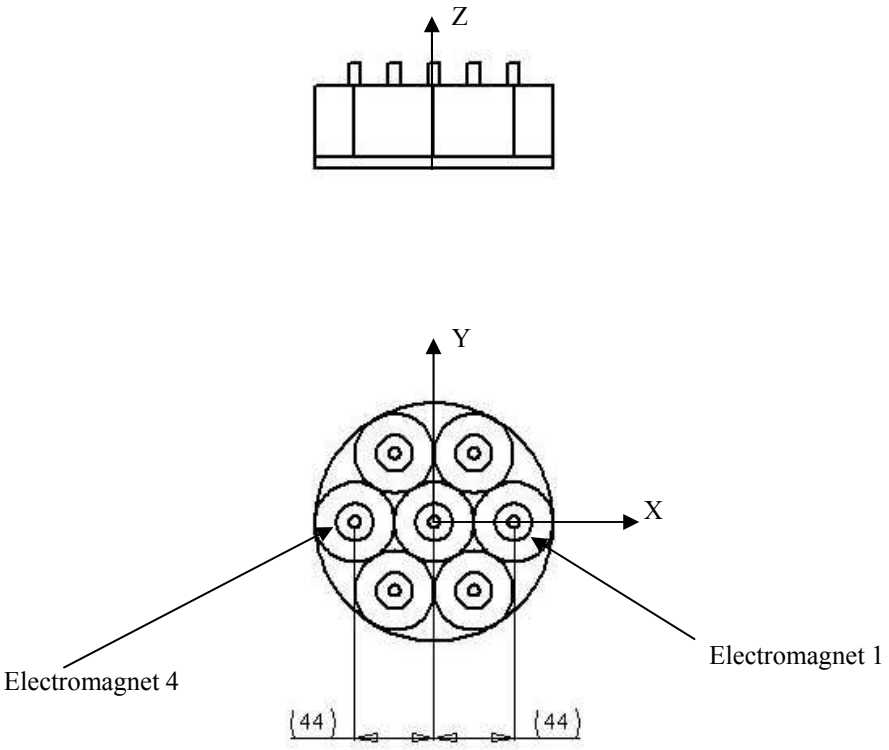

Figure 4-8: Layout of the electromagnets on the pole piece for the ANSYS Simulation. Dimensions are in mm.

appropriately while maintaining a right-hand coordinate frame it will be necessary to use the absolute value of *z*. In general this will never be a problem since it unlikely that levitation will ever occur above the pole piece.

The initial analysis started by attempting to model the force produced by electromagnets 1 and 4 in order to test (4-7). Figure 4-9 shows a comparison of the numerical force and the analytical force produced by the two electromagnets. The individual estimates for electromagnets 1 and 4 as shown in Figure 4-10 and Figure 4-11. It is observed that the analytical equations are able to match the trend of the graph, but that there is deviation in the predicted values. The estimated parameters are presented in Table 4-3. Note that it was necessary to estimate different parameters for both the electromagnets in order to achieve the best possible fit for both. Assuming that the values reported by the model are correct, it is believed that this phenomenon may be due to the effects of the iron yoke. The yoke is not

truly symmetric about the pole piece, and so its effects on the field would not apply equally over the entire operating area of the magnetic drive unit. This would lead to an asymmetric field distribution, requiring different parameter estimates for each of the electromagnets. This can be observed in Figure 4-9. The yoke is located at a negative x position, and it is observed that the force is greater for negative x values.

Beyond this verification, it was found to be extremely difficult to incorporate the third dimension into the equation. The assumed form of the 3D equation for the horizontal force was

$$F_x = \frac{-II_0L_0}{2b\left(1+\frac{z}{a}+\frac{x}{b}+\frac{abs(y)}{d}\right)^2} + c\frac{I}{I_0} \tag{4-9}$$

The absolute value term is used since the force produced by electromagnets 1 and 4 is symmetric about the x axis. The force plots incorporating the y parameter are shown in Figures 4-12 through 4-15. As in the case when only x direction motion is considered the approximation seems to be reasonably good near the centreline of the pole piece, but gets progressively worse as y increases.

Parameter	Electromagnet 1	Electromagnet 4
L_0	$-8\text{x}10^{-4}$	$-6\text{x}10^{-4}$
a	$5\text{x}10^{-3}$	$2.2\text{x}10^{-2}$
b	$3\text{x}10^{-3}$	$2.2\text{x}10^{-2}$
c	$3.02\text{x}10^{-4}$	$4\text{x}10^{-4}$
d	$1\text{x}10^{-2}$	N/A

Table 4-3: Parameters used to estimate the *x*-direction force in the 3D simulation. The force for non-zero values of *y* was not investigated for electromagnet 4 and so no value of *d* was estimated.

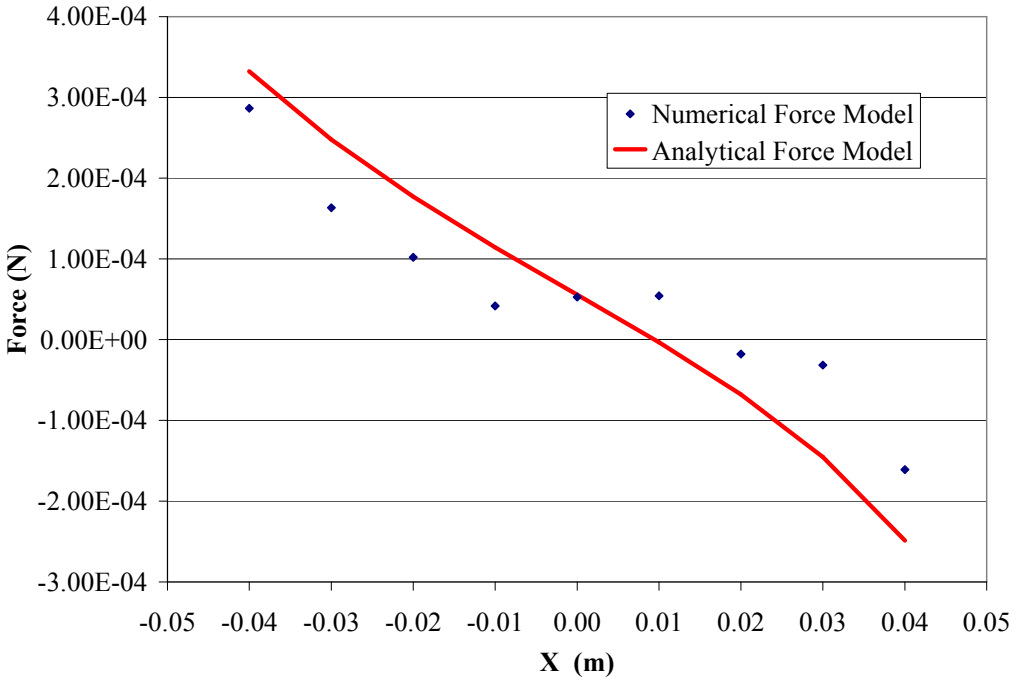

Figure 4-9: Force in the *x* direction for electromagnets 1 and 4 at *z*=-9 cm, *y*=0 cm.

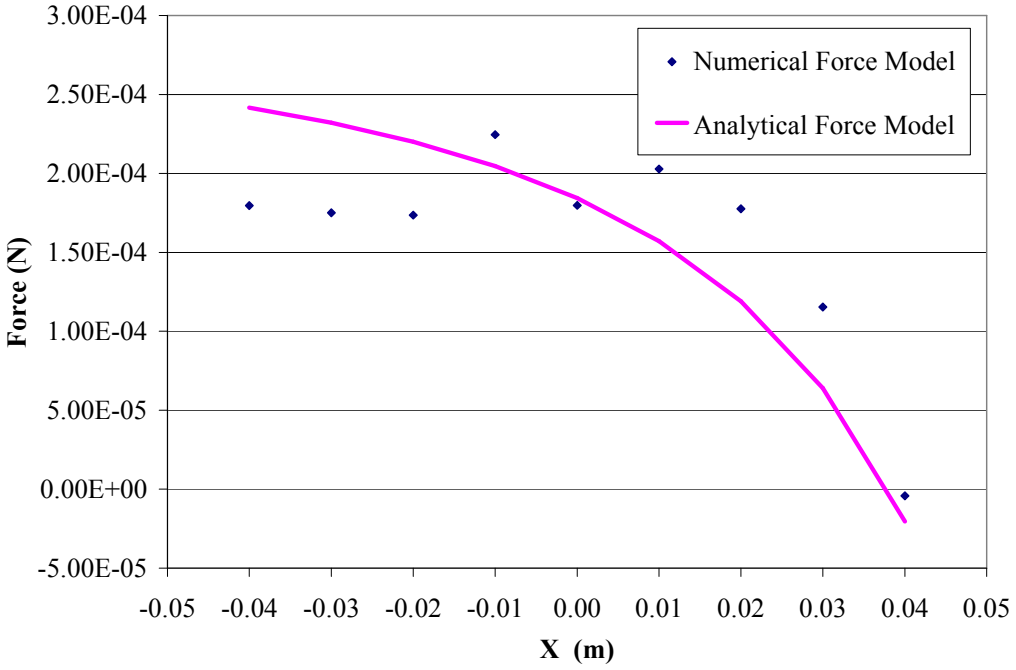

Figure 4-10: X component of the force produced by electromagnet 1 at *z*=-9 cm, *y*=0 cm.

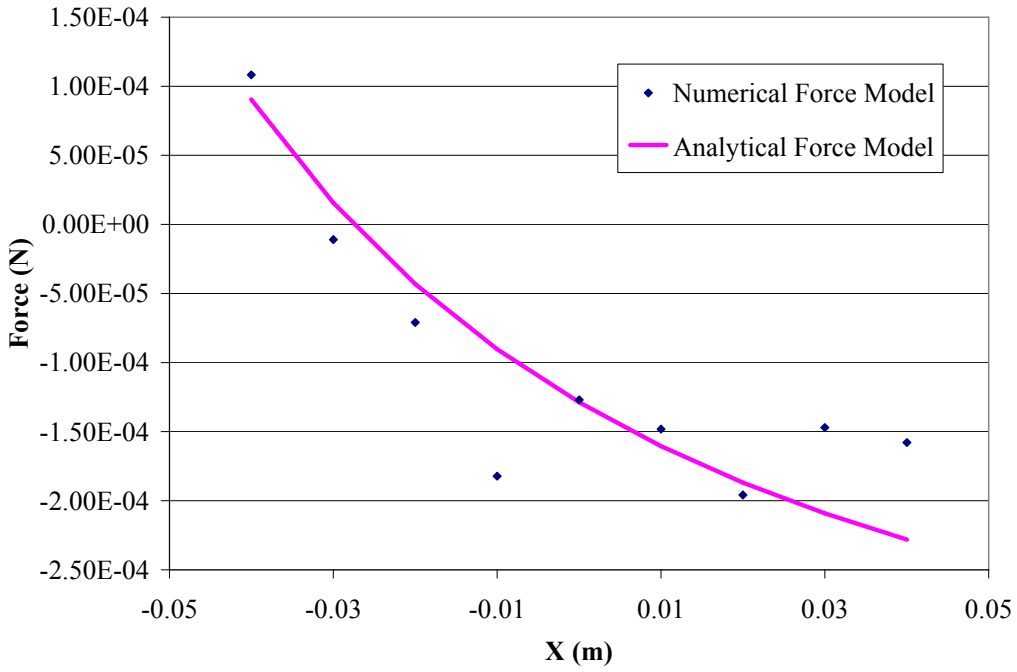

Figure 4-11: X Component of the force produced by electromagnet 4 at *z*=-9 cm, *y*=0 cm.

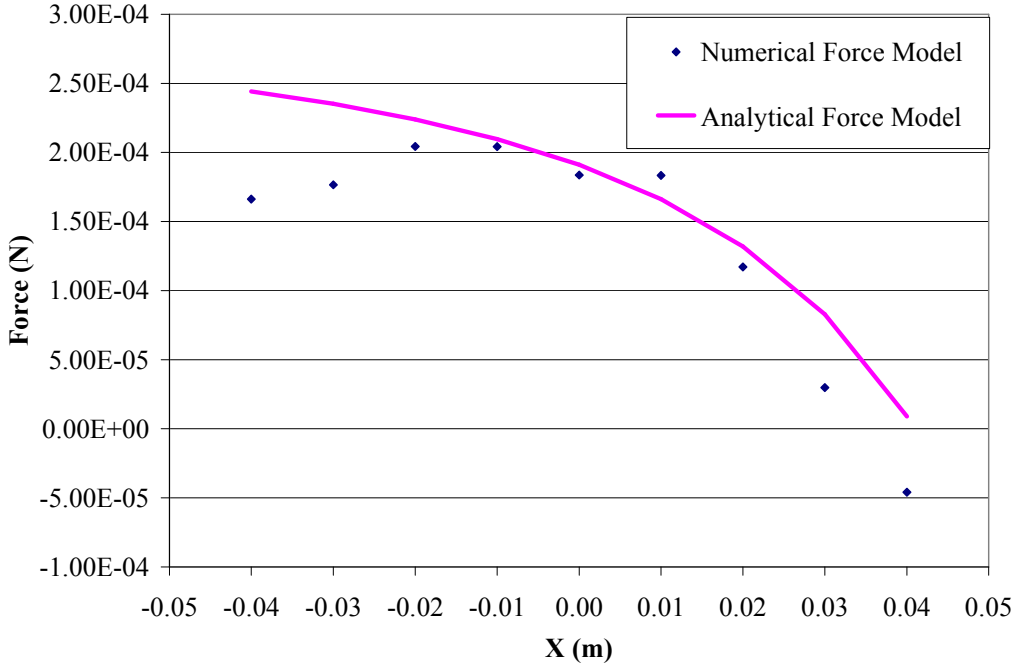

Figure 4-12: X component of the force produced by electromagnet 1 at *z*=-9 cm, *y*=1 cm.

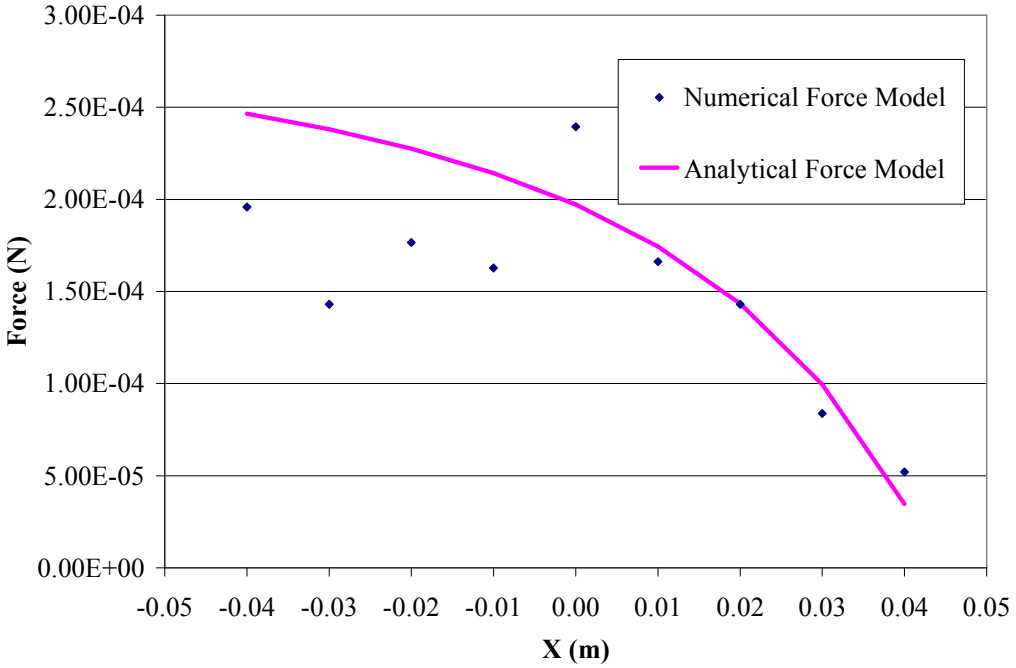

Figure 4-13: X component of the force produced by electromagnet 1 at *z*=-9 cm, *y*=2 cm.

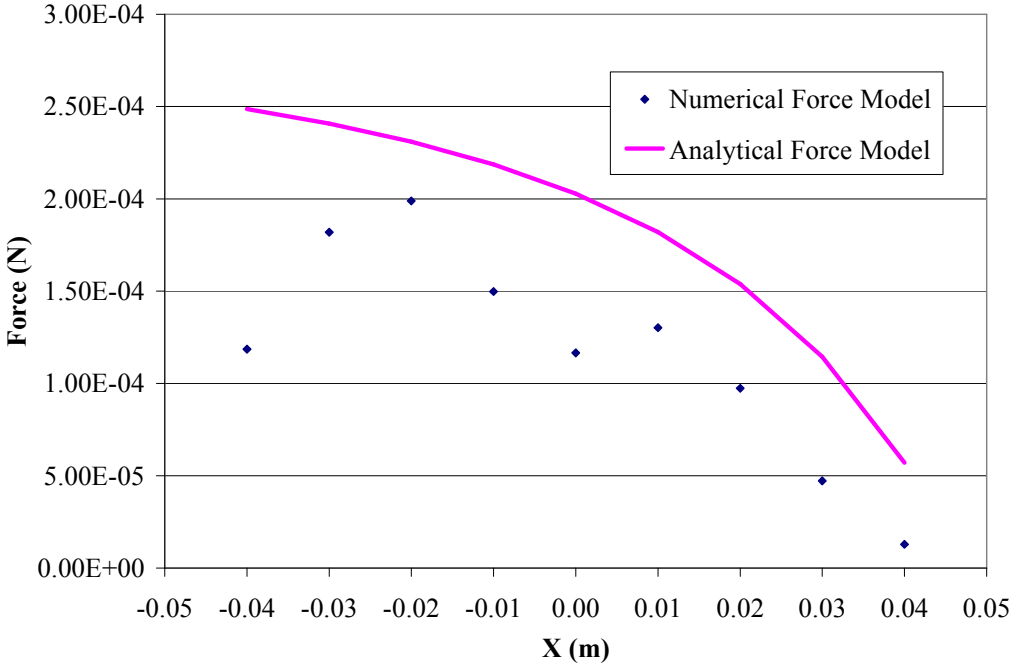

Figure 4-14: X component of the force produced by electromagnet 1 at *z*=-9 cm, *y*=3 cm.

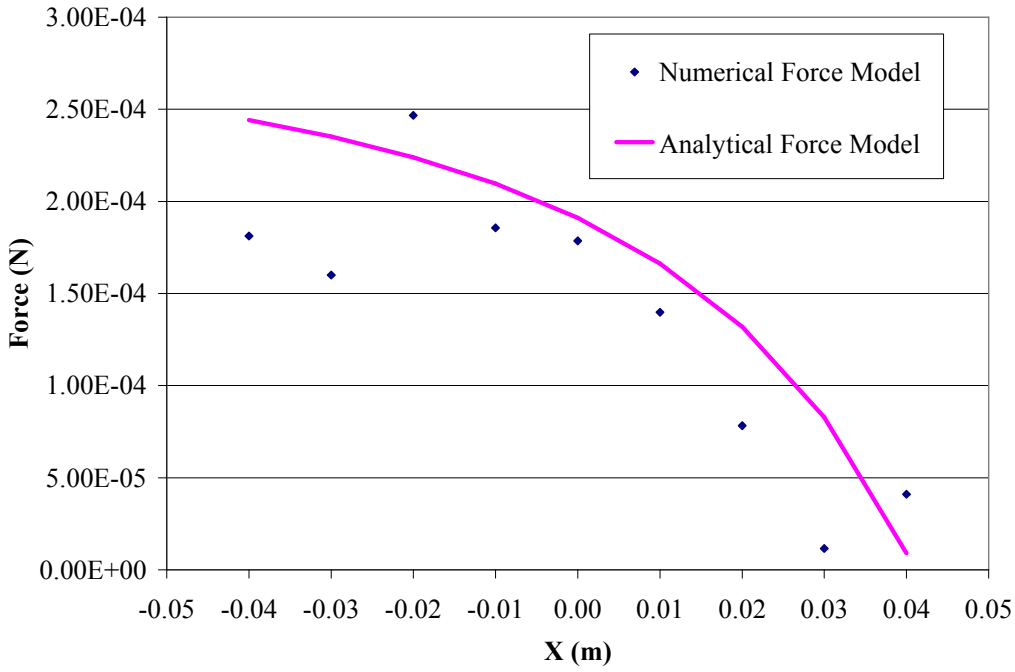

Figure 4-15: X component of the force produced by electromagnet 1 at *z*=-9 cm, *y*=-1 cm.

In general, the high non-linearity of (4-9) has made it somewhat of a challenge to estimate the parameters, and usually a high degree of tuning is required to achieve the fit. This tuning becomes even more complex with the inclusion of a third parameter. It has already been shown that the small error in the force estimation for each individual electromagnet will compound into a significant error as subsequent magnets are added by superposition. Given that the existing system uses six electromagnets and is configurable up to 24 electromagnets, it is important that the force equation be as accurate as possible in order to minimize these errors, otherwise the compounded error will render the equations useless. It is also possible that the assumed form of (4-8) is not correct and that a more complex form of the equation is needed to describe the behaviour of the force field. For example, Figure 4-16 shows the resultant force for the two electromagnets when a quadratic fit is used to describe the individual flux density curves. It is observed that the quadratic equations provide a better fit to the data than (4-8). The equations are of the form

$$F_x = a_0 x^2 + a_1 x + a_2 \tag{4-10}$$

In the general case the coefficients a_0, a_1, and a_2 would be some function of y and z and would vary accordingly as one moved underneath the pole piece.

There are also challenges to extracting data from the finite element model on a scale suitable for use. The existing data spacing is fairly coarse, which may introduce errors into the estimation. The ability to generate a finer mesh on the scale of the 2D estimation will require more computational power.

Although not investigated to a similar extent as the horizontal force, it is expected that the vertical analysis will pose similar challenges. If the linear force approximation is used, it would be reasonable to assume that the vertical force equation would be of the form

$$F_z = (m(x,y)z + b(x,y))\frac{I}{I_0} \tag{4-11}$$

This equation would serve as a suitable starting point, although it is not clear to what degree of complexity or accuracy the equations for the slope and the intercept will have.

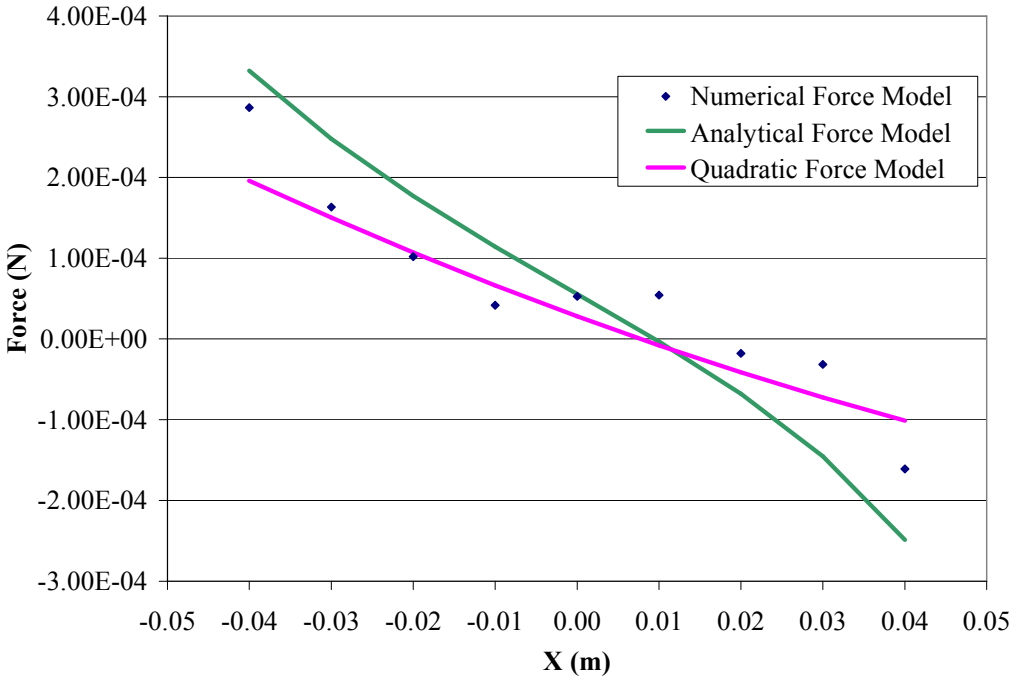

Figure 4-16: 3D Model horizontal force at z=-9, y=0 cm, including the quadratic model.

Chapter 5
Vertical Position Model Estimation

5.1 Closed Loop Identification Theory

Under ideal circumstances identification of an unknown plant occurs under open loop conditions. Occasionally it is necessary to perform identification of a plant with closed loop feedback. A typical occurrence in industry is that the plant is already under feedback control and the estimation data is collected from the day-to-day operations of the system. Another common occurrence, as is the case with magnetic suspension, is that the plant is open loop unstable, and so a controller is needed to stabilize the system in order to collect meaningful data.

Figure 5-1 shows the general form of the closed loop system. Provided input r is a persistently exciting signal and the controller C is not trivially simple, it should be possible to identify the plant P.

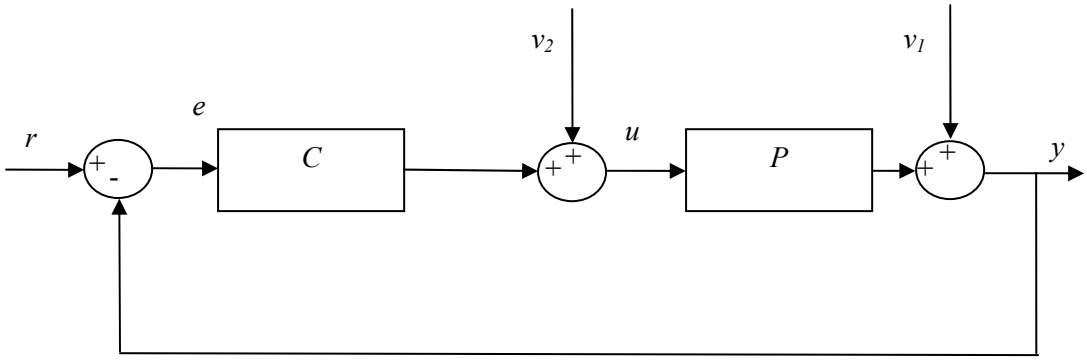

Figure 5-1: General form of a closed loop system.

There are three general approaches to identifying the system from closed loop data [48]. The first involves direct identification of the system using signals y and u. The primary drawback to this method is that an accurate noise model is needed since the input signal u is

no longer independent of the noise. The second approach involves identification of the closed loop transfer function G_{cl}, which is of the form:

$$G_{cl} = \frac{CP}{1+CP} \tag{5-1}$$

This is essentially an open loop problem, and provided the controller dynamics are well known a reasonably accurate model of the system can be extracted from (5-1). The third procedure involves a two-stage calculation in which u and y are treated as outputs to input signal r.

$$y = G_{cl}r + v_1 \tag{5-2b}$$

$$u = G_{ru}r + v_2 \tag{5-2b}$$

The open loop plant P is then estimated from

$$P = \frac{G_{cl}}{G_{ru}} \tag{5-3}$$

5.2 Identification Procedure

The identification process was performed using the modified least squares algorithm. This algorithm was chosen because it was found to provide excellent parameter convergence in a relatively low number of iterations. Attempts were made to use generalized least squares and recursive least squares but it was found that these algorithms did not provide good model estimates due to poor convergence of the system parameters, as shown in Figure 5-2 and Figure 5-3.

The modified least squares algorithm is an iterative search procedure used to eliminate bias due to signal noise [49]. A model of the form

$$A(q)y(t) = B(q)r(t) \tag{5-4}$$

is estimated using a least squares algorithm from input data r and output data y. The data is then filtered by the $A(q)$ polynomial.

$$\hat{y}(t) = \frac{y(t)}{A(q)} \tag{5-5a}$$

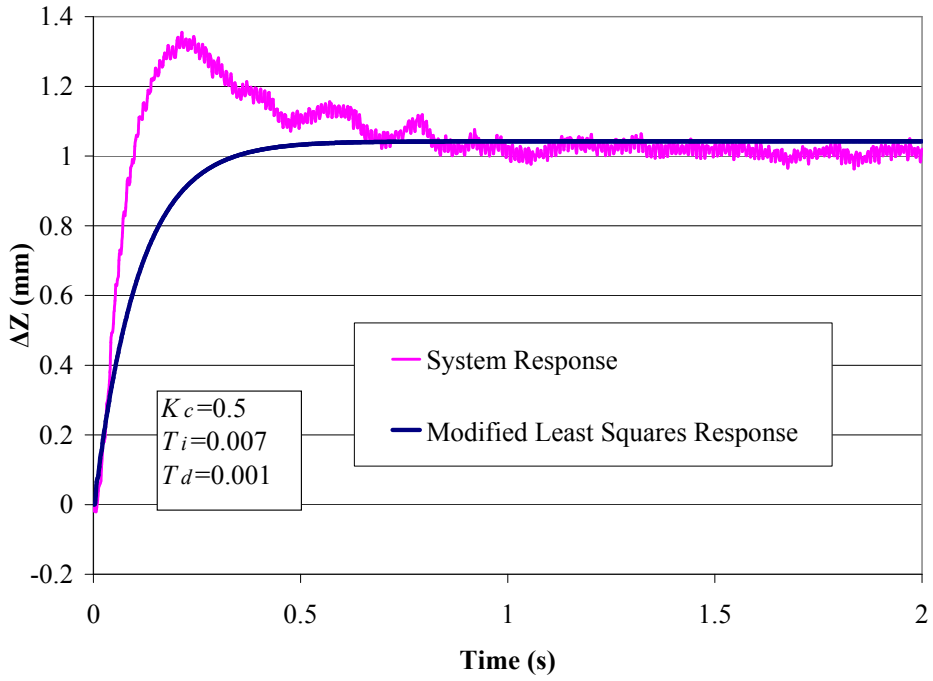

Figure 5-2: Estimated closed loop model from generalized least squares, using the data presented in Figure 5-4 and the model structure of (5-13).

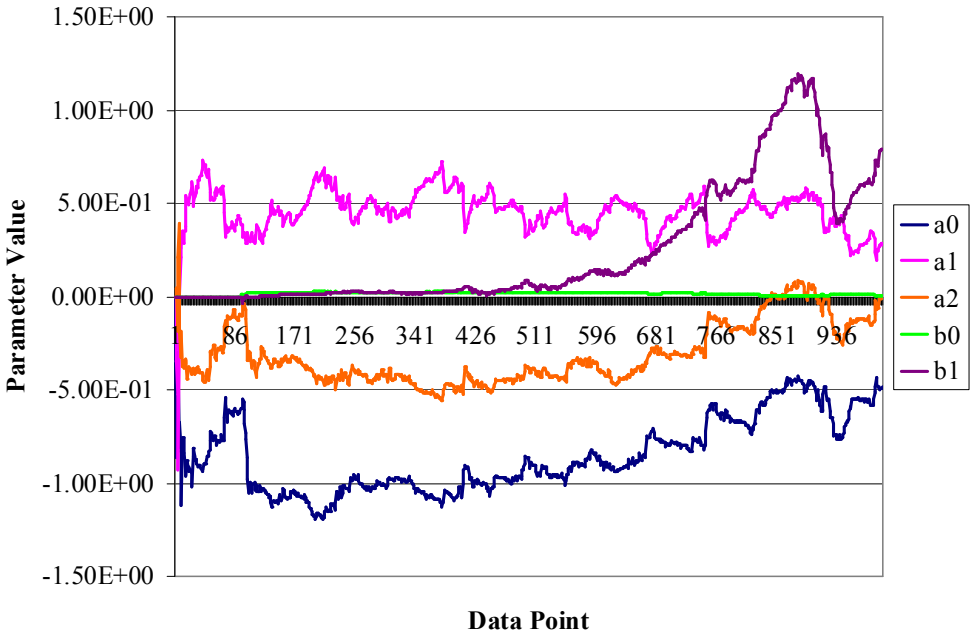

Figure 5-3: Parameter estimates using the 'rarmax' command in MATLAB. A forgetting factor of 0.98 is used.

$$\hat{r}(t) = \frac{r(t)}{A(q)} \tag{5-5b}$$

The polynomials *A(q)* and *B(q)* are estimated again with the filtered data. This process continues until convergence of the parameters is observed. The algorithm is included on the CD as described in Appendix D.

In all cases, the model structure was assumed to be of the ARMAX form. The general form of the model is

$$A(q)y(t) = B(q)r(t) + C(q)v(t) \tag{5-6}$$

where *A(q)*, *B(q)* and *C(q)* are delay operator polynomials. It was found that the exclusion of the *C(q)* term did not significantly impact the outcome of the identified models, and so it was assumed that *C(q)*=1 for the purposes of identification. The measured data for the system included the measured vertical position *z* in the local frame of the sensor, and the control output signal *u*, which represents the control voltage on each amplifier channel. Also recall from Chapter 2 that the error signal *e* is negated in order to counteract the effects of the negative gain in the open loop plant so that traditional controller analysis techniques can be used.

A stabilizing feedback controller is needed in order to measure the dynamics of the system, due to the instability of motion in the *z* direction. The resulting model will be a representation of this closed loop system containing the dynamics of both the plant and the controller.

The approximate open loop transfer function for vertical motion was derived in Chapter 2. The general form of this equation is

$$\frac{\Delta Z(s)}{\Delta I(s)} = \frac{-a}{s^2 - bs - c} \tag{5-7}$$

where *a*, *b,* and c are positive constants. Discretization of the system is performed using the zero order hold method in MATLAB. The resulting z transform is

$$\frac{\Delta Z(q)}{\Delta I(q)} = \frac{-b_0 q - b_1}{q^2 + a_0 q + a_1} \tag{5-8}$$

Note that the discretization introduces a zero into the transfer function. The parameters a_0, a_1, b_0, and b_1 are to be identified via the system identification procedure. Since the system is unstable it is expected that at least one of the roots of the open loop transfer function will be greater than one.

The stabilizing controller structure is estimated from the known structure of the open loop plant model, and final parameters are tuned through implementation on the real system. A PID compensator was chosen for this system, since the system in [30] operated successfully with a PID controller. The LabVIEW software used to develop the control system also provides several tools that allow for easy implementation of the PID control architecture.

In the Laplace domain, a PID controller is of the form

$$\frac{K_c T_d s^2 + K_c s + \frac{K_c}{T_i}}{s} \tag{5-9}$$

where K_c is the controller gain, T_i is the integral time constant and T_d is the derivative time constant.

The discrete output of the controller at time t, as implemented in LabVIEW, is

$$K_c e(t) + \frac{K_c T_s}{T_i} \sum_{i=0}^{t} e(t) + \frac{K_c T_d (e(t) - e(t-1))}{T_s} \tag{5-10}$$

where T_s is the sampling rate. For all experiments performed in this chapter the sampling rate was set at 2 ms. For simulation purposes in MATLAB, the controller is discretized to the following form:

$$\frac{k_1 q^2 + k_2 q + k_3}{q^2 - q} \tag{5-11a}$$

$$k_1 = K_c\left(1 + \frac{T_s}{2T_i} + \frac{T_d}{T_s}\right) \quad k_2 = K_c\left(-1 + \frac{T_s}{2T_i} - 2\frac{T_d}{T_s}\right) \quad k_3 = K_c \frac{T_d}{T_s} \tag{5-11b}$$

This is a modified form of the Tustin approximation that minimizes the oscillating control effects of the derivative action [50].

The discrete PID controller introduces two poles and two zeros to the system in order to change the system dynamics. Note that the pole location is static, as in the continuous case, while the placement of the zeros will depend on the chosen values of T_i and T_d. Trial and error experimentation on the system resulted in the following stabilizing controller parameters:

$$\begin{aligned} K_c &= 0.5 \\ T_i &= 0.007 \\ T_d &= 0.001 \end{aligned} \tag{5-12}$$

The response of the system to a step input is shown in Figure 5-4. The figure shows that the controller achieves the goal of stabilizing the system and provides excellent tracking of the reference point.

5.3 Identification of the Closed Loop Model

With the development of the PID compensator, it is now possible to make measurements of the stable system. The closed loop system transfer functions are of the form

$$\frac{y}{r} = \frac{Z}{Z_{ref}} = \frac{b_0 q^3 + b_1 q^2 + b_2 q + b_3}{q^4 + a_0 q^3 + a_1 q^2 + a_2 q + a_3} \tag{5-13}$$

$$\frac{u}{r} = \frac{b_0 q^4 + b_1 q^3 + b_2 q^2 + b_3 q + b_4}{q^4 + a_0 q^3 + a_1 q^2 + a_2 q + a_3} \tag{5-14}$$

In this particular case the roots of the numerator of (5-13) will contain the two zeros introduced by the PID controller and the zero of the open loop transfer function [51]. Similarly, the numerator of (5-14) will contain the two zeros of the PID controller and the two poles of the open loop transfer function.

In the process of performing the analysis, several problems were encountered. During the estimation of the model structure for equation (5-13), it was found that the location of the two identified zeros of the PID controller did not correspond with the expected values. Further examination of the model revealed that two of the poles in the denominator were

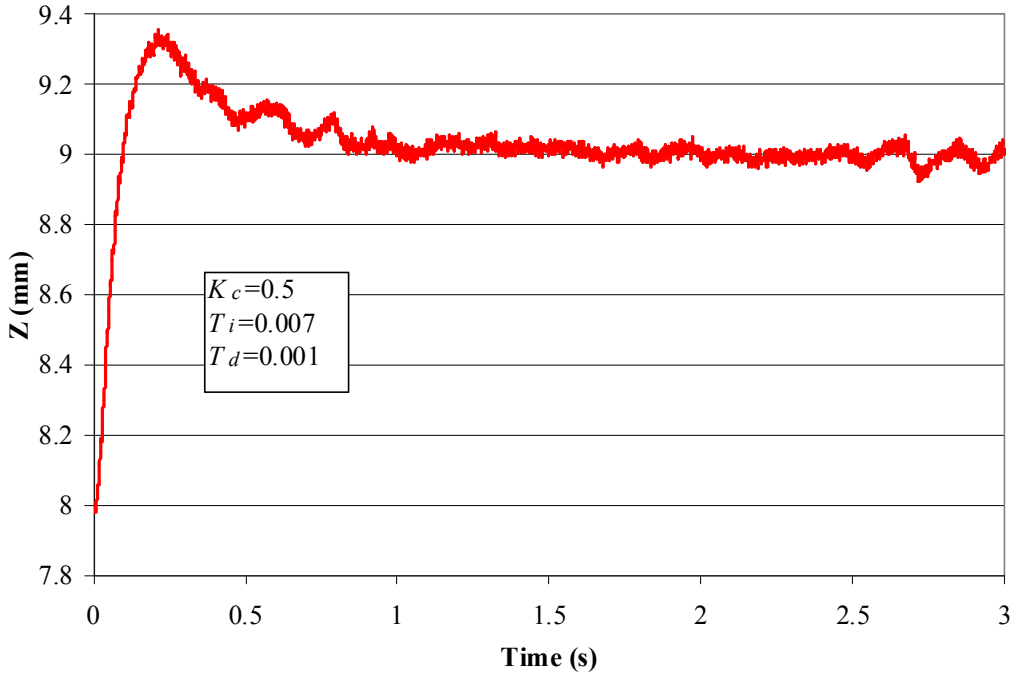

Figure 5-4: Position of the magnetically levitated object due to a unit step input.

sometimes located extremely close to those zeroes, as shown in Table 5-1. Given the probabilistic nature of the estimated parameters it was assumed that the model structure was over-parameterized, and that a reduced order model would suffice for the system. It was hypothesized that the open loop poles and zero would be significantly slower than the dynamics introduced by the controller, and would therefore dominate the response dynamics of the system. If this were the case, it would be difficult to extract the open loop system from the identified closed loop system, since the controller poles and zeros are expected to be modeled and should cancel out when the open loop plant is calculated.

Identified Poles	Identified Zeros
0.9998+/-0.014 0.9973+/-0.0143	0.999+/-0.014 0.9917

Table 5-1: Identified poles and zeros for model structure of (5-13) for *Kc*=0.15, *Ti*=0.007, *Td*=0.001.

Another problem encountered during the estimation of the signal was the measured controller output u. Figure 5-5 shows that the signal to noise ratio on u is extremely low, making it difficult to extract the system dynamics. Attempts to filter the noise were

unsuccessful as it was found that the identification process would yield a poor model estimate. It is assumed that this is due to the fact that u represents an output voltage from the controller that is converted by the amplifier into current at the electromagnets, and that u is a calculated quantity within the controller program, and is not a true measured quantity. This would suggest that the large swings in the value of u may be significant and should not be filtered, and that it is more appropriate to measure the output current instead. Unfortunately the equipment required to perform the measurements was not available at the time the identification process was performed.

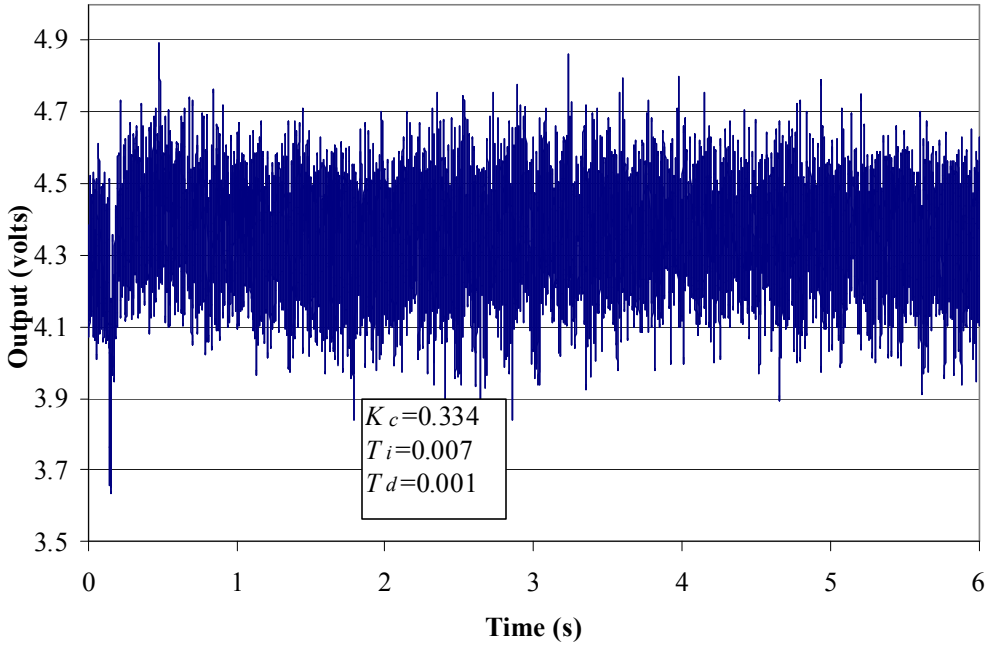

Figure 5-5: Controller output signal u for a step input from 8 to 9 mm. Step occurs at t=0.142 seconds.

In order to work around these problems and gain some intuition as to the location of the poles and zeroes of the open loop plant, several measurements of the system behaviour were made with varying gain K_c for constant values of T_i and T_d. The effect of tuning K_c does not impact the location of the open loop poles or zeroes of the combined controller-plant transfer function; varying K_c only affects the location of the closed loop poles. By varying K_c it was believed that this variation in the closed loop poles could be observed, and that by partially

reconstructing the root locus diagram it would be possible to identify the location of the open loop poles of the system. Because the location of the open loop zeroes does not vary with K_c the same value for the zero should be identified for each simulation, regardless of the controller gain K_c.

Experimentation suggested that a suitable reduced order model for identifying the system was of the form

$$\frac{y}{r} = \frac{b_0 q + b_1}{q^3 + a_0 q^2 + a_1 q + a_2} \tag{5-15}$$

Several experiments were performed by varying the gain K_c from the nominal value described by (5-12). The resulting poles, zeros and system gain are tabulated in Table 5-2. Gains above a value of 0.5 were not investigated as it was found that the output signal u would saturate and impact the response dynamics.

K_c	Poles	Zero	Gain
0.5	0.9959 0.9740 + 0.0301i 0.9740 - 0.0301i	0.9969	0.002099
0.334	0.9920 0.9743 + 0.0246i 0.9743 - 0.0246i	0.9954	0.002197
0.2	0.9899 + 0.0207i 0.9899 - 0.0207i 0.9896	0.9956	0.00125
0.15	0.9956 + 0.0167i 0.9956 - 0.0167i 0.9858	0.9956	0.0009638

Table 5-2: Summary of identified poles and zeros for initial estimation.

As expected, the system is able to return a relatively consistent value for the open loop zero. Examination of the poles also shows that as the gain decreases the complex poles start to move towards the edge of the unit circle. This is to be expected given that one of the poles is unstable. The third identified pole also shows a tendency to move towards the identified zero as the gain of the system is increased, typical of the identified response.

5.4 Identification of the Open Loop Model via the Root Locus

The system model is estimated by attempting to reconstruct the root locus graph. The current known information about the closed loop system is the location of the controller poles and zeros. The equivalent discrete controller is found by substituting the control gains of (5-12) into (5-11b) with T_s=2x10^{-3} seconds. The resulting discrete PID controller is

$$\frac{0.82143q^2 - 0.92857q + 0.25}{q^2 - q} \tag{5-16}$$

This controller will have open loop poles at $q=1$ and $q=0$. The open loop zeros are located at q=0.6882 and q=0.4422.

The assumed information about the system is that the plant has one zero and two poles, one of which is unstable. From the preliminary system analysis the system zero was estimated as being 0.996. Figure 5-6 shows a partial reconstruction of the root locus plot from the data in Table 5-2. As K_c is increased the poles move in an arcing fashion from q=1 towards q=0. Based on this information it appears two completely real poles have met outside the unit circle, diverged into the complex plane, and were subsequently drawn back into the unit circle by a system zero. It is also noted that the poles do not travel very far into the complex plane, as the magnitudes of the imaginary parts of the poles remains relatively small.

Attempts were made to place the plant poles and zeros in such a fashion as to replicate the behaviour of the identified system. The preliminary estimates for poles are shown in Table 5-3. The gain of the system was estimated through simulation of the model as being -0.03. The root locus diagram for the closed loop system is shown in Figure 5-7 and Figure 5-8. In particular, the behaviour of the system around q=1 as depicted in Figure 5-8 is similar to the behaviour of the identified system. Also note that there is always a pole along the real axis for q>0.9, which was also predicted by the estimation of the root locus system. The root locus diagram also suggests that the assumption that the controller zeros are difficult to extract at lower gains is correct. The motion of the closed loop poles at low gains appears to be largely dictated by the existing poles and zeros of the plant, with the controller pole at q=1

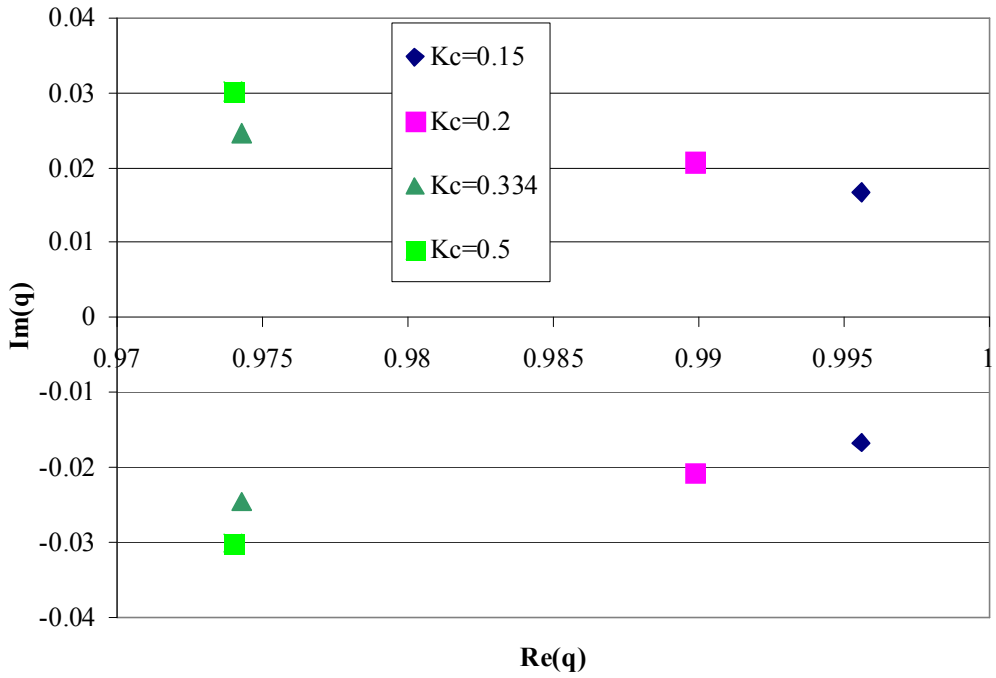

Figure 5-6: Partial reconstruction of the root locus plot from estimated data. Plot shows the location of the complex poles as K_c is varied.

providing means by which the closed loop poles are pulled back into the unit circle. For higher gains it would appear that the effects of the other zeros would start to become more significant, but because of output saturation it is difficult to make these observations.

Unstable Pole	Stable Pole	Zero
$q = 1.01$	$q = 0.9$	$q = 0.996$

Table 5-3: Preliminary estimate of plant transfer function poles and zeroes.

The output of the closed loop model is compared to the real system as shown in Figure 5-9. There is fairly good agreement between the model and the real system. The response of the model is slightly faster, however the overshoot and decay properties are similar to the real system. Another response to the system with a different value of K_c is shown in Figure 5-10.

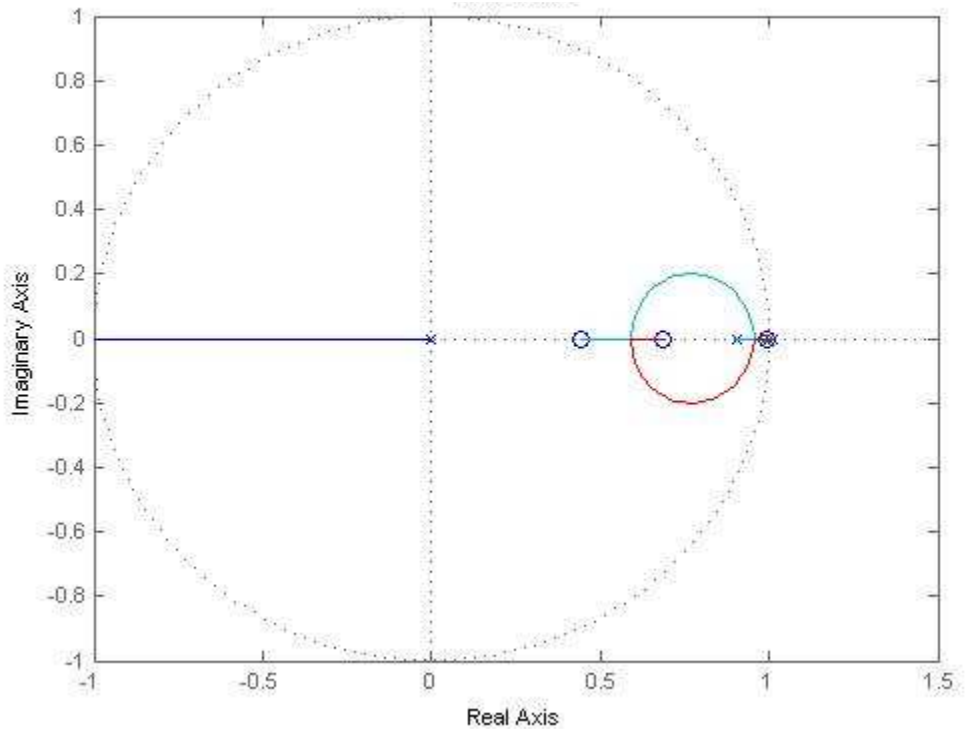

Figure 5-7: Root locus for preliminary model.

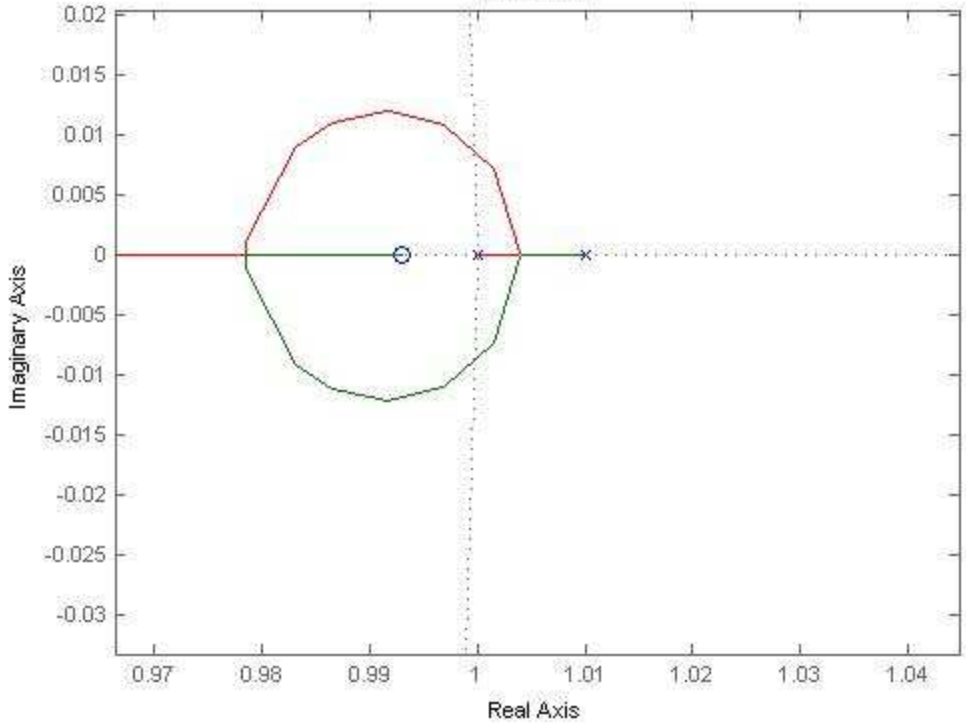

Figure 5-8: Root locus for the preliminary model around q=1.

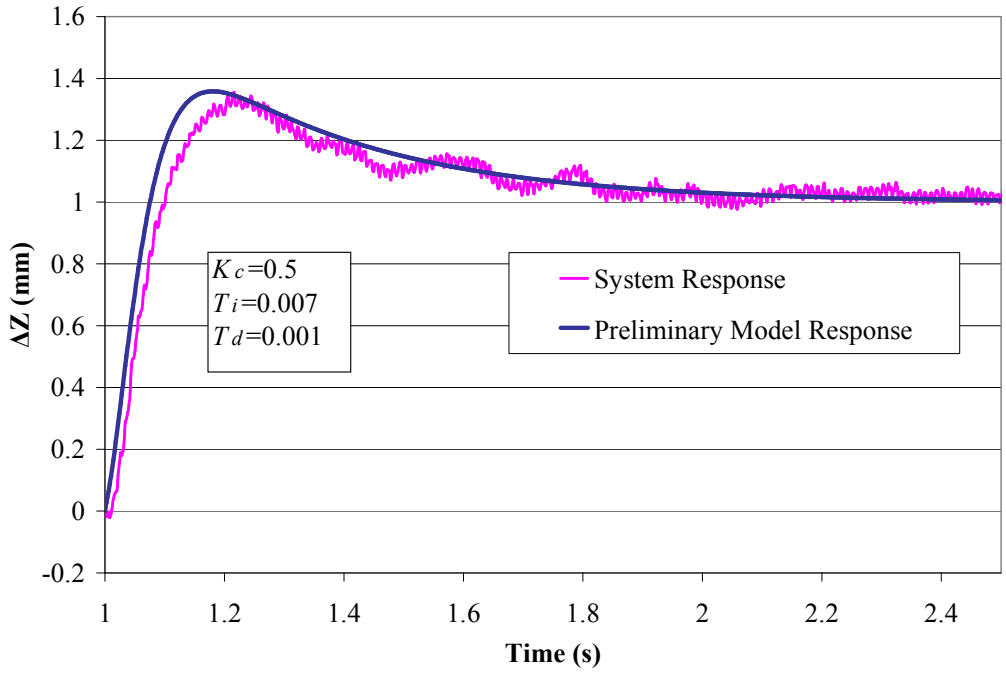

Figure 5-9: Comparison of initial system model to the real system response.

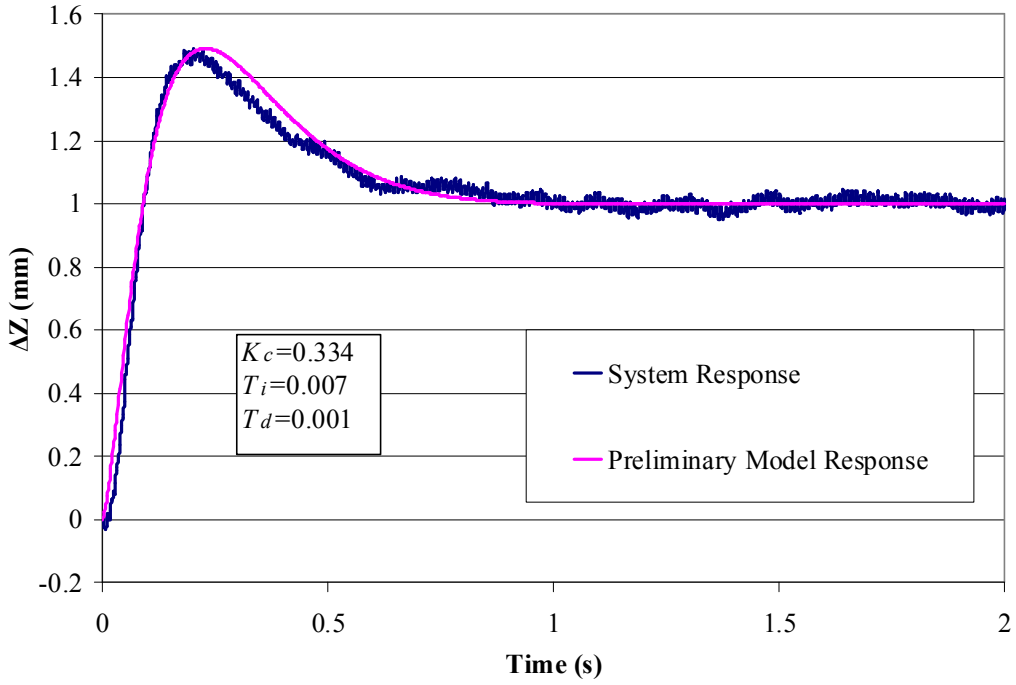

Figure 5-10: Comparison of initial system model to the real system response with a change in the proportional gain.

5.5 Refinement of the Model

In order to improve the accuracy of the model, some slight adjustment of the identified poles and zeros is needed. With the aid of the existing model it was possible to design several new PID controllers for the system. A combination of system identification of the reduced order transfer function and parameter tweaking were used to refine the model so that it provided a reasonable estimation of the plant dynamics. Table 5-4 shows the final parameters of the plant model.

Unstable Pole	Stable Pole	Zero	Gain
$q = 1.01$	$q = 0.905$	$q = 0.9935$	-0.03

Table 5-4: Final Identified Parameters.

5.6 Validation of the Model: PRBS

In order to verify the dynamic response of the final plant, an 8th order pseudo-random binary signal (PRBS) with amplitude of 1 mm was input into the system. In order to minimize the effects of any lateral motion that may occur due to the oscillations, the levitating object was levitated inside of a plastic tube. The inner diameter of this tube was 12.3 mm, which is slightly larger than the 11.8 mm diameter of the body of the levitated object. A slight change in the dynamics of the system was observed, as shown in Figure 5-11. This is likely due the object levitating at a slight angle, resulting in a non-linear dead zone effect resulting from the contact friction between the tube and body. Due to the rapid motion of the object during the PRBS test it was unlikely that this would affect the resulting dynamics in any way.

These results are shown in Figure 5-12 through Figure 5-14 for various controllers. The figures show that there is a fairly good match between the simulated PRBS results and the actual system response. It is therefore believed that the system model

$$\frac{y}{u} = \frac{Z}{I} = \frac{-0.03(q - 0.9935)}{(q - 1.01)(q - 0.905)} \quad T_s = 2\text{x}10^{-3}\ \text{s} \tag{5-17}$$

is a reasonable approximation of the vertical motion of the magnetically levitated system.

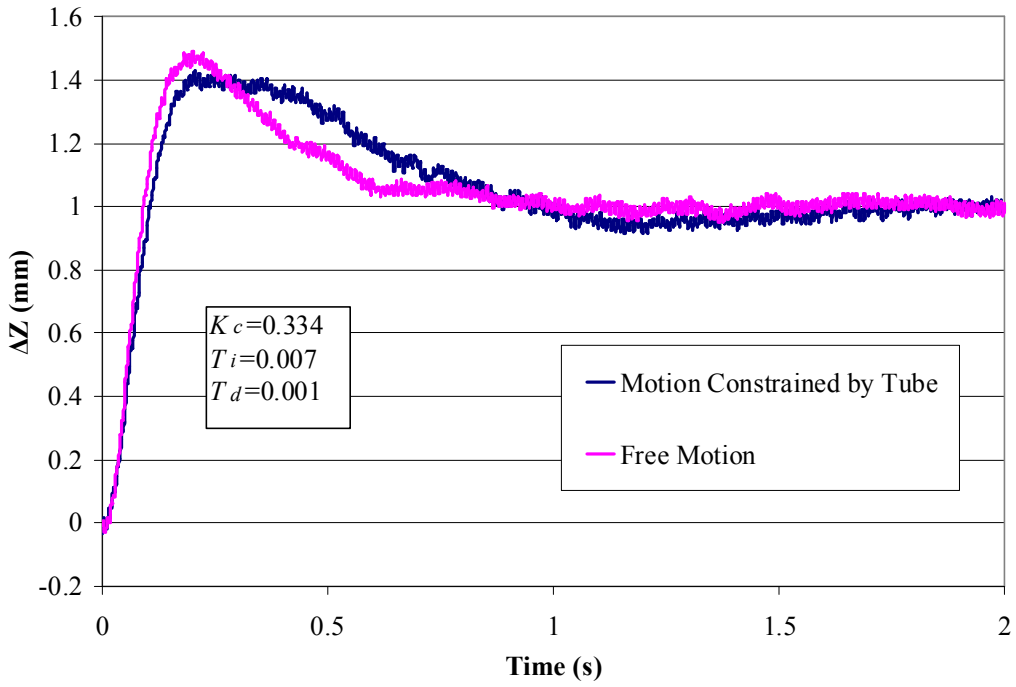

Figure 5-11: Constrained versus free vertical motion.

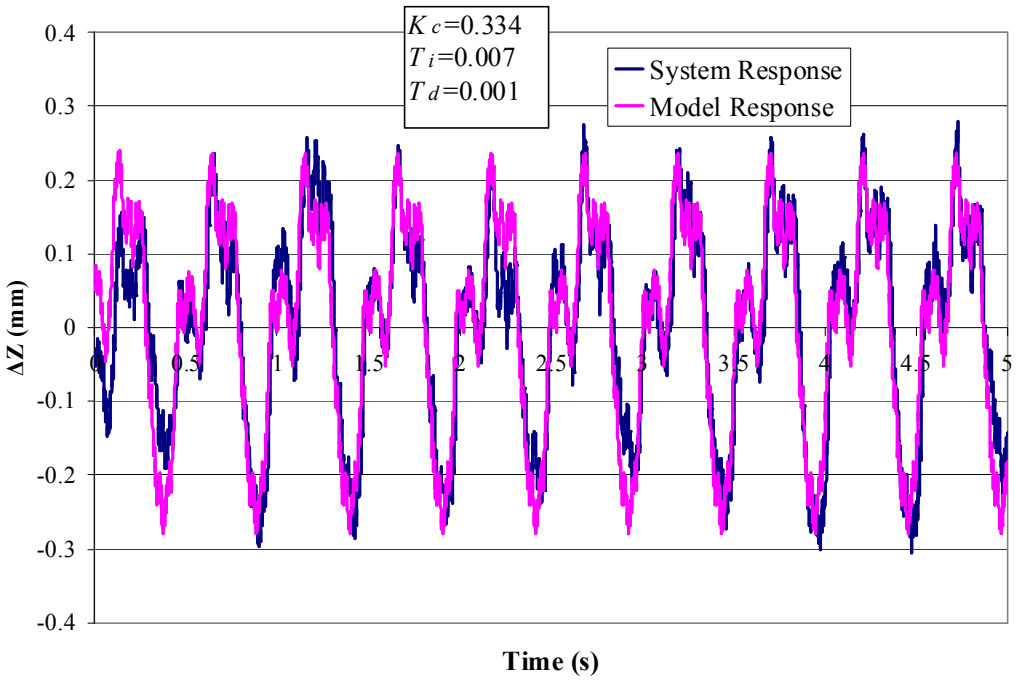

Figure 5-12: System response due to a PRBS input.

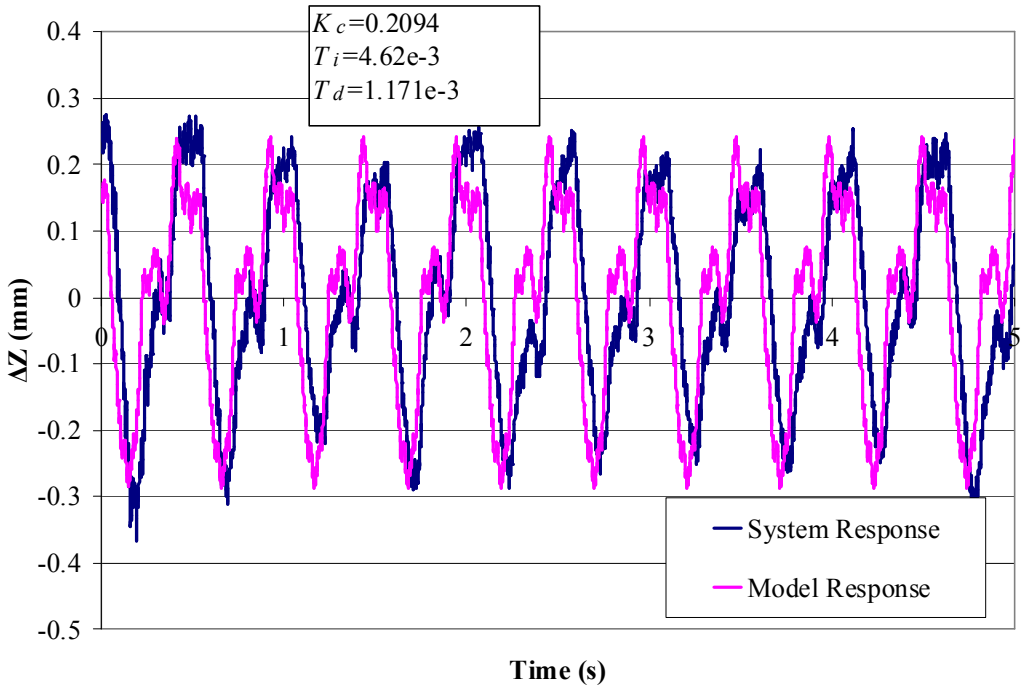

Figure 5-13: System response due to a PRBS input with a second PID controller.

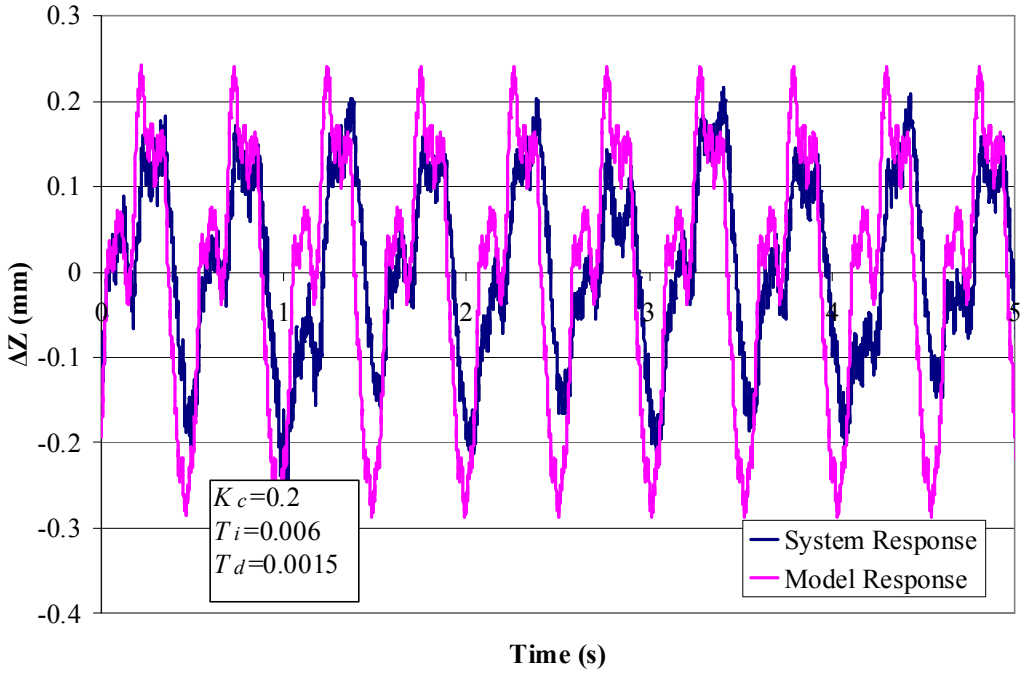

Figure 5-14: System response to a PRBS input with a third PID controller.

5.7 Model Analysis

Figure 5-15 shows a step response for K_c=0.334, T_i=0.007, T_d=0.001. It can be seen that both the preliminary model and the final model provide reasonable estimates of the system behaviour. Figure 5-16 shows a step response for K_c=0.2, T_i=0.006, T_d=0.0015. The preliminary model provides a good estimate of the system behaviour, although the response time of the system is slower than expected. The final model does a much better job of predicting the behaviour of the system.

Figure 5-17 shows the step response for K_c=0.7, T_i=5.934x10^{-3}, T_d=4.6x10^{-4}. In this case the final model is a more reasonable approximation of the system as it does a better job of predicting when the peak time occurs and how the system decays to the final steady state value. It does not do a very good job of predicting the amount of overshoot, and overestimates the amount of damping. Figure 5-18 shows the response of the system with the same controller to a -2 mm input. In terms of the system this represents motion of the levitating object towards the pole piece (against gravity). While the model predicts overshoot, the actual system shows that there is actually an undershoot response. This would suggest that there may be some non-linear damping effects that may not be accounted for in the model. It is possible that two different models are needed to describe the system: one for motion towards the pole piece and one to describe motion away from the pole piece. For example, the shape of the microrobot indicates that the aerodynamic drag should not be the same for motion in the positive and negative z direction, although it is not clear how significantly this impacts the motion. In general it is observed that the unit step change in both the positive and negative direction gives a similar response, an example of which is shown in Figure 5-19.

Figure 5-20 shows the step response for K_c=0.2094, T_i=4.62x10^{-3}, T_d=1.171x10^{-3}. The final model provides a better estimate of the response than the preliminary model, in that it does a better job of predicting the peak time. Neither model captures the overshoot or the damped frequency of the system. By adjusting the plant gain from -0.3 to -0.2 and shifting the plant zero from 0.9935 to 0.9897, the response begins to more closely resemble the actual system. As before, this suggests that some aspect of the system has not been modeled

accurately. This indicates that there may be some non-linear system effects that have not been accounted for in the model. During controller design it may be beneficial to investigate slight variations of the nominal parameters in order to get a more complete picture of what type of system response may be expected when the controller is implemented.

Figure 5-21 and Figure 5-22 show the response of the system to a ramp input with a slope of 5 mm/s for two different controllers. In both cases the start-up behaviour of the model matches the system quite well. In both cases there is a slight discrepancy between both the final steady state error and the slope of the response. Over the operating range of the system this difference is relatively small and that overall the system model is able to predict the response of the system with reasonable accuracy.

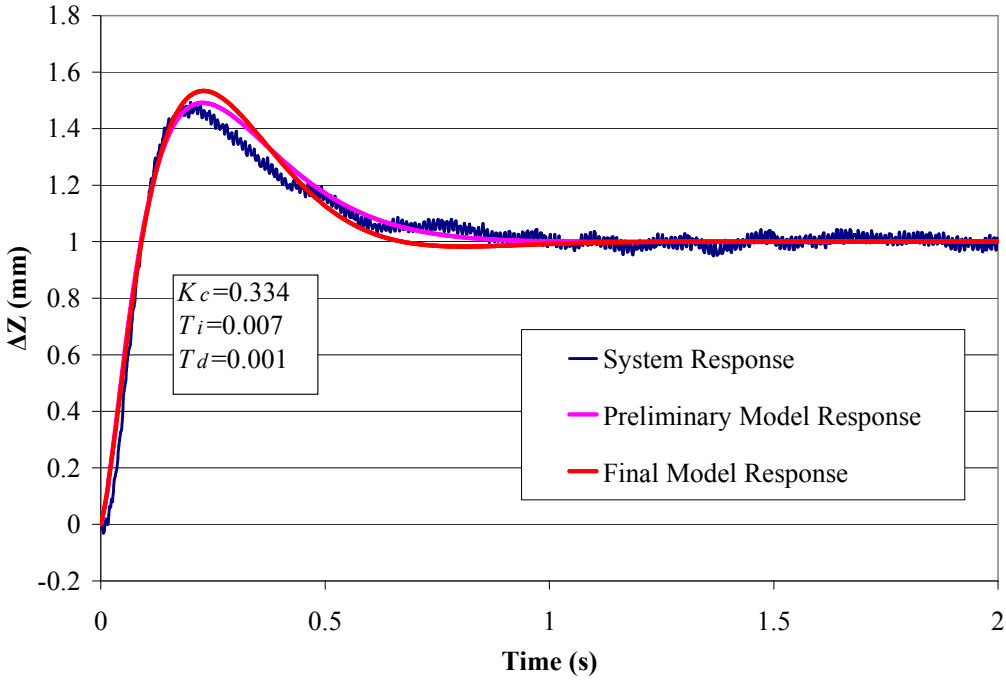

Figure 5-15: Comparison of the system response to the preliminary and final model responses.

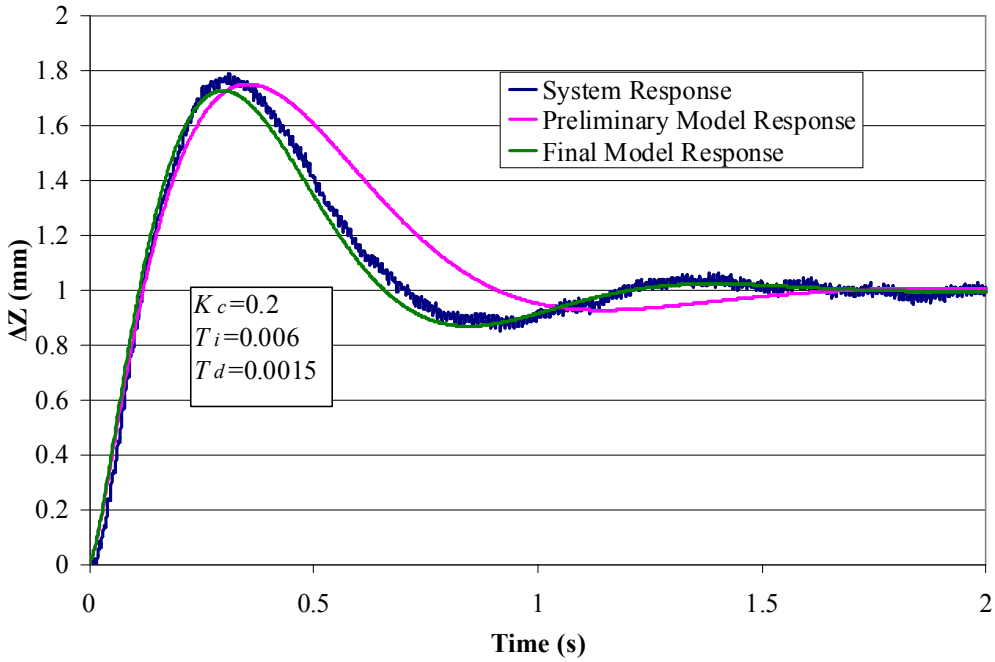

Figure 5-16: Comparison of the system response to the preliminary and final model responses for a second PID controller.

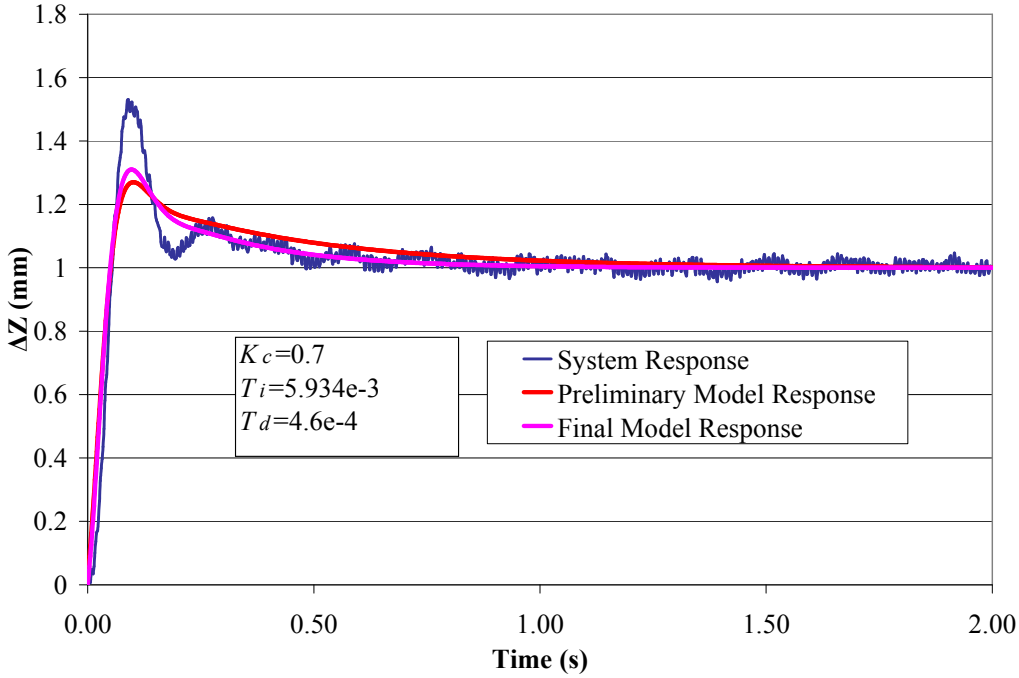

Figure 5-17: Comparison of the system response to the preliminary and final model response for a third PID controller.

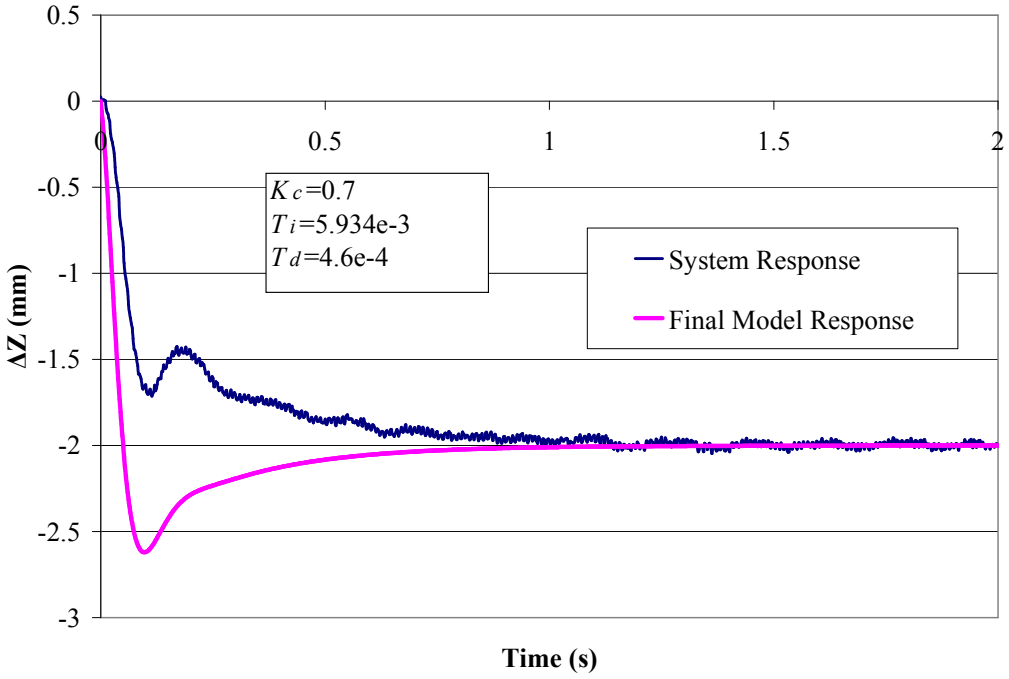

Figure 5-18: Comparison of responses due to a -2mm step.

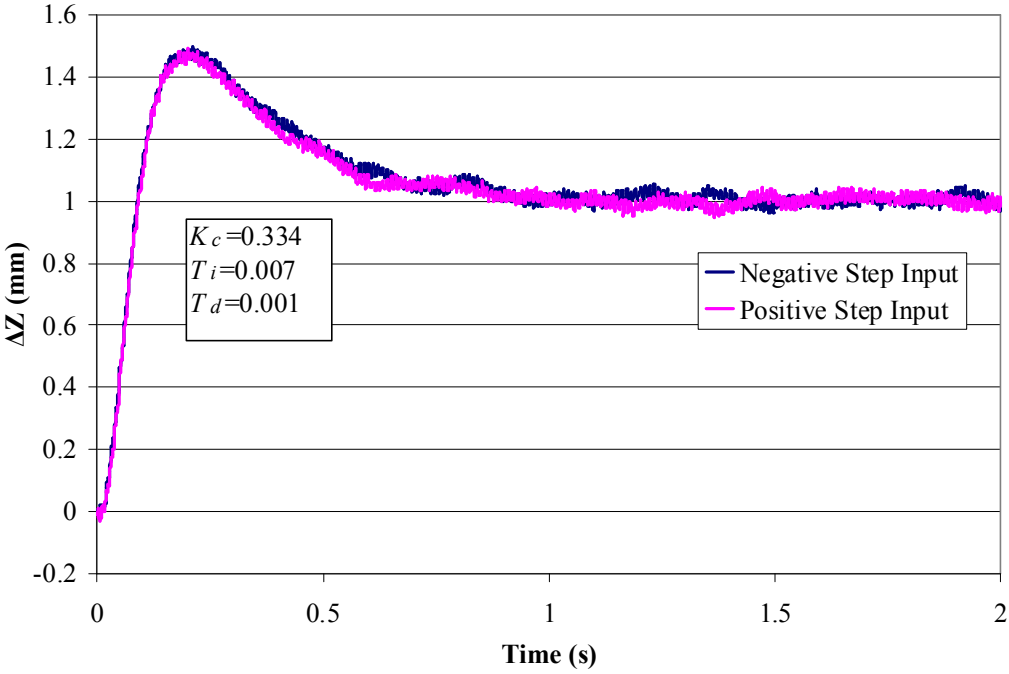

Figure 5-19: Comparison of negative step input to positive step input. The absolute value of the negative input is shown.

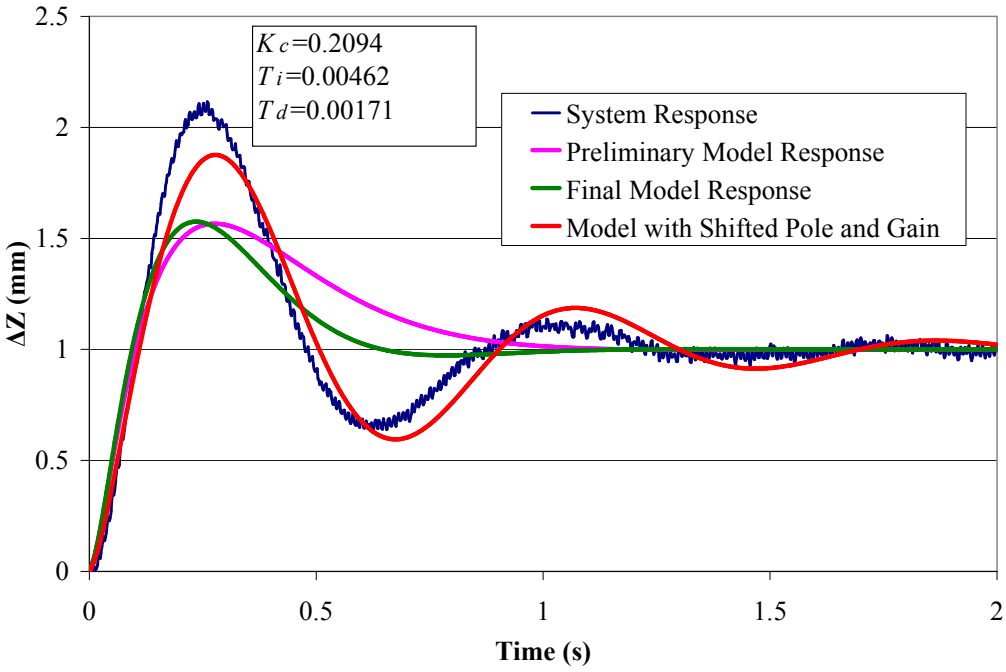

Figure 5-20: Comparison of system response to the model responses, including a model with slight parameter adjustments.

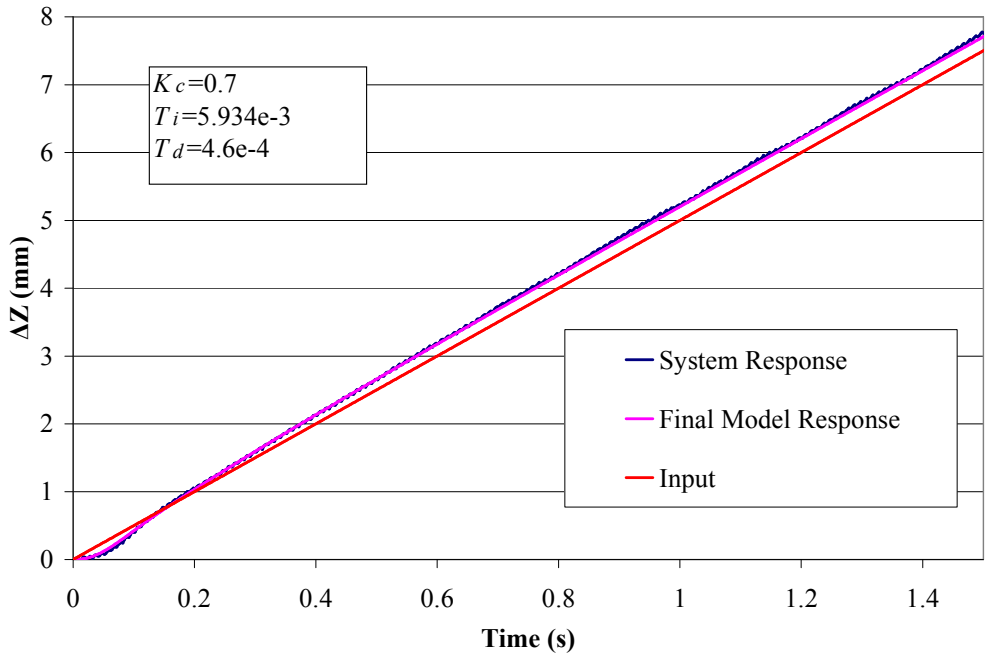

Figure 5-21: Comparison of the system response to the model response for a ramp input.

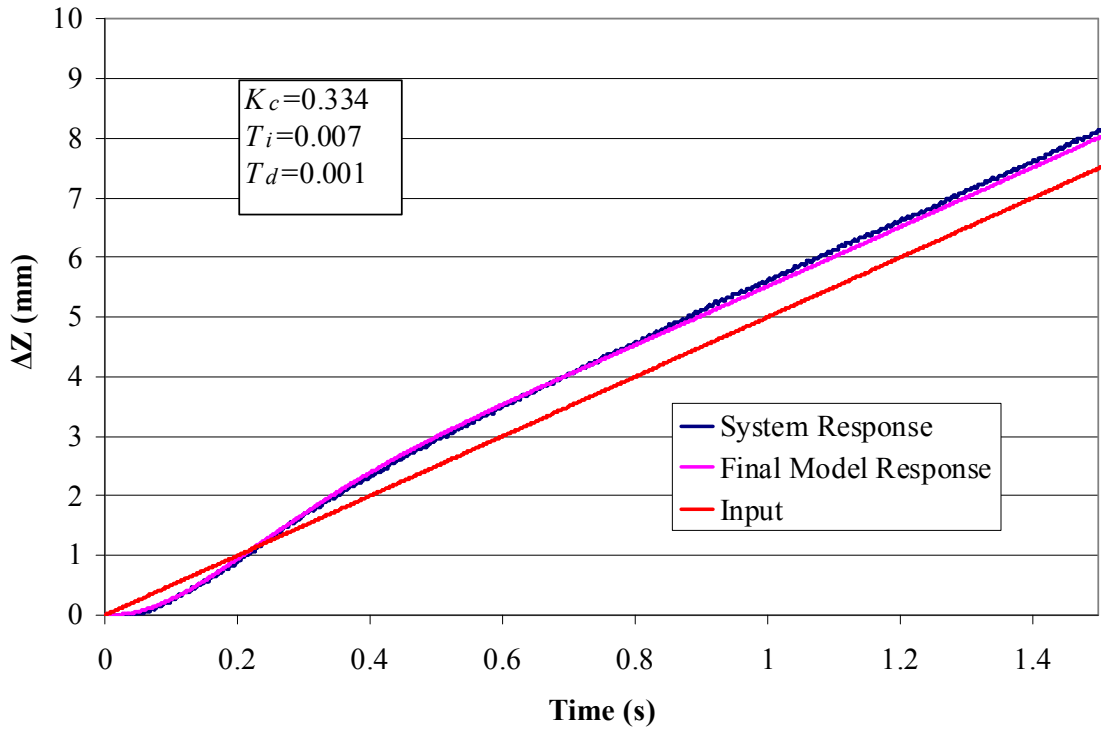

Figure 5-22: Comparison of the system response to the model response for a ramp input with a second PID controller.

Chapter 6
Horizontal Position Model Estimation

6.1 Experimental Methods

All of the horizontal positioning experiments conducted in Chapters 6 and 7 were performed with the microrobot operating a minimum of 2 mm above an aluminum block. This block was used as it was observed that the microrobot would "sway" back and forth in the workspace in the absence of the block. An example of this behavior is shown in Figure 6-1, with a comparable motion with the aluminum block shown in Figure 6-2. It is believed that eddy currents produced in the aluminum block produce a damping effect in order to achieve the motion shown in Figure 6-2 [52]. It has been observed that the block does not significantly impact the dynamics of the vertical positioning system, as shown in Figure 6-3. One possible explanation as to why the microrobot sways in the field is that the microrobot is experiencing small perturbations about the equilibrium point. This is due to the single magnetic dipole moment of the permanent magnet. The disk pole piece used on the drive unit produces an equilibrium area as opposed to an equilibrium point [41]. A microrobot with a single dipole moment will oscillate along the cross-sectional length of this area, since the natural damping of the system is not sufficient to completely stop the microrobot when the magnetic force is removed. Even for a "sharp" equilibrium point it should be noted that the continuity of the field dictates that there will effectively be a small equilibrium area and that some oscillations may still be observed. It is noted that the system in [30] used several permanent magnets attached to axial arms of the microrobot body to take advantage of a large equilibrium area in order to minimize the lateral oscillations. It was determined that the existing setup would be sufficient for providing a preliminary characterization of the horizontal motion of the system.

In all cases the control gains used on the vertical position controller were

$$K_c = 0.334 \qquad T_i = 0.007 \qquad T_d = 0.001 \tag{6-1}$$

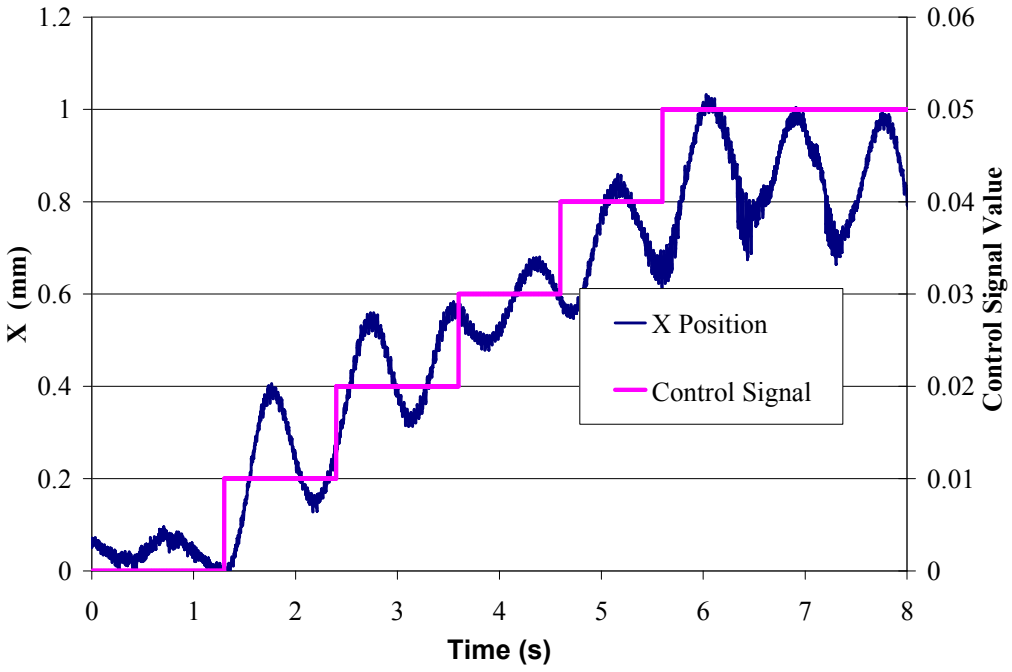

Figure 6-1: Open loop horizontal motion with no aluminum block.

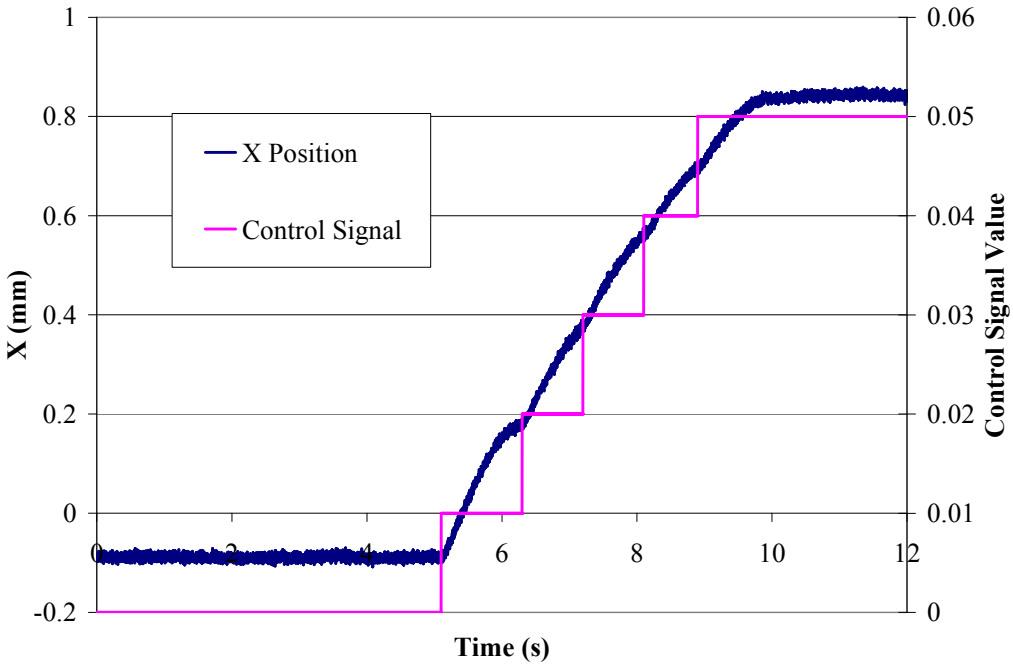

Figure 6-2: Open loop horizontal motion with the aluminum block.

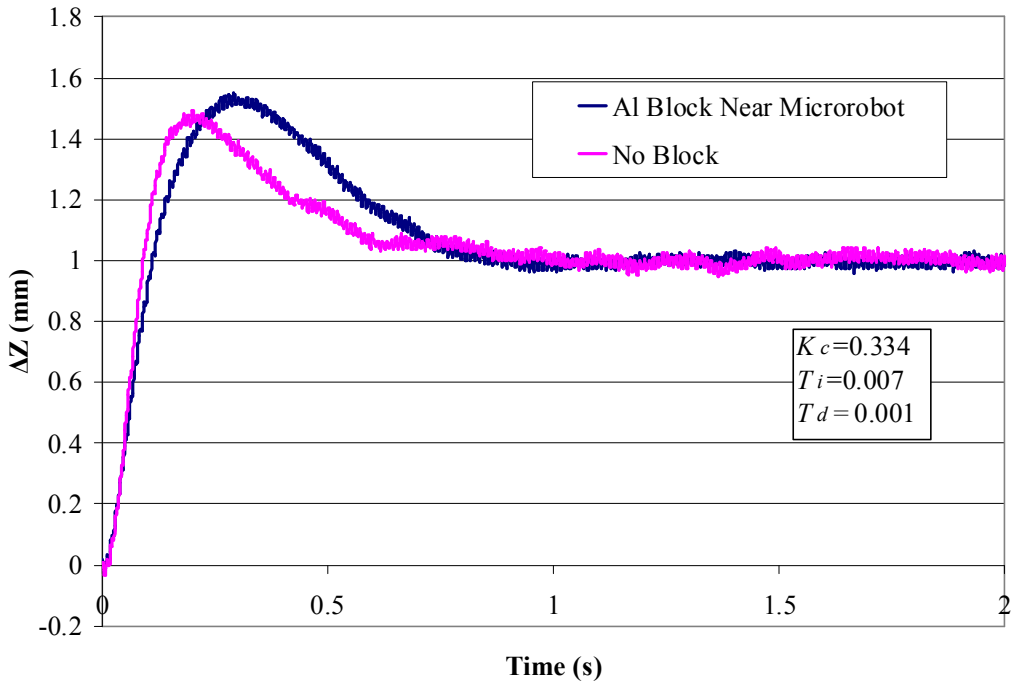

Figure 6-3: Vertical response of the system in the proximity of the aluminum block, compared to the response with no aluminum block.

These controller gains were chosen since they were found to provide reasonable control of the vertical system dynamics and keep the microrobot in a stable levitating position for the horizontal positioning experiments.

6.2 Principle of Operation

As discussed in Chapter 2, horizontal positioning of the microrobot is accomplished by changing the input power to each electromagnet while keeping the total input power to the system constant. This will shift the location of the vertical equilibrium point to a new location in the horizontal plane. The resulting force gradient through the original equilibrium point will move the microrobot towards the equilibrium point.

Figure 6-4 shows the layout of the electromagnets on the pole piece relative to the global coordinate frame. Table 6-1 shows a general overview of how to vary the electromagnet currents in order to produce motion in a given direction. Electromagnet 7 is not used since it was found that horizontal motion was easier to achieve without it. It should be noted that

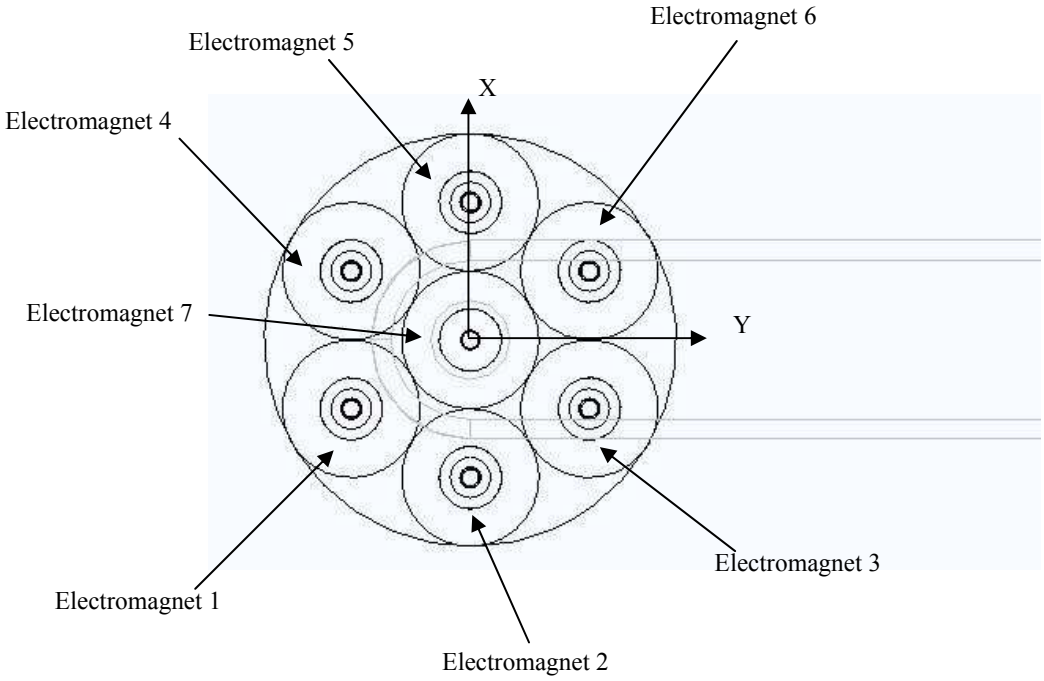

Figure 6-4: Layout of the pole piece electromagnets.

Direction of Motion	Increase Currents in Electromagnets	Decrease Currents in Electromagnets
Increasing X	4,5,6	1,2,3
Decreasing X	1,2,3	4,5,6
Increasing Y	3,6	1,4
Decreasing Y	1,4	3,6

Table 6-1: General overview of current variation required to produce motion in a given direction.

more electromagnets are used to produce motion in the *x* direction when compared to the *y* direction. The implications of this will be discussed in more detail below.

In the absence of any horizontal control, the vertical control signal *u* is sent directly to the electromagnets in order to achieve the desired vertical position. The addition of horizontal control requires further manipulation of *u* after it has been calculated by the vertical position controller. The PID controllers discussed in Chapter 5 calculate the required input for one

electromagnet. The net power u_{sum} is calculated as

$$u_{sum} = 6u \tag{6-2}$$

The algorithms used to produce horizontal motion must ensure that the change in current is symmetric about a given axis without changing the value of u_{sum}. The current ratio algorithms governing the current division are

$$u_1 = \frac{u_{sum}(1-x_{ctrl})(1-y_{ctrl})}{6} \tag{6-3a}$$

$$u_2 = \frac{(u_{sum}-u_1-u_3-u_4-u_6)(1-nx_{ctrl})}{2} \tag{6-3b}$$

$$u_3 = \frac{u_{sum}(1-x_{ctrl})(1+y_{ctrl})}{6} \tag{6-3c}$$

$$u_4 = \frac{u_{sum}(1+x_{ctrl})(1-y_{ctrl})}{6} \tag{6-3d}$$

$$u_5 = \frac{(u_{sum}-u_1-u_3-u_4-u_6)(1+nx_{ctrl})}{2} \tag{6-3e}$$

$$u_6 = \frac{u_{sum}(1+x_{ctrl})(1+y_{ctrl})}{6} \tag{6-3f}$$

where x_{ctrl} and y_{ctrl} are the horizontal input control signals and n is an arbitrary constant. In the simplest case, n=1, and the currents in electromagnets 2 and 5 will have the same values as the currents in electromagnets 1,3 and 4,6, respectively when only x_{ctrl} is actuated. The value of n can be increased so that the currents in electromagnets 2 and 5 will change at a greater rate as x_{ctrl} is varied. Table 6-2 shows a comparison of the steady state open loop positions for the case when n=1.25 and n=1.5 at z=10 mm. For higher values of n it is possible to move the robot further for an equivalent open loop control signal. The tradeoff to this is that the output current to the electromagnet will saturate faster at higher values of n, producing more heat as the power is dissipated in the electromagnets. In the chart below, vertical control of the microrobot is lost just past x_{ctrl}=0.39 for n=1.5. In the case when n=1.25 it is possible to have a maximum control signal of 0.4 although the final position achieved by the microrobot is about 1.34 mm less than for the case when n=1.5.

The operating range is also dependent on the vertical position of the microrobot. Table 6-3 shows the relative motion of the microrobot at z=10 mm and z=11.5 mm for n=1.25. Initially the microrobot moves slightly further at z=11.5 mm, but as the signal continues to increase the microrobot is able to move further at z=10 mm, eventually traveling 0.751 mm further at x_{ctrl}=0.4. A complex control algorithm could conceivably control x_{ctrl}, y_{ctrl}, and n in order to produce a constant horizontal workspace at any z position. For this chapter it was decided to run the horizontal experiments at n=1.25 and z=10 mm as a balance to providing a reasonable operating range while minimizing the input power to electromagnets *2* and *5*.

Control Signal x_{ctrl}	**Mean x Position, n=1.25 (mm)**	**Mean x Position, n=1. 5 (mm)**
0.05	0.844	1.153
0.1	1.346	1.701
0.15	1.978	2.609
0.2	2.862	3.691
0.25	3.961	5.094
0.3	5.514	6.73
0.35	7.259	8.781
0.39	-	10.67
0.4	9.329	-

Table 6-2: Comparison of steady state x positions at z=10 mm achieved for different values of n.

Control Signal x_{ctrl}	**Mean x Position, z=10 mm (mm)**	**Mean x Position, z=11.5 mm (mm)**
0.05	0.844	0.893
0.1	1.346	1.4362
0.15	1.978	2.043
0.2	2.862	2.875
0.25	3.961	3.929
0.3	5.514	5.181
0.35	7.259	6.713
0.4	9.329	8.578

Table 6-3: Comparison of steady state x positions for achieved with n=1.25 at different heights z.

6.3 Open Loop Range

Table 6-4 and Table 6-5 show the open loop position mapping along the x axis at z=10 mm. The tests were performed in two separate runs in order to minimize the size of the recorded data file. The positive x axis measurements were performed in one run and the negative x axis measurements were performed in the second run. Figure 6-5 shows a plot of the mean position versus x_{ctrl}. Table 6-6, Table 6-7 and Figure 6-6 show the corresponding results for the y axis. The tables and the plots indicate that there is a hysteresis behavior present in the open loop control of the system. The cause of this hysteresis is unknown. From a positioning standpoint the hysteresis is undesirable, and so the closed loop control should be capable of eliminating this hysteresis behavior as the microrobot moves. Both plots also show that the response of the system is non-linear, as a constant change in the control signal (increasing or decreasing) does not yield a constant change of position.

In general, the motion is relatively symmetric in the positive and negative axis. For a given control value, it is observed that the relative position of the microrobot from the origin is about the same regardless of whether the input value is positive or negative. The hysteresis of the system does not seem to affect this. For example, inspection of the third columns in Table 6-4 and Table 6-5 shows that the relative distance from the origin is roughly equivalent as the control signal is brought back to a zero value.

The open loop positioning along the x and y directions is not equivalent. This is to be expected given that there are more electromagnets controlling the motion along the x axis than along the y axis. It is possible that tuning of the n parameter could produce equivalent open loop mapping in both the x and y directions, although this may not be desirable given that the open loop y range is less than half of the open loop x range. It should be noted that the open loop mapping in the y direction was arbitrarily stopped at y_{ctrl}=0.3 in order to ensure that the microrobot did not move out of the path of the laser beam from the vertical position sensor.

Control Signal x_{ctrl}	Position due to Increasing Control Signal (mm)	Position due to Decreasing Control Signal (mm)
0	-0.088	-0.776
0.05	0.844	-0.400
0.1	1.346	0.01
0.15	1.978	0.71
0.2	2.862	1.619
0.25	3.961	2.804
0.3	5.514	4.250
0.35	7.259	6.574
0.4	9.329	9.329

Table 6-4: Mean positions along the positive *x* axis.

Control Signal x_{ctrl}	Position due to Decreasing Control Signal (mm)	Position due to Increasing Control Signal (mm)
0	-0.008	0.872
-0.05	-0.85	0.525
-0.1	-1.421	0.06
-0.15	-2.153	-0.736
-0.2	-3.214	-1.731
-0.25	-4.42	-2.949
-0.3	-5.74	-4.527
-0.35	-7.31	-6.585
-0.4	-9.15	-9.15

Table 6-5: Mean positions along the negative *x* axis.

Control Signal y_{ctrl}	Position due to Increasing Control Signal (mm)	Position due to Decreasing Control Signal (mm)
0	0.005	-0.874
0.05	0.641	-0.650
0.1	0.951	-0.350
0.15	1.311	0.105
0.2	1.835	0.833
0.25	2.581	1.968
0.3	3.571	3.571

Table 6-6: Mean positions along the positive *y* axis.

Control Signal y_{ctrl}	Position due to Decreasing Control Signal (mm)	Position due to Increasing Control Signal (mm)
0	-0.004	0.872
-0.05	-0.656	0.605
-0.1	-1.106	0.247
-0.15	-1.595	-0.314
-0.2	-2.191	-1.241
-0.25	-2.984	-2.366
-0.3	-3.791	-3.791

Table 6-7: Mean positions along the negative *y* axis.

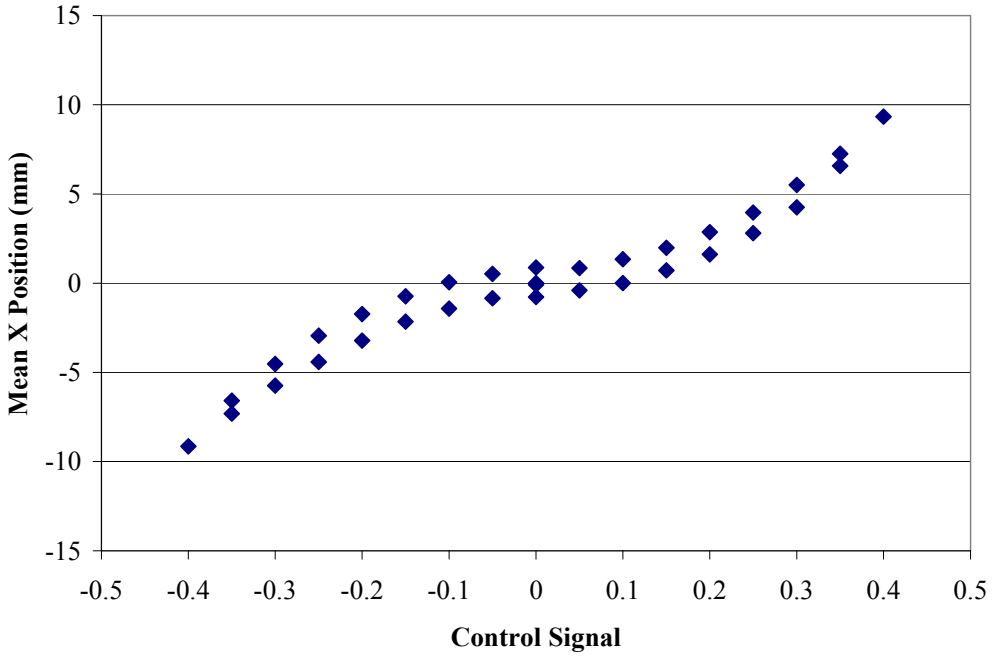

Figure 6-5: Open loop position mapping of the *x* axis.

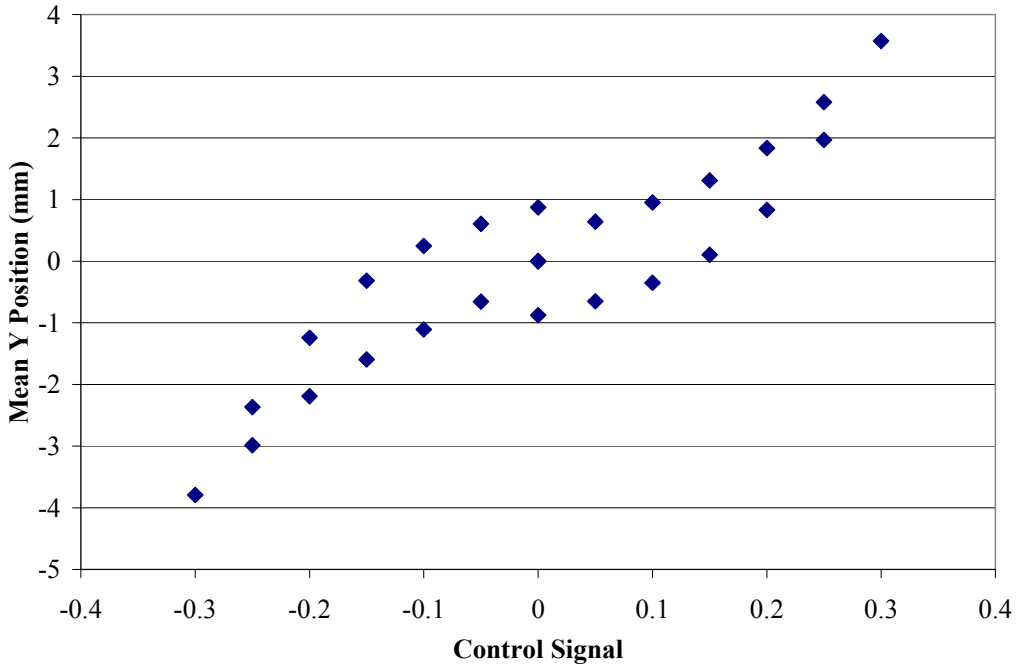

Figure 6-6: Open loop position mapping of the *y* axis.

6.4 System Identification

With the open loop mapping complete, it is possible to determine the required input signal that will produce a 1 mm step input change from the origin. These step changes can be used to identify a transfer function for the open loop horizontal positioning. The transfer function should provide a reasonable description of the open loop dynamics, but some error is expected given the non-linear and hysteresis characteristics of the system.

In order to estimate the required input signal, a fourth order polynomial fit is applied to the portion of the open loop position graphs that describes motion along the positive axis for an increasing control signal. The polynomial fit equations are

$$x = -525.95(x_{ctrl})^4 + 521.17(x_{ctrl})^3 - 120.55(x_{ctrl})^2 + 21.961(x_{ctrl}) - 0.0707 \qquad (6\text{-}4)$$

$$y = -708.12(y_{ctrl})^4 + 589.76(y_{ctrl})^3 - 132.48(y_{ctrl})^2 + 17.654(y_{ctrl}) + 0.0081 \qquad (6\text{-}5)$$

Using an iterative search it was determined that the required inputs for a 1 mm step were 0.0665 for x_{ctrl} and 0.1053 for y_{ctrl}. The actual inputs to the system varied slightly from these

parameters due to the uncertainties of the polynomial estimation and the natural error of the system.

The model estimation was performed using the same modified least squares approach used in Chapter 5. The primary reason for using this algorithm was that it was able to provide acceptable results for the vertical identification procedure, and it was believed that it would also be suitable for identifying the horizontal system parameters.

The identification process determined that a second order system with no zeros provided a good description of the system dynamics. The identified equations governing the x and y motion are

$$\frac{x}{x_{ctrl}} = \frac{8.764 \times 10^{-4}}{z^2 - 1.9878z + 0.98782} \quad T_s = 2\text{x}10^{-3}\ \text{s} \tag{6-6}$$

$$\frac{y}{y_{ctrl}} = \frac{6.214 \times 10^{-4}}{z^2 - 1.9877z + 0.98779} \quad T_s = 2\text{x}10^{-3}\ \text{s} \tag{6-7}$$

The model response is compared to the actual system response in Figure 6-7 through Figure 6-10. In each case a constant Δx_{ctrl} and Δy_{ctrl} were sent to the system in an attempt to produce a constant change in position of 1 mm over the entire open loop range of the microrobot. Due to the non-linear nature of the position mapping this was not achieved in every case. However, the measured position dynamics could be compared to the linearized identified model by adjusting the model input until the desired steady state output was achieved.

Figure 6-7 through Figure 6-10 show that the system models describing the x and y motions are a reasonable approximation of the true system response. The initial dynamic response of the system is generally similar, and although the model values do not match the system values in all cases the general tends of the graphs, such as the slowing down of the system as it approaches steady state, generally occur at about the same time.

It is worth noting the estimated characteristic equation of the transfer functions for the x and y motions are extremely similar. This suggests that the dynamic characteristics of the x and y motion are the same in spite of the fact that six electromagnets are used to produce x

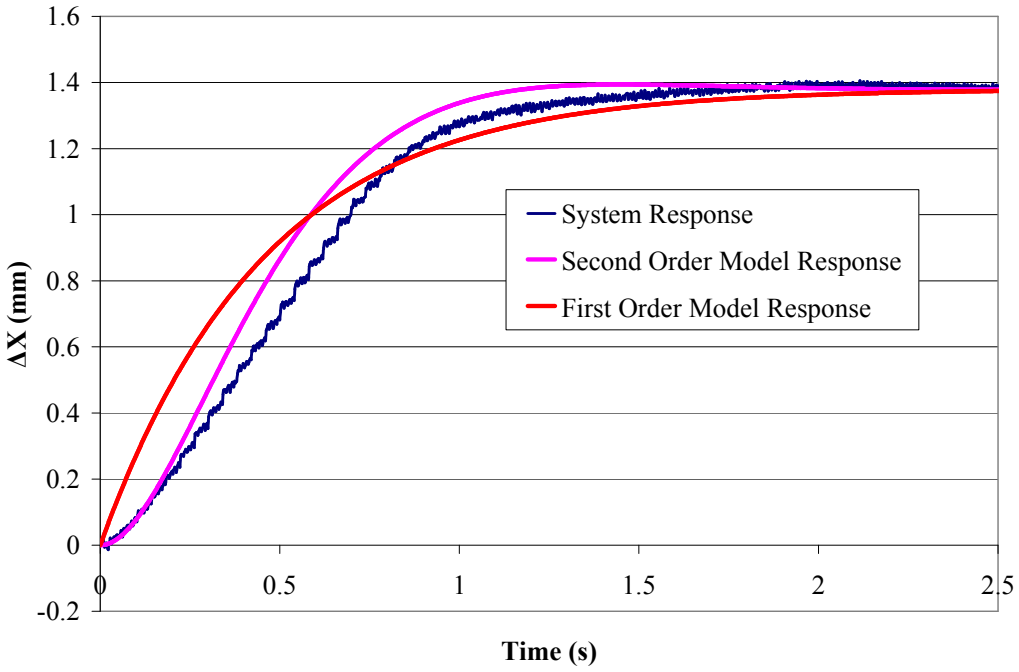

Figure 6-7: Open loop *x* response to a steady state value of 1.4 mm.

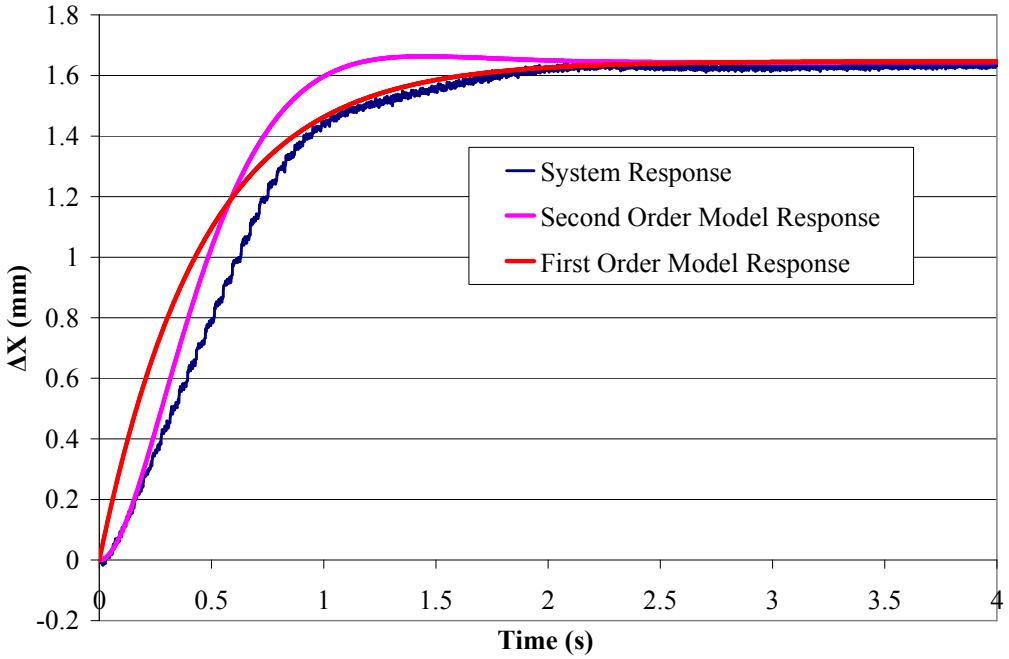

Figure 6-8: Open loop *x* response to a steady state value of 1.65 mm.

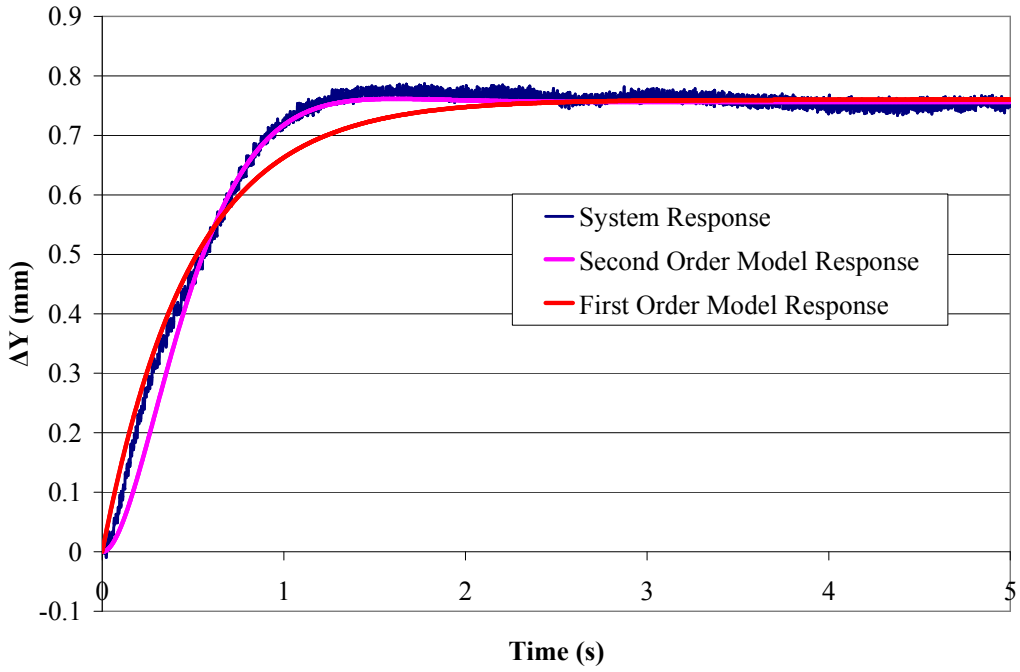

Figure 6-9: Open loop *y* response to a steady state value of 0.75 mm.

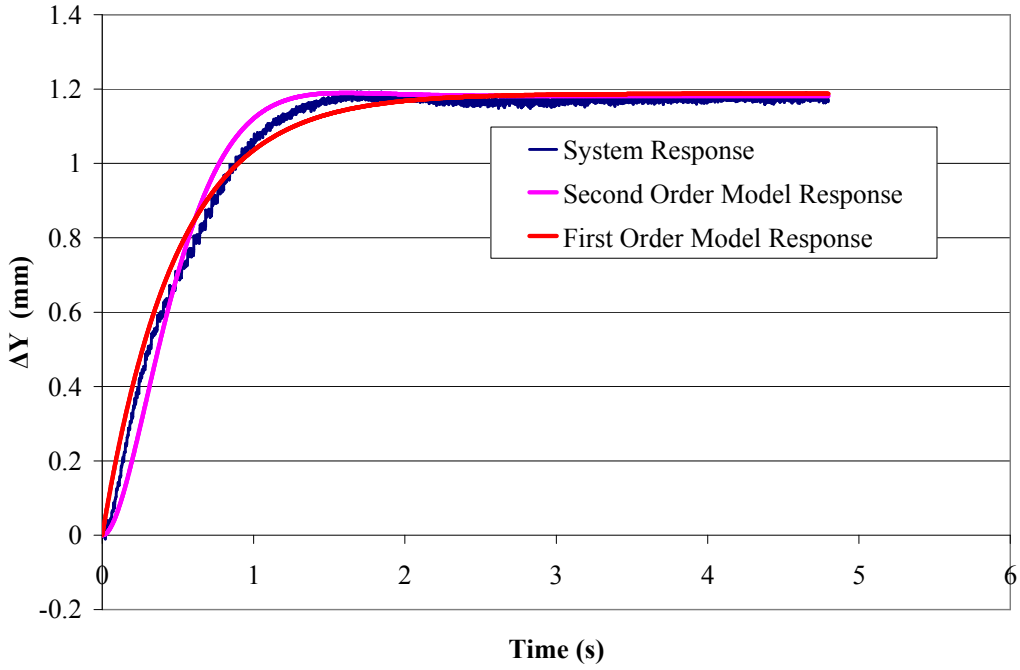

Figure 6-10: Open loop *y* response to a steady state value of 1.18 mm.

motion while four electromagnets are used to produce *y* motion. The potential benefit of this symmetry is that it may be possible to use the same controller for both *x* and *y* positioning. This will simplify the design process and will allow for faster and easier implementation of the controller on the true system.

After examining the model under feedback control, it was determined that a first order system may provide a better estimate of the dynamics under certain conditions. These equations are

$$\frac{x}{x_{ctrl}} = \frac{0.0686}{z - 0.9956} \quad T_s = 2\text{x}10^{-3}\ \text{s} \tag{6-8}$$

$$\frac{y}{y_{ctrl}} = \frac{0.0487}{z - 0.9959} \quad T_s = 2\text{x}10^{-3}\ \text{s} \tag{6-9}$$

The first order open loop responses are also plotted in Figure 6-7 through Figure 6-10. In general the first order model does not match the start-up dynamics of the system as well as the second order model, but the first order model response starts to more closely match the system response as the steady-state value is reached.

6.5 PD Control of the System

PD control is used as a preliminary method for providing control of the horizontal position. A PID control algorithm was used on the experimental setup of [30], and so it was assumed that PD control would work in this case as well. Integral control was not used for the initial control investigation as it had been determined during the prior work [30] that the integral control could produce some unpredictable and unstable behavior in the system. PID control of the system is discussed in the next section.

Preliminary estimates with the system model suggested that suitable values for the system parameters would be K_c=1 and T_d=1x10^{-6}. Figure 6-11 compares the system response to the model response in the *x* direction. The initial rise of the second order model response matches the system response quite well. There appears to be a small amount of overshoot in the system model, but certainly not to the degree that is observed in the second order model

response. The response of the first order model is faster than the system model, but there is no overshoot. This is in line with the observation that the first order model does a better job of matching the final steady state dynamics. There is also a discrepancy in the final steady state values achieved by the system and the models. This is likely due to the non-linearity of the true open-loop response. As expected, neither the models nor the system are able to track the reference signal.

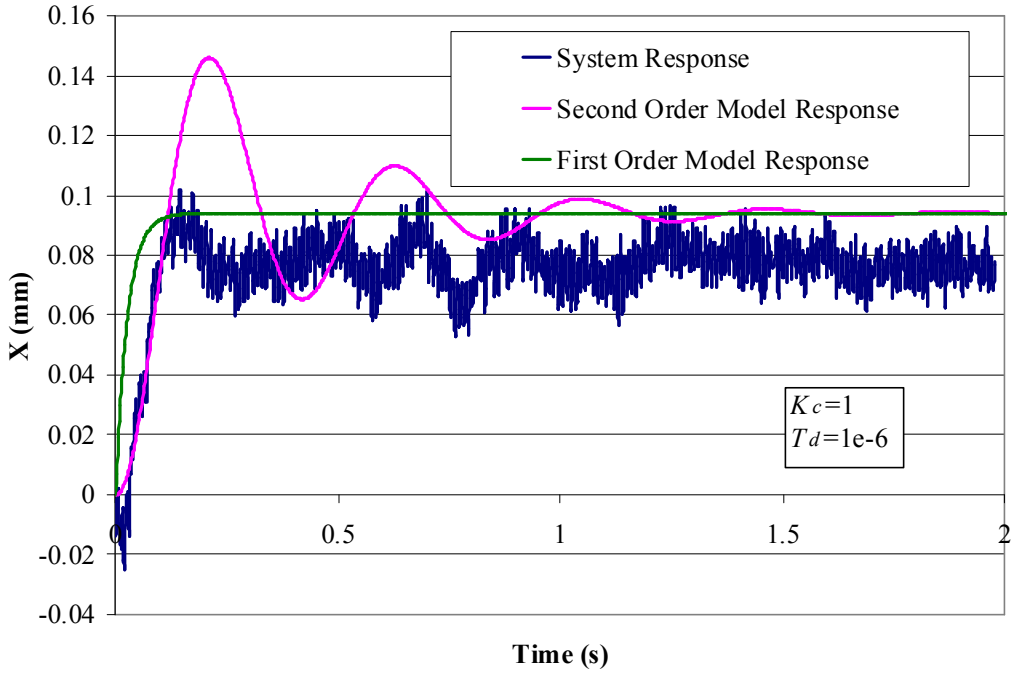

Figure 6-11: Comparison of the closed loop system response to the closed loop first and second order model response for a 0.1 mm step input.

From the FEM analysis presented in Chapter 2, it is known that the microrobot will always move to a point where the horizontal force is zero, which is the point where the vertical flux density gradient in the horizontal direction is zero. It is also known that the horizontal flux density gradients are much less than the vertical flux density gradients. This means that the horizontal forces on the microrobot will be much less than the vertical force counteracting the weight of the microrobot. Because these forces are so small, the microrobot will have relatively small acceleration and velocity, meaning that the microrobot will travel at a relatively slow rate towards the equilibrium point. This also means that the deceleration

force needed to stop the microrobot at the desired position does not need to be excessively large, especially in consideration of the fact that the aerodynamic drag on the microrobot will also act to minimize the overshoot as the flux density gradient decreases to zero. It is therefore expected that, provided that the equilibrium area is sufficiently small, there should be sufficient braking forces that will act to minimize overshoot and settling time. By designing a more appropriate microrobot/pole piece combination this theory can be investigated further without the aid of the aluminium block. Some overshoot may be expected in cases where the gain is high. This appears to be happening in the system shown in Figure 6-11, although there appears to also be some disturbance rejection that is affecting the position tracking. The linearized model does not account for the changes in the force profile, which is why the oscillatory behavior is observed.

These effects can also be observed in the open loop responses of Figure 6-7 to Figure 6-10, which show that it takes nearly two seconds to reach the steady state point. Contrast this with the vertical position responses in Figure 6-3, where the settling time is approximately 1 second. Additionally, the first and second order models occasionally overestimate the actual position of the microrobot as it approaches steady-state.

There are two main drawbacks to using PD control for horizontal positioning. The first drawback, as mentioned, is that the controller does not permit zero steady state tracking of the reference input. The second issue is that the controller does not completely eliminate the hysteresis behavior that was observed in the open loop response. Figure 6-12 shows the step response of the system from 0.9 mm to 1 mm and the return step from 1 mm to 0.9 mm. The microrobot starts at a mean position of 0.792 mm, and moves to a new mean position of 0.882 mm when the control signal is changed from 0.9 to 1. When the command signal is reset to 0.9 mm, the mean position of the microrobot is 0.809 mm. This may seem like a small discrepancy, but inspection of Figure 6-12 shows that it is quite apparent that the microrobot did not return to the starting position when the command signal was changed back.

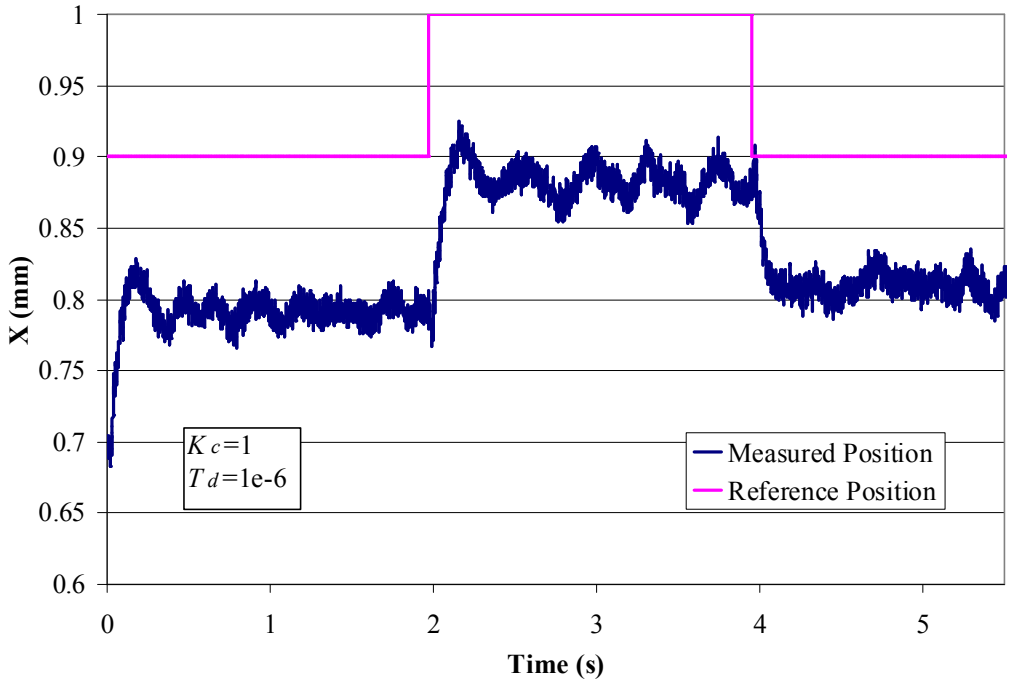

Figure 6-12: Step responses in the positive *x* direction with the PD controller.

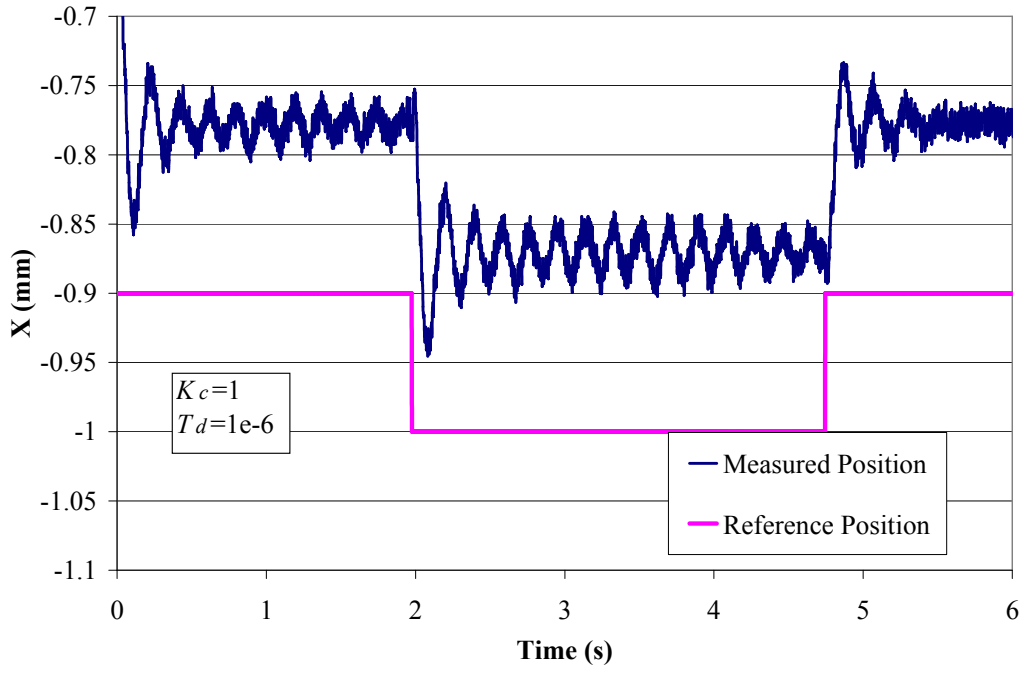

Figure 6-13: Step responses in the negative *x* direction with the PD controller.

Subsequent testing showed that this hysteresis behavior is only temporary. The test run that Figure 6-12 was produced from consisted of moving the microrobot in 0.1 mm steps from 0 mm to 1 mm, then from 1 mm to -1 mm in -0.1 mm increments, and then returning to 0 mm. The hysteresis behavior in the controlled position is present along the positive x axis as the microrobot moves between 0 mm and 1 mm. The exception is when the command signal returns to 0 mm. In this case it is observed that the mean position of the microrobot is 0.03 mm, while the mean position at the start of the test was -0.01 mm. As the microrobot moves through the negative quadrant, this hysteresis behavior is not observed at all. Figure 6-13 shows the step response from -0.9 mm to -1 mm, and from -1 mm to -0.9 mm, and it can be seen that the start position and end position of the microrobot are the same. The mean position at the start of Figure 6-13 is -0.778 mm, and when the command signal is changed from -0.9 mm to -1 mm the microrobot moves to a mean position of -0.870 mm. The robot then returns to a mean position of -0.778 mm when the command signal is changed back to -0.9 mm.

Based on these results it would appear that the hysteresis only exists on start-up, and that by moving away from and returning to the origin the hysteresis error can be removed from the system. Ideally the system should be able to track the same point for the same input immediately on startup of the system, and it would be desirable if this calibration procedure did not need to be performed every time the system was started.

Although the PD analysis for the horizontal motion has focused on motion along the *x* axis, the discussion applies equally to motion along the *y* axis. Figure 6-14 compares the response of the first and second order models under closed loop PD feedback. The first and second order model responses are similar to those for the *x*-axis motion shown in Figure 6-11. In this case the second order model does not match the system model as well, but it still provides a reasonable approximation of the system behavior. Figure 6-15 shows the response of the system from 0.9 mm to 1 mm and back to 0.9 mm using the same PD controller implemented for the *x* axis. It can be seen that the damping in the *y* direction is not as great as in the *x* direction, possibly due to the fact that fewer electromagnets are controlling the

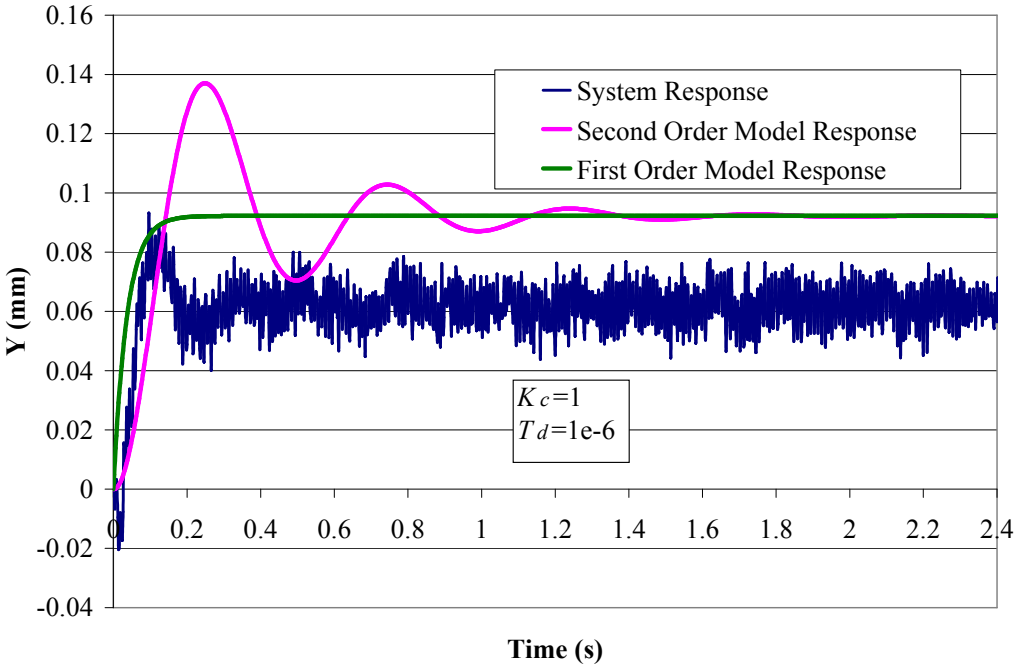

Figure 6-14: Comparison of the system response to the model responses under PD control.

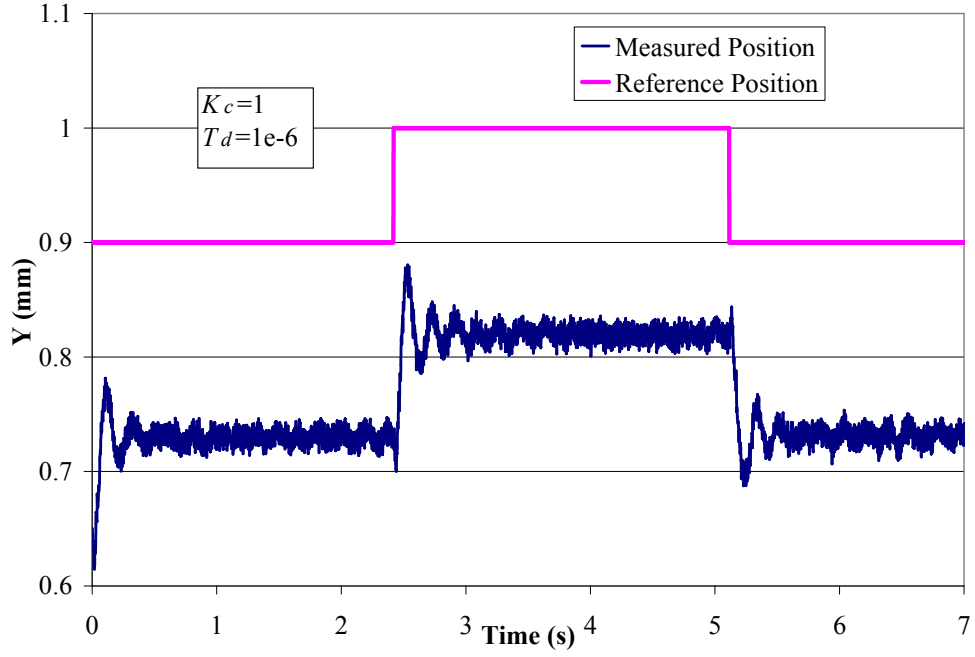

Figure 6-15: Step responses in the *y* direction from 0.9 mm to 1 mm, and back to 0.9 mm.

force. This would also explain why the steady-state values reached by the system are smaller than for the *x* axis motion, although this is not entirely unexpected as the identified gain of the *y* axis transfer function is less than the *x* axis transfer function. Although the hysteresis effect is not readily apparent in Figure 6-15, Figure 6-16 demonstrates that the hysteresis is present at lower values of the control signals. In particular, when the control signal is increased from 0 mm to 0.1 mm the mean value of the y position is 0.0618 mm, while the mean position is 0.008 mm when the control signal is changed from 0.2 mm to 0.1 mm.

6.6 Horizontal PID Control

In order to improve the horizontal response it was decided to implement integral control with the existing PD controller in an attempt to eliminate the steady state error and hysteresis effects. The PID controller is implemented by first using PD control to stabilize the microrobot at the origin, and then adding in the integral term after a few seconds before performing any system motion. This helps to minimize large integral control signals during system startup. Figure 6-17 shows the 0.1 mm step responses of the system from x=0 mm to x=0.5 mm. The control gains in this situation are K_c=1, T_i=0.005, and T_d=1x10^{-6}. It can be seen that the microrobot is able to successfully track the reference with zero steady state error. In addition, the PID controller is also able to successfully eliminate the hysteresis effect, as shown in Figure 6-18. Figure 6-19 shows the equivalent results for the motion along the *y* axis with the same controller.

6.7 Model Response with the PID Controller

During the simulation of the model response under PID control, it was found that implementation of the correct integral gain would cause the system to go unstable. Conversely, an integral gain that would produce a reasonably fast response on the model could be implemented on the system, but would result in an unacceptably slow response on the actual system.

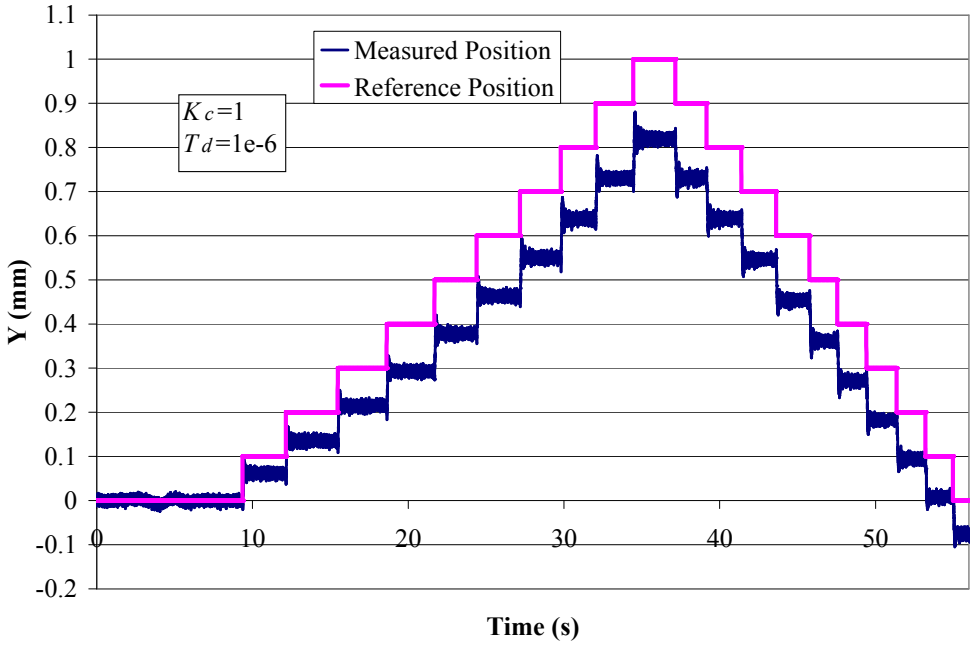

Figure 6-16: Step responses of 0.1 mm in the y direction from 0 mm to 1 mm, and back to 0 mm.

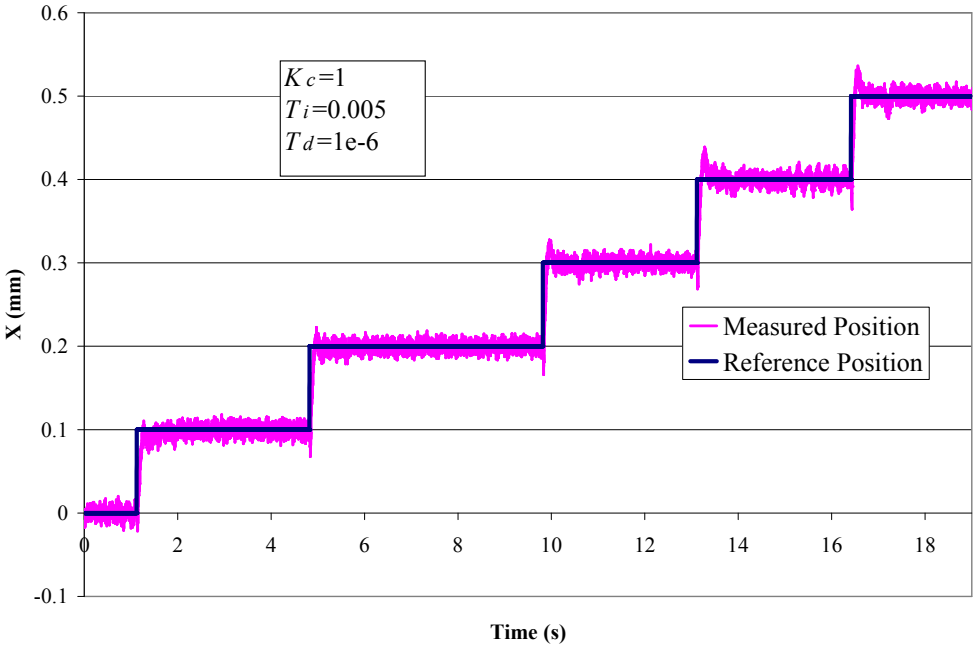

Figure 6-17: PID Control of the horizontal *x* position.

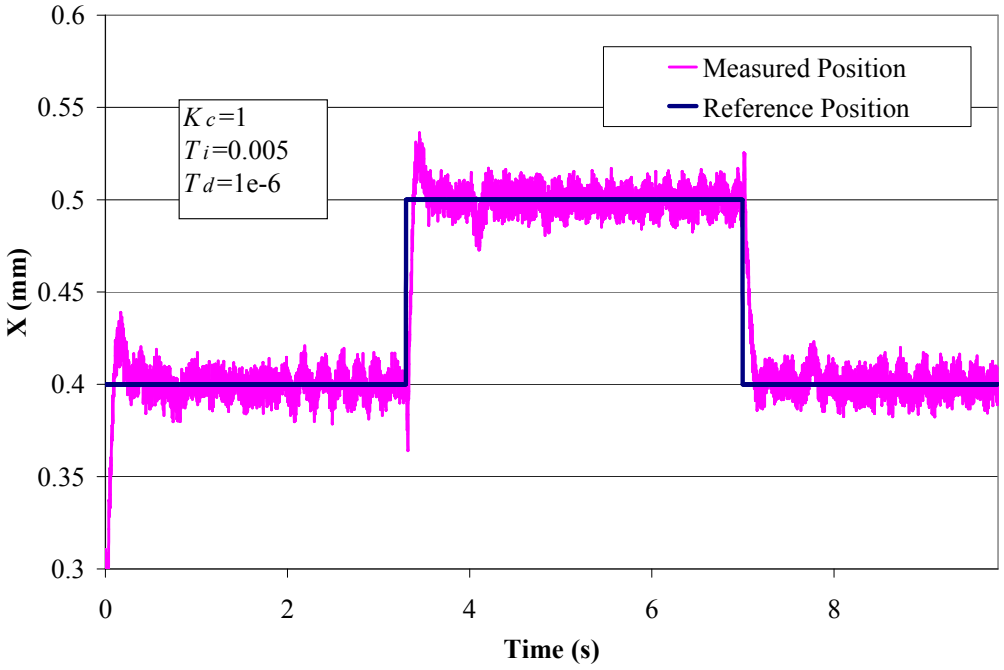

Figure 6-18: Step responses in the *x* direction from 0.4 mm to 0.5 mm, and back to 0.4 mm. Note that the hysteresis effect has been eliminated.

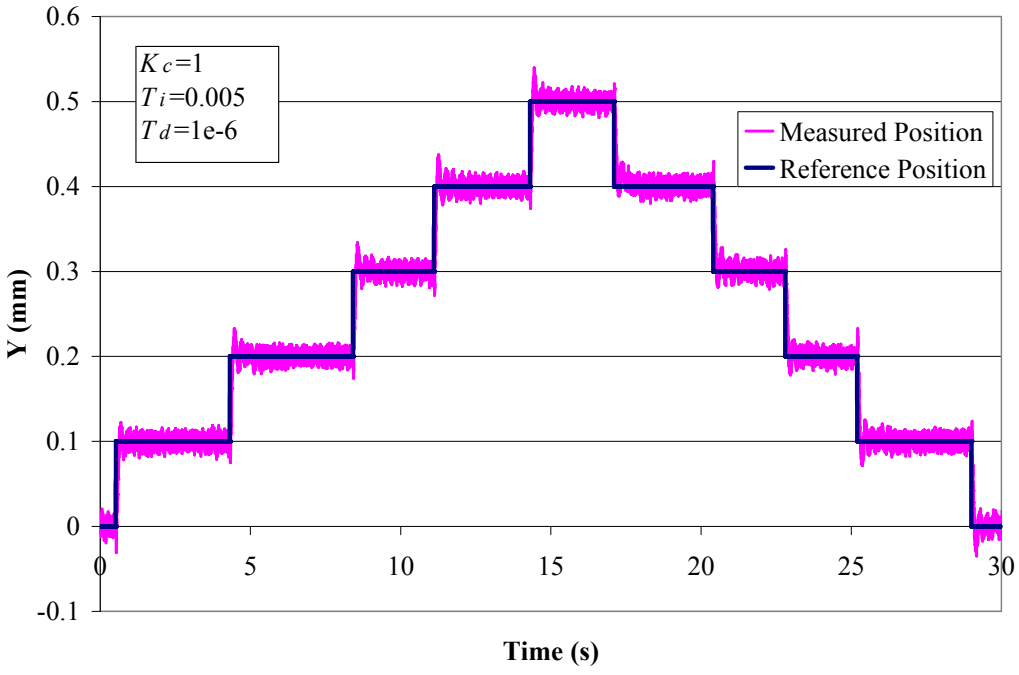

Figure 6-19: Motion along the *y* axis with a PID controller.

Figure 6-20 compares the step response of the first and second order models to the real system. For the system response, K_c=0.025, T_i=0.006, and T_d=1x10^{-4}. For the model responses K_c and T_d are the same, but T_i=0.125. In this case, the first order model does a better job of approximating the system response than the second order model. Figure 6-21 compares the system and model responses when K_c=0.025, T_i=0.125, and T_d=1x10^{-4}. These are the same gains used on the system models in Figure 6-20, and so it would be expected that the response of the model would match the system. However, this is not the case. The actual system response is significantly different than the predicted model response. The model responses in Figure 6-21 were generated by assuming that the integral time constants could be scaled linearly between the models and the system. From Figure 6-20, the ratio of the system integral constant to the model integral constant is

$$\frac{0.006}{0.125} = 0.048 \tag{6-10}$$

In Figure 6-21, the system integral time constant is 0.125. The required model integral time constant T_{im} is

$$\frac{0.125}{T_{im}} = 0.048$$
$$T_{im} = 2.604 \tag{6-11}$$

From Figure 6-21, it can be seen that the second order model response is a slightly better match to the system response, although both systems tend to the same point once the startup dynamics are dissipated.

Figure 6-22 and Figure 6-23 show the equivalent results for the *y* axis. In this case the second order model provides a slightly better estimate of the system response when compared to the first order model response.

Preliminary estimates suggest that the scaling of the integral time constant is dependent on the gains K_c and T_d. In Figure 6-24, a PID controller with gains K_c=0.1, T_i=0.007, and T_d=1x10^{-6} is applied to the system. The equivalent integral time constant needed on the

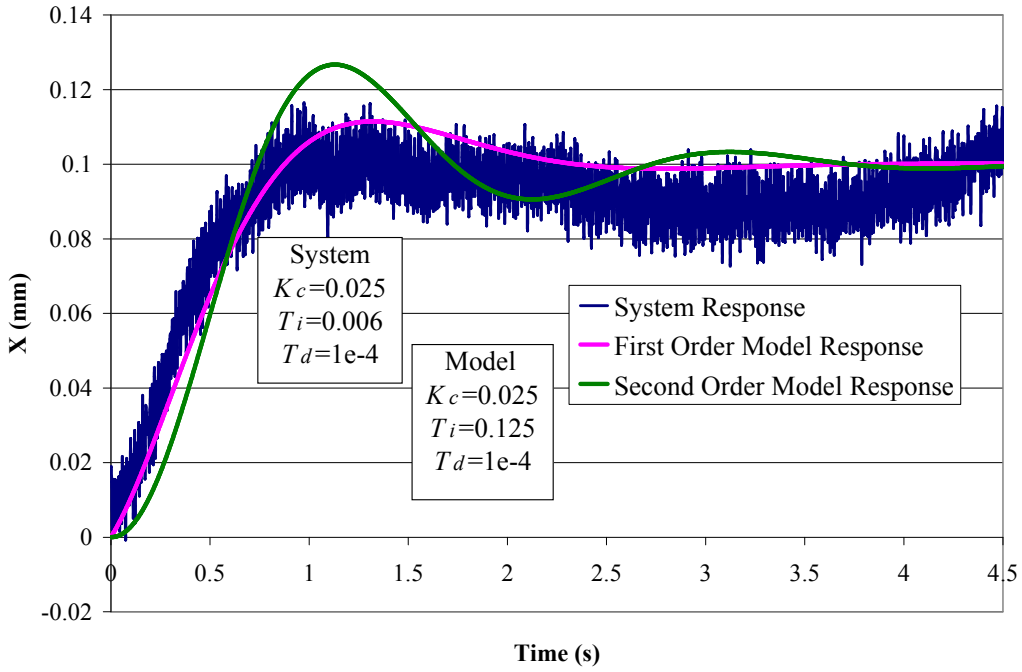

Figure 6-20: Comparison of the *x* model response to the system response under PID control.

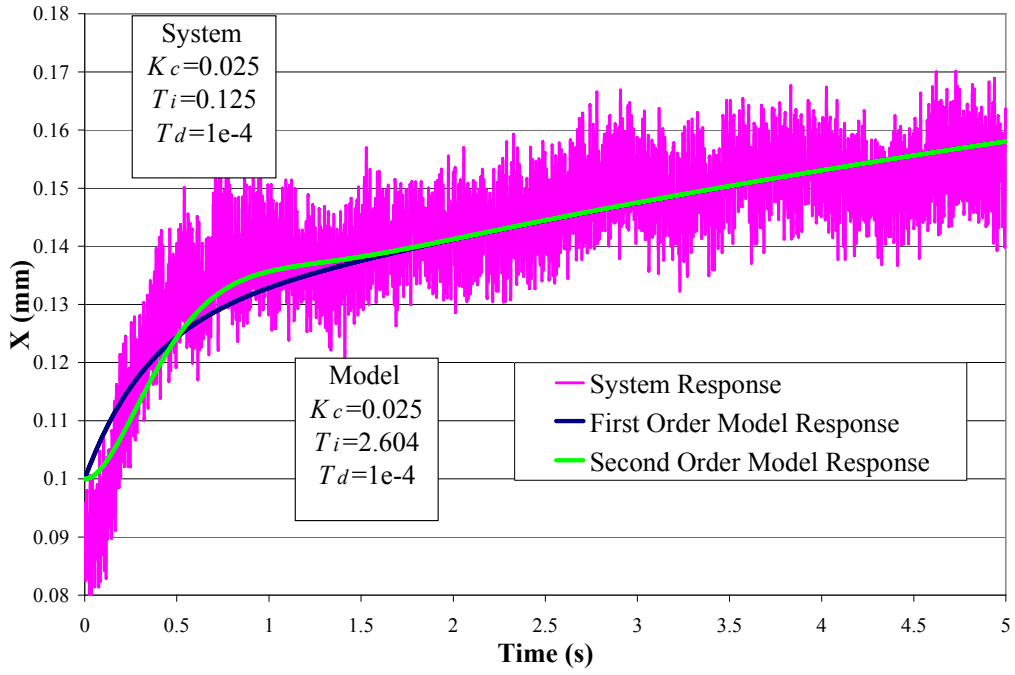

Figure 6-21: Response using estimated model gain of Figure 6-20 as the system gain.

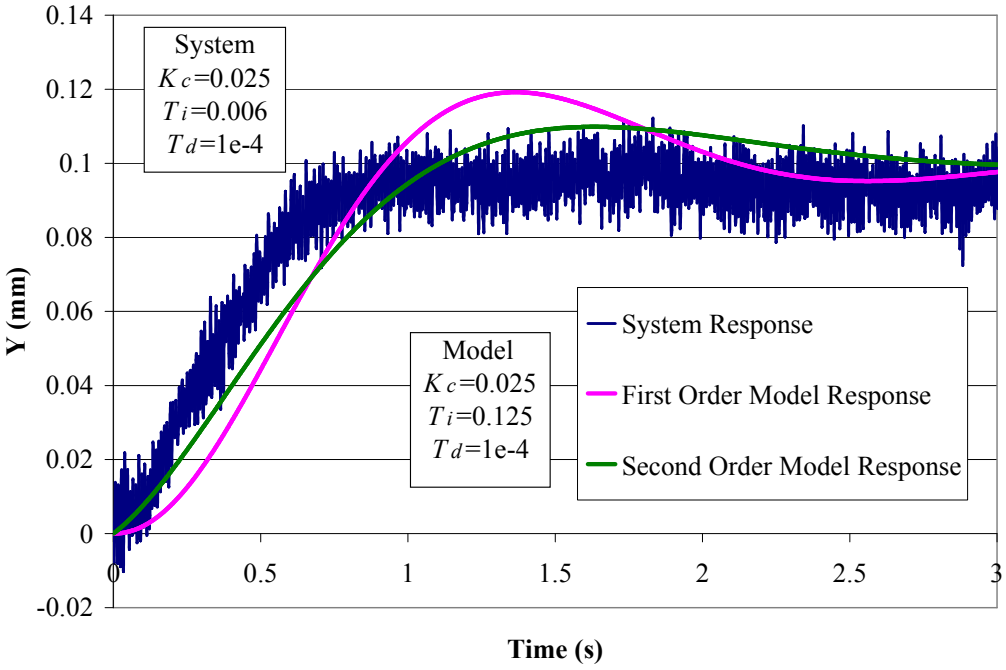

Figure 6-22: Comparison of the *y* model response to the system response under PID control.

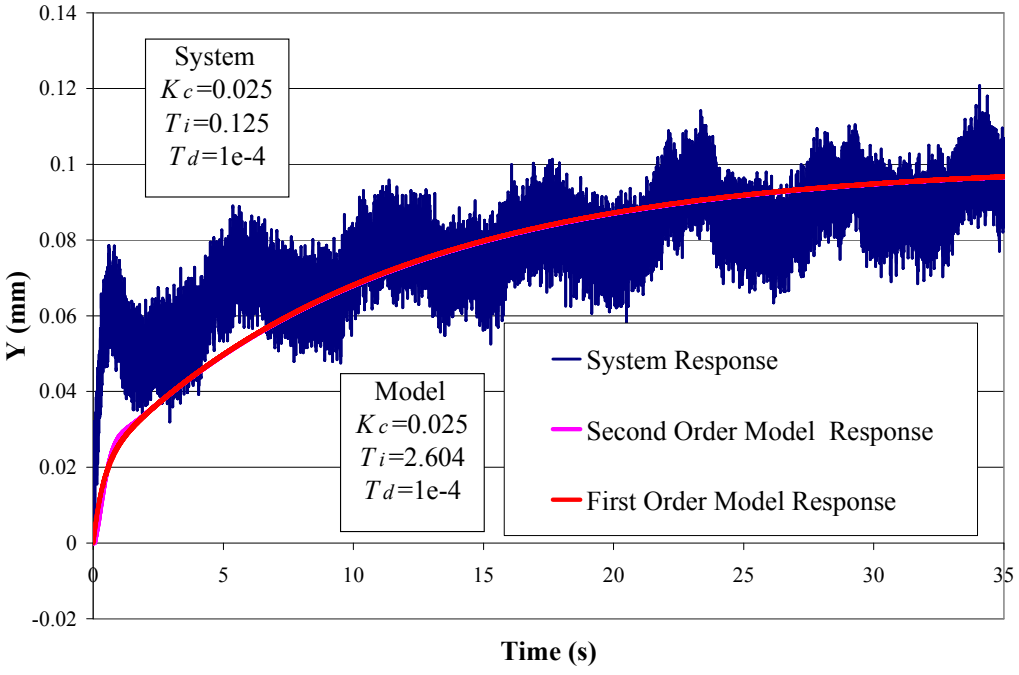

Figure 6-23: Y response using estimated model gain of Figure 6-22 as the system gain.

model was determined to be 0.098. The resultant ratio is 0.0714. Figure 6-25 validates that this ratio is correct. The gains on the system are K=0.1, T_i=0.01, and T_d=1x10^{-6}. The equivalent integral time constant for the model must be 0.14 in order to preserve the ratio. It can be seen in both cases that the first order model provides a good fit to the system response.

Based on these results, the preferred method for tuning the PID controller would be to design the PD portion of the system to meet the response time design criterion, and then tune the integral gain online in order to meet steady state performance requirements. Once a preliminary integral gain is found, the integral gain of the model can be tuned to match the system response. This will yield the integral time constant ratio that can be used to convert desired integral gains from the model into the required gains for the system.

Figure 6-26 and Figure 6-27 show the horizontal response of the system at z=18 mm. The model responses are a poor fit for the system response. This is due to the fact that the system model was identified at z=10 mm. Although the rise times of the system and model responses do not match, the controller is still able to eliminate the steady state error and minimize the overshoot of the system.

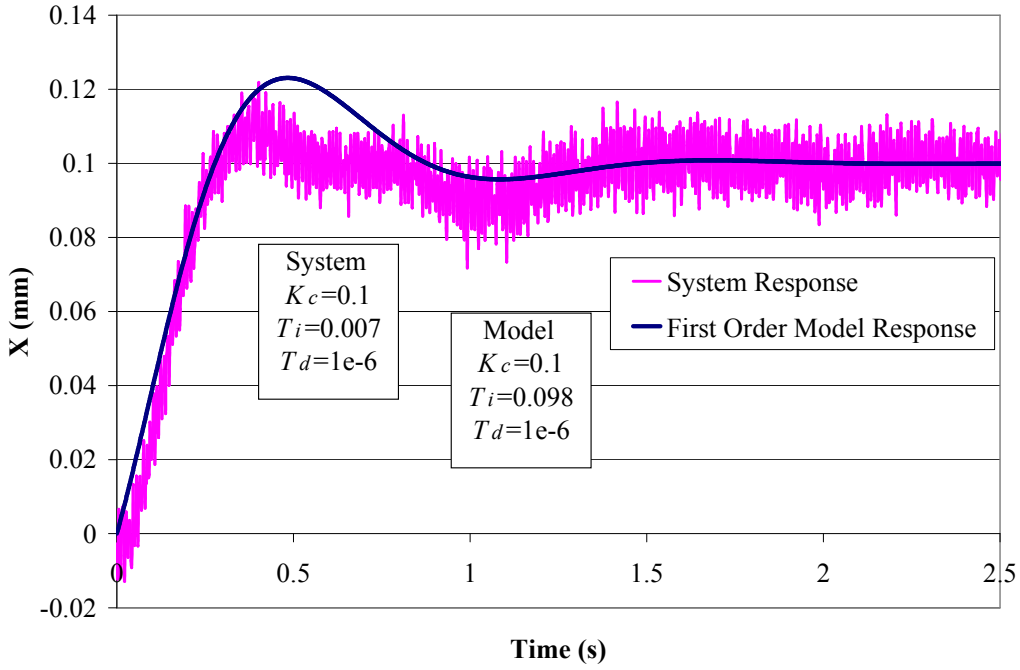

Figure 6-24: Comparison of step response to first order response used to determine the integral gain ratio.

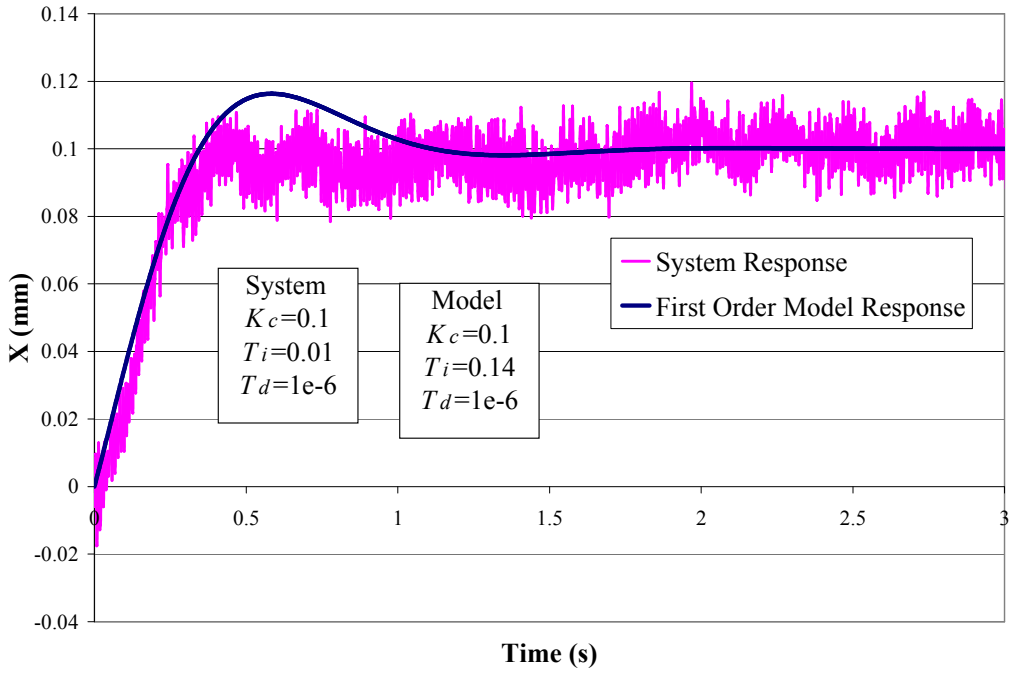

Figure 6-25: Validation of the integral gain ratio between the system and the model.

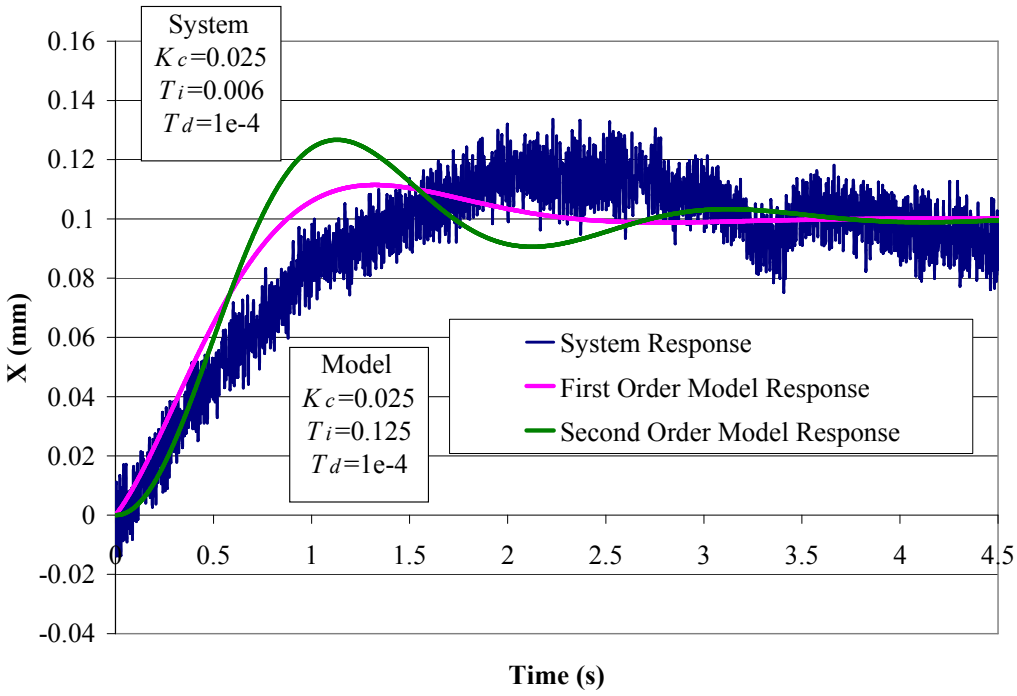

Figure 6-26: Motion in the *x* direction at *z*=18 mm.

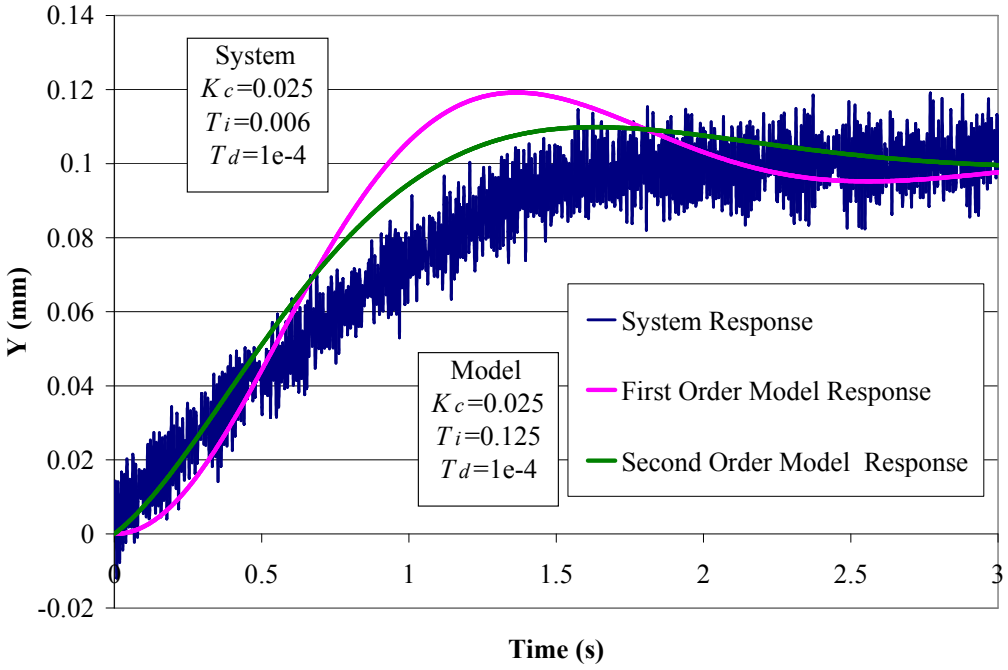

Figure 6-27: Motion in the *y* direction at *z*=18 mm.

Chapter 7
System Performance and Advanced Control

7.1 Combined Motion Effects

Vertical and Horizontal positioning of the microrobot is accomplished by changing the input current to the electromagnets of the magnetic drive unit. It is therefore expected that whenever motion is performed along one axis, the resulting change in currents may induce a disturbance motion in the other axes. It is important that the disturbance is minimal and that the controller is able to compensate by returning the object to the current reference position. Although system models have been identified for the horizontal and vertical motion of the system, these models are independent of each other, and so it is not possible to simulate how changes in position along one axis will affect the positioning on the other axes. Experimentation and control tuning is needed to determine a control strategy that will produce suitable microrobot motion.

7.1.1 Combined X and Y Motion

Previous discussion of horizontal motion has only considered closed loop control along one axis at a time. The initial control parameters used during these tests were K_c=1, T_i=0.005, and T_d=1x10^{-6}. Attempts were made to use these control gains for simultaneous horizontal and vertical position control, but it was found that the system would go unstable. It was therefore necessary to re-estimate the control parameters in order to produce stable horizontal control. As previously mentioned, one of the drawbacks of the existing system models is that they are not interlinked, and so this behaviour could not be observed prior to implementation on the real system. The subsequent parameter tuning suggested that the gain K_c of the system was too high for combined horizontal and vertical motion. The resultant tuned gains of the system were determined to be K_c=0.025, T_i=0.006, and T_d=1x10^{-4}. Figure 7-1 compares the x direction response for this controller when only the x position is controlled and when both

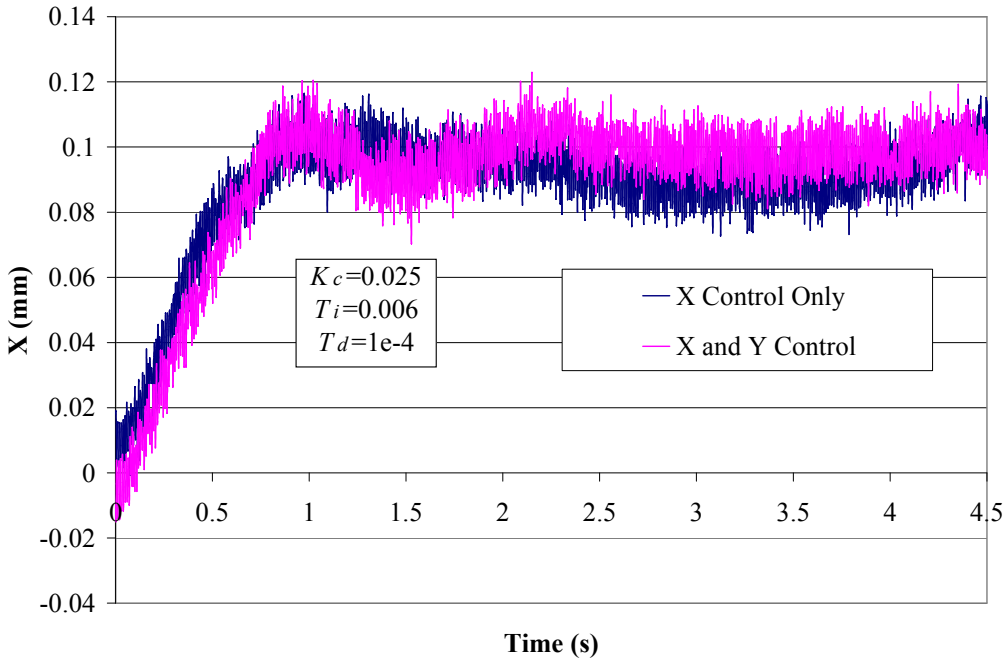

Figure 7-1: Comparison of the *x* direction response under single axis and dual axis horizontal control.

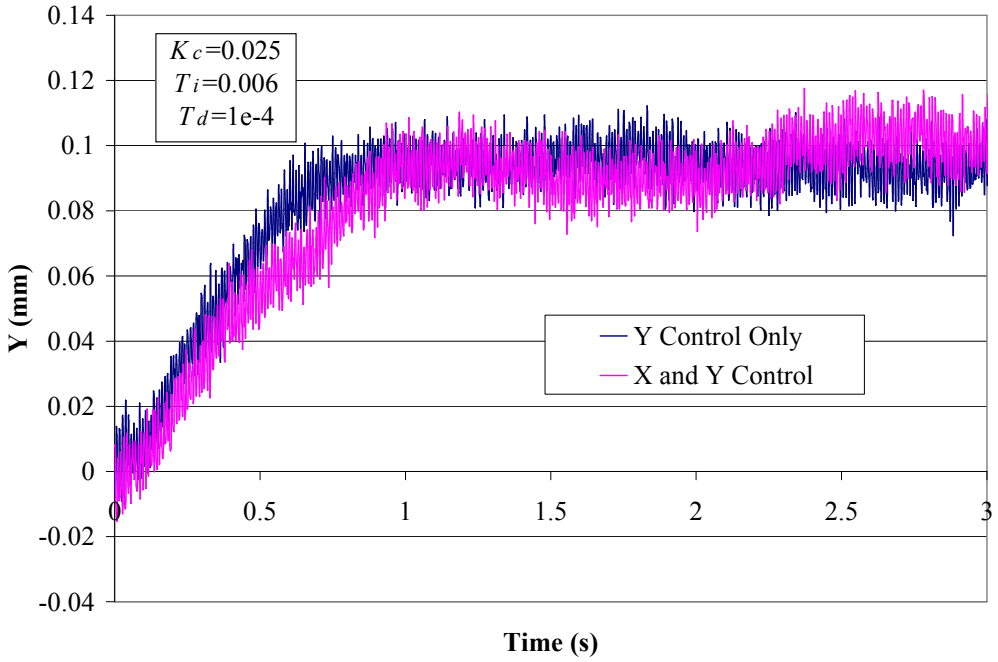

Figure 7-2: Comparison of the *y* direction response under single axis and dual axis horizontal control.

the *x* and *y* position are simultaneously controlled, and Figure 7-2 shows the equivalent results for the *y* axis. In both cases a slight decrease in the rise time of the system is observed, however for the most part the response of the system under single axis control matches the response of the system under dual axis control. This suggests that the identified system models for horizontal motion are suitable for predicting the behaviour of the system when both the *x* and *y* axis positions are controlled, provided said motion is stable.

Figure 7-3 shows the *x* and *y* response when a 0.1 mm step input is applied to the *x* axis. The microrobot moves 0.1 mm in the *x* direction, as expected. It can also be seen that there is a disturbance motion on the *y* axis during this motion. This type of disturbance may be undesirable for certain types of applications. Experimentation has suggested that the disturbance is due to the magnitude of the step input. Figure 7-4 shows the measured position along the *x* and *y* axis when a series of small 0.01 mm steps (essentially a ramp motion) are used to move the microrobot to the desired position. In Figure 7-3 the disturbance is on the magnitude of 0.04 mm, but that in Figure 7-4 no disturbance can be discerned from the regular noise of the system. This suggests that trajectory planning can be used to help minimize the effects of disturbances in the horizontal plane.

Figure 7-5 shows the horizontal response of the system due to a simultaneous input of 0.1 mm. The responses are extremely similar, suggesting that it is suitable to use the same controller for both the *x* and *y* axis positioning in order to produce similar response dynamics. A comparison of Figure 7-5 to Figure 7-1 and Figure 7-2 shows that the system behaviour has changed. In particular the response of Figure 7-5 displays more overshoot and is slightly more oscillatory. This suggests that, while the identified system models are suitable for predicting the motion of the microrobot while both the *x* and *y* position are controlled, the fact that the *x* and *y* position models are not interconnected means that the predicted response will not match the output response if both the *x* and *y* positions are changed simultaneously.

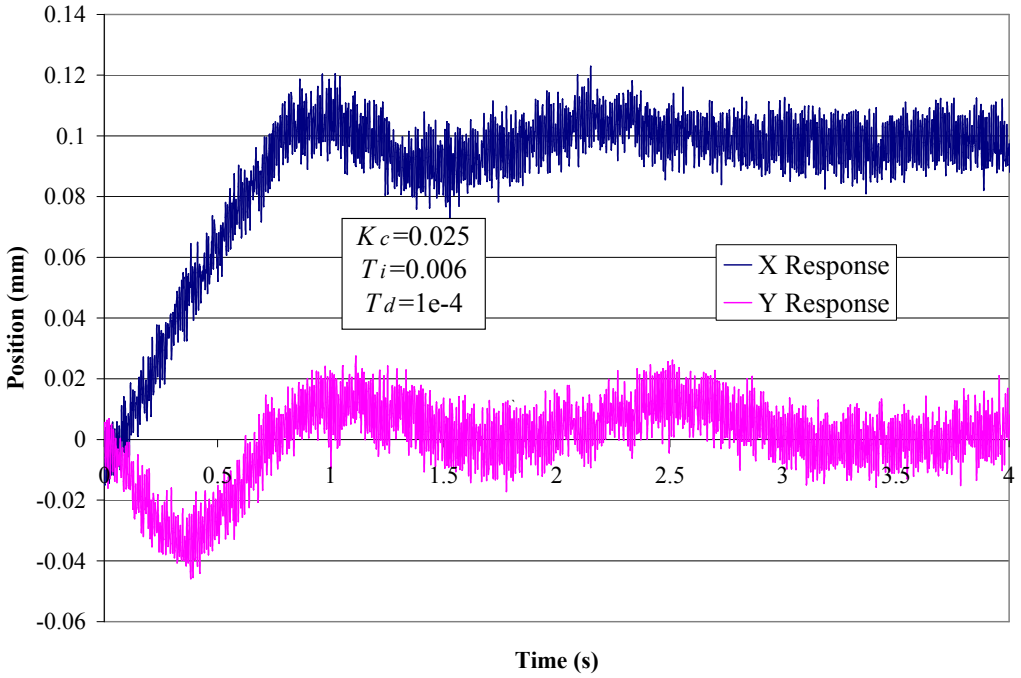

Figure 7-3: Disturbance motion due to combined closed loop horizontal control.

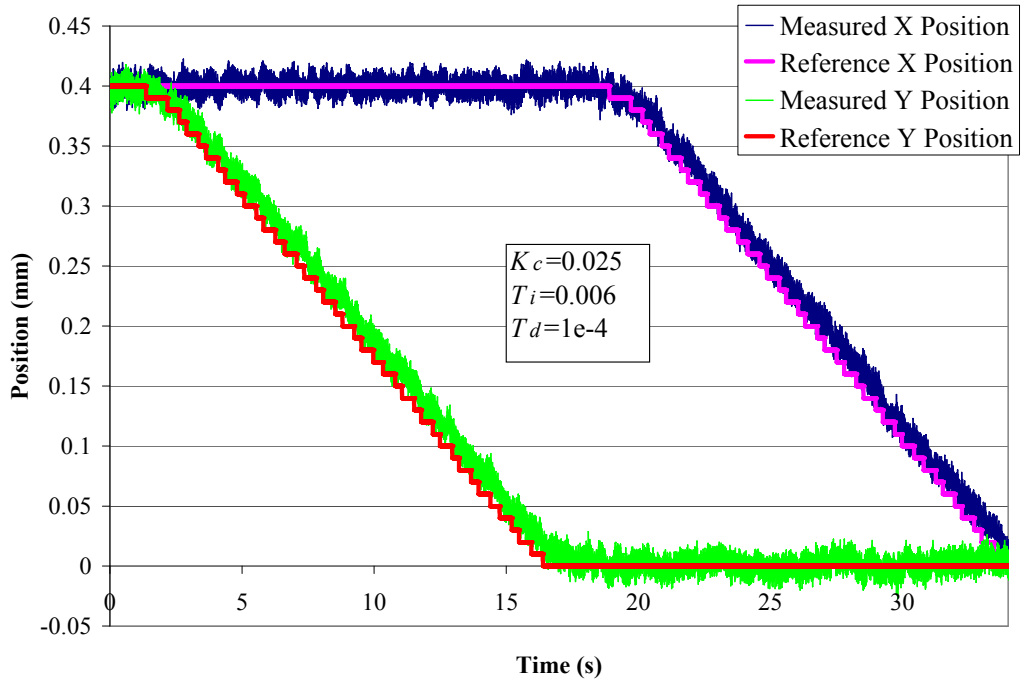

Figure 7-4: Motion in the horizontal plane using incremental 0.01 mm step inputs.

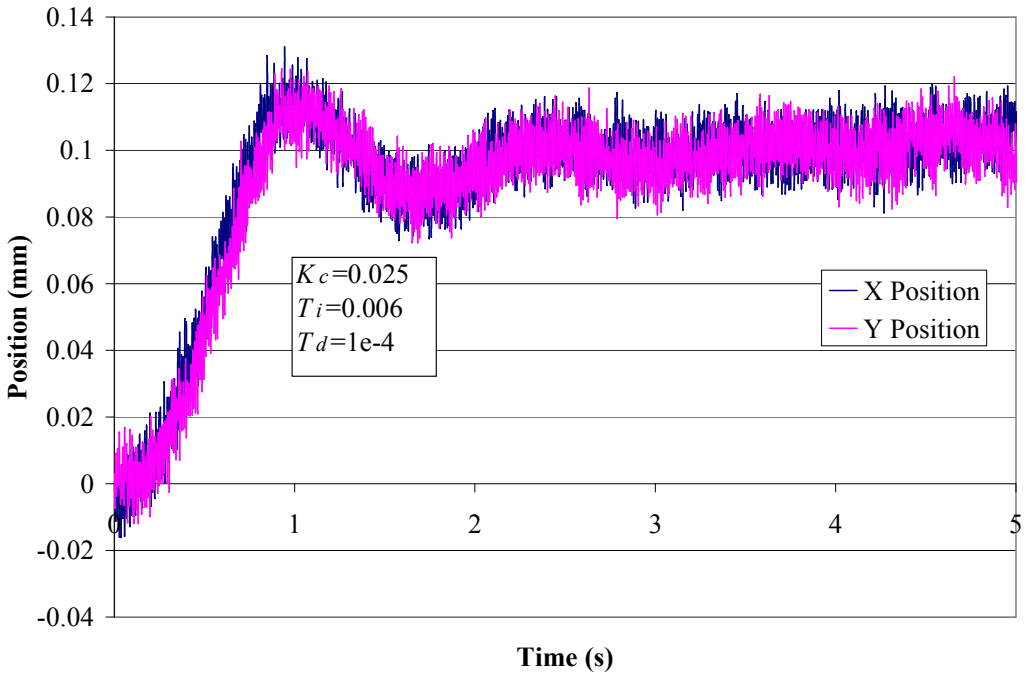

Figure 7-5: Horizontal response due to a simultaneous 0.1 mm step input on *x* and *y*.

7.1.2 Effect of Horizontal Motion on the Vertical Position

Figure 7-6 shows a series of step responses in the *x* direction using a PID controller (K_c=1, T_i=0.005 T_d=1x10^{-6}). Note that only the *x* axis is under control during this motion. The equivalent *z* position for the step responses is shown in Figure 7-7. Whenever there is a step response in the horizontal direction, there is a significant spike in the vertical position of the microrobot. The magnitude of the spike is dependant on the value of the horizontal control signal and whether or not the signal is increasing or decreasing. There is also a noticeable delay as the system returns back to the reference position, occasionally accompanied by an overshoot response. In order to improve the system it is desired to minimize the size of the disturbance peaks and the amount of time it takes for the microrobot to return back to the reference position.

Since the *z* position was changing in response to the horizontal motion, it was decided to counteract the spike by briefly adjusting the vertical reference signal. This would briefly

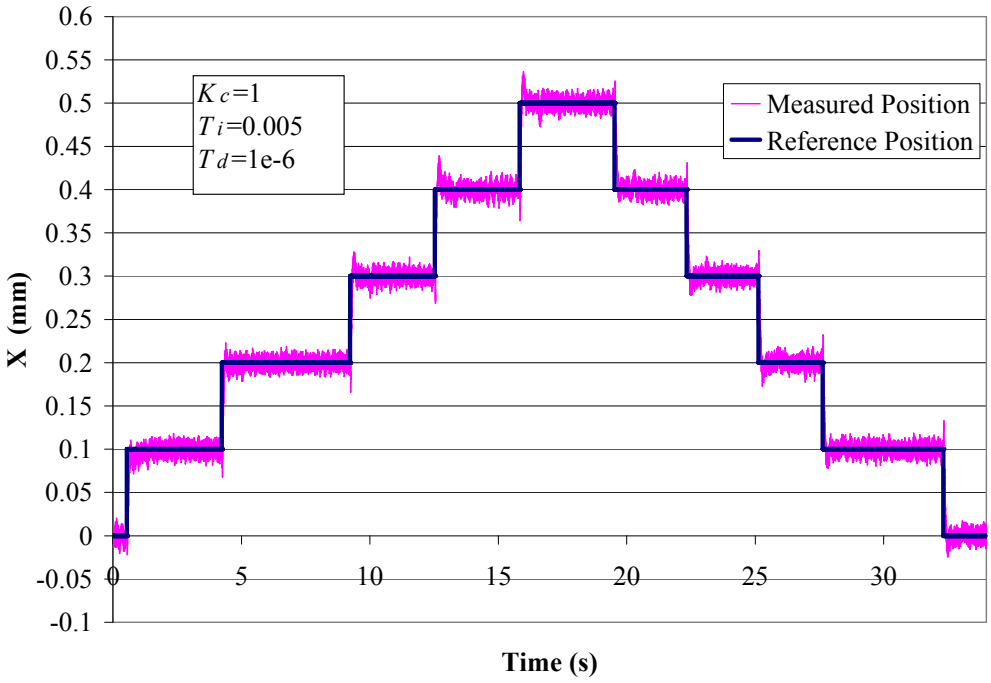

Figure 7-6: Motion in the *x* direction due to PID control.

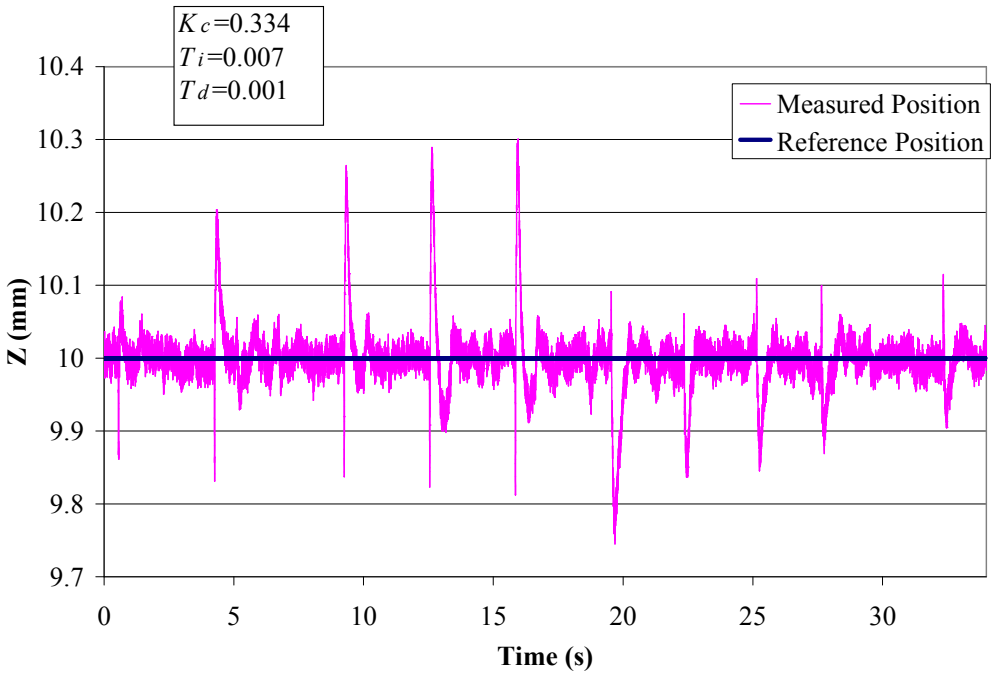

Figure 7-7: Deviations in the vertical position of 10 mm due to horizontal motion.

change the current input to each electromagnet, which would help to counteract the position spike. In terms of pseudocode, the compensator worked as follows: If the horizontal control signal is changed, change the vertical reference signal from z to z-z_{comp} for t seconds, at which point the vertical reference signal becomes z again. The sign of z_{comp} is positive for an increasing horizontal control signal and negative for a decreasing control signal

Experimentation showed that optimal results were obtained when z and t were kept as small as possible. It was found that setting $|z_{comp}|$=0.05 mm and t=10 ms produced the best results for minimizing the disturbance effect. Figure 7-8 and Figure 7-9 show the effects of the implemented vertical position compensation algorithm. While the chosen compensation parameters were determined to be optimal it can be seen that the compensation code is unable to minimize the amplitude of the spikes to a significant degree. For example, the peak vertical position spike in Figure 7-7 when moving from 0.4 mm to 0.5 mm in the x direction is approximately 10.3 mm. With the compensator code the peak vertical spike in Figure 7-9 for the same horizontal step is approximately 10.27 mm. While this is a noticeable change, it is still a significant deviation from the reference position. Figure 7-10 shows that the compensator does improve the decay rate back towards the reference position, and does eliminate the overshoot dip that is observed when no compensation is in place. Figure 7-11 shows a comparison of the horizontal position with and without the compensation code. It can be seen that the compensator introduces slightly more overshoot into the system, and that there is a slight oscillatory effect present at steady state, which is representative of the microrobot "swinging" in the workspace. Based on these results it can be said that the vertical position compensation code has slightly improved the vertical position disturbance rejection, but has also made the horizontal position response slightly worse.

As an alternative to the vertical position compensation code, it was found that tuning the horizontal control parameters would have a greater impact on both improving the vertical position disturbance and the horizontal response. Figure 7-12 and Figure 7-13 show the horizontal and vertical position response with the horizontal PID gains tuned to K=0.1,

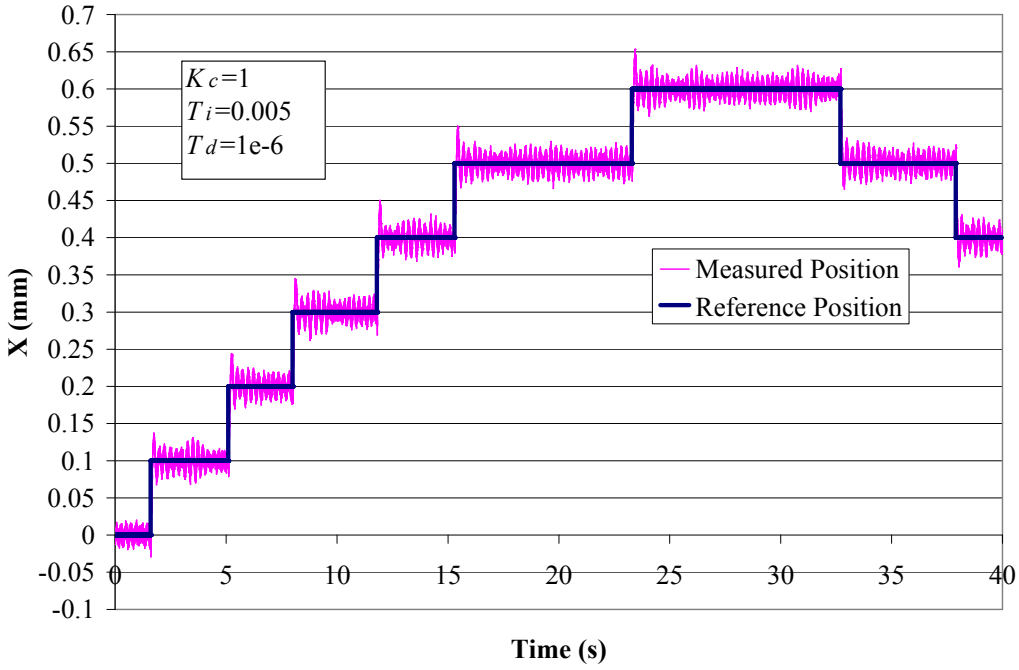

Figure 7-8: Horizontal position with vertical position compensation.

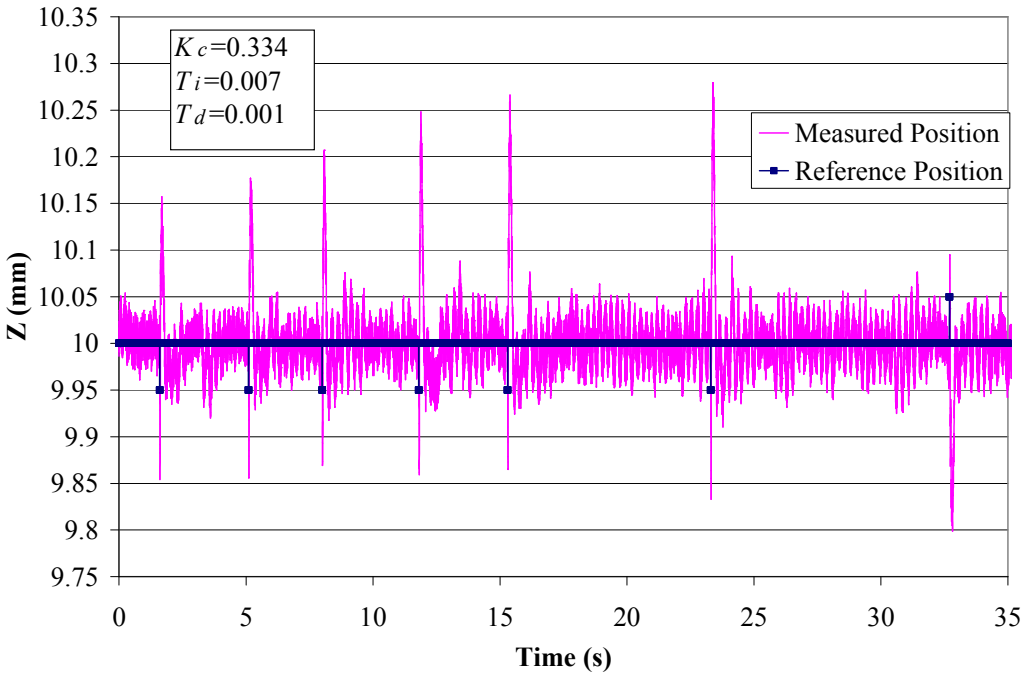

Figure 7-9: Effects of the vertical position compensation algorithm.

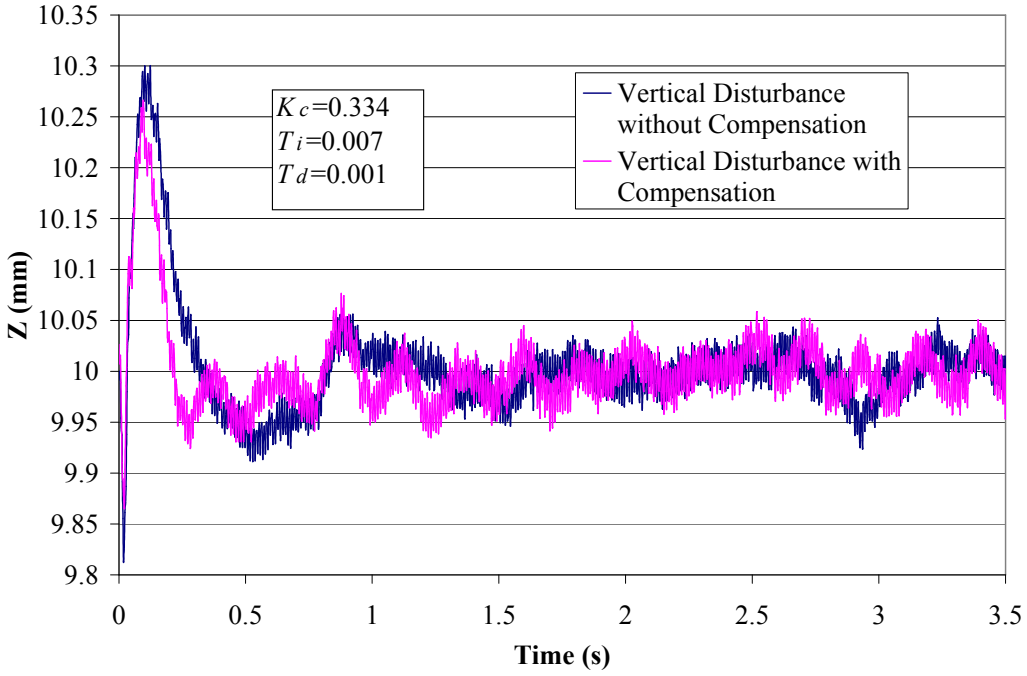

Figure 7-10: Comparison of the disturbance rejection in the z position.

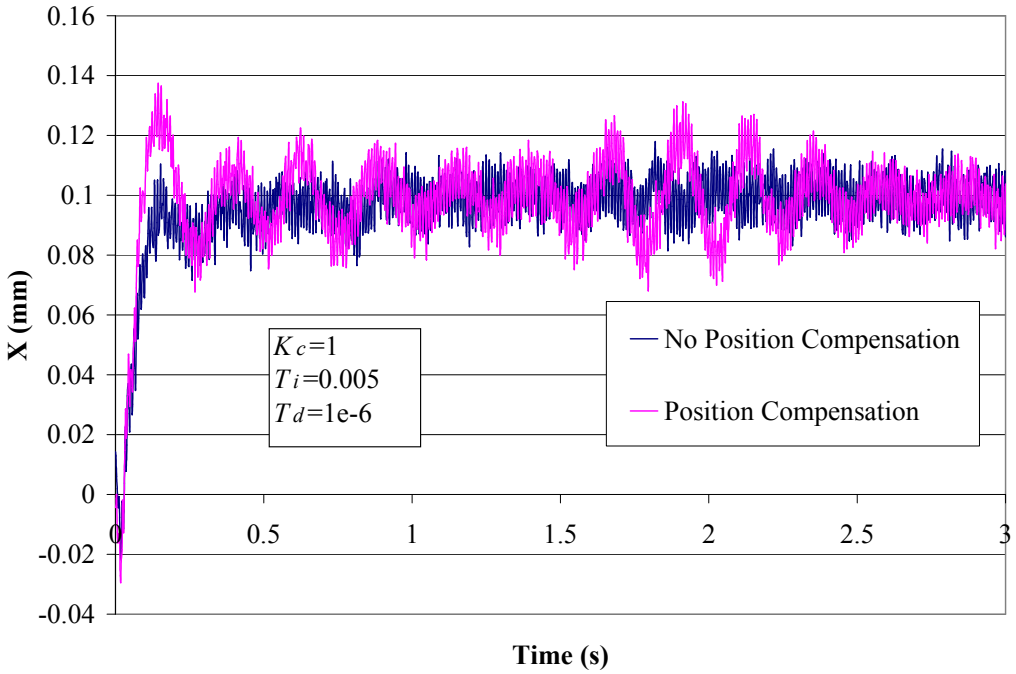

Figure 7-11: Comparison of the horizontal response with and without the compensator.

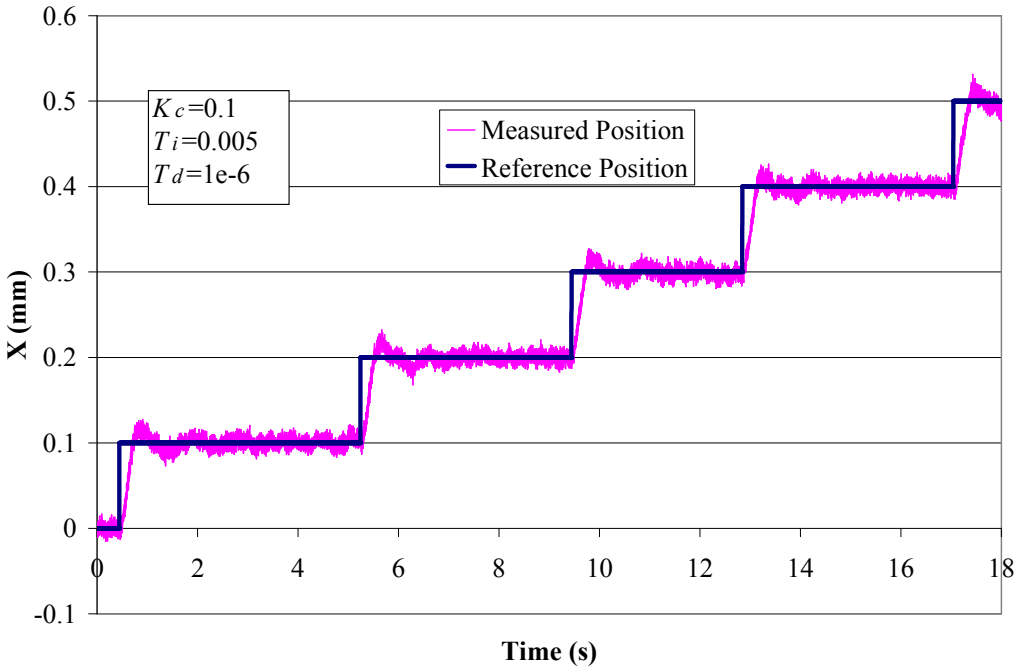

Figure 7-12: Horizontal position with PID gains tuned to minimize vertical disturbance.

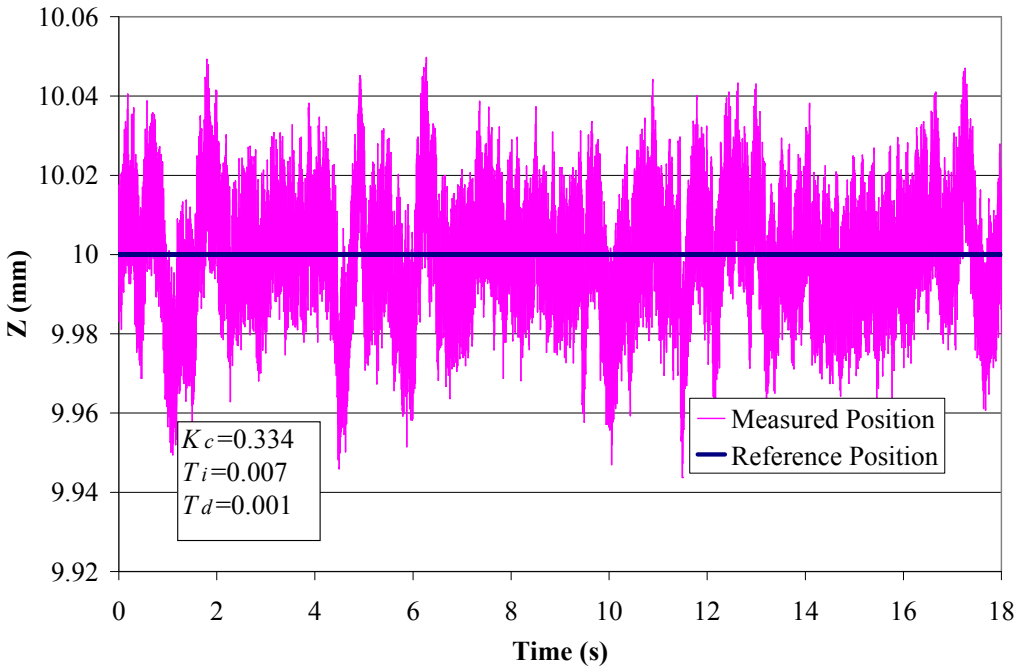

Figure 7-13: Measured vertical position for Figure 7-12.

T_i=0.005, and T_d=1x10^{-6}. Figure 7-13 shows that the vertical position disturbance experienced during the horizontal motion of the microrobot has been reduced considerably. Figure 7-14 shows the value of the measured z position prior to starting horizontal motion. It can be seen that the parameter tuning has eliminated the disturbance spikes that were observed when the vertical position compensation algorithm was used.

Figure 7-15 compares the horizontal position response when the compensation algorithm is used and when the horizontal control parameters are tuned. It can be seen that the tuning of parameters has resulted in a slower system response, but that the overshoot and "swinging" effects have been reduced. Further tuning of the parameters can be used in order to further improve the horizontal response.

7.1.3 Effect of Vertical Motion on the Horizontal Motion

As with horizontal motion at a constant vertical position, it has been observed that deviations in the horizontal position due to vertical motion can be minimized if the positional changes are minimized. Figure 7-16 shows the microrobot undergoing a series of 0.1 mm steps from z=10 mm to z=11 mm at (x,y)=(0,0). Figure 7-17 shows that there is negligible deviation from the origin. Figure 7-18 shows the microrobot moving from z=11 mm to z=10 mm at (x,y)=(1,1). As shown in Figure 7-19 there is negligible deviation. This behaviour also demonstrates that vertical motion of the microrobot does not have to be confined to (x,y)=(0,0) on the horizontal plane.

7.2 System Performance

7.2.1 Vertical Performance Comparison with Previous Experimental Setup

Table 7-1 compares the performance of the current experimental setup with the experimental setup of [30]. For the existing setup the controller is chosen as the PID controller with K_c=0.334, T_i=0.007 T_d=0.001, as it was felt that these control parameters produced the best system performance of all of the designed PID controllers. A typical response is shown in

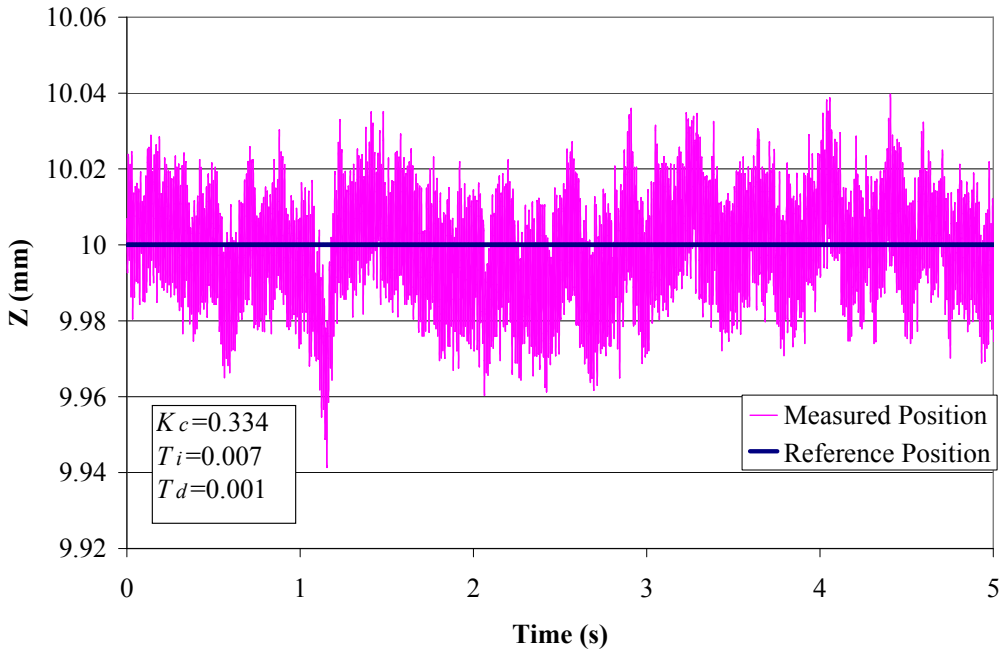

Figure 7-14: Measured z position with no horizontal motion.

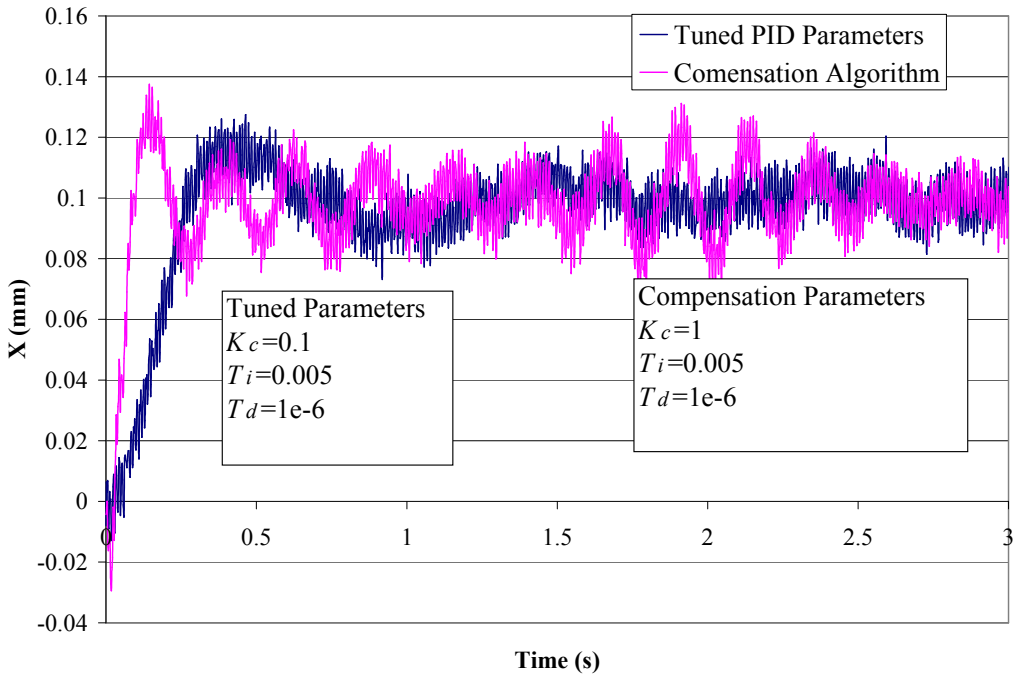

Figure 7-15: Comparison of the horizontal response due to tuning of PID parameters and the compensation algorithm.

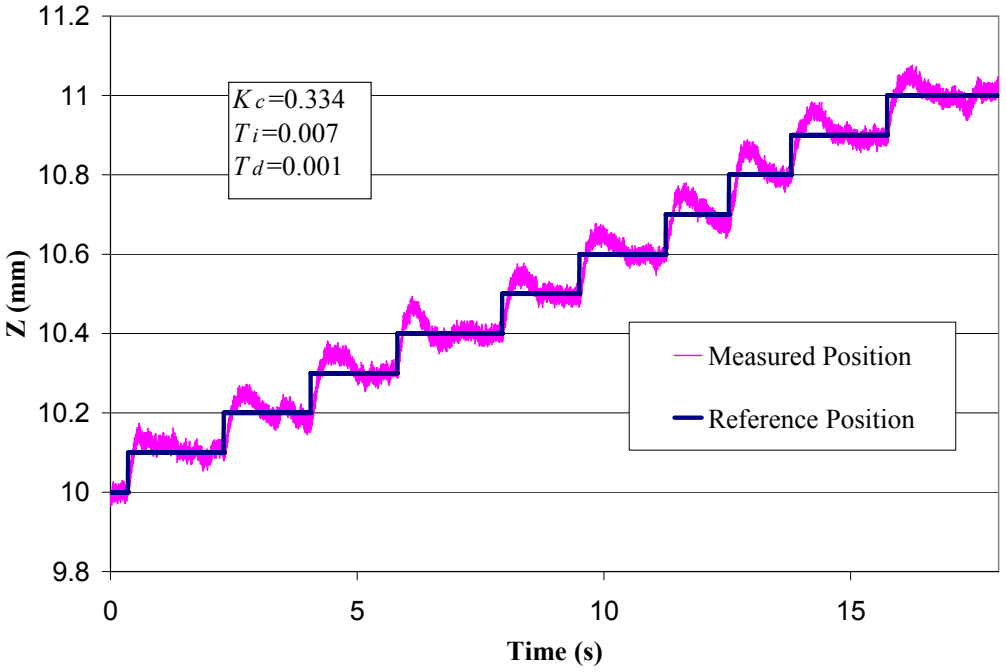

Figure 7-16: Vertical motion of the microrobot at (x,y)=(0,0).

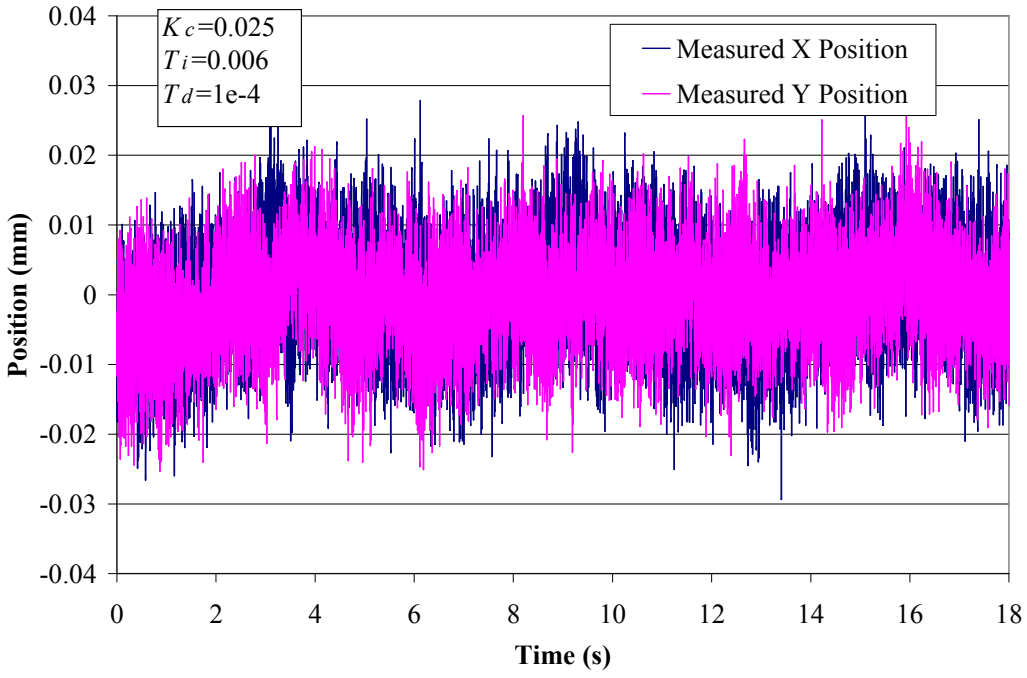

Figure 7-17: Horizontal position of the microrobot during the motion of Figure 7-16.

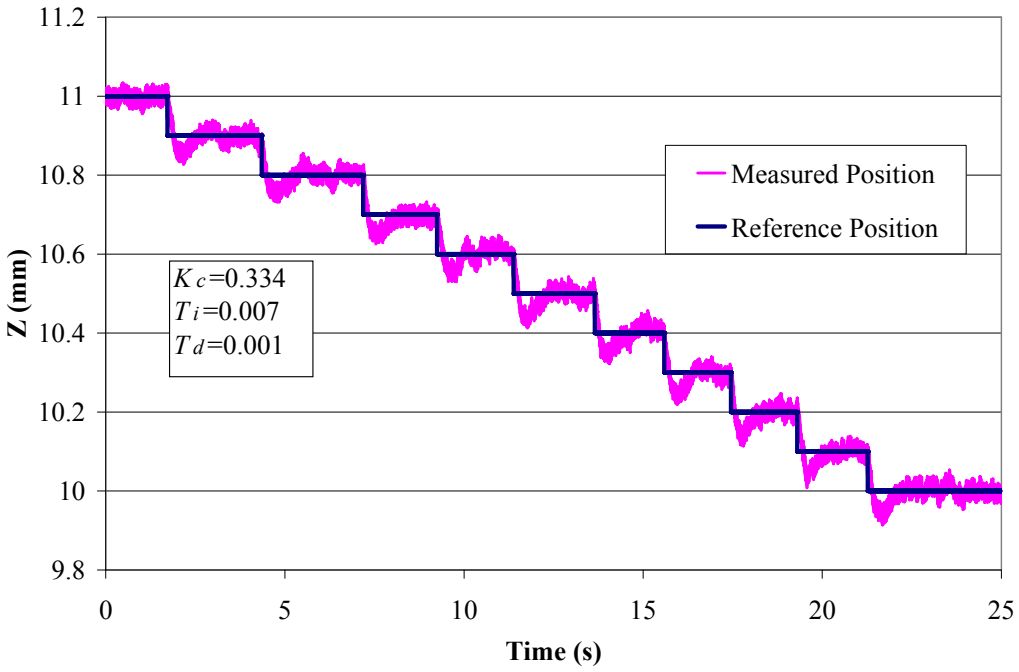

Figure 7-18: Vertical motion of the microrobot at (x,y)=(1,1).

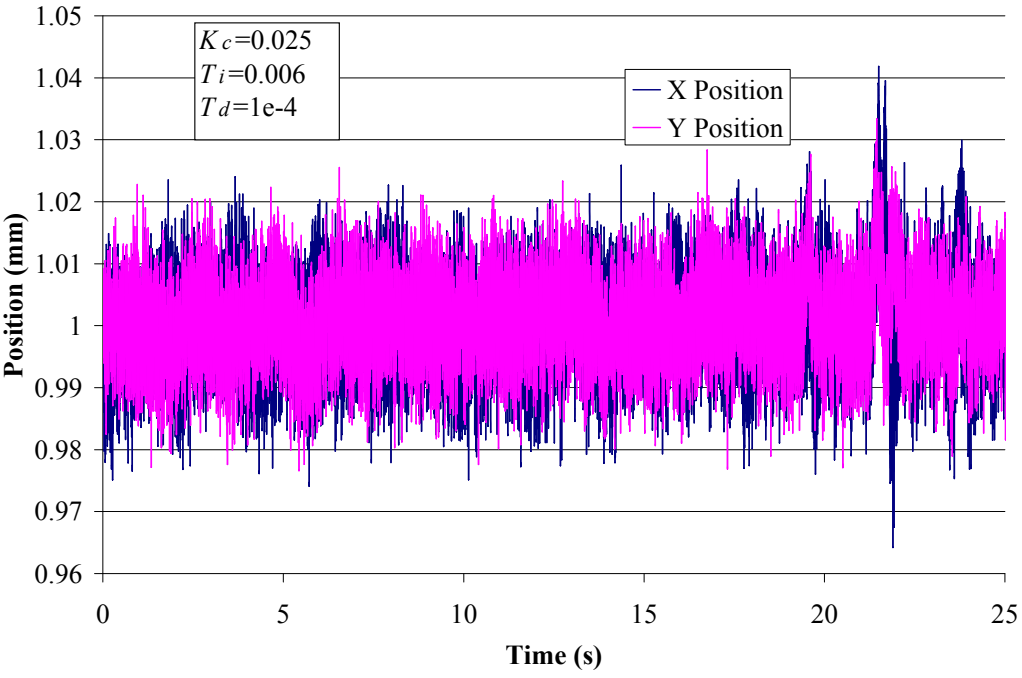

Figure 7-19: Horizontal position of the microrobot during the motion of Figure 7-18.

Figure 5-15. Figure 7-20 demonstrates the levitation of the microrobot with this controller.

Table 7-1 shows that the current experimental setup shows that the system is able to reach the steady state operating point in slightly more than half the time than the setup of [30], offsetting the poorer rise time and overshoot characteristics. There is also a considerable improvement in the steady state RMS position error, which is largely due to improved equipment. Note that the RMS position error of the levitated object is due to both the error of the sensors and the fact that the microrobot is in constant motion about the reference point due to the instability of the open loop plant.

Parameter	Existing Setup	Setup of [30]
T_p (s)	0.2	0.08
T_r (s)	0.102	0.05
T_s (s)	0.846	1.5
% OS	50	32
RMS Error at Steady State (mm)	0.018197	0.090

Table 7-1: Comparison of the vertical performance characteristics between the current experimental setup and the setup of [30] for a step input at (*x*,*y*)=(0,0).

7.2.2 Horizontal Performance

Table 7-2 shows the performance of the horizontal controllers for the existing setup. Comparable data for the setup of [30] is not available. The responses are for a 0.1 mm step input with control parameters K_c=0.025, T_i=0.006, T_d=1x10^{-4} at z=11 mm, shown in Figure 7-21. Figure 7-22 and Figure 7-23 demonstrate the motion of the microrobot along the x and y axes. From Chapter 3, it is known that the standard deviation σ_{lx} on the local x measurement is 0.00542 mm and the standard deviation σ_{ly} on the local y measurement is 0.00838 mm. If the variance on the microrobot radius is neglected, the resulting variances σ_{gx}^2 and σ_{gy}^2 in the global x and y directions due to the coordinate transform is

$$\sigma_{gx}^2 = \sigma_{gy}^2 = \frac{\sigma_{ly}^2 + \sigma_{lx}^2}{2} \tag{7-1}$$

Figure 7-20: Microrobot levitating under PID control at (0,0,6) mm.

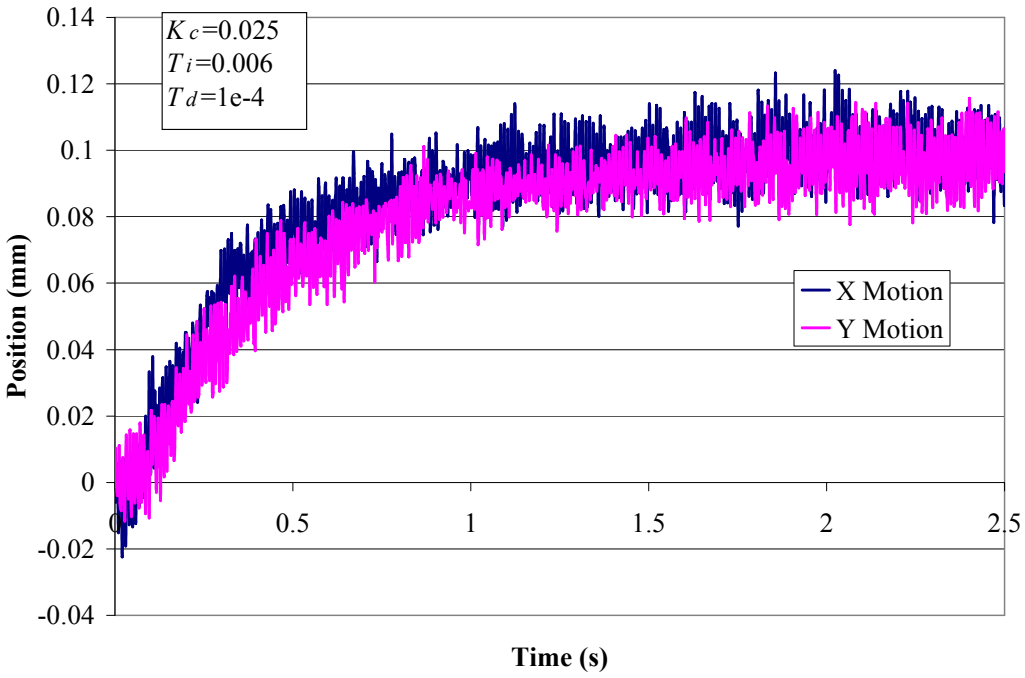

Figure 7-21: 0.1 mm steps in the horizontal direction at x=11 mm.

Parameter	X Position	Y Position
T_r (s)	0.7	0.9
% OS	0	0
RMS Error at Steady State (mm)	0.008228	0.008121

Table 7-2: Horizontal motion performance characteristics under PID control for a step input.

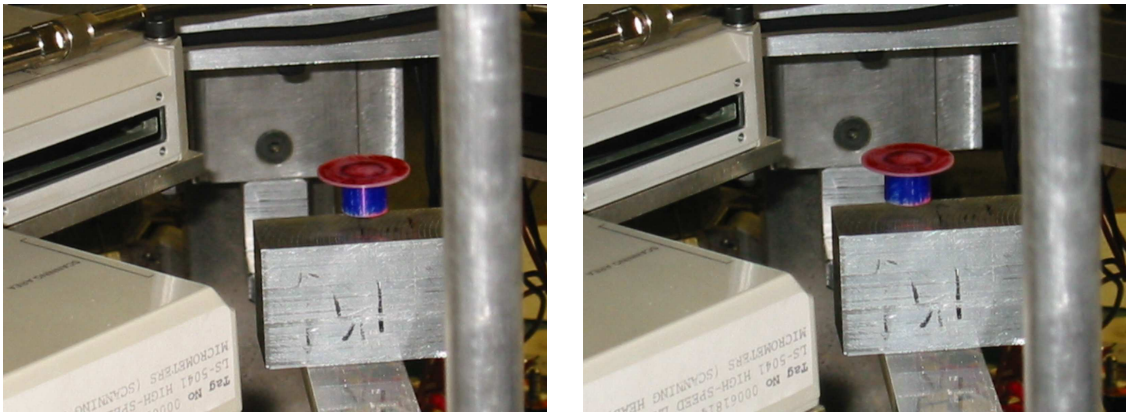

Figure 7-22: Microrobot at (0,0,11) and (9,0,11)

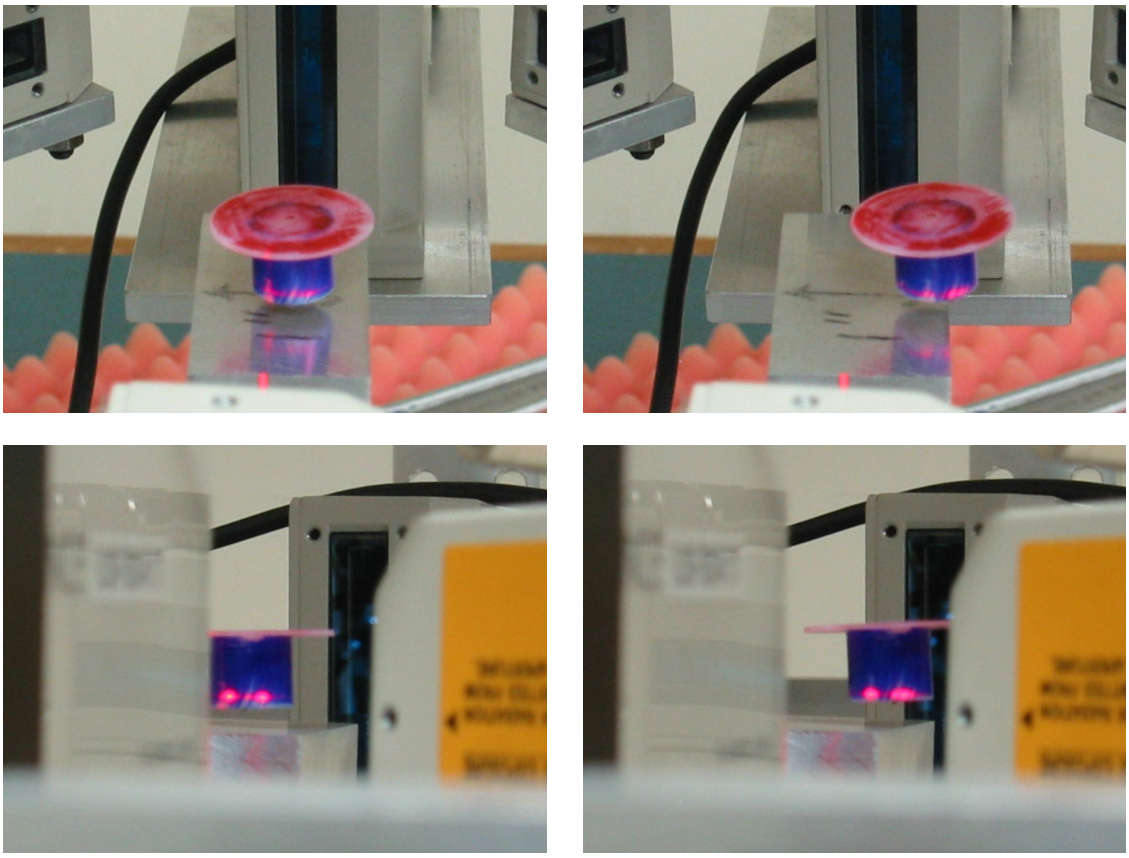

Figure 7-23: Top and side view of the microrobot at (0,0,11) and (0,9,11).

The resulting standard deviation in the global x and y frame will be 0.00706 mm. This is consistent with the RMS of the position errors presented in Table 7-2 considering that disturbance motions during controlled levitation will increase the error.

7.2.3 Range

The vertical range of the microrobot is approximately 30 mm ($0<z<30$). This is consistent with the operating range of [30]. Care must be taken when working near the limits of the range as overshoot may move the microrobot outside of the measurement beam or past the point where the flux density gradient is sufficient for supporting the weight of the microrobot.

The horizontal range of the system depends on the z position of the microrobot. At z=11.5 mm, the x range is approximately 20 mm ($-10<x<10$) and the y range is 22 mm ($-13<y<9$). The asymmetry on the absolute range of y is due the fact that the vertical position laser beam is not perfectly centered on the origin and does not bisect the larger disk on top of the microrobot into equal halves. It should be noted that the diameter of the larger disk on top of the microrobot is 23.4 mm in diameter, and so the y motion is limited due to the requirement that the microrobot remain within the measurement field of the vertical position sensor.

At z=18 mm, the x range is approximately 10 mm ($-5.5<x<4.5$) and the y range is 14 mm ($-7<y<7$). The reduction in range is due to the fact that the current required to keep the microrobot in a stable position increases as z increases. As previously discussed in Chapter 2 the microrobot requires greater shifts in current at higher values of z in order to achieve the same horizontal position that could be obtained at a lower value of z. Due to output current saturation there will be a limit on the maximum current shift, which will result in a reduced range.

It is interesting to note that the range on y is greater than the range on x at both z locations, given that in open loop control the microrobot could move further in x than in y for the same input command. Open loop experimentation had shown that the maximum input value x_{ctrl} was 0.4, while the value of y_{ctrl} was limited to 0.3 to ensure that the microrobot remained in the field. In actuality, the upper limit on y_{ctrl} appears to be on the order of 0.5. Although the

value of n in the horizontal control algorithms could be adjusted to increase the x range, these results suggest that the current value of 1.25 is fairly close to an optimal value that would provide equivalent x and y ranges at the same height z.

Currently the minimum z position for measuring the horizontal position of the microrobot is z=10 mm. Based on the results discussed above it is logical to assume that the horizontal range at lower z values will be greater than at z=10 mm. This could not be investigated in detail due to the need to maintain the experimental setup in the current configuration in order to meet the needs of other students using the apparatus. The horizontal range of [30] is 29 mm x 29 mm and based on the results discussed above it is believed that this range could be reached at some position below z=10 mm.

7.3 Advanced Trajectory Generation

In order to perform useful work the microrobot needs to be capable of navigating complex paths and trajectories. To date the motion of the microrobot has been limited to motion along straight lines coincident with the principle axis or the 45° origin bisector (simultaneous x and y motion). This section will discuss the performance of the microrobot as it traces out a circle in the horizontal plane at a constant height z. The circle trajectory was chosen as it represented a reasonably complex shape for the microrobot to trace out that differentiated from the straight line trajectories, while still being relatively simple to implement.

The circles are generated by first moving the microrobot along the x axis to the desired radial length. The trajectory code computes the reference inputs at time t from

$$x_{ref}(t) = \sqrt{(x_{ref}^2(t-1) + y_{ref}^2(t-1))}\cos\theta(t) \tag{7-2a}$$

$$y_{ref}(t) = \sqrt{(x_{ref}^2(t-1) + y_{ref}^2(t-1))}\sin\theta(t) \tag{7-2b}$$

where x_{ref} and y_{ref} are the reference inputs and θ is the reference angle. The reference angle starts at 0° is incrementally increased at each time step. The value of this $\Delta\theta$ is computed by multiplying the desired rotational velocity by the sampling time T_s. The rotational velocity

itself is calculated by dividing the number of revolutions to be performed by the desired runtime of the experiment.

Figure 7-24 shows the resultant path traced by the microrobot for a radius of 0.5 mm and a rotational velocity of 0.16 rad/s. The path traced by the microrobot is somewhat smaller than the reference. This is to be expected, since the circle trajectory represents a sinusoidal input on both the *x* and *y* axes. Figure 7-25 shows the time response for the *x* and *y* axis, which demonstrates the phase lag of the system. In Figure 7-24 it can be seen that there is more deviation in the first and third quadrants than in the second and fourth quadrants. Inspection of Figure 7-25 shows that when the microrobot is near an amplitude peak, the variance on the position tends to increase. When the microrobot is in quadrants 2 and 4 the microrobot tends to be at points in its trajectory where the variance is minimized, which is why the deviation from the expected trajectory is more noticeable.

Figure 7-26 shows the vertical position of the microrobot during the motion. The microrobot is able to remain at a reasonably constant position over the course of the trajectory. The RMS deviation of the position error is 0.025647 mm. The RMS position error with no horizontal motion is 0.018197 mm, which shows that the deviation of the microrobot from the vertical reference position is greater in the case where horizontal motion occurs.

Figure 7-27 shows the trajectory plot for a circle with a radius of 3 mm and a rotational velocity of 0.16 rad/s. The motion of the microrobot is much more haphazard than in Figure 7-24. Figure 7-28 shows that the *z* position of the microrobot also varies significantly as the microrobot moves around the desired path. The RMS error on the position is 0.0439 mm, which is almost 1.8 times greater than the RMS error when the radius of the circle was 0.5 mm. The large source of the error seems to be related to the tangential velocity of the microrobot. The tangential velocity of the microrobot when it is tracing the 1 mm diameter circle is 0.08 mm/s, while the tangential speed for the 6 mm diameter circle is 0.48 mm/s. The relatively fast motion of the microrobot may make it difficult to track the rapidly changing position, resulting in a relatively poor response.

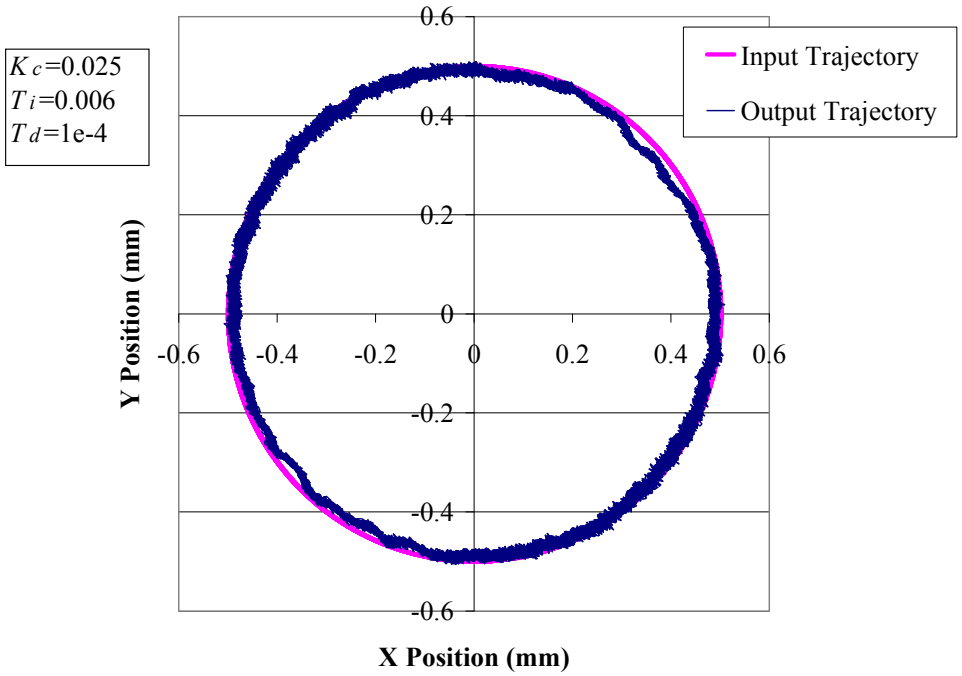

Figure 7-24: 1 mm diameter circle trajectory traced by the microrobot with a rotational velocity of 0.16 rad/s.

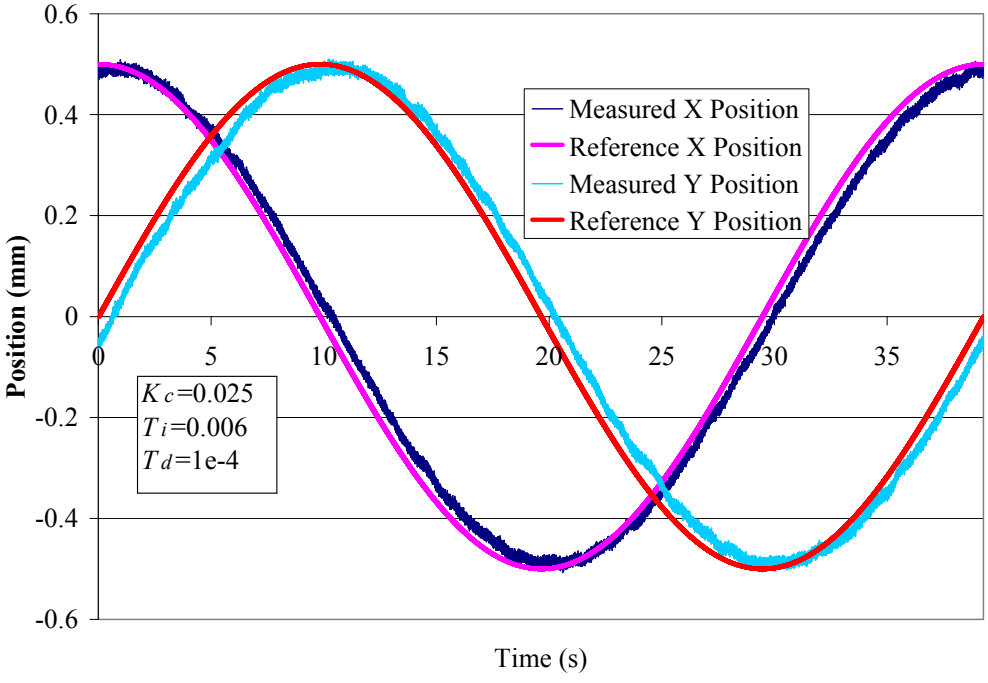

Figure 7-25: Motion in the *x* and *y* axes over time from Figure 7-24.

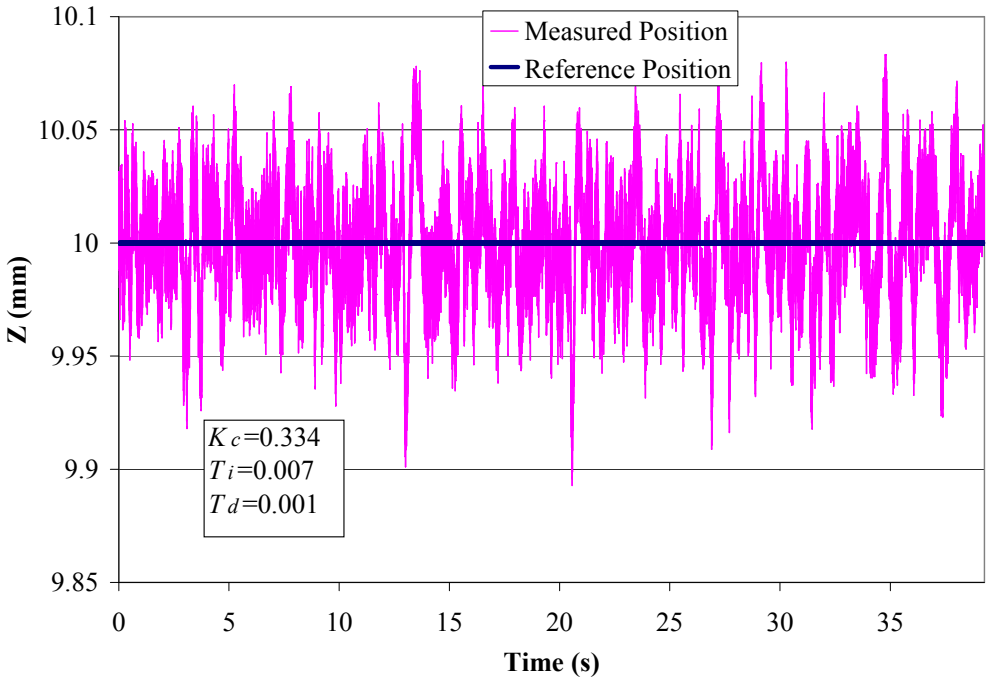

Figure 7-26: Vertical position of the microrobot during the trajectory of Figure 7-24.

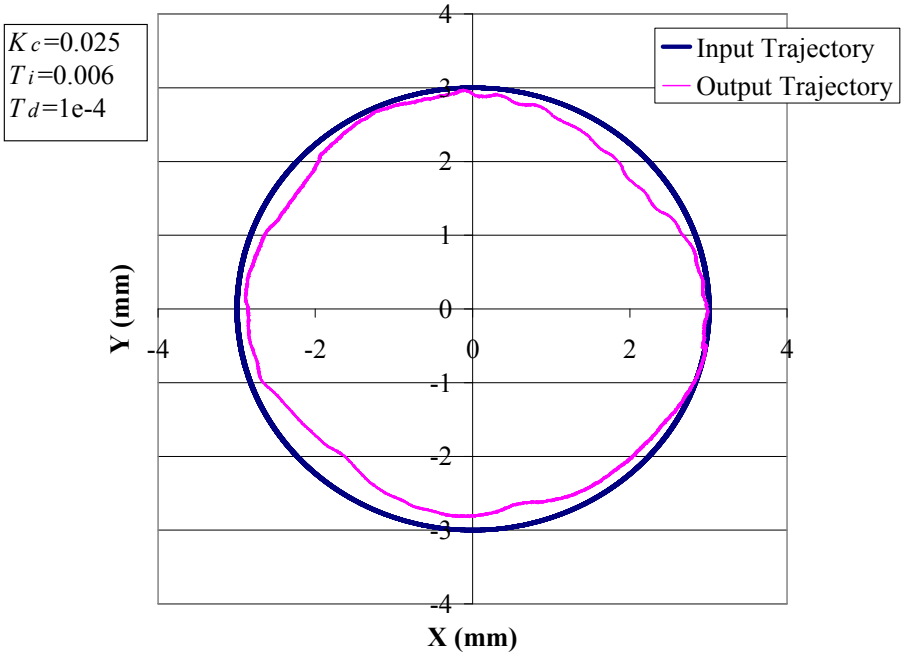

Figure 7-27: 6 mm diameter circle trajectory traced by the microrobot with a rotational velocity of 0.16 rad/s.

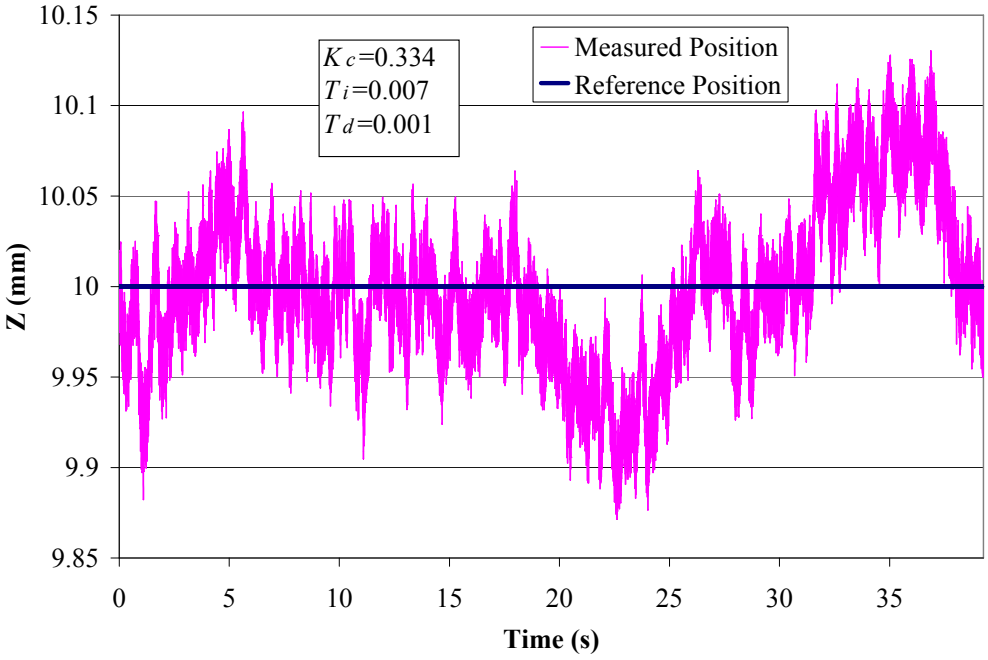

Figure 7-28: Z position from the trajectory of Figure 7-27.

Figure 7-29 shows the trajectory plot for a half-circle with a radius of 3 mm. The rotational velocity is 0.0502 rad/s. Due to the relatively low rotational velocity only half of a circle was plotted in order to keep the size of the data file manageable. The figure shows that the reduction in the rotational velocity has yielded a smoother trajectory that shows a relatively constant decrease in the radius of the circle. Figure 7-30 shows the corresponding *z* position. Aside from one unexplained disturbance, the z position of the microrobot does not deviate as much from the reference position. The RMS error, including the disturbance, is 0.029 mm, and the RMS error for data points just prior to the disturbance is 0.0243 mm. Even with the disturbance motion included it can be seen that a reduction in the rotational velocity has resulted in a reduction in the RMS error.

In order to improve the position tracking of the microrobot more advanced control strategies (such as feed-forward control) need to be developed.

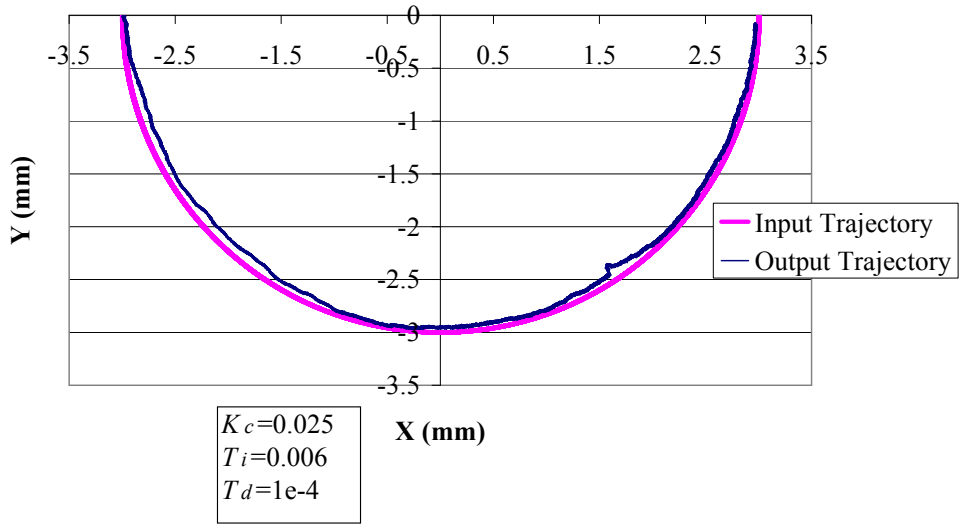

Figure 7-29: 6 mm diameter half-circle trajectory traced by the microrobot with a rotational velocity of 0.0502 rad/s.

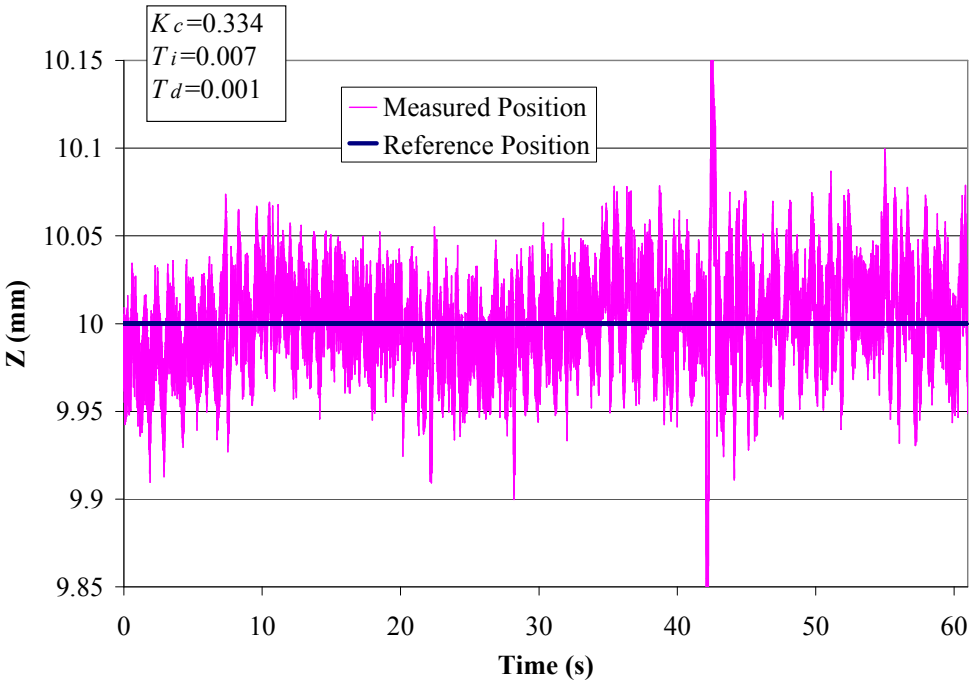

Figure 7-30: Measured z position for Figure 7-29.

7.4 Advanced Vertical Position Control – LQR Design

The vertical position controllers developed to date have all been PID controllers. In order to improve on the PID system performance and test the performance of the vertical system model under different control conditions it is desired to develop a different type of controller for the system. It was decided to design a state feedback controller using the state space realization of the system model. For a continuous state space model

$$\dot{x} = Ax + Bu \tag{7-3a}$$

$$y = Cx + Du \tag{7-3b}$$

The optimal feedback gain matrix k for $u = -kx$ is found by minimizing the cost function

$$\int_{t_o}^{\infty} (x^T Qx + u^T Ru)dt \tag{7-4}$$

In general $k = R^{-1}B^t P$ where the value of P is solved via the Algebraic Riccati equation

$$A^T P + PA + PBR^{-1}B^T P + Q = 0 \tag{7-5}$$

The goal to finding k is to change the values in matrices Q and R until the desired system performance is achieved. This controller is known as a linear quadratic regulator (LQR) [53]. In addition to providing optimal control for a state space model, there are several design tools available in MATLAB that allow for rapid design of the controller.

From Chapter 5, the discrete transfer function of the model is

$$\frac{Y}{U} = \frac{Z}{I} = \frac{-0.03z + 0.0298}{z^2 - 1.915z + 0.9141} \quad T_s = 2\text{x}10^{-3}\ \text{s} \tag{7-6}$$

In order to design the regulator it is necessary to convert the transfer function to a continuous state space realization. The equivalent zero order hold continuous time model is

$$\frac{Z}{I} = \frac{-15.63s - 50.97}{s^2 + 44.94s - 248.3} \tag{7-7}$$

In principle the regulator is designed to eliminate disturbances at a specified equilibrium point. Therefore, it is appropriate to talk about the model in terms of the change in the input

and output instead of in absolute terms. Since the model is already linear this does not change the transfer function in any way.

$$\frac{Z - Z_{ref}}{I - I_{ref}} = \frac{\Delta Z}{\Delta I} = \frac{-15.63s - 50.97}{s^2 + 44.94s - 248.3} \tag{7-8}$$

The state-space realization is

$$A = \begin{bmatrix} -44.94 & -248.3 \\ 1 & 0 \end{bmatrix} B = \begin{bmatrix} 1 \\ 0 \end{bmatrix} \; C = \begin{bmatrix} -15.63 & -50.97 \end{bmatrix} D = 0 \tag{7-9}$$

In order to ensure that the system has zero steady-state error, it is necessary to introduce a third state into the model. This third state is equal to the output Δz. This provides the system with a form of integral control since the state space model now integrates the error over time.

$$A = \begin{bmatrix} -44.94 & -248.3 & 0 \\ 1 & 0 & 0 \\ -15.63 & -50.97 & 0 \end{bmatrix} B = \begin{bmatrix} 1 \\ 0 \\ 0 \end{bmatrix} \; C = \begin{bmatrix} -15.63 & -50.97 & 0 \end{bmatrix} D=0 \tag{7-10}$$

Now that the equivalent state matrices have been discovered the system can be converted back to discrete time. The equivalent discrete time matrices A_d and B_d are

$$A_d = \begin{bmatrix} 0.9145 & 0.4750 & 0 \\ 0.0019 & 1.0005 & 0 \\ -0.03 & -0.1095 & 1 \end{bmatrix} B_d = \begin{bmatrix} 0.0019 \\ 0 \\ 0 \end{bmatrix} \; T_s=2\text{e-}3 \tag{7-11}$$

In order to determine the required gain matrix k, the 'lqrd' command is used in MATLAB. The inputs to this command are the continuous time state matrices A and B, the weighting matrices Q and R, and the sampling time T_s. The weighting matrices are chosen through trial and error as

$$Q = \begin{bmatrix} 5000 & 796.64 & 0 \\ 796.64 & 5000 & 0 \\ 0 & 0 & 10000 \end{bmatrix} \qquad R = 1x10^{-10} \tag{7-12}$$

The resulting feedback matrix is

$$k = [627.22 \quad 2306 \quad -914.07] \tag{7-13}$$

The values of Q and R were chosen in order to preserve the response time of the controller as shown in Table 7-1, while reducing the overshoot to approximately 12%.

Two of the three states required for feedback control have no physical meaning due to the fact that the state space model is a transfer function realization. A Kalman state estimator is required to estimate states x_1 and x_2 [54]. MATLAB also provides several design tools that aid in the design of a state estimator.

For a discrete time system with disturbance noise w and measurement noise v

$$x[n] = A_d x[n-1] + B_d u[n-1] + w[n-1] \tag{7-14a}$$

$$y[n-1] = Cx[n-1] + Du[n-1] + v[n-1] \tag{7-14b}$$

MATLAB provides an optimal Kalman state estimator of the form

$$\hat{x}[n \mid n-1] = A_{est}\hat{x}[n-1 \mid n-2] + B_{est}\begin{bmatrix} y[n-1] \\ u[n-1] \end{bmatrix} \tag{7-15a}$$

$$\begin{bmatrix} \hat{y}[n-1 \mid n-1] \\ \hat{x}[n-1 \mid n-1] \end{bmatrix} = C_{est}\hat{x}[n-1 \mid n-2] + D_{est}\begin{bmatrix} y[n-1] \\ u[n-1] \end{bmatrix} \tag{7-15b}$$

The state estimator only estimates states x_1 and x_2. State x_3 is unobservable and so it must be calculated directly from Δz.

$$x_3[n] = x_3[n-1] + T_s * \Delta z[n-1] \tag{7-16}$$

Based on the RMS error of Table 7-1 the measurement variance v is estimated as $4\text{x}10^{-4}$ mm^2. It was unclear what the magnitude of the state disturbance values w should be, and so it was assumed that the disturbance noise was equal to the system noise, i.e. $4\text{x}10^{-4}$ mm^2. The MATLAB command 'kalmd' is used to estimate the discrete version of the filter based on the continuous time state space equation, the sampling time T_s, and the variance of the disturbance and measurement noise. The resulting state estimation matrices are detailed in (7-17).

The LQR controller is designed to minimize disturbances about an equilibrium point. Therefore a weight compensation algorithm is needed to calculate the equilibrium current

$$A_{est} = \begin{bmatrix} 0.8989 & 0.4224 \\ -0.000495 & 0.9926 \end{bmatrix} B_{est} = \begin{bmatrix} 0.001913 & -0.001032 \\ 1.942e-6 & -0.0001541 \end{bmatrix}$$

$$C_{est} = \begin{bmatrix} -15.25 & -49.74 \\ 0.9836 & -0.05349 \\ -0.002376 & 0.9923 \end{bmatrix} D_{est} = \begin{bmatrix} 0 & 0.02415 \\ 0 & -0.001049 \\ 0 & -0.000152 \end{bmatrix} \quad T_s\text{=2e-3} \qquad (7\text{-}17)$$

i_{ref} (A) at equilibrium position z_{ref} (mm) that will theoretically support the weight of the microrobot, with the controller providing the necessary current variations required to actually levitate the microrobot. Based on current readings from the amplifier while the vertical position of the microrobot is under PID control the required equilibrium current in each electromagnet is

$$i_{ref} = 0.0343 z_{ref} + 1.215 \qquad (7\text{-}18)$$

From the amplifier gain discussion of Chapter 3, the required equilibrium voltage output u for each electromagnet is

$$v_{ref} = (0.0343 z_{ref} + 1.215) / 0.355 \qquad (7\text{-}19)$$

7.4.1 Modeling and Simulation

One of the issues discovered during the implementation of this controller is that the input current on the discrete model does not correspond to the measured input current. This discrepancy is due to the fact that only part of the model could be identified, based on the reference and measured position. The current signal was deemed to be too noisy to identify the dynamics describing the relation between the current and the reference position. By identifying these dynamics the system model can be improved and it will be possible to implement a more accurate controller and state estimator.

Another issue with the model is that it is a state space realization of a SISO transfer function. Since the states do not have any physical meaning it is difficult to determine the accuracy of the estimated states, and determine the magnitude of the disturbances that may

be acting on the states. Ideally the state space model in the future can be derived directly from the dynamic model, so that states like position, velocity, and acceleration can be used.

Figure 7-31 shows the control schematic of the system. There are two differences between the simulated model and the actual system implementation. For the model the weight compensation algorithm is

$$i_{ref} = 4.8178 z_{ref} \tag{7-20}$$

The control signals for x_1 and x_2 used in the model are based on $\hat{x}[n-1 \mid n-1]$, as this is the output of the Kalman state estimator. On the real system the actual control signals used are $\hat{x}[n \mid n-1]$ since it was found that the system could not be stabilized using $\hat{x}[n-1 \mid n-1]$. Technically using $\hat{x}[n \mid n-1]$ is more correct since it is an estimate of the current state, and the value of x_3 is also always a measure of the current state of the system.

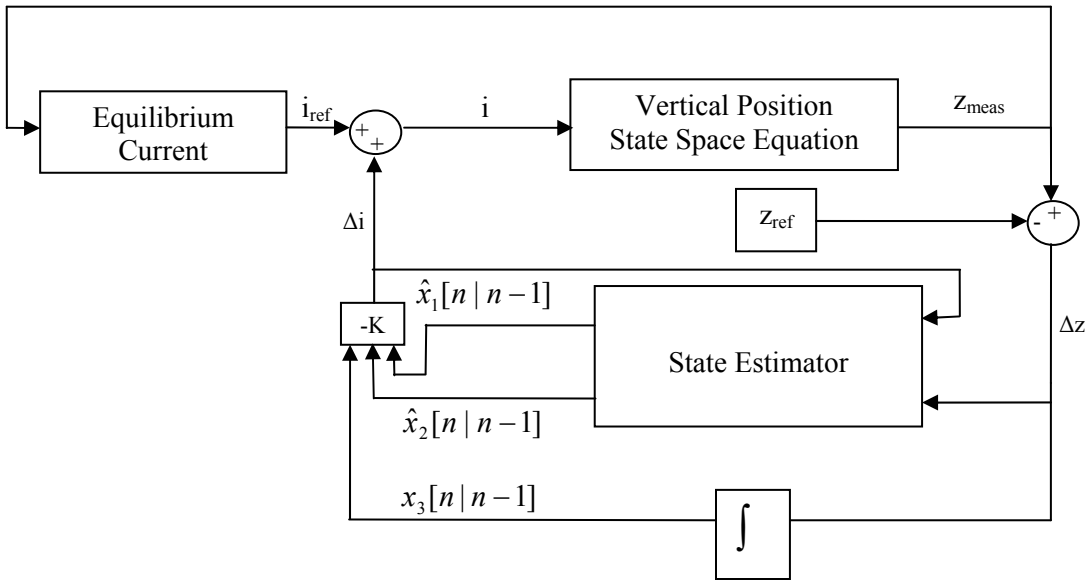

Figure 7-31: Control Schematic of the LQR Regulator.

Implementation of the controller proved to be difficult. It was found that the system could not be stabilized without the aid of the aluminium block. The response characteristics of the system were also found to be quite poor. Figure 7-32 compares the measured position of the microrobot versus the position of the microrobot predicted by the model. It can be seen that

the response is considerably underdamped when compared to the model. The damping shown in Figure 7-32 was optimized by dividing the control signal u=-kx by 0.69 before adding it to the output control voltage. It was also determined that using the current position z_{meas} instead of z_{ref} to calculate the equilibrium current produced a faster transient response. Based on these modifications the effective electromagnet input voltage is

$$v = \frac{(0.0343 z_{meas} + 1.215)}{0.355} - \frac{kx}{0.69} \tag{7-21}$$

Figure 7-33 and Figure 7-34 compares the measured values of $\hat{x}_1[n-1 \mid n-1]$ and $\hat{x}_2[n-1 \mid n-1]$ to the model values predicted by the system. It appears as though the magnitudes of the states are correct, although this may simply be due to the nature of the state estimator.

The microrobot can only move about 1 mm way from the aluminium block before the system goes unstable. This operating range is quite poor when compared to the 30 mm range of the PID controller. Table 7-3 lists the performance characteristics of the regulator and compares them with the response characteristics of the PID controller. The transient characteristics of the LQR controller are quite poor, with double the overshoot of the PID controller and a settling time that is 15 times greater than the rise time (versus a ratio of 8.5 for the PID controller). It can be seen that the RMS of the steady state position error is significantly lower than for the PID controller. It should be noted that the RMS calculation for the PID controller was performed with the microrobot at the same position relative to the aluminum block as during the LQR response. In this case the microrobot's position is z=12.9 mm, which is 0.6 mm above the aluminium block. This suggests that the regulator is better suited to minimizing the steady-state oscillations of the system. Recall that the standard deviation of a static measurement made by the vertical position sensor is approximately 0.01 mm, which indicates that the variance of the microrobot due to oscillating control is relatively small. Due to the fact that the system is unstable without the aid of the aluminium block the RMS error has a tendency to increase as the microrobot moves further away from the block, as shown in Table 7-4.

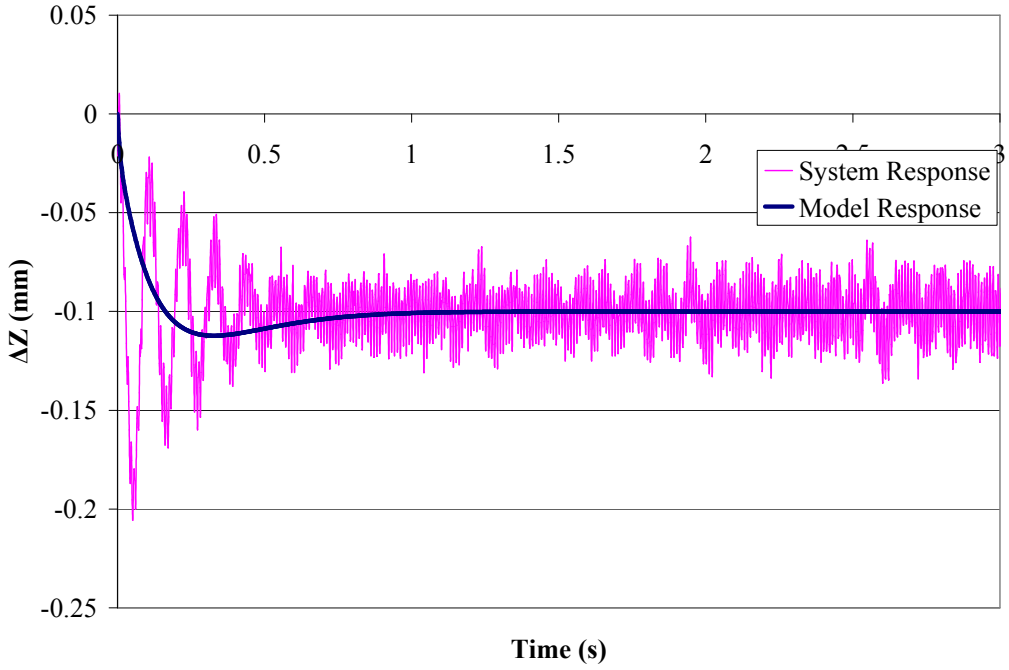

Figure 7-32: Comparison of the system response to the model response for a -0.1 mm step change from z=13 mm to z=12.9 mm.

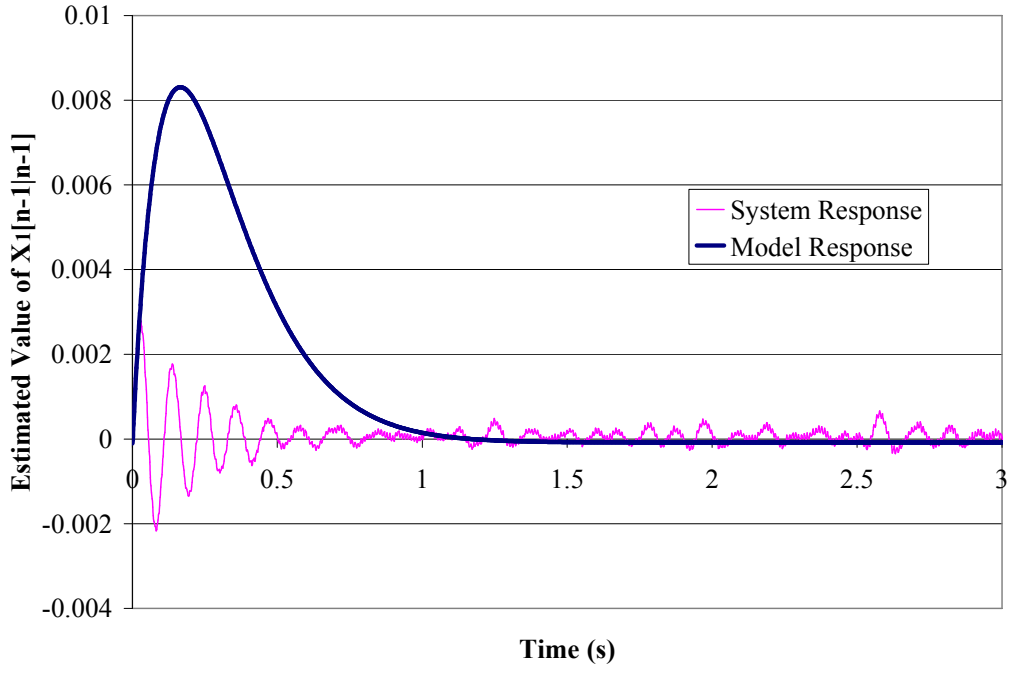

Figure 7-33: Value of $\hat{x}_1[n-1 \mid n-1]$ for the response of Figure 7-32.

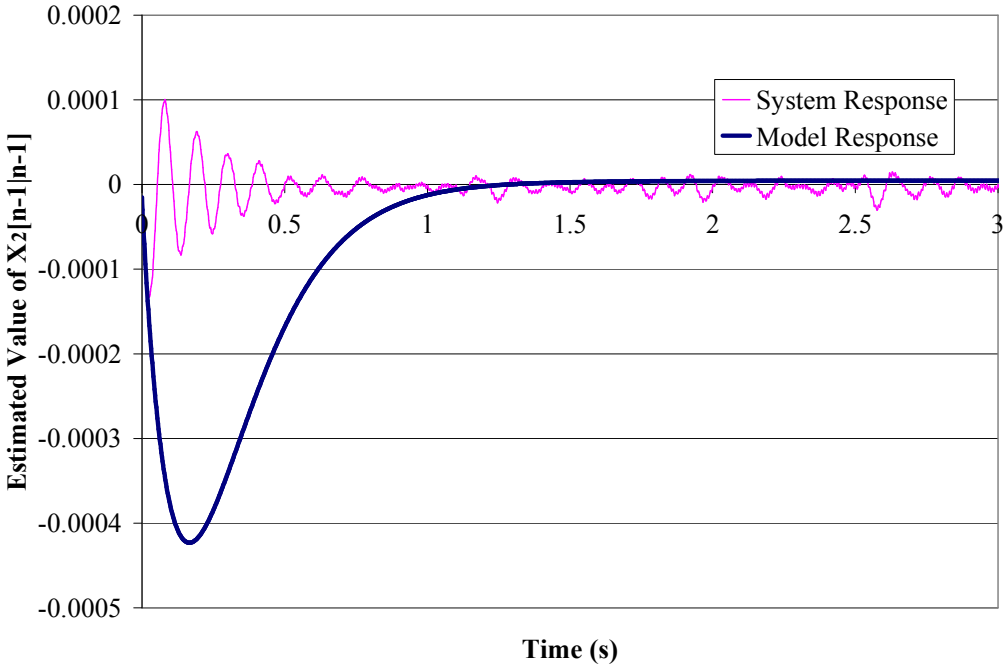

Figure 7-34: Value of $\hat{x}_2[n-1 \mid n-1]$ for the response of Figure 7-32.

Parameter	PID Control (K_c=0.334, T_i=0.007, T_d=0.001)	LQR Control k=[627.22 2306 -914.07]
T_p (s)	0.2	0.0502
T_r (s)	0.102	0.034
T_s (s)	0.846	0.5
Overshoot	50%	100%
RMS Error at Steady State (mm)	0.0192 mm	0.014 mm

Table 7-3: Comparison of the vertical performance characteristics between the PID controller and the LQR controller.

Height Above Aluminium Block (mm)	RMS Position Error (mm)
0.5	0.0139
0.6	0.0143
0.7	0.0148
0.8	0.0151
0.9	0.0189

Table 7-4: RMS error due to LQR control as position above the aluminium block changes.

Figure 7-35 and Figure 7-36 show the position of the microrobot during a series of horizontal motions. Figure 7-37 and Figure 7-38 show the comparable motions under PID control. The LQR controller does a better job of maintaining the vertical position of the microrobot when compared to the PID controller. The RMS of the position error is 0.0132 for the LQR controller and 0.0205 for the PID controller. Based on these results, the LQR regulator has demonstrated potential for minimizing the variance in the *z* position of the microrobot. Further refinement of the controller and, by extension, the system model is needed to improve the transient characteristics of the system.

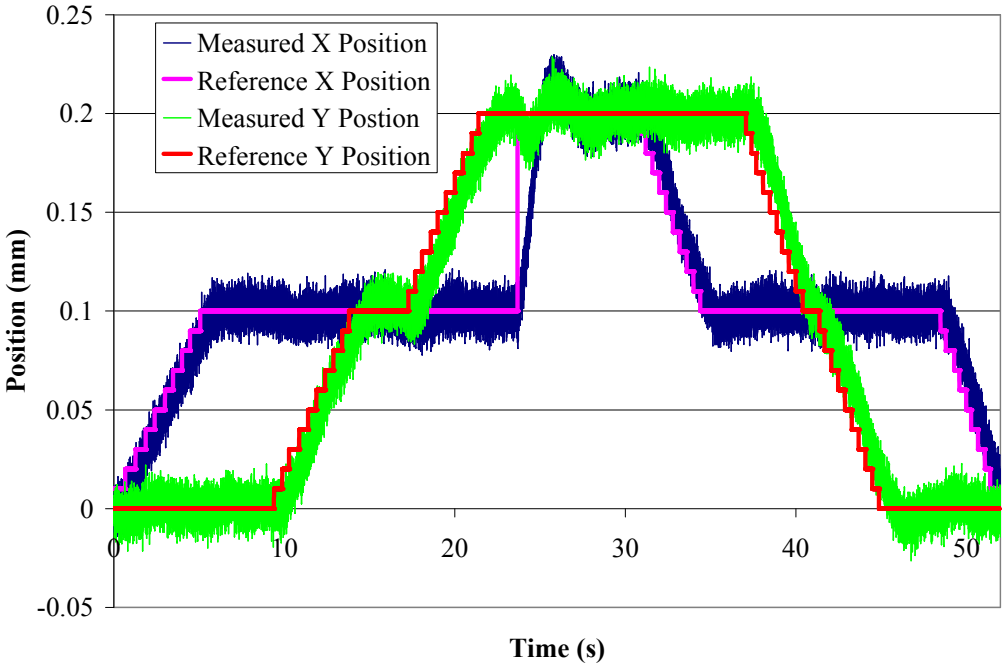

Figure 7-35: Horizontal motion with the LQR Controller.

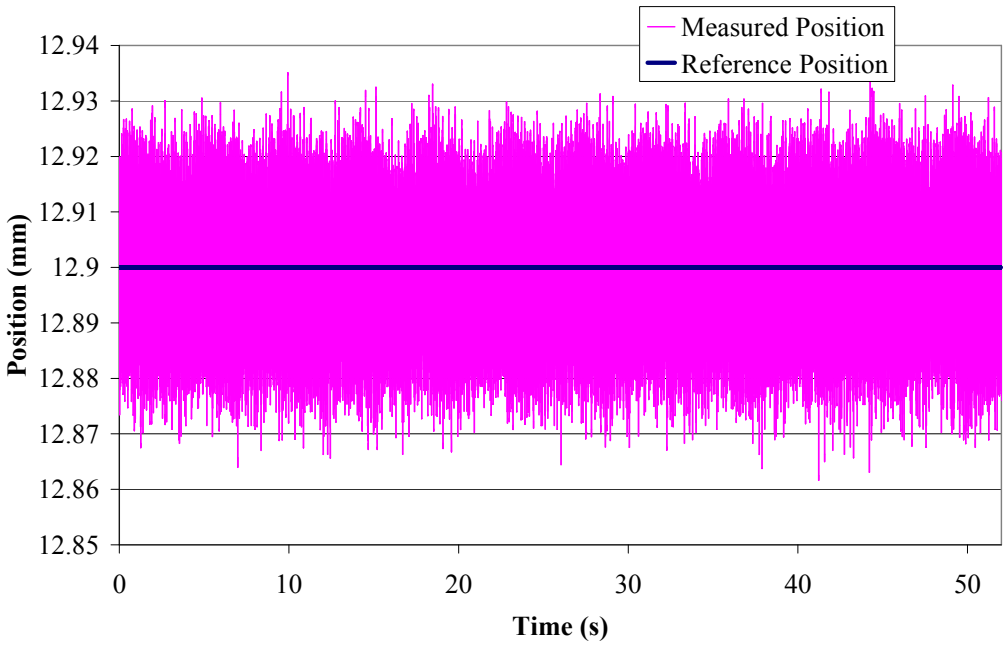

Figure 7-36: Vertical position of the microrobot during horizontal motion with LQR control.

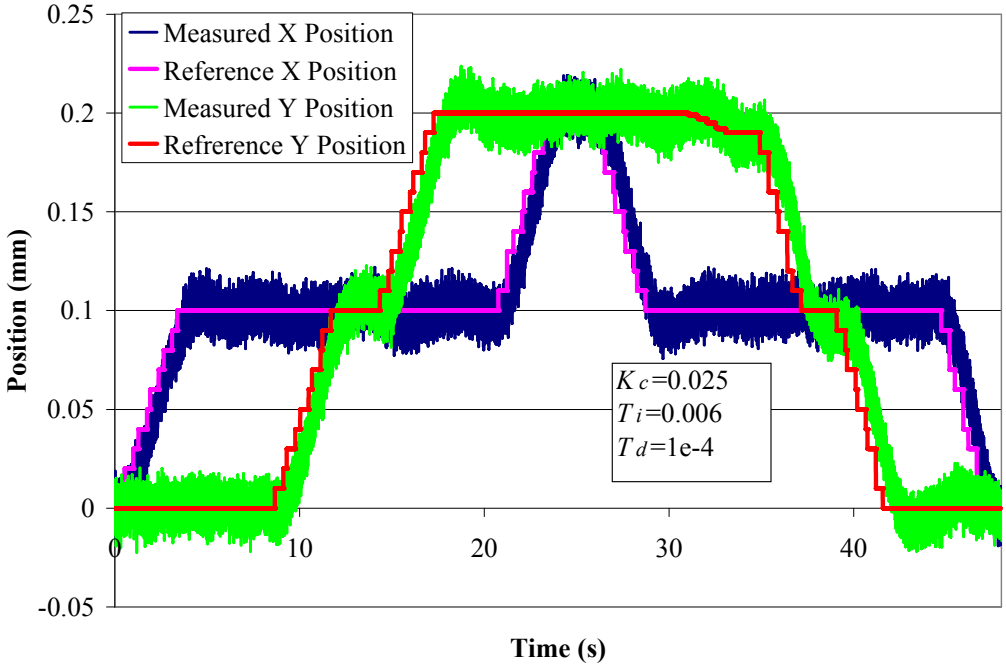

Figure 7-37: Horizontal motion with a PID controller.

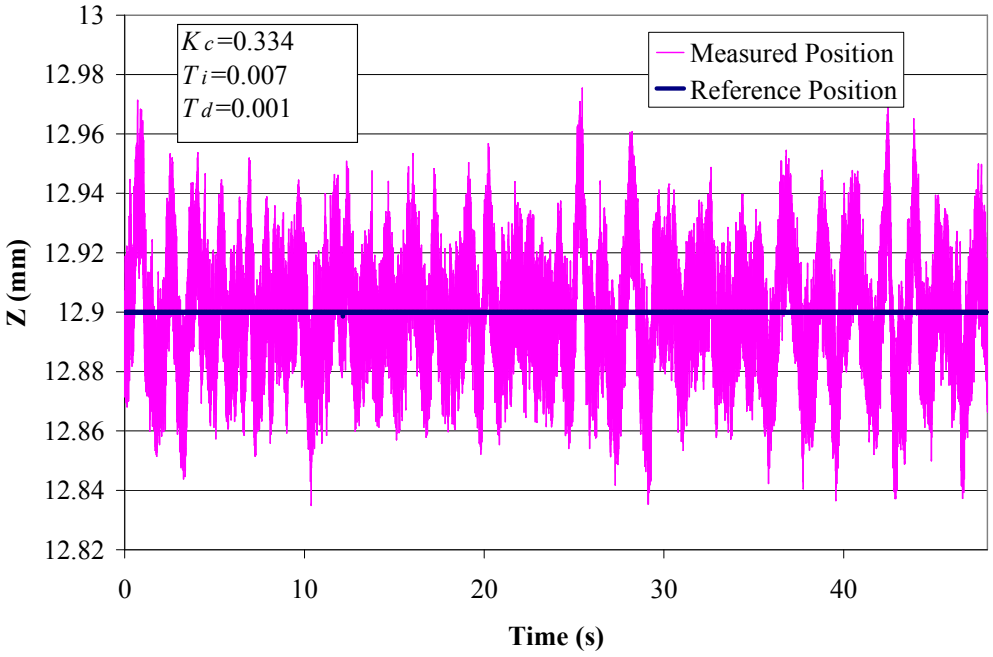

Figure 7-38: Vertical position of the microrobot during horizontal motion with PID control.

Chapter 8
Conclusions and Recommendations

8.1 Conclusions

Large gap magnetic suspension systems have shown promise for use in microrobotic applications such as clean room operations, pipe inspection, and surgical operations. The magnetic field used to levitate a magnetic object in the workspace is produced by a series of electromagnets attached to a pole piece. The pole piece acts to unify the individual poles of the electromagnets in order to produce a unique point in a given horizontal plane where the magnetic force will counteract the weight of the microrobot. Vertical motion is achieved by changing the amount of power input to each electromagnet by an equal amount. Horizontal motion is achieved by varying the amount of power each electromagnet receives. Provided the total input power is kept constant the horizontal motion will occur at the same vertical point.

One of the challenges in modeling the dynamics of the system is estimating the force produced by the magnetic drive unit. With the aid of a finite element simulation of the magnetic drive unit attempts were made to derive an analytical equation to describe the force produced by one electromagnet attached to the magnetic drive unit. For a simplified 2D simulation these equations were of the form

$$F_z = (m(x)z + b(x))\frac{I}{I_0} \tag{8-1}$$

$$F_x = \frac{-II_0L_0}{2b\left(1+\frac{z}{a}+\frac{(x-x_0)}{b}\right)^2} + c\frac{I}{I_0} \tag{8-2}$$

where $F_{z\ \text{is}}$ the vertical force, $m(x)$ and $b(x)$ are slope and intercept parameters that are a function of the horizontal position x, L_o, a, b and c are constants, z is the vertical position of the microrobot, I is the current in the electromagnet, I_0 is the current at which the constants were identified and x_0 is the distance to the edge of the pole piece where the electromagnet is

located. It was found that these formulas were able to predict the general trend of the force profiles. Superposition could be used to find the resultant force for several electromagnets, but it was found that the small errors in the estimation for one electromagnet would compound as more electromagnets were added. Attempts were made to extend the analysis to a 3D model of the magnetic drive unit, but parameter estimation proved difficult due to the high non-linearity of the analytical equations and the addition of the *y* dimension. The 3D model also requires a significant amount of computational power to solve, which limits the resolution of the output.

The black box model describing the vertical motion of the system *z* due to the input current *i* is

$$\frac{Z}{I} = \frac{-0.03z + 0.0298}{z^2 - 1.915z + 0.9141} \quad T_s = 2\text{x}10^{-3}\ \text{s} \tag{8-3}$$

Due to the unstable nature of open loop vertical position control, the model was estimated by tuning the gain on a PID controller and observing the motion of the closed loop poles from the identified models on a root locus chart. Other closed loop identification techniques could not be used as it could not be determined if the input voltage to the current amplifier was a noisy signal or if the large current fluctuations were significant, and at the time no means were available to measure the current directly. The system model tended to provide a reasonable approximation of the system response for various PID controllers under various input conditions. Some of the responses suggested that some slight parameter tweaking may still be necessary, or that the dynamic model may change depending on whether the microrobot is moving towards or away from the pole piece. Further improvements in the system model could be made by including the dynamics of the input current.

Horizontal motion of the microrobot is achieved by placing an aluminium block beneath the microrobot. It is presumed that the eddy currents in the block act to minimize the lateral disturbance oscillations of the microrobot, making it easier to identify the open loop characteristics of the horizontal motion. The aluminium block is also used for closed loop horizontal motion as it was found that the disturbance oscillations could not be damped out by the controller.

Open loop horizontal motion of the microrobot is characterized by a non-linear hysteresis response. Motion in the *x* direction is achieved by changing the currents in all six electromagnets, while motion in the *y* direction is achieved by changing currents in four of the electromagnets. For motion in the *x* direction a scaling factor *n* is used so that the current in the outermost electromagnets are changed by a greater amount in order to increase the open loop *x* range. It was found that for a given control signal input the microrobot would move further in *x* than in *y*, but that the maximum value for the *y* control signal was 0.5 while the maximum *x* control signal was 0.4. For a given value of n=1.25 this allowed the microrobot to have the same approximate range in both the *x* and *y* directions.

The open loop response of the system can be characterized by either a first or second order system model describing the position (x,y) based on a control value (x_{ctrl},y_{ctrl}) that changes the current in each electromagnet . The second order models are

$$\frac{x}{x_{ctrl}} = \frac{8.764\times10^{-4}}{z^2 - 1.9878z + 0.98782} \quad T_s=2\text{x}10^{-3}\text{ s} \tag{8-4a}$$

$$\frac{y}{y_{ctrl}} = \frac{6.214\times10^{-4}}{z^2 - 1.9877z + 0.98779} \quad T_s=2\text{x}10^{-3}\text{ s} \tag{8-4b}$$

while the first order models are

$$\frac{x}{x_{ctrl}} = \frac{0.0686}{z - 0.9956} \quad T_s=2\text{x}10^{-3}\text{ s} \tag{8-5a}$$

$$\frac{y}{y_{ctrl}} = \frac{0.0487}{z - 0.9959} \quad T_s=2\text{x}10^{-3}\text{ s} \tag{8-5b}$$

In both cases the characteristic equations for *x* and *y* are extremely similar, suggesting that the same controller could be used on the *x* and *y* axes. For a PD controller the second order model provided a better estimate of the rise time of the system, but the response was more oscillatory. On the real system it is expected that this low damping will not be observed if the dipoles of the microrobot are spread out over the horizontal equilibrium area, as finite element methods have shown that the applied horizontal force is generally less than the applied vertical force, and as the microrobot approaches the new equilibrium point the

decrease in the applied force and the retarding motion of the aerodynamic drag will act to minimize the overshoot and oscillations.

On the real system it was observed that PD control of the system did not provide zero steady state error tracking and did not completely eliminate the hysteresis effects observed in open loop control. PID control was successfully implemented in order to eliminate the hysteresis error and provide zero steady state tracking error. In order to minimize large integral control values during system startup the system must first be stabilized at the origin with a PD controller before adding in the integral control. It was found that the integral time constant predicted by simulating the closed loop model response would result in a significantly slower system response. The model integral time constant could be tuned to achieve a model response that was equivalent to the system response. The resulting ratio of system integral time constant to model integral time constant could be used to convert an estimated integral model time constant to system integral constant and vice versa. This ratio is dependent on the value of the proportional gain and the derivative gain. Because the x and y models were derived independently of each other controller gains that work during single axis control may not work when attempting to control the position on both the x and y axis.

Full spatial PID control of the system was achieved using a microrobot prototype consisting of one cylindrical 10 mm x 10 mm neodymium magnet with a remnant flux density of 1.3 T. For a 1 mm step input the vertical PID controller K_c=0.334, T_i=0.007 T_d=0.001 demonstrated 50% overshoot and a settling time of 0.846 s. In the horizontal direction at z=11 mm the x and y 0.1 mm step input responses with PID controller K_c=0.025, T_i=0.006, T_d=1x10^{-4} had rise times of approximately 0.8 seconds and displayed zero overshoot. The rise time will increase as z increases. The vertical range of the microrobot is approximately 30 mm. The horizontal xy range at z=11.5 mm is 20 x 22 mm and the xy range at z=18 mm is 10 x 14 mm. The reduction in range is due to the fact that larger changes in current are required to move the microrobot horizontally when it is further away from the pole piece, and so the microrobot will not move as far before the saturation limits

are reached. The total input current i_{tot} to the system at a given height z is estimated from

$$i_{tot} = 6(0.0343z + 1.215) \tag{8-6}$$

During vertical motion at the origin the RMS position error on the vertical position is 0.018 mm and the RMS error on the horizontal position is 0.008 mm. The relatively large RMS error on the vertical position appears to be due to vibration effects caused by the sensor motor and the fact that the microrobot is constantly in motion due to the unstable nature of the system. Neither the vibration effects or the instability appear to be present in the horizontal direction, which is why the RMS error on the horizontal motion is less than half as large. During horizontal motion the RMS error of the vertical position will increase. In theory the horizontal RMS error can be decreased through the use of averaging measurements, although it is not clear how many averaging measurements should be used or if any averaging should be used when horizontal motion is achieved without the aid of the aluminium block. Measurement averaging is not suitable for the vertical position measurement as it will cause system instability. Some of the positional variance is also caused by fluctuations in the output, which will produce variance in the magnetic field. However, this variance is difficult to quantify analytically.

As with the horizontal models the vertical model is not linked to the horizontal models and so it is difficult to predict what will happen during full spatial motion. The increase in the error is dependant on several factors, including the horizontal PID gains and the relative horizontal velocity. For example, when the microrobot traces out a circle with a radius of 3 mm at a rotational velocity of 0.16 rad/s, the RMS error is approximately 0.043 mm. When the rotational velocity is reduced to 0.0502 rad/s, the RMS error is reduced to a value of 0.024 mm. This reduction in velocity also improved the horizontal tracking capabilities of the microrobot. For 0.1 mm step motions with a horizontal PID controller K_c=1, T_i=0.005, T_d=1x10^{-6}, large disturbance spikes on the order of 0.2 mm are observed on the vertical position. These disturbance spikes can be effectively eliminated when the controller gains are tuned to K_c=0.025, T_i=0.006, T_d=1x10^{-4}.

An LQR controller designed for vertical position control using a state space realization derived from the black box model had poor dynamic characteristics when compared to the PID controller. The estimated range of the LQR controller was 1 mm, and the observed overshoot was typically 100%. The aluminium block was also needed to stabilize the motion. The primary advantage of the LQR controller is that it improves the RMS position error of the system. At an equivalent height above the aluminium block the RMS position error of the LQR controller is 0.014 mm, while the RMS position error of the PID controller was 0.019 mm. While the PID RMS position error appears to be relatively independent of the position, it was found that the RMS position error of the LQR controller increased as the microrobot moved away from the aluminium block. The deficiencies of the LQR controller are due to the inaccuracies in the system model, particularly as they relate to the estimation of the current input to the system.

8.2 Recommendations

The identified system models serve as a suitable starting point for modeling the system. The vertical system model can be improved by incorporating the electromagnet currents into the closed loop system response. This will depend on the ability to obtain a suitable current signal from the amplifier of the system. Improvements made in the experimental setup during the writing of this thesis have shown that this is indeed possible.

Although the linearized black box models have shown some promise their main weakness is that they cannot be linked together to see how generalized motion of the microrobot will occur. It would be more beneficial to derive a system model based on the known dynamics of the system. The resulting multi-input multi-output system would allow for observation of the linked behavior, and would also allow for more advanced controller design. For example, the circular trajectories presented in Chapter 7 could be improved by the use of feed-forward control. This would allow for more accurate position tracking and could also allow for faster rotational speeds at larger radii. A model based on the known system dynamics would also aid in improving the design of the LQR controller, as it would allow actual physical system states to be used instead of attempting to estimate the states via a

system realization. Even if the states could not be directly observed the design of the Kalman filter would be simplified since it would be possible to get a better estimate of the disturbances on the states based on the known measurements of the system. A linked model would also allow for better characterization of the positional errors introduced by the variance of the magnetic field.

The analytical force equation work presented in this thesis would be useful for developing a non-linear dynamic equation. The ability to develop an accurate analytical model will depend on deriving a method for accurately estimating the equation parameters, which will also require a reasonably accurate FEM simulation that can quickly and reliably compute the flux density gradients produced by the system. Knowing the rough working range of the microrobot narrows the required working range of the analytical equation, which may allow a linear fit equation to be used in place of a more complex equation.

In order to improve the horizontal performance of the system methods should be investigated to eliminate the need for the aluminium block. This may require FEA modeling to determine the exact nature of how the eddy currents affect the system performance. A more appropriate pole piece/microrobot combination could also be used. For example, the existing cylindrical pole piece could be replaced with a pole piece that produces a much smaller equilibrium area, which is better suited to levitation of a microrobot with a single dipole moment.

Further investigation on how the use of averaging measurements can improve the horizontal RMS error is needed. The design of the sensor mounting bracket should also be examined to see if there is a way in which the vertical position RMS error can be minimized by reducing the vibrational effects caused by the motor in the laser micrometer.

Provided that the general characteristics of the magnetic drive unit remain the same, different microrobots consistent with the parameters of the existing prototype can be developed and implemented on the system using the controllers presented in this thesis. This will allow for parallel development of microrobot technologies, such as power supplies and actuator technologies.

References

[1] Kortschak, A., A. Shirinov, T. Truper and S. Fatikow. "Development of mobile versatile nanohandling microrobots: design, driving principles, haptic control." Robotica v 23 (2005): 419-434.

[2] Shibata, Takayuki, Takanari Sasaya, and Nobuaki Kawahara. "Development of In-Pipe Microrobot Using Microwave Energy Transmission." Electronics and Communications in Japan, Part 2 v 84 n 11 (2001): 1-8.

[3] Suzumori, Koichi , Toyomi Miyagawa, Masanobu Kimura, and Yukihisa Hasegawa. "Micro Inspection Robot for 1-in Pipes." IEEE/ASME Transactions on Mechatronics, v 4 n 3 (1999): 286-292.

[4] Dario, P et al. "A Micro Robotic System for Colonoscopy." Proceedings - IEEE International Conference on Robotics and Automation v 2 (1997): 1567-1572.

[5]Chan, Yawen, Max Q.-H. Meng and Xiaona Wang. "A Prototype Design of Wireless Capsule Endoscope". Proceedings of the IEEE International Conference on Mechatronics & Automation (2005): 400-403.

[6] Arai, K.I. and T.Honda. "Micromagnetic Actuators." Robotica v 14 (1996): 477-481.

[7] Dario, P et al. "Microactuators for Microrobots: A Critical Survey." Journal of Micromechanics and Microengineering v 2 n 3 (1992): 141-157.

[8] Rembold, U. and Fatikow, S. "Autonomous Microrobots". Journal of Intelligent and Robotic Systems v 19 (1997): 375–391.

[9] Guo, Shuxiang, Toshio Fukuda, and Kinji Asaka. "A New Type of Fish-Like Underwater Microrobot." IEEE/ASME Transactions on Mechatronics v 8 n 1 (2003): 136-141.

[10] Stefanini, C., M.C. Carrozza, and P. Dario. "A Mobile Microrobot Driven by a new Type of Electromagnetic Micromotor". Seventh International Symposium on Micro Machine and Human Science. (1996): 195-201.

[11] Lyshevski, Sergey Edward. "Micromanipulators Actuated By Micromotors". Proceedings of the 41st IEEE Conference on Decision and Control. (2002):3658-3663.

[12] Suzumori, Koichi, Kohei Hori, and Toyomi Miyagawa. "A Direct Drive Pneumatic Stepper Motor for Robots: Designs for Pipe Inspection Microrobots and Human Care Robots. Proceedings of the 1998 IEEE International Conference on Robotics and Automation. (1998): 3047-3052.

[13] Shibata,Takayuki, Takanari Sasaya, and Nobuaki Kawahara. "Development of In-Pipe Microrobot Using Microwave Energy Transmission." Electronics and Communications in Japan, Part 2 v 84, n 11 (2001):704-710.

[14] Hollar, Seth et al. "Solar Powered 10 mg Silicon Robot." Proceedings of the IEEE Micro Electro Mechanical Systems (MEMS). (2003): 706-711.

[15] Sakakibara, Takahisa et al. "Multi-Source Power Supply System Using Micro –Photovoltaic Devices Combined with Microwave Antenna." Proceedings of the IEEE Micro Electro Mechanical Systems (MEMS) (2001): 192-195.

[16] Park, K.h., K. Y. Ahn, S. H. Kim, and Y. K. Kwak. "Wafer Distribution System for a Clean Room Using a Novel Magnetic Suspension Technique". IEEE/ASME Transactions on Mechatronics v 3 n 1 (1998): 73-78.

[17] Mathieu, Jean-Baptiste et al. "Preliminary Studies for using Magnetic Resonance Imaging Systems as a Mean of Propulsion for Microrobots in Blood Vessels and Evaluation of Ferromagnetic Artefacts". Canadian Conference on Electrical and Computer Engineering v 2 (2003): 835-838.

[18] Honda, T., K.I. Arai, and K. Ishiyama. "Micro Swimming Mechanisms Propelled by External Magnetic Fields." IEEE Tranactions on Magnetics, v 32 n 5 (1996): 5085-5087.

[19] Bonsor, Kevin. "How Maglev Trains Work." Online. Internet. Available at http://travel.howstuffworks.com/maglev-train.htm. First accessed June 3 2006.

[20] Campo, Alexandre and Felipe Pait. "Propulsion Control in a Linear Electrodynamic Motor with Two Degrees of Freedom." Proceedings of the 2001 IEEE International Conference on Control Applications (2001): 52-57.

[21] Han, Hyung-Suk. "A Study of the Dynamic Modeling of a Magnetic Levitation Vehicle." SME International Journal, Series C: Mechanical Systems, Machine Elements and Manufacturing, v 46 n 4 (2003): 1497-1501.

[22] Lin**,** Chin E. and Ming The Huang. "Implementation of Roll Motion in Magnetic Suspension Wind Tunnel." Proceedings of the IEEE 2000 National Aerospace and Electronics Conference. (2000): 758-765.

[23] Jung, Kwang Suk and Yoon Su Baek. "Study on a Novel Contact-Free Planar System Using Direct Drive DC Coils and Permanent Magnets". IEEE/ASME Transactions On Mechatronics, v 7 n 2 (2002): 35-43.

[24] Maggiore, Manfredi and Rafael Becerril. "Modeling and control design for a magnetic levitation system**."** Interational Journal of Control v 77, n 10 (2004): 964-977.

[25] Kim, Won-Jong and David L. Trumper. "High-precision magnetic levitation stage for photolithography." Precision Engineering v 22 n 2 (1998):66-77.

[26] Salcudean, S. E., N.M Wong and Ralph L. Hollis. "Design and Control of a Force-Reflecting Teleoperation System with Magnetically Levitated Master and Wrist." IEEE Transactions on Robotics and Automation. v 11, n. 6 (1995): 844-858.

[27] Verma, S. Development Of Novel High-Performance Six-Axis Magnetically Levitated Instruments For Nanoscale Applications. Texas: Texas A&M University, 2005.

[28] Verma, S., Won-Jong Kim and Jie Gu. "Six Axis Nanopositioning Device With Precision Magnetic Levitation Technology." IEEE/ASME Transactions on Mechatronics v. 9 n. 2 (2004): 384-391.

[29] Cui, Tianshi, Yusuke Fujiwara, and Koichi Oka. "2 DOF maglev system with permanent magnet motion control." Proceedings of the SICE Annual Conference (2005): 3859-3862.

[30] Khamesee, Mir Behrad et al. "Design and Control of a Microrobotic System Using Magnetic Levitation." IEEE/ASME Transactions on Mechatronics v 7 n 1 (2002): 1-14.

[31] Haddab, Y., N. Chaillet, and A. Bourjault. "A Gripper using smart Piezoelectric actuators." IEEE International Conference on Intelligent Robots and Systems v 1 (2000): 659-664.

[32] Yesin, K, B., Karl Vollmers and Bradley J. Nelson. "Analysis and Design of Wireless Magnetically Guided Microrobots in Body Fluids." Proceedings of the IEEE International Conference on Robotics and Automation (2004):1333-1338.

[33] Tsuda, Naoaki, Norihiko Kato, Yoshihiko Nomura, and Hirokazu Matsui. "Design framework of teleoperating system for magnetically levitated robot with force-feedback" Proceedings of SPIE - The International Society for Optical Engineering v 4570 (2001): 25-33

[34] Guru, Bhag Sing and Huseyin R. Hiziroglu. Electromagnetic Field Theory Fundamentals. Toronto: PWS Publishing Company, 1998.

[35] Shameli, Ehsan. Design, Implementation and Control of a Magnetic Levitation Device for Microrobotics Applications. Waterloo: University of Waterloo, 2006.

[36] Jeans, Sir J.H. The Mathematical Theory of Electricity and Magnetism. Cambridge: University Press, 1958.

[37] "Rare Earth Magnets." Online. Internet. Available at http://www.magnetsource.com/Solutions_Pages/rareerth.html. Last Accessed July 5, 2006.

[38] "Metric Neodymium Rare Earth Magnets". Online. Internet. Available at http://www.indigo.com/magnets/gphmgnts/metric-neodymium-rare-earth-magnets.html. First accessed September 15, 2004.

[39] Sen, P.C. Principles of Electric Machines and Power Electronics. New York: John Wiley and Sons, 1989.

[40] Williams, James H. Fundamentals of Applied Dynamics. New York: John Wiley and Sons, 1996.

[41] Khamesee, M.B., and Ehsan Shameli. "Pole Piece Effect on Improvement of Magnetic Controllability for Non-Contact Micromanipulation." Submitted to the IEEE Journal of Magnetism, July 2006.

[42] Gastmeier, Mark, QAM Engineer, S.G. Smallwood Inc. Personal communication regarding electromagnet properties. June 7, 2006.

[43] "Product Evaluation Report". Waterloo: S.G. Smallwood Inc, 2005.

[44] High Speed Laser Scan Micrometer LS-5000 Series Instruction Manual. Japan: Keyence Corporation, 1996.

[45] "NI-625x Specifications." Online. Internet. Available at http://www.ni.com/pdf/manuals/371291d.pdf. Last accessed July 8, 2006.

[46] "NI-PXI-6733 Data Sheet". Online. Internet. Available at http://www.ni.com/pdf/products/us/4daqsc362-365_372-373_368.pdf. Last accessed July 8, 2006.

[47] "Sorensen DCS series Data Sheet". Online. Internet. Available at http://www.elgar.com/pdfs/datasheets/DCS.pdf. Last accessed July 8, 2006.

[48] Ljung, Lennart. "System Identificaion: Theory for the User." New Jersey: Prentice Hall, 1999.

[49] Wilson, W.J. System Identification: ECE 683. Waterloo: Department of Electrical and Computer Engineering, 2004.

[50] Moudgalya, Kannan M. "Discrete PID Controller." Online. Internet. Available at http://www.che.iitb.ac.in/faculty/km/cl692/07oct05-3.pdf. Accessed May 2, 2006.

[51] Linard, N., B.D.O Anderson, and F. DeBruyne. "Closed Loop Identification of Nonlinear Systems." Proceedings of the 36th IEEE Conference on Decision and Control (1997): 2998-3003.

[52] Elbuken, Caglar, M.B. Khamesee and M. Yavuz. "Eddy current damping for magnetic levitation: Downscaling from macro to micro levitation." Submitted to Journal of Physics D: Applied Physics July 2006.

[53] "LQR. (Control System Toolbox)." Online. Internet. Available at http://www.mathworks.com/access/helpdesk/help/toolbox/control/ref/lqr.html . Accessed June 19, 2006.

[54] "Kalman (Control System Toolbox.)". Online. Internet. Available at http://www.mathworks.com/access/helpdesk/help/toolbox/control/ref/kalman.html . Accessed June 19, 2006.

Appendix A
FEM Model Descriptions

This appendix gives a brief overview of the setup parameters for the FEM models used in this thesis. All model files are located on the Appendix CD.

A-1. FEMLAB Single Electromagnet Models

These models are set up as 2D magnetostatic axisymmetric problems with azimuthal induction currents. The system consists of the core, the coil, and the air workspace. The core is modeled as a rectangle and the coils are modeled as circles. The system solves for the magnetic vector potential A of each element (Wb/m). The vector potential represents a base quantity of the field from which other magnetic properties are easily written. See [34] for more information.

The domain equation solved by the system is $\nabla \times (\mu^{-1}(\nabla \times A)) = J^e$, where μ is the permeability of the subdomain and J^e is the current density in the subdomain.

FEMLAB contains default physical parameters for common working materials. The core subdomain is set as iron, and the coils are set as copper. Air is the default setting for all other subdomains. Each coil is also assigned the required current density for the given problem.

Boundary conditions where continuity is required are automatically set by FEMLAB. The boundary conditions set by the user are typically those of the workspace boundary. The boundary lying along the line of symmetry is set for axial symmetry. All other boundaries are set as magnetic insulation (no flux through the boundary). Point conditions are not used.

Default meshing parameters are used. Default meshing parameters are available with different levels of coarseness. In general the coarseness of the mesh is chosen to balance the accuracy of the results with the amount of extra computation time that comes with the increase in the number of elements.

The choice of solver is left to the software, and is chosen from any of the standard linear stationary solvers.

A-2. FEMLAB Electromagnet and Pole Piece Models

The setup of these models is largely similar to the model described above. The main difference is that the system is now purely a 2D model as opposed to a 2D axisymmetric model, and all external boundaries are set as magnetic insulation. Currents are perpendicular to the plane and the system still solves for the vector potential. The pole piece subdomain is set as iron. The currents are set so that the coil models on one side of an electromagnet flow into the page and the currents on the other side of the coil flow out of the page. The currents must flow in the same manner in both electromagnets. Figure A-1 shows the meshed model.

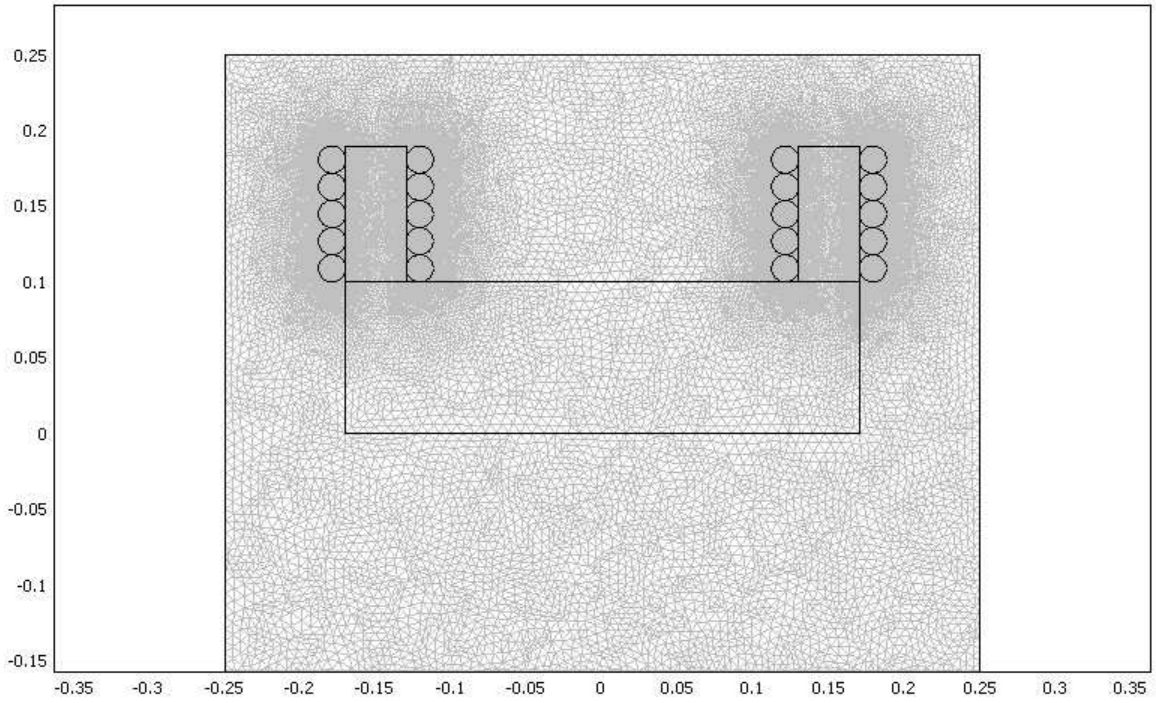

Figure A-1: Meshed 2D model of the magnetic drive unit.

A-3. ANSYS Model

The setup file for the ANSYS model is shown below. This model was developed by Ehsan Shameli, a Ph.D candidate at the University of Waterloo. ANSYS also solves for the magnetic vector potential.

```
! Air is Volume 16

FINISH
/CLEAR,START

*SET,N,1350
*SET,I1,0.001
*SET,I2,0.001
*SET,I3,0.001
*SET,I4,1
*SET,I5,0.001
*SET,I6,0.001
*SET,I7,0.001
*SET,L,0.04000

*SET,A,0.1200
*SET,B,0.200
*SET,C,0.05000
*SET,GAP,0.12
*SET,W,0.035

*SET,HEIGHT,0.018+A+L+C+GAP
*SET,WIDTH,0.066+B-W/2
*SET,XC,0.012+L+A-HEIGHT/2
*SET,ZC,0.012+L+A-HEIGHT/2
*SET,XC,0.006-WIDTH/2

/PREP7
CYL4,0.4400000E-01,0.000000,0.01000, , , ,L
CYL4,0.2200000E-01,0.3810512E-01,0.01000, , , ,L
CYL4,-0.2200000E-01,0.3810512E-01,0.01000, , , ,L
CYL4,-0.4400000E-01,0.000000,0.01000, , , ,L
CYL4,-0.2200000E-01,-0.3810512E-01,0.01000, , , ,L
CYL4,0.2200000E-01,-0.3810512E-01,0.01000, , , ,L
CYL4,0.00000,0.00000,0.01000, , , ,0.04000

CYL4,0,0,0.066, , , ,0.006

FLST,5,7,6,ORDE,2
FITEM,5,1
FITEM,5,-7
VSEL,S, , ,P51X
FLST,3,7,6,ORDE,2
FITEM,3,1
```

```
FITEM,3,-7
VGEN, ,P51X, , ,0,0,0.006, , ,1
ALLSEL,ALL
FLST,2,8,6,ORDE,2
FITEM,2,1
FITEM,2,-8
VGLUE,P51X

NUMCMP,VOLU

BLOCK,-W/2,W/2  ,-W/2,W/2,0.006+L+0.006,0.006+L+A-W+0.006,
BLOCK, W/2,W/2-B,-W/2,W/2,0.006+L+A-W+0.006,0.006+L+A+0.006,
BLOCK, W/2-B,W/2-B + W,-W/2,W/2,0.006+L+A-W+0.006,-GAP-0.006-C+W,
BLOCK, W/2-B,W/2,-W/2,W/2,-GAP-0.006-C+W ,-GAP-0.006-C,
BLOCK, -W/2,W/2 ,-W/2,W/2,-GAP-0.006-C+W,-GAP-0.006,

CYL4,0,0,0.066, , , ,0.006
VSEL,S, , ,      14
FLST,3,1,6,ORDE,1
FITEM,3,14
VGEN, ,P51X, , ,0,0,0.006+L, , ,1
CYL4,0,0,0.066, , , ,0.006
VSEL,S, , ,      15
FLST,3,1,6,ORDE,1
FITEM,3,15
VGEN, ,P51X, , ,0,0,-0.006-GAP, , ,1
ALLSEL,ALL

FLST,2,15,6,ORDE,2
FITEM,2,1
FITEM,2,-15
VGLUE,P51X
NUMCMP,VOLU

CYL4,XC,0,2.2*WIDTH, , , ,2.2*HEIGHT
FLST,3,1,6,ORDE,1
FITEM,3,16
VGEN, ,P51X, , ,0,0,ZC-1.1*HEIGHT, , ,1

FLST,2,16,6,ORDE,2
FITEM,2,1
FITEM,2,-16
VOVLAP,P51X
NUMCMP,VOLU
```

```
!!!!!!!!E L E M E N T   D E F I N I T I O N  !!!!!!!!!!!!!!!!!!!!!!!!!!!!!!!!!!!!!!!!!!!!!!!!!!

/NOPR
/PMETH,OFF,1
KEYW,PR_SET,1
KEYW,PR_STRUC,0
KEYW,PR_THERM,0
KEYW,PR_FLUID,0
KEYW,PR_ELMAG,1
KEYW,MAGNOD,1
KEYW,MAGEDG,0
KEYW,MAGHFE,0
KEYW,MAGELC,0
KEYW,PR_MULTI,0
KEYW,PR_CFD,0
/GO
ET,1,SOLID96
!!!!!!!!!!!!!!!!!!!!!!!!!!!!!!!!M A T E R I A L   P R O P E R T I E S  !!!!!!!!!!!!!!!!

/PREP7
TB,BH,1,1,30,                                    ! Material 1 (Iron Core)
TBTEMP,0
TBPT,,355,0.70
TBPT,,405,0.80
TBPT,,470,0.90
TBPT,,555,1.00
TBPT,,673,1.10
TBPT,,836,1.20
TBPT,,1065,1.30
TBPT,,1220,1.35
TBPT,,1420,1.40
TBPT,,1720,1.45
TBPT,,2130,1.50
TBPT,,2670,1.55
TBPT,,3480,1.60
TBPT,,4500,1.65
TBPT,,5950,1.70
TBPT,,7650,1.75
TBPT,,10100,1.80
TBPT,,13000,1.85
TBPT,,15900,1.90
TBPT,,21100,1.95
```

```
TBPT,,26300,2.00
TBPT,,32900,2.05
TBPT,,42700,2.10
TBPT,,61700,2.15
TBPT,,84300,2.20
TBPT,,110000,2.25
TBPT,,135000,2.30
TBPT,,200000,2.41
TBPT,,400000,2.69
TBPT,,800000,3.22
MPTEMP,,,,,,,,
MPTEMP,1,0
MPDATA,MURX,1,,4000

MPDATA,MURX,2,,1                                    ! Material 2 (Air)
MPTEMP,,,,,,,,
MPTEMP,1,0

!!!! E L E M E N T   A T T R I B U T E   !!!!!!!!!!!!!!!!!!!!!!!!!!!!!!!!!!!!!!!!!!!!!!!!!!!

FLST,5,16,6,ORDE,2
FITEM,5,1
FITEM,5,-16
CM,_Y,VOLU
VSEL, , , ,P51X
CM,_Y1,VOLU
CMSEL,S,_Y
CMSEL,S,_Y1
VATT,     1, ,   1,      0
CMSEL,S,_Y
CMDELE,_Y
CMDELE,_Y1
VSEL,S, , ,     16
CM,_Y,VOLU
VSEL, , , ,     16
CM,_Y1,VOLU
CMSEL,S,_Y
CMSEL,S,_Y1
VATT,     2, ,   1,      0
CMSEL,S,_Y
CMDELE,_Y
CMDELE,_Y1
ALLSEL,ALL
!!!!!!!!!!!!!!!!   M E S H I N G   T H E   P A R T S   !!!!!!!!!!!!!!!!!!!!!!!!!!!!!!!!!!!!!!!!!!!!
```

```
SMRT,8
MSHAPE,1,3D
MSHKEY,0
FLST,5,16,6,ORDE,2
FITEM,5,1
FITEM,5,-16
CM,_Y,VOLU
VSEL, , , ,P51X
CM,_Y1,VOLU
CHKMSH,'VOLU'
CMSEL,S,_Y
VMESH,_Y1
CMDELE,_Y
CMDELE,_Y1
CMDELE,_Y2
!!!!!!!!! D E F I N I N G   T H E   C O I L S      !!!!!!!!!!!!!!!!!!!!!!!!!!!!!!!!!!!!

LOCAL,1000,0,0.044,0,0.026, , , ,1,1,
WPCSYS,-1,1000,
RACE,0.016,0.016,0.015,N*I1,0.010,0.039, , , 'C1'

LOCAL,2000,0,0.022,0.03810512,0.026, , , ,1,1,
WPCSYS,-1,2000,
RACE,0.016,0.016,0.015,N*I2,0.01,0.039, , , 'C2'

LOCAL,3000,0,-0.022,0.03810512,0.026, , , ,1,1,
WPCSYS,-1,3000,
RACE,0.016,0.016,0.015,N*I3,0.01,0.039, , , 'C3'

LOCAL,4000,0,-0.044,0,0.026, , , ,1,1,
WPCSYS,-1,4000,
RACE,0.016,0.016,0.015,N*I4,0.01,0.039, , , 'C4'

LOCAL,5000,0,-0.022,-0.03810512,0.026, , , ,1,1,
WPCSYS,-1,5000,
RACE,0.016,0.016,0.015,N*I5,0.01,0.039, , , 'C5'

LOCAL,6000,0,0.022,-0.03810512,0.026, , , ,1,1,
WPCSYS,-1,6000,
RACE,0.016,0.016,0.015,N*I6,0.01,0.039, , , 'C6'
LOCAL,7000,0,0.0000,0.0000,0.026, , , ,1,1,
WPCSYS,-1,7000,
RACE,0.016,0.016,0.015,N*I7,0.01,0.039, , , 'C7'
```

```
!! D E F I N I N G   T H E   B O U N D A R Y   C O N D I T I O N S   !!!!!!!!!!!!!!!!!

/SOL
FLST,2,1,1,ORDE,1
FITEM,2,1
D,P51X,MAG,0,

!!!

MAGSOLV,3, , ,0.001,25,1

!!!!!

*SET, Z , -0.030

/POST1

PATH,P1,34,30,16,

 PPATH, 1,0,-0.08, 0.08,Z,0,
 PPATH, 2,0, 0.08, 0.08,Z,0,
 PPATH, 3,0, 0.08, 0.07,Z,0,
 PPATH, 4,0,-0.08, 0.07,Z,0,
 PPATH, 5,0,-0.08, 0.06,Z,0,
 PPATH, 6,0, 0.08, 0.06,Z,0,
 PPATH, 7,0, 0.08, 0.05,Z,0,
 PPATH, 8,0,-0.08, 0.05,Z,0,
 PPATH, 9,0,-0.08, 0.04,Z,0,
 PPATH,10,0, 0.08, 0.04,Z,0,
 PPATH,11,0, 0.08, 0.03,Z,0,
 PPATH,12,0,-0.08, 0.03,Z,0,
 PPATH,13,0,-0.08, 0.02,Z,0,
 PPATH,14,0, 0.08, 0.02,Z,0,
 PPATH,15,0, 0.08, 0.01,Z,0,
 PPATH,16,0,-0.08, 0.01,Z,0,
 PPATH,17,0,-0.08, 0.00,Z,0,
 PPATH,18,0, 0.08, 0.00,Z,0,
 PPATH,19,0, 0.08,-0.01,Z,0,
 PPATH,20,0,-0.08,-0.01,Z,0,
 PPATH,21,0,-0.08,-0.02,Z,0,
 PPATH,22,0, 0.08,-0.02,Z,0,
 PPATH,23,0, 0.08,-0.03,Z,0,
 PPATH,24,0,-0.08,-0.03,Z,0,
```

PPATH,25,0,-0.08,-0.04,Z,0,
PPATH,26,0, 0.08,-0.04,Z,0,
PPATH,27,0, 0.08,-0.05,Z,0,
PPATH,28,0,-0.08,-0.05,Z,0,
PPATH,29,0,-0.08,-0.06,Z,0,
PPATH,30,0, 0.08,-0.06,Z,0,
PPATH,31,0, 0.08,-0.07,Z,0,
PPATH,32,0,-0.08,-0.07,Z,0,
PPATH,33,0,-0.08,-0.08,Z,0,
PPATH,34,0, 0.08,-0.08,Z,0,

PDEF, ,B,Z,AVG

Appendix B

DAQ Accuracy Calculation

The Relevant DAQ properties are:

Input Range	+/- 10 volts
Number of Bits	16
Resolution	0.305 mV
Random Noise Variance	280 μVrms
Gain Error	83e-6 V/V
Offset Error	20e-6 V/V
Gain Temperature Sensitivity	13e-6 V/(V°C)
Offset Temperature Sensitivity	21e-6 V/(V°C)
Reference Temperature Sensitivity	1e-6 V/(V°C)
Integral Non-Linearity Error	60e-6 V/V

Table B-1: NI-PXI-6251 Characteristics. [45]

The accuracy for a given measurement is calculated as follows:

$$Net\ Gain\ Error = Gain\ Error + Gain\ Temperature\ Sensitivity * \Delta T_i + Reference\ Temperature\ Sensitivity * \Delta T_{e.}$$

where ΔT_i is the temperature change since the last internal calibration and $\Delta T_{e.}$ is the temperature change since the last external calibration.

$$Net\ Offset\ Error = Offset\ Error + Offset\ Temperature\ Sensitivity * \Delta T_i + Integral\ Non\text{-}Linearity\ Error$$

$$Noise\ Uncertainty = Random\ Noise * 3 * n^{-0.5}$$

Where n is the number of averaging measurements. For the current setup, n=1.

$$Absolute\ Accuracy = Reading * Net\ Gain\ Error + Range * Net\ Offset\ Error + Noise\ Uncertainty.$$

Assume ΔT_i=1 °C and ΔT_e=10 °C. These are the standards given by [45]. Then

Net Gain Error = 83×10^{-6} V/V

Net Offset Error = 101×10^{-6} V/V

Noise Uncertainty=840×10^{-6} V.

At 0 V, *Accuracy*= 101×10^{-6} V/V*10 + 840×10^{-6} V = 1850 μV.

At 10 V, *Accuracy* = 83×10^{-6} V/V *10+101×10^{-6} V/V*10 + 840×10^{-6} V = 2680 μV.

Appendix C

Position Measurement Accuracy Calculation

A nominal measurement N by the laser micrometer will have an associated accuracy *a*. So the actual measurement may be

$$\begin{matrix} N + a \\ N - a \end{matrix} \tag{C-1}$$

This measurement will be converted into a voltage by the laser micrometer. The voltage will be

$$\begin{matrix} V = \dfrac{(N + a - 20)}{2} \\ V = \dfrac{(N - a - 20)}{2} \end{matrix} \tag{C-2}$$

It is assumed that the board rounds to the nearest resolution point, which is 0.01 mm.

The DAQ resolution is 305 μV. The number of bits *n* required to represent the input voltage is calculated as.

$$n = \frac{V}{305 \times 10^{-6}} \tag{C-3}$$

This must be rounded to the nearest integer value, and then *n* must be multiplied by the resolution to find the actual input voltage seen by the board.

Based on the DAQ accuracy discussed in Appendix B, the absolute accuracy of the measurement can be calculated and the worst case actual input voltages can be calculated. This will yield four V_{DAQ} measurements, a high and low worst case voltage for each of the possible two worst case inputs.

Finally, the voltage is converted back into the actual position measurement $N_{measured}$.

$$N_{measured} = 2V_{DAQ} + 20 \tag{B-4}$$

A sample calculation is shown in Table C-1.

Nominal Measurement	30.001	millimetres
Accuracy +/-	0.004	millimetres
So actual measurement may be	30.005 29.997	millimetres millimetres
Keyence Board Resolution	0.01	millimetres
Measurement if board rounds to nearest	30.01 30	millimteres
Equivalent Voltage	5.005 5	Volts
DAQ resolution	0.000305	volts
# bits needed	16409.84 16393.44	
Effective # bits	16410 16394	
Effective Input Voltage	5.00505 5.00017	Volts
DAQ accuracy	2.27E-03	Volts
Voltage Measured as	5.007315 5.002785 4.997905 5.002435	Volts
Effective Measurement	30.01463 30.00557 29.99581 30.00487	mm
Error	-0.01363 -0.00457 0.00519 -0.00387	mm

Table C-1: Sample accuracy calculation.

Appendix D

List of Files on the CD

Filename	Location	Description
Accuratemagnet2.mph	Chapter 2	FEMLAB model of a 500 turn electromagnet
SimplifiedElectromagnetModel.fl	Chapter 2	Simplified FEMLAB model of a 500 turn electromagnet
twoemtest.fl	Chapter 2	FEMLAB model of a 2D representation of a pole piece, consisting of 2 electromagnets and a 10 cm pole piece
Force on a Sphere.xls	Chapter 2	Calculation of the levitation force on a sphere due to levitation with a single electromagnet
Single Electromagnet Levitation.zip	Chapter 2	Data files related to simulation of levitation with a single electromagnet
2D Pole Piece Simulations.zip	Chapter 2	Data files related to estimation of the flux density from a simplified 2D pole piece
sensoraccuracytesting.vi	Chapter 3	LabVIEW VI used for recording data from the laser micrometer
Comparison of a Sample Hold process to a sampling process.xls	Chapter 3	Data collected to estimate the variance of the DAQ. For a hold process on the laser micrometer the input is constant and all variance in the measurement is due to the DAQ
static sensor error.xls	Chapter 3	Standard deviation measurements for the three laser micrometers

Filename	Location	Description
inchmeasurement.zip	Chapter 3	Data collected by the laser sensor measuring a one inch gauge block
2dinductanceestimation.fl	Chapter 4	2D FEMLAB simulation for one electromagnet and 1 cm pole piece
2emmodel.fl	Chapter 4	2D Femlab simulation for 2 electromagnets and 1 cm pole piece
main.log	Chapter 4	Setup file for the ANSYS simulation
pp.log	Chapter 4	path file for exporting data from ANSYS
2D Femlab Force Estimation.zip	Chapter 4	2D Femlab force estimation data files
3D Ansys Analysis.xls	Chapter 4	Ansys force estimation data files
Mod_gen.m	Chapter 5	Generalized least squares algorithm for use in MATLAB
Mod_ls.m	Chapter 5	Modified least squares algorithm for use in MATLAB
manual_ramp.zip	Chapter 5	LabVIEW RT program that can send be used for closed loop z positioning using step or ramp inputs
ramp.zip	Chapter 5	LabVIEW RT program used to generate a PRBS input to the system
verticalposition.mat	Chapter 5	MATLAB mat file storing vertical position model parameters
verticalpositionmodel.mdl	Chapter 5	Simulink representation of the vertical position model
PRBS Responses.zip	Chapter 5	PRBS response files

Filename	Location	Description
Step Responses.zip	Chapter 5	Vertical position step response files
Vertical Ramp Inputs.zip	Chapter 5	Ramp input response files
1withgenandrecursive.mat	Chapter 5 /rlocusestimation	MATLAB mat file containing the results of preliminary model estimation using generalized least squares and recursive least squares
0.3.mat	Chapter 5 /rlocusestimation	Modified Least Squares Identification, K_c=0.15 T_i=0.007 T_d=0.001
0.4.mat	Chapter 5 /rlocusestimation	Modified Least Squares Identification, K_c=0.2 T_i=0.007 T_d=0.001
0.667.mat	Chapter 5 /rlocusestimation	Modified Least Squares Identification, K_c=0.334 T_i=0.007 T_d=0.001
1.mat	Chapter 5 /rlocusestimation	Modified Least Squares Identification, K_c=0.5 T_i=0.007 T_d=0.001
1.43.mat	Chapter 5 /rlocusestimation	Modified Least Squares Identificaition, K_c=0.7 T_i=0.007 T_d=0.001
2.43.mat	Chapter 5 /rlocusestimation	Modified Least Squares Identification, K_c=1.43 T_i=0.007 T_d=0.001
poleestimation.xls	Chapter 5 /rlocusestimation	Preliminary Root Locus Estimation
xidentification.mat	Chapter 6	Modified least squares identification of the *x* response
yidentification.mat	Chapter 6	Modified least squares identification of the *y* response
xmodel.mdl	Chapter 6	Simulink open loop *x* model

Filename	Location	Description
ymodel.mdl	Chapter 6	Simulink open loop y model
closedloopxmodel.mdl	Chapter 6	Closed loop x model
closedloopymodel.mdl	Chapter 6	Closed loop y model
manual_ramp2.zip	Chapter 6	LabVIEW RT files for open loop *x* and *y* control
x control.zip	Chapter 6	LabVIEW RT files for closed loop *x* control
y control.zip	Chapter 6	LabVIEW RT files for closed loop *y* control
Open Loop Horizontal Responses.zip	Chapter 6	Horizontal Open Loop Data
Horizontal PD Control.zip	Chapter 6	Horizontal PD control data
Horizontal PID Control.zip	Chapter 6	Horizontal PID control data
discretestatespacemodel.mdl	Chapter 7	Simulink Model of the LQR Controller
discretestatespaceparameters.mat	Chapter 7	LQR parameters for the Simulink Model
full control.zip	Chapter 7	LabVIEW RT files for 3 axis motion using PID control
LQR Control.zip	Chapter 7	LabVIEW RT files for implementing the LQR controller
trajectory.zip	Chapter 7	LabVIEW RT files for generating circular trajectories
circle trajectory.zip	Chapter 7	Circle trajectory data files
LQR.zip	Chapter 7	LQR control data files
disturbance motions.zip	Chapter 7	Disturbance motion investigation data files
weightcompensation.xls	Chapter 7	Data used to estimate the equilibrium current algorithm for LQR control